Fall 2016

Functional nanoporous polyamide aerogels

Malik Adnan Saeed

Department: Chemistry

FUNCTIONAL NANOPOROUS POLYAMIDE AEROGELS

by

MALIK ADNAN SAEED

A DISSERTATION

Presented to the Faculty of the Graduate School of the

MISSOURI UNIVERSITY OF SCIENCE AND TECHNOLOGY

In Partial Fulfillment of the Requirements for the Degree

DOCTOR OF PHILOSOPHY

in

CHEMISTRY

2016

Approved

Dr. Nicholas Leventis, Advisor
Dr. Chariklia Sotiriou-Leventis, Co-Advisor
Dr. Amitava Choudhury
Dr. Manashi Nath
Dr. Muthanna H. Al-Dahhan

DEDICATED TO

MY BELOVED WIFE SADAF MALIK

&

CHILDREN

AREEB MALIK

SHAHEER MALIK

ALAYA MALIK

PUBLICATION DISSERTATION OPTION

This dissertation consists of the following three manuscripts which have been published, or submitted for publication in the format of Chemistry of Materials.

Paper I: Pages 35-101 have been submitted to *Chemistry of Materials.*

Paper II: Pages 102-174 have been published in *Chemistry of Materials* 2016, *28,* 4867−4877.

Paper III: Pages 175-250 have been published in *Chemistry of Materials* 2016, *28,* 67–78.

ABSTRACT

Aerogels are low-density materials consisting of 3D assemblies of nanoparticles with high open porosities and surface areas. Inspired by the extraordinary mechanical strength of polymer crosslinked aerogels, our recent attention is focused on inexpensive multifunctional isocyanates reacting with a variety of aromatic, organometallic and inorganic monomers. Three such systems discussed here are:

(A) Polymeric aerogels synthesized via a room temperature reaction of an aromatic triisocyanate with pyromellitic acid. Using solid-state CPMAS ^{13}C and ^{15}N NMR, it was found that the skeletal framework was a statistical co-polymer of polyamide, polyurea and polyimide. Stepwise pyrolytic decomposition followed by reactive etching of those components yielded microporous carbon aerogels with good gas sorption selectivities that may find application in CO_2 capture and sequestration.

(B) Ferrocene-polyamide aerogels prepared in one pot via reaction of an aromatic triisocyanate and ferrocene dicarboxylic acid. Upon pyrolysis (≥800 °C / H_2), monolithic Fe(0)-doped C-aerogels were obtained followed by quantitative transmetalation with noble metals (M: Au, Pt, Pd). The latter were demonstrated as heterogeneous catalysts in high yield reduction, oxidation and Heck coupling reactions. The monolithic catalysts were reused several times without loss of activity.

(C) Polyureas formed via reaction of an aromatic isocyanate with several mineral acids, (H_3BO_3, H_3PO_4, H_3PO_3, H_2SeO_3, H_6TeO_6, H_5IO_6 and H_3AuO_3). The residual boron in the H_3BO_3 model system was very low (≤0.05 % w/w), leaving pure polyurea as product and ruling out any process, in analogy to that with carboxylic acids, for systematic incorporation of H_3BO_3 in the polymeric chains.

ACKNOWLEDGEMENTS

Undertaking this PhD has been a truly life-changing experience for me and it would not have been possible to do without the support and guidance by many people. I owe my deepest gratitude to my advisor, Professor Nicholas Leventis and co-advisor Professor Chariklia Sotiriou-Leventis for their continuous guidance, positive criticism and support throughout the completion of my graduate studies at Missouri S&T. Their influence is spread throughout this dissertation, and I am sure that it will be evident well beyond this dissertation into the future. In short, I look at them as my real role models in science.

It gives me great pleasure to acknowledge my committee members, Dr. Amitava Choudhury, Dr. Manashi Nath and Dr. Muthanna H. Al-Dahhan for devoting their precious time reading my dissertation and their valuable suggestions. I thank the Department of Chemistry of Missouri S&T for providing teaching assistantships and its resources. Special thanks are reserved for Dr. Terry Bone and Dr. Arif Mumtaz for their encouragements and guidance for all these years. I would also like to thank all the past and present fellow group members especially Dhiru, Chakar, Shruti, Abhishek, Suraj, Hojat, Tara, Parwani, Chandana and Rushi for their help, encouragement and more importantly their friendship. The warm support and my new friends in Rolla is unforgettable.

Finally, I would like to express my love and affection to my parents, Mr. & Mrs. Saeed Anwar Malik, my grandparents, Mr. and Mrs. Shafi Mohammad, my uncles and aunts Mr. and Mrs. Sharif Bhatti and Riaz Malik, my brothers Dr. Mudassir, Maj. Aamir, Bilal Saeed and sisters Anilla and Saira for their unconditional love. Special thanks to my mother in law Shagufta Malik, phophoo Shameem and my sister in laws Shafaq, Sahar, Anika and Zhoiya, words alone cannot express my feelings for how much I owe them.

TABLE OF CONTENTS

Page

LIST OF ILLUSTRATIONS

SECTION Page

LIST OF TABLES

SECTION Page

LIST OF SCHEMES

SECTION Page

PAPER II

PAPER III

1. INTRODUCTION

1.1. AEROGELS

At first the name “aerogel” may sound deceptive, because there is nothing gelly about them: they are dry, fairly rigid foam-like materials. The “gel” part comes from the fact that they are derived from wet-gels, physically similar to edible gels, in which the liquid component has been replaced with air while maintaining the gel’s sparse solid intricate architecture and porous backbone.[1] Kistler in 1931 first synthesized silica aerogels and described them as “gels in which the liquid has been replaced by air, with very moderate shrinkage of the solid network.”[2] This has remained the most widely used definition, and for quite some time aerogels were synonymous with silica aerogels commonly known as “frozen smoke.” Thus, silica aerogels have emerged as the most studied type of aerogels and are known for their ultralow thermal conductivities (as low as 10 mW m^{-1} K^{-1}), extremely low densities (as low as 0.001 g cm^{-3}), high specific surface areas (500-2000 m^2 g^{-1}), low dielectric constants (as low as 1.02), and excellent optical transparency (~91% per cm). Those properties render silica aerogels valuable high-performance thermal and electrical insulators, as well as supports for chemical sensors and catalysts.[1]

Over the years, aerogel research moved slowly from silica to several other kinds of non-silica oxides, resorcinol formaldehyde (RF), carbonized-RF (CRF), and aerogel composites.[3] With the advent of the 21st century, aerogels experienced an accelerated growth. A number of novel non-silica oxide aerogels,[4] chalcogenide aerogels,[5] and other aerogel composites sprang up one after another.[6] Recently, new types of aerogels such as carbon nanotube (CNT),[7] graphene,[8] silicon and carbide (or carbonitride) aerogels[9] have

been added to the array of known aerogels regularly. It can be expected, without exaggeration, that hardly any substance could not be converted into an aerogel!

Technically, an aerogel is "an open-celled, mesoporous, solid foam that is composed of a three-dimensional network of interconnected nanostructures that exhibits a porosity (non-solid volume) of no less than 50%."[10] In general, aerogels are chemically identical to the bulk form of the skeletal material. Aerogels, however, possess many dramatically enhanced material properties over the dense (non-porous) form of the same substance (e.g., substantial increased surface areas and catalytic activity), while frequently other material properties (such as mechanical strength) are compromised.[10] The low densities and length-scale effects of aerogels are due to their nanostructures that consist of 3D assemblies of nanoparticles. The densities of solids and liquids are much the same, but the densities of liquids and gases differ by 3–4 orders of magnitude. In addition, the enthalpy of liquids and gases differs greatly as shown in Figure 1.1. The aerogel could, to a great extent, fill the gap between the liquid and gas state. Hence aerogels are recognized not only as functional materials, but they have been also suggested to comprise a new state of matter.[11]

1.2. THREE DIMENTIONAL ASSEMBLY OF NANOPARTICLES BY SOL-GEL CHEMISTRY

The uncanny array of extreme material properties of aerogels emanates from their porous (3D) structure shown in Figure 1.2. Their solid framework consists of a complex hierarchical network of aggregates comprising of small bead-like primary nanoparticles gathering together to form fractal porous secondary particles, which finally agglomerate to a pearl-necklace like structure.

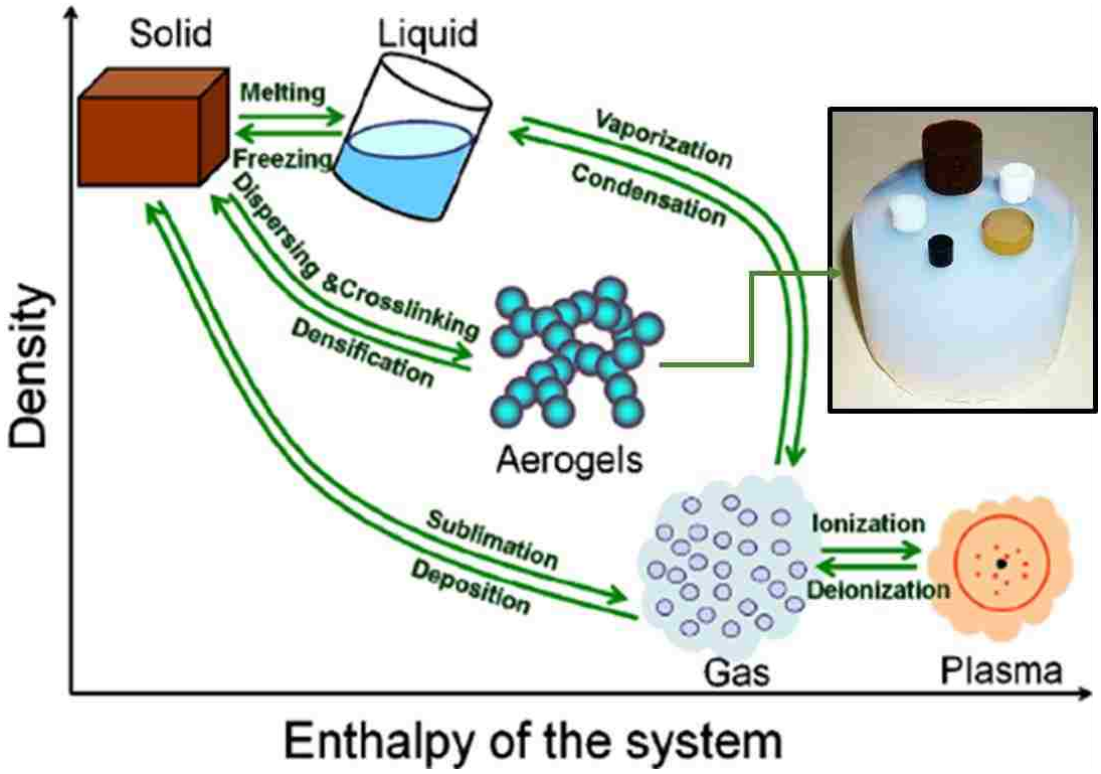

Figure 1.1. The distribution and transition of different states of matter in "density" vs. "enhalpy of the system" diagram.[12]

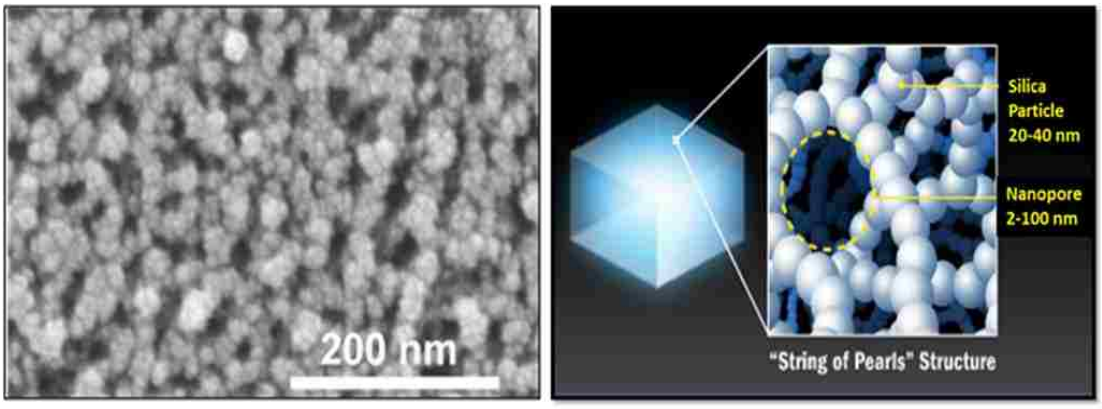

Figure 1.2. The typical nanostructure of a silica aerogel (left) and its microscopic appearance (right) showing a pearl-necklace like structure.[13]

The sol-gel process (Figure 1.3) is a multifaceted "bottom up" wet-chemistry synthetic process, originally designed for the manufacturing of glasses and ceramic materials with high purity and high homogeneity. The sol-gel process offers a degree of control on composition and structure at molecular level. In turn, gels can be made from reactive sols.[14] More precisely, a "sol" is a liquid colloidal system, in which the dispersed particles are either solid or large molecules, and their dimensions are in the colloidal range (1-1000 nm). A "gel" is a solid colloidal system, in which the dispersed substance forms a continuous, coherent skeletal framework that interpenetrated by a system (usually liquid) consisting of kinetic units smaller than the colloidal entities.[15]

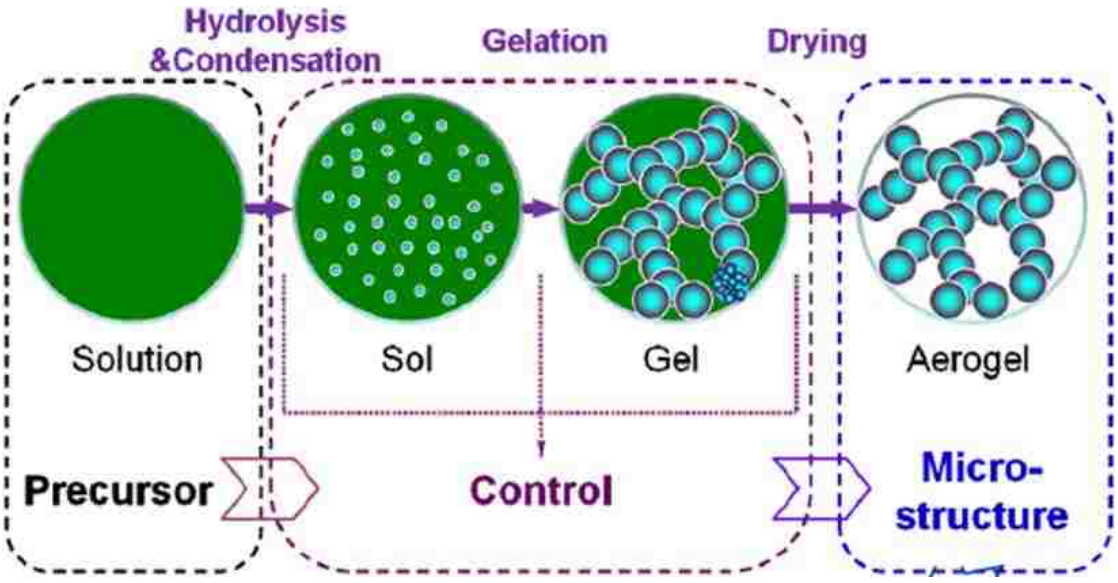

Figure 1.3. Preparation of an aerogel via the sol-gel process.[12]

The sol-gel synthesis of silica aerogels, typically starts with alkoxy silane precursors which include tetramethylorthosilicate ($Si(OCH_3)_4$, abbreviated as TMOS) or tetraethylorthosilicate ($Si(OC_2H_5)_4$, abbreviated as TEOS). These monomers are dissolved in their corresponding alcohols, and water is added for hydrolysis. The first step of the process is either an acid- or a base-catalyzed hydrolysis of the alkoxy silane to form silanols, which undergo a condensation reaction *in situ* to form Si-O-Si linkages[16] as shown in Scheme 1.1.

Scheme 1.1. Formation of a silica network from hydrolysis and condesnsation of TMOS.

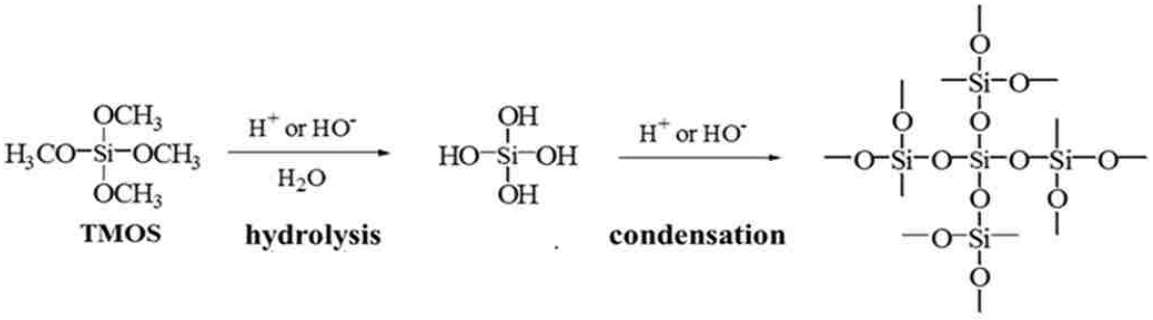

In practice, hydrolysis and condensation reactions continue, the viscosity of the reaction mixture increases until the "sol" ceases to flow, forming a "gel." The resulting solvent-filled wet-gels are aged for a period of time to allow the gel network to undergo Ostwald ripening and become stronger. Solvent is exchanged with alcohol to remove gelation water from the pores, and at this stage silica wet-gels can be dried by two different methods: either by (a) evaporation of pore-filling solvent at ambient conditions or (b) conversion of the pore-filling solvent to a supercritical fluid (SCF). Generally, supercritical

drying is carried out after solvent-exchange of the pore-filling solvent with liquid CO_2 is an autoclave. It is CO_2 then that is converted to a SCF (critical point of CO_2 : 31.1 °C at 1072 psi),[17] which is vented off isothermally. The first method results into collapsed porous structures with extensive macroscopic shrinkage. Those materials are referred to as xerogels. In the second method, the volume of the wet-gel is preserved into the final dry object, which is referred to as an aerogel.

1.3. POLYMER-CROSSLINKED AEROGELS

Because of their nanostructure-related properties, silica aerogels can be a potentially employed as thermal and acoustic insulators,[18] dielectrics,[19] catalyst supports,[20] and as hosts for functional guests in chemical, electronic and optical devices.[21] Silica aerogels, however, have actually been used only in some special environments, for example as Cerenkov radiation detectors in certain nuclear reactors, aboard spacecraft as collectors for cosmic particles (NASA's Stardust program),[22] and for thermal insulation in planetary vehicles on Mars. The main issue against wider commercialization of silica aerogels is their fragility and poor mechanical properties. The poor mechanical properties of silica aerogels are generally credited to the well-defined narrow interparticle necks.[23] The fragility issue of silica aerogels has been resolved by our group, by introducing crosslinked silica aerogels with organic polymers.[24] For that, silica nanoparticles having hydroxyl group on the surface reacted with commercially available polyisocyanates. Polyurethane tethers generated after the reaction, bridge (crosslinked) silica nanoparticles chemically, and reinforce interparticle necks. Conformal coating of polymer is formed on the entire skeletal framework, without compromising the porous structure (Figure 1.4). The resulting

materials have been referred to as polymer-crosslinked aerogels (X-aerogels). By crosslinking, the mechanical strength of an aerogel increases by 300 times for a nominal increase in density by only a factor of 3.[24]

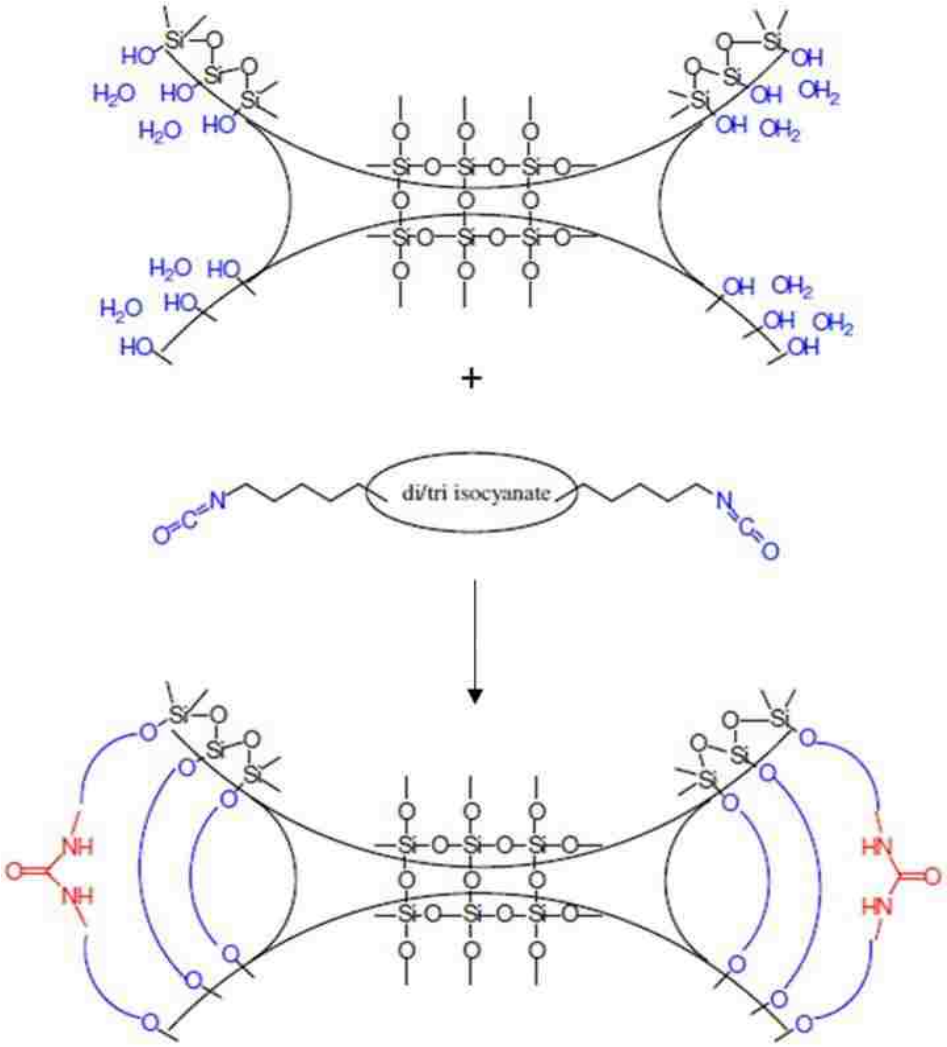

Figure 1.4. Polyurethane tethers connecting interparticle necks in polymer crosslinked aerogels.

A variety of different chemistries can be introduced to form polymeric bridges between the skeletal particles. For this, by a careful choice of the molecular precursors used in the sol-gel process, the surface of silica is provided with functional groups other than -SiOH. Amine modification for example is carried out by co-gelation of (3-aminopropyl) triethoxy silane (APTES) with tetramethyl orthosilicate (TMOS). Owing to the slow hydrolysis of APTES, the surface of silica nanoparticles is decorated with $–NH_2$ groups from APTES.[25] These dangling $–NH_2$ groups have been used for crosslinking with polyurea[24a,b] as shown in Figure 1.5 and in similar fashion with epoxy resins,[26] polystyrene,[24c] and polymethyl methacrylate.[24d]

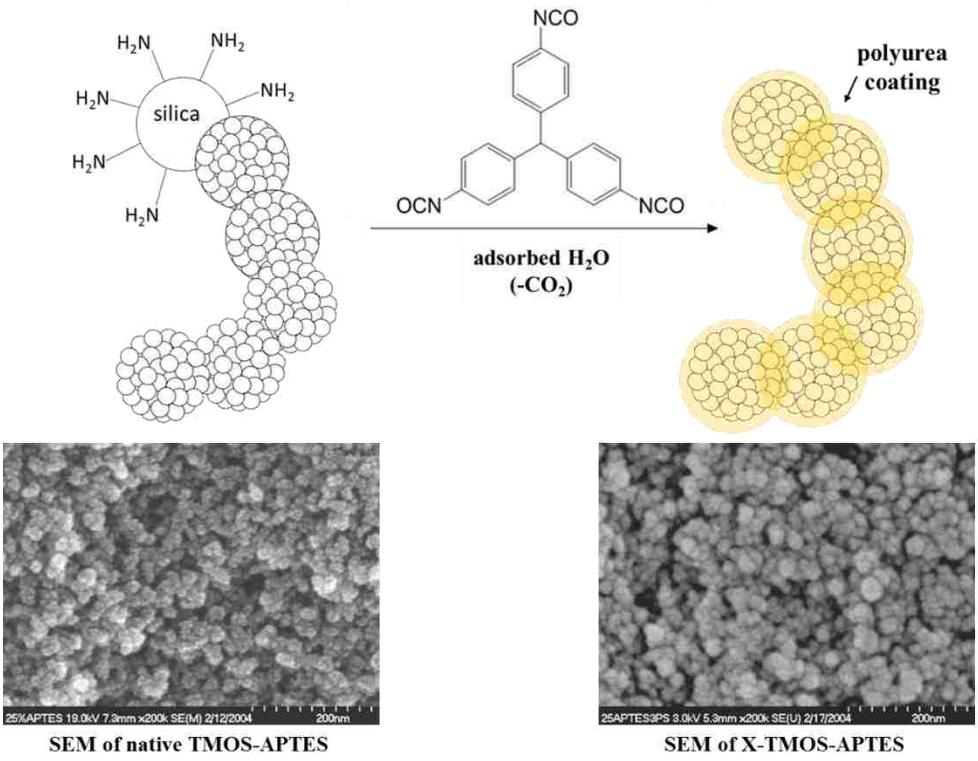

Figure 1.5. A thin polymer layer is formed conformally on the skeletal silica nanoparticles.

X-aerogels are exceptionally strong materials in comparison not only with their non-crosslinked counterparts (native aerogels), but also with other materials that are usually considered strong, such as steel, Kevlar and silicon carbide ceramics.[27] Since, the mechanical strength of X-aerogels is due to the conformal polymer, it was reasoned that purely polymeric aerogels with the structure of X-aerogels should have similar mechanical properties.

Typically, isocyanate-derived polymeric materials (polyurethanes, polyurea) are usually very sturdy and mechanically strong. Keeping in mind the rich chemistry of isocyanates, we introduce some novel tough robust porous materials for gas storage, and as catalyst supports.

1.4. ISOCYANATE CHEMISTRY

The isocyanate, -N=C=O, is a very reactive electrophile. This is because of the electron withdrawing capabilities of both the oxygen and nitrogen atoms rendering the electron density at the carbon much smaller than in a typical carbonyl group Scheme 1.2. Therefore, the isocyanate group is susceptible to nucleophilic attack as shown in (Scheme 1.3).

Scheme 1.2. Resonance within the isocyanate group.

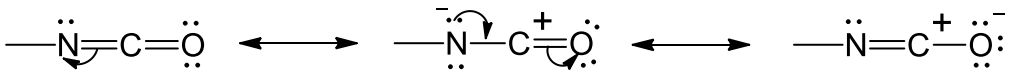

Scheme 1.3. Nucleophilic attack on the isocyanate group.

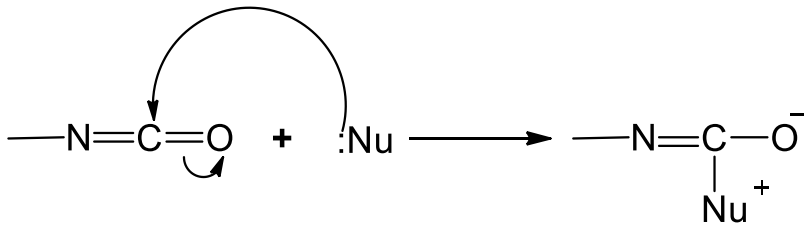

General nucleophiles and their relative reactivity are summarized in Table 1.1.

Table 1.1. Active-hydrogen compounds ordered by decreasing nucleophilicity towards the isocyanate group[28].

Active Hydrogen Compound	Typical Structure	Relative Reaction Rate (uncatalyzed at 25 °C)
Primary Aliphatic Amine	$R\text{-}NH_2$	100,000
Secondary Aliphatic Amine	$R_2\text{-}NH$	20,000 - 50,000
Primary Aromatic Amine	$Ar\text{-}NH_2$	200-300
Primary Alcohol	$R\text{-}CH_2\text{-}OH$	100
Water	H-O-H	100
Carboxylic Acid	RCOOH	40
Secondary Alcohol	$R_2CH\text{-}OH$	30
Urea	R-NH-CO-NH-R	15
Tertiary Alcohol	$R_3C\text{-}OH$	0.5
Urethane	R-HN-CO-OR	0.3
Amide	$RCO\text{-}NH_2$	0.1

The reactivity pattern of the isocyanate group is modulated by electron donating and withdrawing groups.[29] In that regard, the aromatic isocyanates are more reactive than their aliphatic counterparts. Isocyanates show very rich chemistry, reacting with a large variety of nucleophiles like water, alcohols, anhydrides etc., summarized in Figure 1.6.

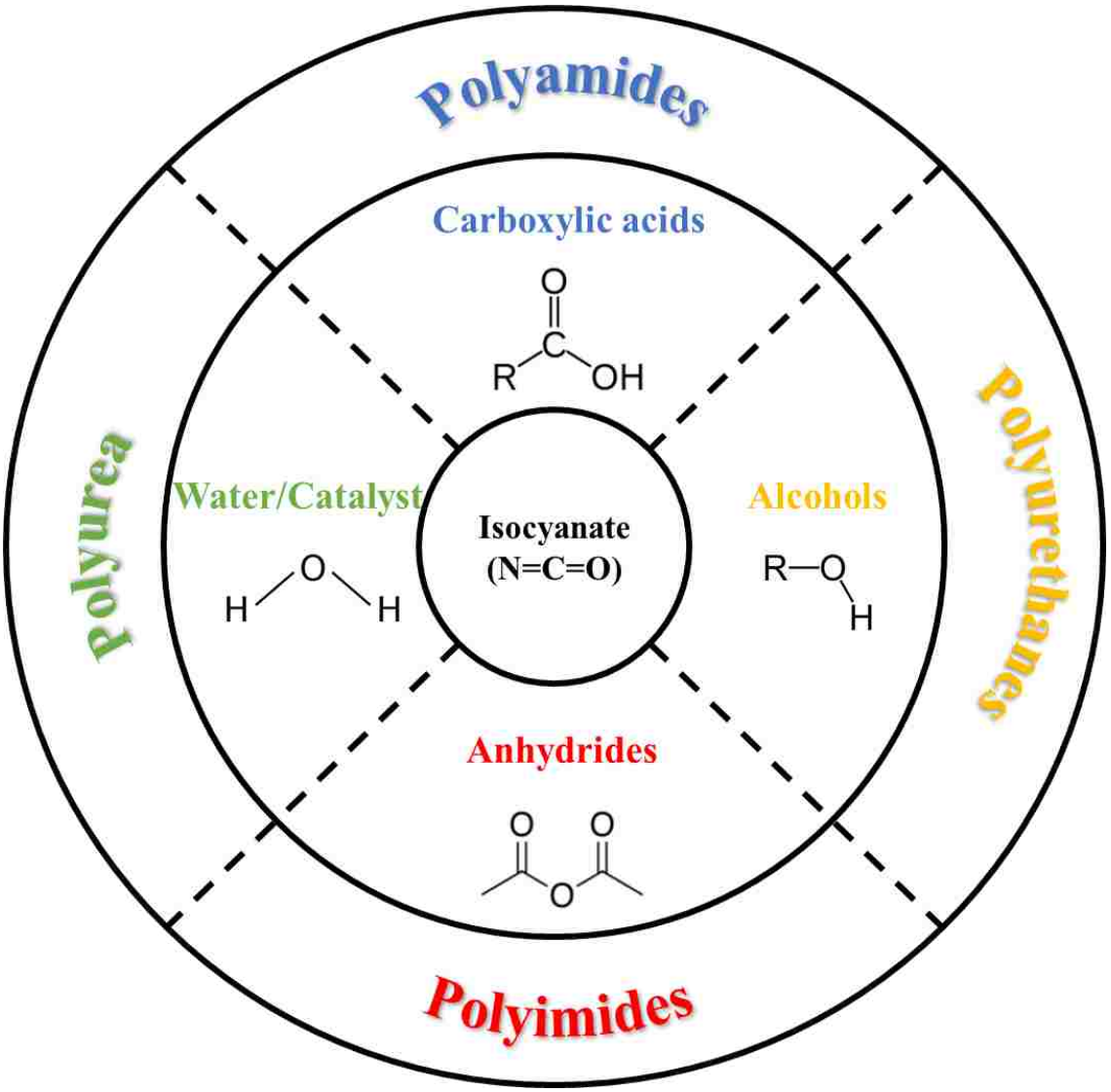

Figure 1.6. Reaction of isocyanate with some common nucleophiles.

This dissertation is based on the reaction of isocyanates with carboxylic acids towards polyamides, thereby that reaction is discussed in more detail.

Conventionally, polyamides are synthesized from acid halides and amines. In order to circumvent the use of acid halides, the idea of preparing polyamides directly from dicarboxylic acid and diisocyanates has also been explored.[30] The reaction can take place without catalyst at room temperature (23 ^{o}C) or slightly above. Using suitable catalysts, the reactions will be much faster.[31] For example, there are reports of fast synthesis of high molecular weight polyamides via polymerization of dicarboxylic acids with aromatic diisocyanates using Lewis acids as catalysts at relatively low temperatures (<100 ^{o}C) and with relatively short reaction times.[32] The reaction of an isocyanate with a carboxylic acid yields a condensation product: a carbamic-anhydride adduct (Scheme 1.4).

Scheme 1.4. Amide synthesis from isocyanates and carboxylic acids.

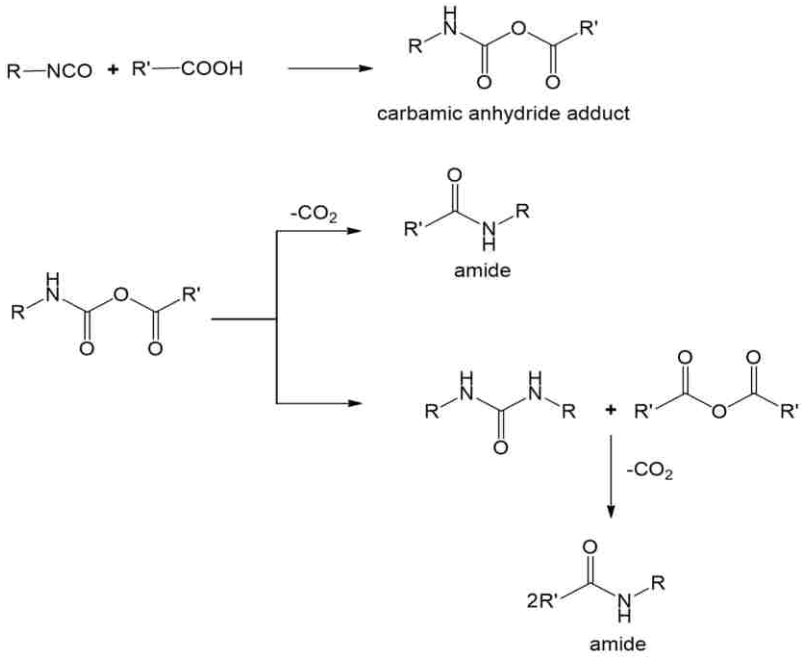

The carbamic-anhydride adduct may react intramolecularly (Scheme 1.5) to yield amide, or it may react bimolecularly with another molecule of the same kind towards symmetric urea and acid anhydride (Scheme 1.4). The latter two may react further towards the same amide obtained via the intramolecular route.

Scheme 1.5. Intramolecular decomposition of a carbamic carboxylic anhydride towards an amide.

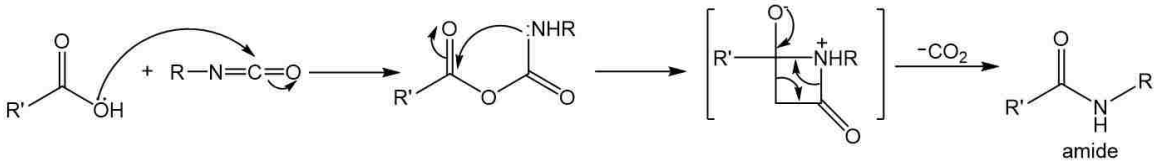

1.5. POLYAMIDES

Polyamides are commonly used as smart engineering materials. These materials are more sophisticated than most of the other currently known thermoplastics. Owing to their thermal stability, strong intermolecular forces, chain rigidity, and the inherent stability of the aromatic moiety, polyamides have exceptional strength coupled with excellent thermal resistance. They can replace steel, ceramics and glass fibers in many applications, and they are of particular interest in the aerospace industry, because of their low density.[33]

1.5.1. Synthesis of Polymides. There are several well-established methods for preparing polyamides.

1.5.1.1. Aromatic polyamides (aramids). An aramid is a polyamide where at least 85% of the amide bonds are attached to aromatic rings. The term “aramid” is short form of “aromatic polyamide.” They come as fibers in which the chain molecules are

highly oriented along the fiber axis. Aromatic polyamides were first introduced commercially as meta-aramid fibers in the early 1960's. Para-aramid fibers were developed in between 1960's and 1970's. These two aramids are similar in basic structure and are sometimes produced in the same production plants. Nomex® is a meta-aramid while Kevlar® is a para-aramid (Figure 1.7). The first aramid Nomex® was introduced by Du Pont in 1961 for products that needed dimensional stability and good heat resistance, and is prepared via the reaction of m-phenylenediamine and isophthaloyl chloride.

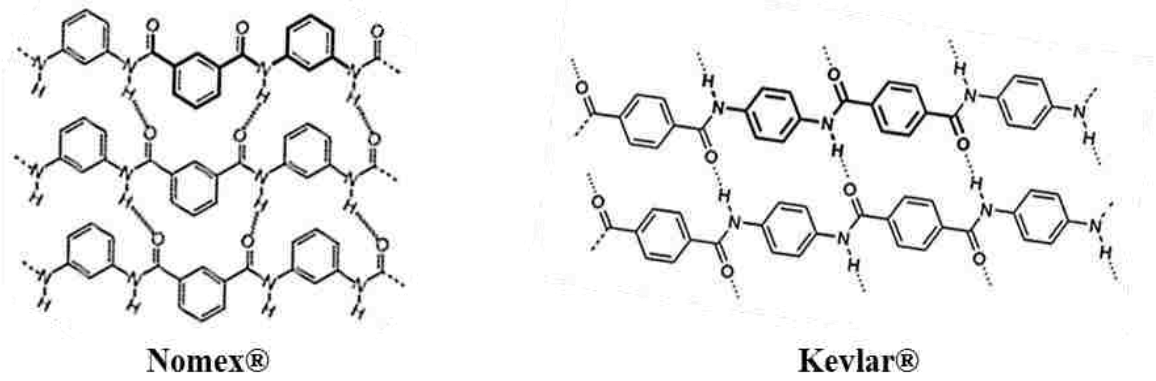

Figure 1.7. Nomex® is a meta-aramid while Kevlar® is a para-aramid.

Kevlar® involves the step-growth polymerization of a dicarboxylic acid with a diamine. This synthesis is typically a multi-step process at high reaction temperatures. For example, poly(hexamethylene adipamide) can be prepared from the corresponding stoichiometric dicarboxylic acid – diamine salt followed by pre-polymerization of the salt at a lower temperature to produce a lower molecular weight polymer in order to prevent the diamine from sublimation, and further polymerization to afford high molecular weight polyamide at 260-270 ^{o}C.[34] The high temperature treatment can be avoided by replacing

the carboxylic acid with its acid halide. However, this process requires the removal of hydrogen halide, which is the byproduct of the polymerization process (Scheme 1.6).

Scheme 1.6. Synthesis of Kevlar.

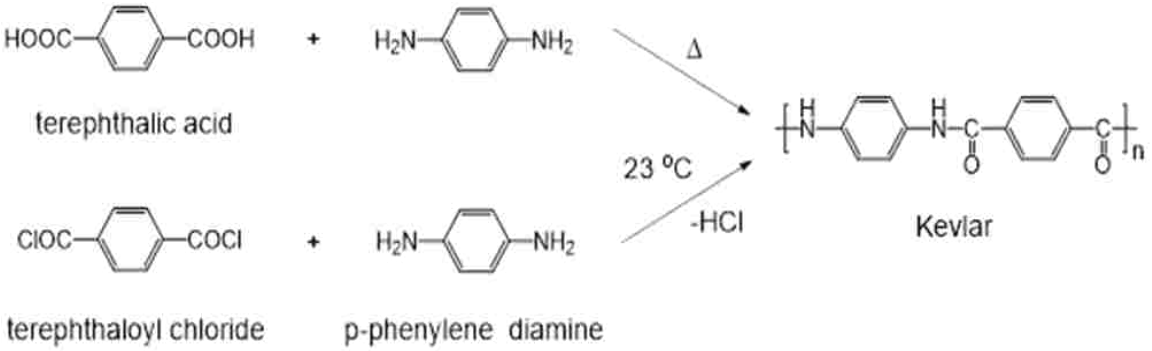

1.5.1.2. Organometallic polyamides. Organometallics are renowned as versatile species due to the range of accessible structural and bonding diversity to design the compounds to be used in a number of applications.[35] Ferrocene is a typical metallocene consisting of a central metal atom bound to two cyclopentadienyl rings on opposite sides forming a sandwiched complex.[36] Ferrocene can be easily functionalized on either one or both cyclopentadienyl rings with the same or variable substituents. The most common method used to synthesize ferrocene derivatives is represented in Scheme 1.7 which in turn can be used to prepare ferrocene amides.[37]

Scheme 1.7. Typical synthesis of ferrocene derivatives.

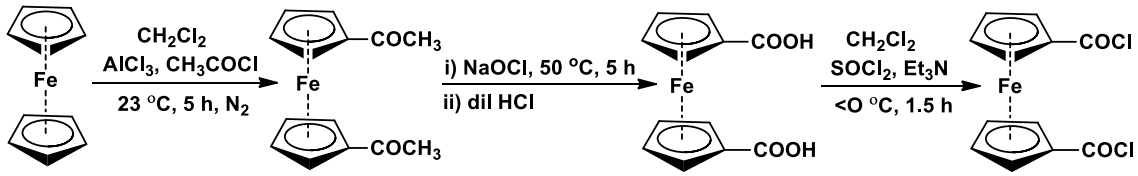

Ferrocene amides can be synthesized generally by following peptide coupling reaction protocols.[38] They may be prepared either by direct amide substitution on the cyclopentadienyl (Cp) ring, or on the alkyl/phenyl spacers as shown in Figure 1.8.

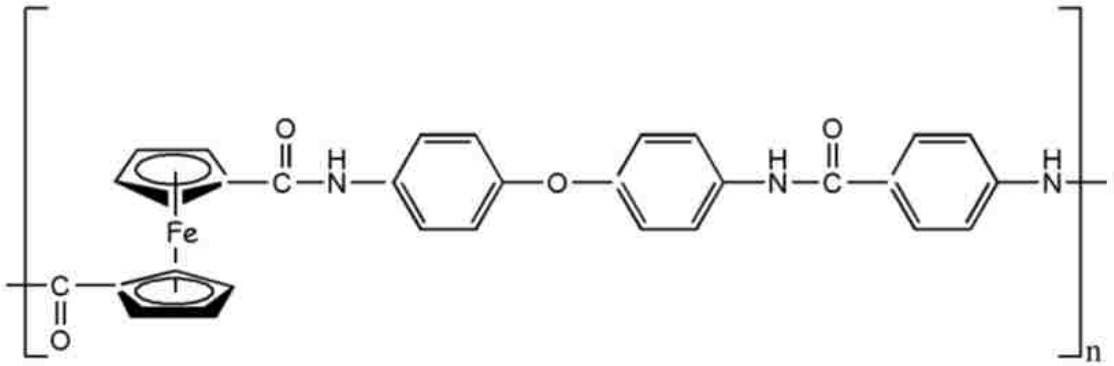

Figure 1.8. Ferrocene-incorporating polyamides synthesized via solution polycondensation.

In the 1960s, Knobloch and Rauscher considered room temperature interfacial polycondensation routes as convenient alternatives to the classic condensation reactions for the preparation of polyamides from 1,1'-ferrocenedicarbonyl chloride and several diamines.[39] In general, those polymers were not fully characterized, with rather low

molecular weights. Later in 1984, Rausch et. al reported the synthesis of elastomeric polyamides in high yields from 1,1'-bis(*β*-aminoethyl)-ferrocene and diacid chlorides.[40] Interestingly, since the amide functionality has hydrogen bonding properties. Ferrocene amides can form self-assembled structures. Therefore, isolated amide molecules are often linked *via* intermolecular hydrogen bonds into larger networks.[41] Recently, interest has been developing in the synthesis of polymers containing ferrocene in the main chain because of their catalytic[42] and magnetic properties,[43] thereby ferrocene-incorporated polyamides are again at the forefront.

1.5.1.3. "Polyamides" from isocyanates and mineral acids. Covalent linking of inorganic moieties (e.g. building blocks) with polymers is persued because it renders the structures extremely robust.[44] In that regard, amide derivatives of boronic acid have been disclosed. For example, the reaction of benzeneboronic acid with hexamethylene diisocyanate gives polymeric *N, N'*-hexamethylenebenzeneboronamide.[45] In another report, B-N-H linkages were formed in a 1960 patent[46] via direct reaction of anhydrous boric acid and a di-isocyanate as shown in Figure 1.9. No solvent was reported for that reaction.

Recently, the same reaction between an isocyanate and another mineral acid, a phosphoric acid derivative, was reported.[47] Again P-N-H linkages were proposed as shown in Figure 1.10 but evidence for the reported chemical composition was weak.

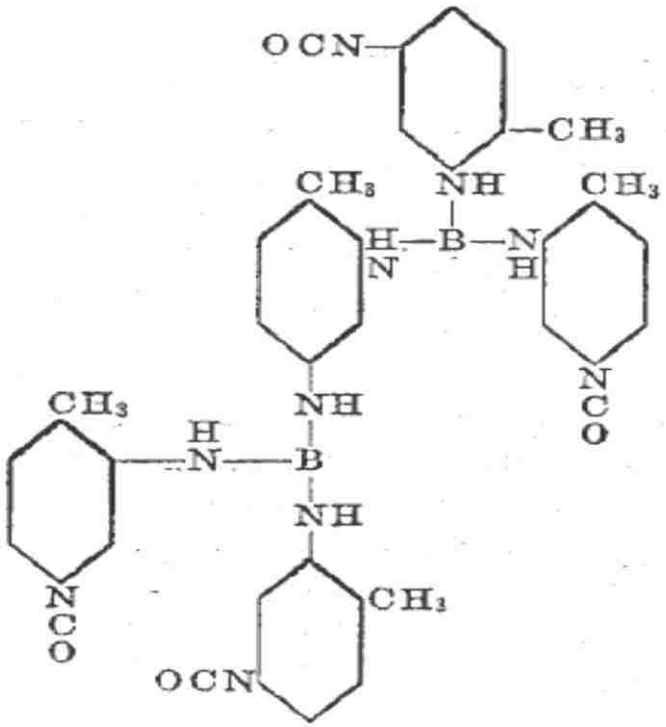

Figure 1.9. Structure given in US Patent 2,945,841 (1960) for a polyboronamide synthesized via reaction of boric acid and toluene diisocyanate.[46] As it is shown in this dissertation no boramide is formed by that reaction.

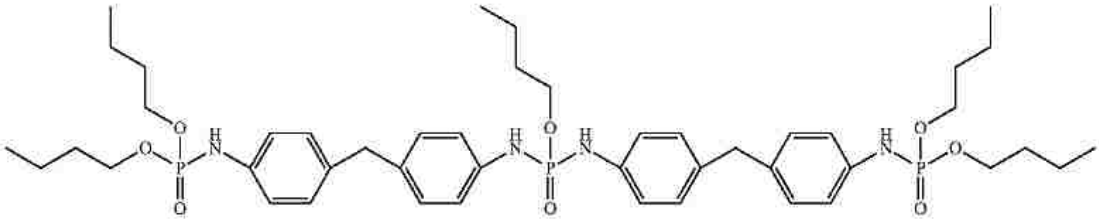

Figure 1.10. Proposed structure of a polymer synthesized from a phosphoric acid derivative and a diisocyanate.

1.5.2. Polyamide Aerogels. Designing Kevlar-type aerogels from *p*-phenylenediisocyanate and terephthalic acid imposes several interrelated chemical and

structural issues. Starting with their linear polymeric backbones, there is a limited chance for interparticle crosslinking, which in turn is a prerequisite for formation of the aerogel skeletal framework. Our group has bypassed that issue with hyperbranched structures based on trifunctional core monomers synthesized from the reaction of isocyanates and carboxylic acids.[48] That route offers several advantages, two of which stand out: (a) trifunctional aromatic isocyanates are low-cost bulk chemicals, while the corresponding aromatic amines are in general expensive; and, (b) the only by-product during polyamide formation is CO_2. Recently Williams and Meador proposed a new route to crosslinked polyamide aerogels by synthesizing amine end-capped oligomers from *m*-phenylenediamine and di or tri acid chloride in NMP followed by cross-linking with benzenetricarbonyl trichloride as shown in Scheme 1.8.[49]

1.6. CARBON AEROGELS

Carbon aerogels have been pursued for their electrical conductivity, thermal and chemical stability combined with the usual high surface area and porosity of aerogels. They are generally derived from pyrolysis of various types of organic aerogels in inert atmosphere.[50] Porous carbons are used for separations,[51] hydrogen storage,[52] CO_2 adsorption,[53] and as catalyst supports.[54] Porous carbons come in a wide range of forms, not only at the microscopic but also at the macroscopic level. Macroscopically, a porous monolithic carbon has several distinct advantages over powders.[55] Microscopically, monolithic carbon aerogels display the typical aerogel 3D bicontinuous hierarchical porosity. Combination of monolithicity and hierarchical porosity work synergistically towards low pressure drops, fast heat and mass transfer, high contacting efficiency, and

easy handling.[56] Those features render monolithic carbons suitable for gas sorption and separation, and that was explored here with CO_2 capture.

Scheme 1.8. Synthesis of cross-linked polyamide aerogels.

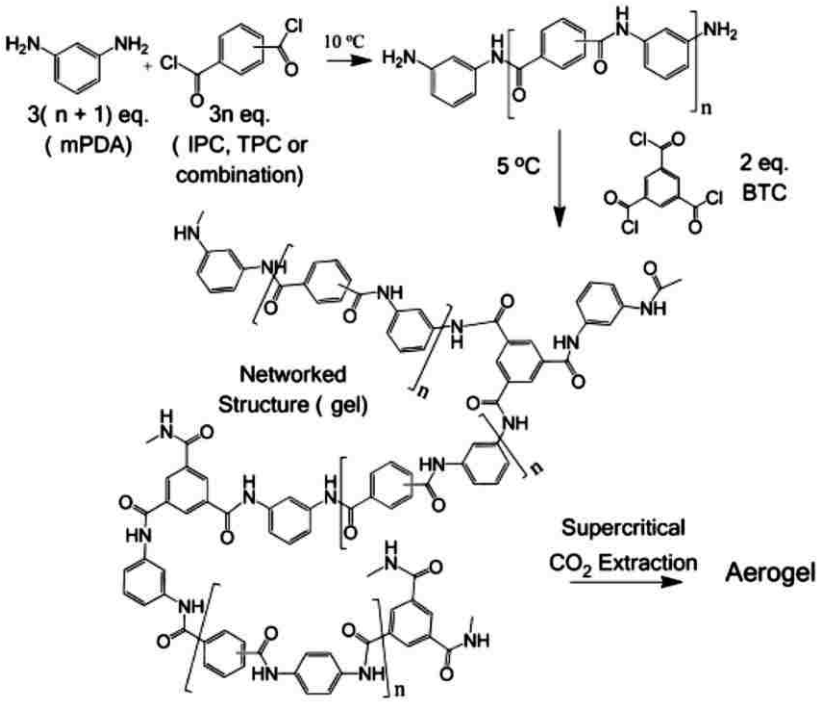

The first carbon aerogels were reported by Pekala and they were based on pyrolysis of phenolic-resin type of organic aerogels from condensation of resorcinol and formaldehyde.[57] We entered the field of carbon aerogels after we discovered an acid catalyzed (HCl) time-efficient synthetic route to resorcinol-formaldehyde aerogels, cutting Pekala's week-long gelation process to a couple of hours.[58] Then we discovered that numerous other aerogels derived from inexpensive isocyanate chemistry could be converted to monolithic carbon aerogels in high yields. Those polymeric aerogels include polyureas,[59] polyurethanes,[60] polyimides[61] and polyamides.[48]

1.7. METAL-DOPED CARBON AEROGELS

Transition metals are introduced in carbon aerogels in order to modify structure, conductivity or catalytic activity. The metal dopant is usually nano-sized with properties atypical of the corresponding bulk metals. Applications as electrodes in batteries, supercapacitors, adsorbents, molecular sieves and catalysts are all possible. Conventionally, metal-doped carbon aerogels can be prepared by three main strategies. The first is by addition of the soluble metal precursor (metal salt) in the initial sol.[62] The second involves use of a resorcinol derivative containing an ion exchange moiety, such as a -COOH group. Thus, the repeating unit of the organic polymer contains binding sites for metal ions to latch on and ensure uniform dispersion.[63] The third approach is to deposit the metal precursor on the organic or carbon aerogel by one of various methods including incipient wetness,[64] wet impregnation,[65] adsorption, sublimation and supercritical deposition.[63] There are drawbacks related to the aforementioned methods, for example changing the pH of the sol, hence making pore-size control difficult. Few authors have suggested that doped metal particles are anchored to the carbon structure in a way such that micropores act as nucleation sites for the metal nanoparticles. Anchoring of metal particles blocks entrance to micropores, hence the surface area of such carbon aerogels decreases.[63] Also anions of salts used as either polymerization catalysts, or in an ion exchange process have an effect on the sol-gel chemistry as well as on the resulting gel.[66]

Certain transition metals are also known as catalysts that induce low-temperature graphitization of carbon and iron is one such metal. Ferrocene was discovered by Keally and Pausan in 1951,[67] and has been used as a source of metallic iron.[68] Thus, one way to incorporate iron into carbons is by incorporating ferrocene in the backbone of a precursor

polymer.[37] For example, Furukawa et. al reported ordered mesoporous carbon (well-ordered porous structure with uniformly sized mesopores along with a narrow pore size distribution in regular carbon frameworks) prepared from ferrocene derivative using furfuryl alcohol as the main carbon source.[69] Schnitzler et. al reported a route to make iron and iron oxide-filled carbon nanotubes using ferrocene as precursor.[70] Ndamanisha et. al synthesized ordered mesoporous carbon containing iron oxides by using ferrocene carboxylic acid as the metal precursor and sucrose as the main carbon precursor.[71] Here we have introduced iron into porous materials by rendering ferrocene a polymer repeat unit in polyamide aerogels.

1.8. MOTIVATION AND SCOPE OF THE PRESENT WORK

The quest for novel functional materials has always been at the forefront of human civilization for survival, growth and betterment of life. In the modern reality, synthesis of functional materials should be based on reliable synthetic protocols using inexpensive starting materials and having visible applications. Here, we work with polyamide aerogels synthesized via an isocyanate route from organic, organo-metallic and inorganic precursors. Polyamides are typically synthesized from carboxylic acid chlorides and amines. In our group, we have developed and patented synthesis of polyamide aerogels from inexpensive multifunctional isocyanates and carboxylic acids. In the current research work we expand that isocyanate route to functional polyamide aerogels synthesized under milder conditions, which, therefore, are more energy efficient. Specifically, polyamide aerogels are synthesized via reaction of tris(4-isocyanatophenyl)methane (**TIPM**), an inexpensive monomer for several carbonizeable polymers,[59,61] and several multifunctional

aromatic/organo-metallic carboxylic acids in anhydrous solvents at ambient temperatures. Those polyamide aerogels were pyrolyzed to microporous/mesoporous sturdy monolithic carbon aerogels or to metal doped carbon aerogels. In an attempt to substitute mineral acids for carboxylic acids, we discovered a new route for metal or oxide doped polyurea aerogels.

1.9. AROMATIC POLYAMIDES (Aramids) AEROGELS

Before this dissertation work, polyamide aerogels were synthesized by our group with a tricarboxylic acid (trimesic acid) and a trifunctional isocyanate.[48] Here, we report milder conditions by increasing the active sites available for reaction by choosing a tetrafunctional carboxylic acid In a typical procedure 1,2,4,5-benzenetetracarboxylic acid (pyromellitic acid, PMA) was dissolved in variable amounts of anhydrous THF and that solution was added to a TIPM solution (Scheme 1.9).

Using solid-state CPMAS ^{13}C and ^{15}N NMR, it was found that the skeletal framework of the resulting PA-xx aerogels was a statistical co-polymer of polyamide, polyurea and polyimide. PA-xx aerogels were stable up to 250 ^{o}C by TGA (Figure 1.11), while in N_2 they carbonize with yield ~ 50% w/w and can be considered as precursors to porous carbons. Porous carbons are pursued as sorbents for CO_2 sequestration.[72] Since polyamides generally have good carbonization yields,[73] it was deemed reasonable to explore our polyamide aerogels. Carbonizeable polymers are capable of either cyclizing or undergoing ring fusion and chain coalescence by heating. For this the chain should either contain aromatic moieties or be aromatizable, usually by oxidation. For high carbonization yields, there should be just one carbon atom between aromatic rings; otherwise, pyrolytic

chain scission will prevail leading to loss of fragments.[74] Materials under this investigation fulfill these criteria. Thus, stepwise pyrolytic decomposition of those components yielded microporous carbon aerogels. Reactive etching increased microporosity by almost a four-fold.

Scheme 1.9. Reaction of 1,2,4,5-benzenetetracarboxylic acid (pyromellitic acid, PMA) with tris(4 isocyanatophenyl) methane (TIPM).

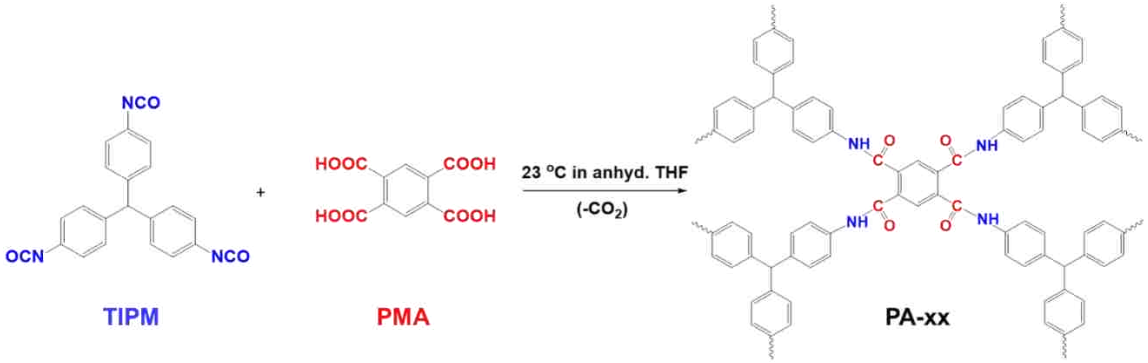

Pre-combustion, post combustion and oxy combustion are three main stages, in which CO_2 capture is relevant. Pre-combustion refers to removal of CO_2 from syngas prior to its combustion in power production, while post-combustion is generally used to separate CO_2 after burning of fossil fuels, and hence it gets difficult to treat large masses of flue gases (CO_2 15-16%, with N_2 70-75% and vapors around 5-7%).[75] We investigated our PA-xx derived carbons as absorbers for CO_2 sequestration and results show enhanced capacity and selectivity towards CO_2 under ambient conditions as shown in Figure 1.12.

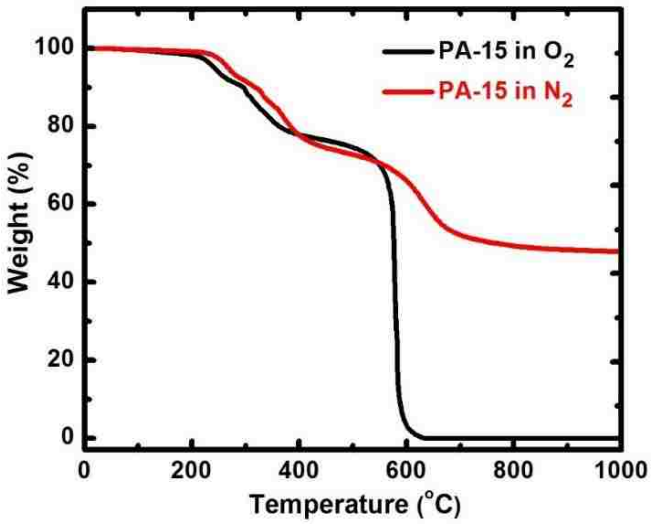

Figure 1.11. TGA analysis of PA-15 aerogels in O_2 as well as in N_2 as indicated.

Overall, the co-polymer of polyamide, polyurea and polyimide aerogels (PA-xx) was synthesized successfully via by a straightforward route at room temperature. Microscopically PA-xx consisted of nanoparticles. Upon pyrolysis, they were converted to microporous C-aerogels with satisfactory gas sorption and selectivity. These materials are excellent CO_2 adsorbents, taking up to 21% of their mass in CO_2 at ambient conditions. These materials are promising for scale-up because of their rapid synthesis, and low cost of the starting materials.

1.10. FERROCENE POLYAMIDE AEROGELS

Ferrocene based polyamide aerogels were prepared via a one pot synthesis of just two monomers without any polymerization catalyst directly resulting into wet gels that were dried into aerogels. Our motivation was based on the fact that inclusion of ferrocene as a polymer repeat unit in a carbonizeable polymer would create a 3D aerogel network

with the metal as a part of the polymer chain, that is Fe would be covalently bonded to the network (as opposed to doping, impregnating or ion exchange). The synthesis of polyamide aerogels incorporating ferrocene as a polymer repeat unit is shown in Scheme 1.10.

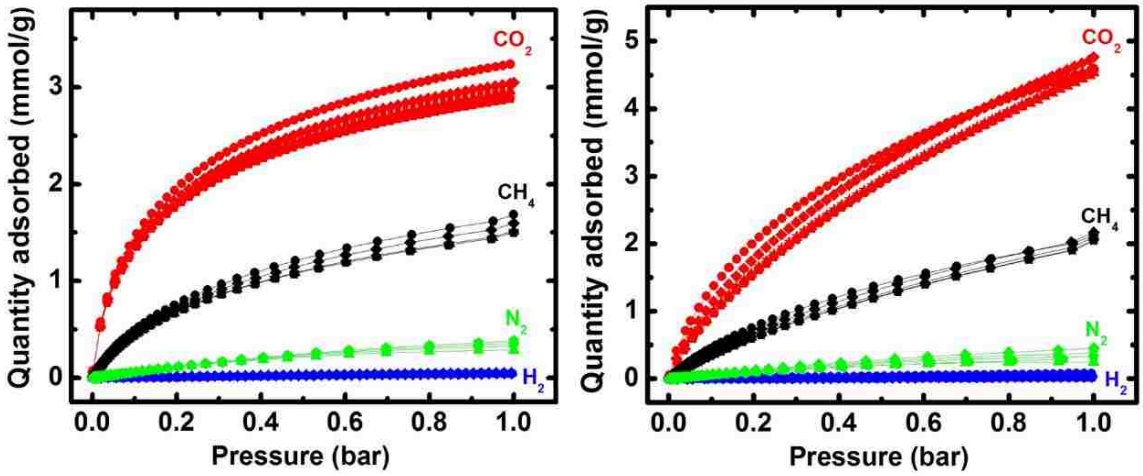

Figure 1.12. Selective adsorption of CO_2, CH_4, H_2 and N_2 by PA-xx carbon (left) and etched carbon aerogels (right) at 273 K and 1 bar.

Scheme 1.10. Reaction of $Fc(COOH)_2$ with TIPM.

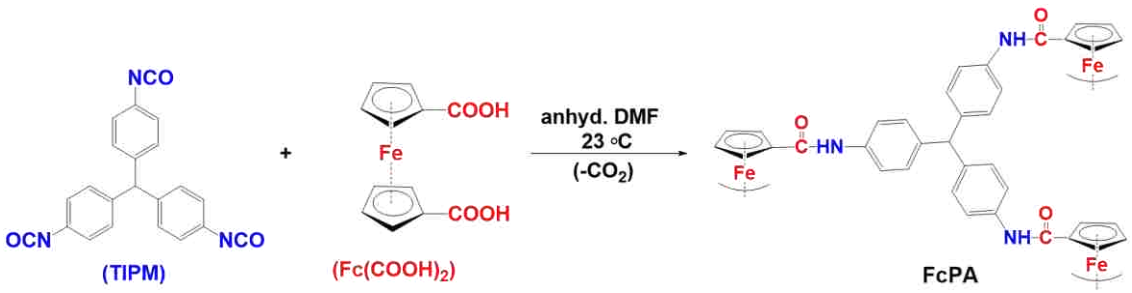

1.10.1. Pyrolysis and Galvanic Transmetalation of Ferrocene Polyamide Aerogels. Pyrolysis of ferrocene-based polyamide aerogels (FcPA-see Figure 1.13) gave monolithic carbon aerogels bearing Fe(0) nanoparticles dispersed throughout their volume. Apart from their own catalytic activity, those materials were transmetalated with selected metallic ions, replacing Fe(0) nanoparticles with Au, Pt, Pd, Ni and Rh (Figure 1.13). All materials were characterized along all processing steps in terms of their chemical composition, and their micro/nanomorphology.

As summarized in Figure 1.13, above 800 $^{o}C/H_2$ samples were electrically conducting, Fe(0) became chemically accessible (e.g., they would start reacting with ions in solution filling the pores), and carbon showed signs of graphitization.[76] Samples at the onset of those properties, namely those obtained at 800 ^{o}C, comprised the basis for further study and are referred to as Fe@C. The chemical accessibility of Fe(0) in Fe@C, as manifested by our ability to dissolve Fe(0) away with aq. HCl, made possible to replace Fe(0) with Au, Pt or Pd (M)[77] via reaction with complex ions of the corresponding metals, $[M]^{n+}$, according to Eq 1. In all three cases, the corresponding reactions are highly exothermic with standard redox potentials of over 1.0 V.

$$n\ Fe(0) + 2\ [M]^{n+} \text{---> } n\ Fe^{2+} + 2\ M(0) \qquad (1)$$

Experimentally, Fe@C monoliths were infiltrated quickly with aqueous solutions of $[M]^{n+}$ using capillary action under reduced pressure. Transmetalated monoliths (referred to as *tm*-M@C) were washed with water, acetone and were dried under ambient pressure without noticeable changes in their size relative to their Fe@C precursors (Figure 1.14).

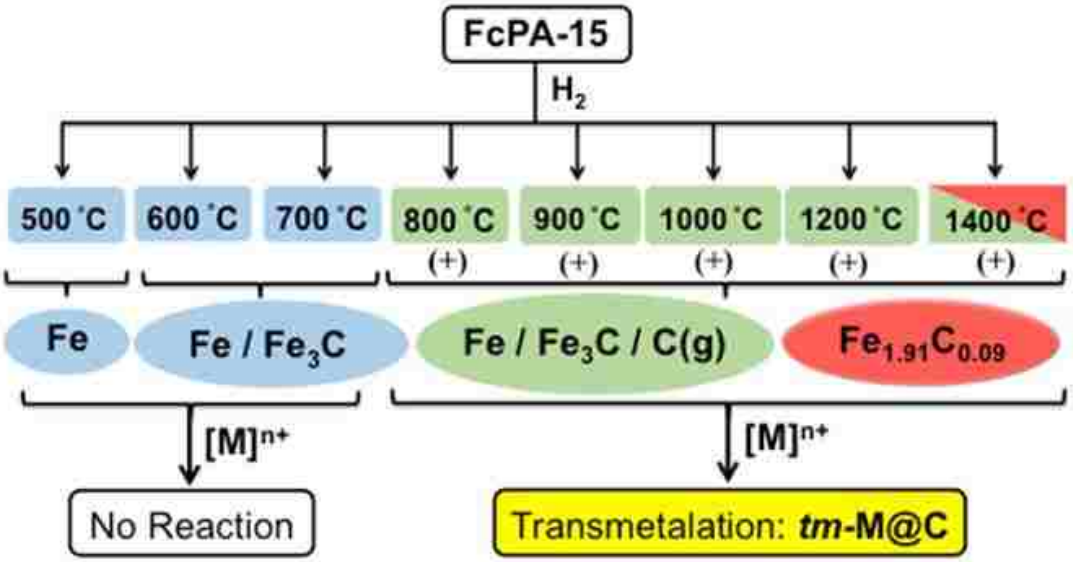

Figure 1.13. Chemical composition, electrical conductivity (+), and ability for transmetalation via reaction with metal ions, $[M]^{n+}$, of the product from pyrolysis of FcPA-15 at different temperatures.

1.10.2. Catalytic Activity of Fe@C and *tm*-M@C. In order to assess catalytic activity, Fe@C and *tm*-M@C were dipped under vigorous magnetic stirring in 0.1-0.9 M solutions of reaction mixtures that can be catalyzed by the respective metals.[78] Based on the weight of each monolith, the metal-to-limiting reagent ratio was adjusted at 5% mol/mol. Aliquots were taken in regular intervals and were analyzed with gas chromatography. At the end of the prescribed period (typically 24 h – Table 1.2), catalytic monoliths were picked up with a pair of tweezers, rinsed briefly with the reaction solvent and were transferred into new solutions to continue catalysis. The procedure was repeated five times with each catalyst. All monoliths were very robust. Yields always remained ≥70% (Table 1.2).

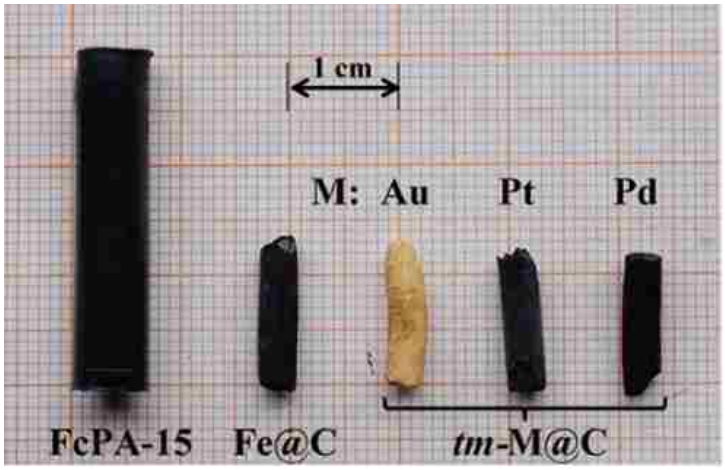

Figure 1.14. Photograph of samples after different stages of processing as shown.

Figure 1.15 shows results from catalysis (yields at a function of catalytic cycle) with Fe@C, and transmetalated *tm*-M@C (M: Au, Pt, Pd). It was noted that all catalysts discussed in this study behaved similarly, independent of reaction and catalytic metal.

Table 1.2. Photograph of samples after different stages of processing as shown.

Catalyst	RXN (t) [a]	Yield % mol/mol				
		1st	2nd	3rd	4th	5th
Fe@C	1 (24 h)	89	84	75	83	86
***tm*-Au@C**	2 (24 h)	98	89	75	71	70
***tm*-Pt@C**	2 (24 h)	85	84	79	80	71
***tm*-Pd@C**	3 (24 h)	98	84	74	62	75
***tm*-Pd@C**	4 (2 h)	91	92	79	73	71

[a] RXN (t): Reaction (run time):
1. nitrobenzene + hydrazine ⟶ aniline
2. benzyl alcohol + O_2 ⟶ benzaldehyde
3. iodobenzene + styrene ⟶ *cis*- + *trans*-stilbene
4. iodobenzene + butyl acrylate ⟶ butyl cinnamate

In summary, we successfully synthesized and characterized ferrocene based polyamide aerogels. The key feature of our approach is dispersion of catalytic nanoparticles in a 3D porous monolithic medium. With regards to the C-supported catalysts at hand, it is a rather straightforward route to incorporate metallocenes. Another attractive feature of these materials is galvanic replacement, which is atom-efficient, steps-down the particle size, and is a room-temperature process, which precludes sintering.

1.11. ATTEMPTED SYNTHESIS OF POLYAMIDE AEROGELS VIA REACTION OF ISOCYANATES AND MINERAL ACIDS

Considering our aforementioned patented technology, we attempted the synthesis of poly(boramide) aerogels via reaction of TIPM and H_3BO_3 in analogy to the reaction of isocyanates with carboxylic acids leading to the formation of –B-NH– linkage as shown in Scheme 1.11.

Chemical characterizations using advanced instrumental techniques including PGNAA (prompt gamma neutron activation analysis) reveal that rather than a polyboronamide, instead we obtained a clean room-temperature polymerization towards the same polyurea (PUA) aerogels obtained from reaction of TIPM with water. The new reaction pattern appears to be general for isocyanates and mineral acids: besides H_3BO_3, TIPM reacted with H_3PO_4, H_3PO_3, H_2SeO_3, H_6TeO_6, H_5IO_6 and H_3AuO_3, and we always obtained the same polyurea as shown in Scheme 1.12. No evidence could be found for any quantitative formation of –B-NH–linkage.

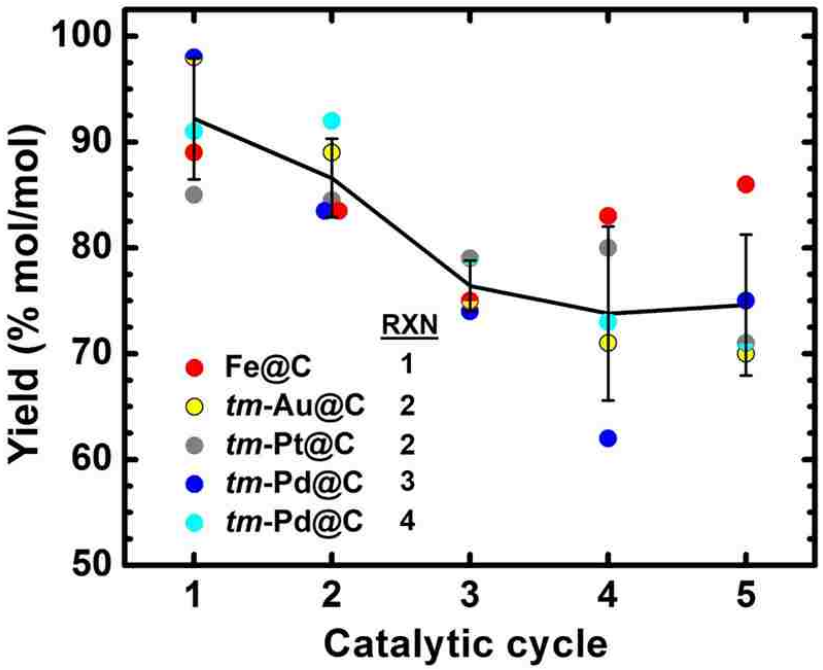

Figure 1.15. Cumulative graph of % Yield versus Catalytic cycle for all catalysts used in this study (data from Table 1.2). The solid black line connects the average % yields after each cycle. Error bars are one standard deviation from the average % yields.

Scheme 1.11. Attempted reaction of boric acid (H_3BO_3) with tris(4-isocyanatophenyl)methane (TIPM), according to US Patent No 2,945,841 (1960) - see Figure 1.9.

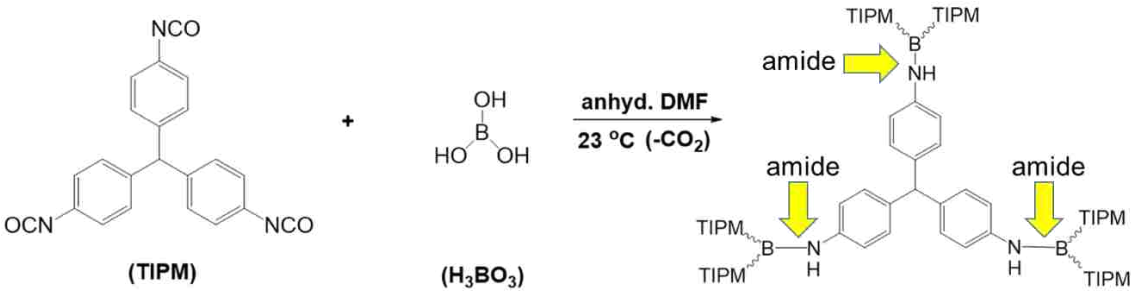

There was one important difference, however: side products from the reaction with H_3BO_3 could be removed easily from the porous structure, whereas side products from the

reaction with the other mineral acids were insoluble rendering process characterization more difficult. To our knowledge, this comprises a new route to polyurea-based materials, different from the classical routes that involve isocyanates reacting with amines or water.[59] We envision the utility of this new reaction pathway emerging from the fact that it provides the means for in situ doping of nanoporous polymers with nano-dispersed oxides as depicted in Figure 1.16.

Scheme 1.12. Reaction of mineral acids with tris(4-isocyanatophenyl)methane (TIPM).

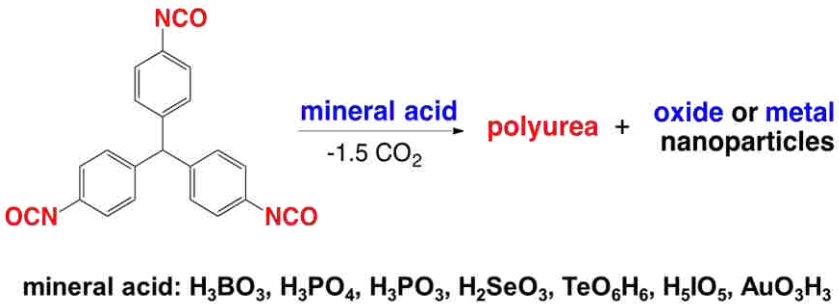

Although there was absolutely no indication that boron became part of the network in any systematic fashion, still those polyureas were extremely robust and mechanically strong. We reasoned that was due to exhaustive nature of the reaction of carbamic-boric anhydride adduct with –BOH maximizing the urea linkages and in turn pulling the polymeric strands closer together. In turn, no dangling functionality and exhaustive interparticle bridging was observed and is believed that was reflected upon macroscopic properties that depend precisely on the extent of interparticle bridging. Those include the macroscopic elastic modulus *E* of these materials. Figure 1.17 compares the elastic moduli of all polymeric aerogels that have been reported by our group. All the mechanically strong

aerogels are categorized based on their densities, and boric acid derived aerogels stand out at every density level.

Overall investigations revealed that an aromatic triisocyanate (TIPM) reacts with mineral acids under mild conditions and yields a clean reaction to polyurea, which is basically identical to polyurea obtained via reaction of TIPM with water. That reaction pathway is distinctly different from the conventional path followed by isocyanates (including TIPM) with carboxylic acids to amides. Nevertheless, we introduced new H_3BO_3-mediated pathway for the synthesis of symmetric ureas from inexpensive isocyanates. Use of other mineral acids may prove convenient for preparing porous polymers and porous pyrolytic carbons doped *in situ* with oxide or metallic nanoparticles (case of Au), which in turn may find applications in catalysis.

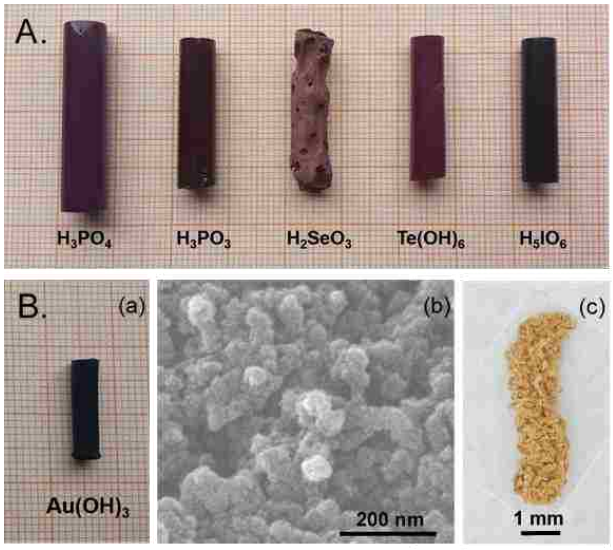

Figure 1.16. A. Polyurea aerogel monoliths prepared from tris(4 isocyanatophenyl)methane (TIPM) and the acids indicated. B. (a) A polyurea aerogel monolith prepared in DMF from tris(4-isocyanatophenyl)methane (TIPM) and H_3AuO_3. (b) Its microstructure. (c) Residue after pyrolysis at 600 °C/air underwent partial sintering and significant shrinkage, proves though that Au was evenly distributed throughout the monolith.

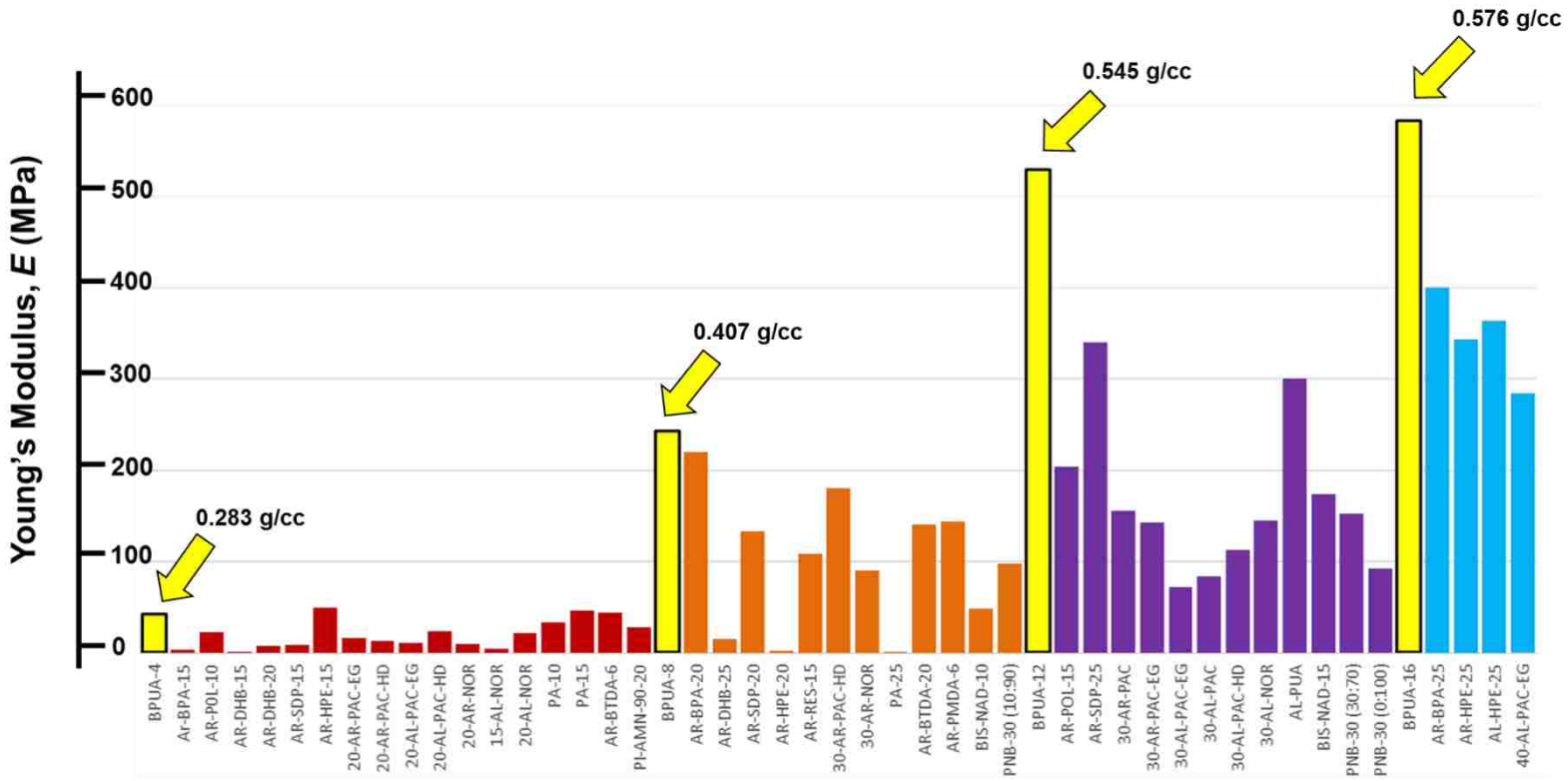

Figure 1.17. Comparison of Young's modulus (E) of boric acid derived aerogels with the Young's modulus of all other organic aerogels.

PAPER

I. Selective CO_2 Sequestration with Monolithic Bimodal Micro/Macroporous Carbon Aerogels Derived from Polyamide-Polyimide-Polyurea Random Co-polymers

Adnan M. Saeed, Parwani M. Rewatkar, Hojat Majedi Far, Tahereh T. Yazdeli, Suraj Donthula, Chandana Mandal, Chariklia Sotiriou-Leventis,* Nicholas Leventis*

Department of Chemistry, Missouri University of Science and Technology, Rolla, MO 65409, U.S.A.; Tel.: 573-341-4391 (NL), 573-341-4353 (CSL);
E-mail: leventis@mst.edu, cslevent@mst.edu

Submitted for Publication as an Article to the *Chemistry of Materials*

Graphical Abstract

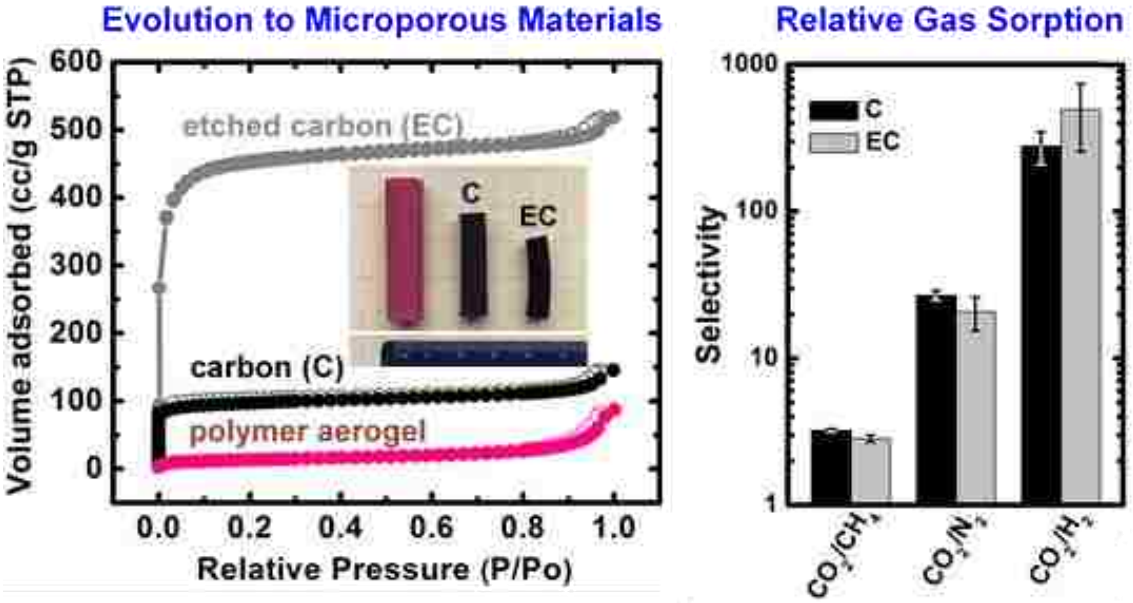

ABSTRACT: Studies are showing that designer materials for CO_2 capture and sequestration (CCS) may rely on microporous polymers. Porous multiscale monolithic materials classified as aerogels may comprise a sensible approach to the quest for packaging microporous polymers in application-friendly forms. Going one step further, pyrolytic conversion of polymeric aerogels to carbon aerogels may add physicochemical stability, and perhaps additional microporosity. Along those lines, we report pyrolysis and subsequent reactive etching (with CO_2) of polymeric aerogels (PA-xx) synthesized via a room-temperature reaction of an aromatic triisocyanate with pyromellitic acid. Using solid-state CPMAS ^{13}C and ^{15}N NMR, it was found that the skeletal framework of PA-xx was a statistical co-polymer of polyamide, polyurea, polyimide, and that it also contained a reaction intermediate – a carbamic-anhydride adduct. Stepwise pyrolytic decomposition of those components yielded carbon aerogels with both open and closed microporosity. At that point, micropore surface areas had increased from <15 $m^2\ g^{-1}$ (in PA-xx) up to 340 $m^2\ g^{-1}$ in the resulting carbons. Based on skeletal density data, it was concluded that reactive etching opened access to closed pores and the micropore area increased by almost four-fold, up to 1150 $m^2\ g^{-1}$ (out of 1750 $m^2\ g^{-1}$ of total surface area – by N_2 sorption). Such carbon aerogels demonstrated a good balance of adsorption capacity for CO_2 (up to 4.9 mmol g^{-1}), and selectivity towards other gasses. Their CO_2 adsorption capacity did not correlate well with surface areas, and it is suggested that pyridinic and pyridonic N (identified with XPS) engaged CO_2 in an energy-neutral surface reaction, which eventually filled micropores with CO_2. The selectivity towards H_2 (up to 928:1) is suitable for pre-combustion fuel purification. Relevant to post-combustion CCS, the selectivity towards N_2 was in the 17:1 to 31:1 range, which, in combination with the attractive CO_2 adsorption

capacity, low monomer cost, and the innate physicochemical stability of carbon renders those materials reasonable candidates for further practical consideration. Overall, we perceive plenty of scope in exploring micropores created not only by stepwise decomposition during pyrolysis, but also by purposeful manipulation of the carbonization chemistry in the spirit of the well-known oxidative aromatization of acrylonitrile, or more recently of polybenzoxazines, and aerogels comprise an attractive platform for doing so.

1. INTRODUCTION

Atmospheric CO_2 is part of the carbon cycle, in which life plays a key role.[1] For eons, the CO_2 concentration was balanced by earth's oceans and ecosystems (phytoplankton, rainforests).[2-5] A recent third factor with accelerating significance is related to the massive combustion of fossil fuels. According to the Scripps Institute of Oceanography, the CO_2 concentration increased from ca. 315 ppm in March 1958 to 409 ppm in April 2016.[6] Increasing concentrations of atmospheric CO_2 contributes to global warming, a dangerous prospect for life on Earth.[7] With the current rate, it is estimated that 2,000-3,000 mega tones of anthropogenic CO_2 will be injected in the atmosphere in the next two centuries.[8] That amount is about what was injected over a period of one million years by the Siberian Traps and is believed that caused the Great Permian Extinction, in which 90% of all life on the planet disappeared.[9]

CO_2 capture and sequestration (CCS) is becoming rapidly an issue of survival for the human species.[8] Since anthropogenic CO_2 production is related to combustion, there are two stages in that process where CO_2 capture is relevant: pre-combustion (e.g., of CO_2 from H_2 in fuel/air mixtures),[10] and post-combustion (of CO_2 from the flue gas).[11]

Regarding global warming, post-combustion CCS is most important. For the past 60 years, the most well-established industrial method for CO_2 removal involves aqueous amine solutions.[12] That method works well in pre-combustion reducing environments, while the oxidizing environment of the post-combustion flue gas degrades the amine. Thus, the second most popular approach to CCS uses microporous sorbents, which, owing to their high accessible surface areas and low heat capacities, are deemed promising candidates for gas separation.[13] Furthermore, since the adsorption properties of those porous sorbents are due to relatively weak Van der Waals forces,[14] as opposed to covalent bonding in the case of amines, regeneration of the CO_2 scrubber is more energy efficient, thereby contributes minimally in terms of additional CO_2 in the atmosphere.

Current commercial microporous sorbents include mainly zeolites,[15,16] and activated carbon,[17] and are used pre-combustion for H_2 purification and removal of CO_2 from natural gas. At present, their current capacity does not seem to be high enough for CO_2 scrubbing from post-combustion flue gas. To change that, during the last decade, numerous classes of microporous solids have been investigated, each with its unique advantages and issues.[18] First, in the spirit of traditional zeolites, new microporous inorganic materials include metal organic frameworks (MOF),[19-21] whose limited physicochemical stability, has encouraged research into conjugated microporous polymers (CMP),[22] hyper cross-linked polymers (HCP),[23] microporous organic polymers (MOP),[24] porous aromatic frameworks (PAF),[25] covalent organic frameworks (COF),[26,27] porous organic frameworks (POF),[28] covalent organic polymers (COP),[29] porous organic polymers (POP),[30] and porous polymer frameworks (PPF).[31] The central idea in the design of micropores in all those materials is molecular-level rigidization via crystallization, or via

spatial fixing of polymeric chains by using rigid multifunctional monomers. A special place in the last category, which in fact became the point of conceptual departure for this work, is occupied by a large variety of polymers derived from tetra *para*-subsituted tetraphenyl methane, and includes, for example, covalent organic polymers based on azo-bridging,[32] nanoporous polymers based on *N*-heterocyclic carbenes,[33] and microporous organic polyimides.[34] Furthermore, in order to increase interactions with the adsorbate, oftentimes, the efficiency of the adsorbent is augmented by heteroatoms or polar functional groups incorporated in the polymer network (e.g., NH_2, OH, NO_2, COOH, and SO_3).[35,36]

Microporous carbons on the other hand are attractive because they are chemically inert and physiochemically stable.[37,38] Classical CO_2 adsorbents based on carbon have variable pore size distributions ranging from macro to micropores, and are derived from carbonization and activation of renewable biomass precursors such as coconut husk, bamboo, wood peat, cellulose etc.[39-41] Advanced porous carbons for CO_2 adsorption are derived from synthetic polymers,[42] which allow tunable pore systems and incorporation of nitrogen that augments CO_2 sorption.[43,44]

Owing to extensive crosslinking, most designer sorbent materials undergo precipitation as part of their synthetic protocol, and are obtained as powders. For practical systems though, powders must be packaged in ways that allow easy handling, low pressure drops, fast heat and mass transfer and high contact area with the adsorbate.[45-47] At this point, drawing analogies with systems having similar requirements (e.g., chromatographic columns,[48] gas-phase fuel cells[49] and catalytic converters[50,51]) an answer to the quest for practical packaging is monolithic, yet nanostructured adsorbers with hierarchical porosity:

macropores will permit fast mass transfer to the active sites, and micropores will provide the thermodynamic and kinetic parameters for separation.[52]

Ideally, monolithicity and hierarchical porosity should be all introduced in one step. One class of materials that may fit this bill is aerogels.[53,54] Aerogels are made by drying wet-gels under conditions that preserve their size, shape and nanomorphology. Wet-gels are prepared via sol-gel chemistry, whereas multifunctional monomers react in a suitable solvent and yield crosslinked polymers that phase-separate into tiny primary nanoparticles that comprise the foundation of the continuous aerogel skeletal framework. Aerogels can be inorganic (e.g., silica) or organic (polymeric). Most organic polymer aerogels derived from aromatic monomers are carbonizeable to robust monolithic nanoporous carbons, referred to as carbon aerogels.[55-57] Carbon aerogels combine the desirable chemical inertness and physicochemical stability of carbon adsorbers with the aerogel monolithicity and hierarchical porous structure.

By this point it is evident that both microporous polymers and aerogels share a common requirement: extensive crosslinking. Along those lines, in this work we borrow the idea of designer-polymers from rigid aromatic tetrafunctional monomers, and fit it into carbonizable aerogels. With an eye to short-term practical implementation of the resulting materials, a key factor in our experimental design was cost, thus we opted for materials synthesized from monomers off-the-shelf, sort of speak. In that regard, our conceptual point of departure, tetraphenyl methane derivatives, were not considered, choosing rather to work with polyamide aerogels[58,59] derived from a reaction between a rigid aromatic trifunctional isocyanate, TIPM, with a rigid aromatic tetracarboxylic acid, pyromellitic acid (PMA), under sol-gel conditions (Scheme 1). Owing to the special pairwise *ortho*

relationship of the –COOH groups in PMA, it turns out that aerogels consisted of a co-polymer of polyamide, polyurea and polyimide. Upon pyrolysis, successive thermal decomposition of those constituents yielded macro/microporous carbon aerogels. Micropore surface area was quadrupled by reactive etching with CO_2. All carbon aerogels (pre- and post-etching) were monolithic and showed enhanced CO_2 adsorption relative to other gases (CH_4, H_2, N_2), which is partly attributed to a 25% w/w post-pyrolytic retention of the N initially present in the co-polymeric precursor.

Scheme 1. Idealized reaction of TIPM (a triisocyanate) with pyromellitic acid (PMA, a tetracarboxylic acid). Atom labeling refers to ^{13}C NMR peak assignment; abbreviations refer to the monomeric fragments used in Scheme 3.

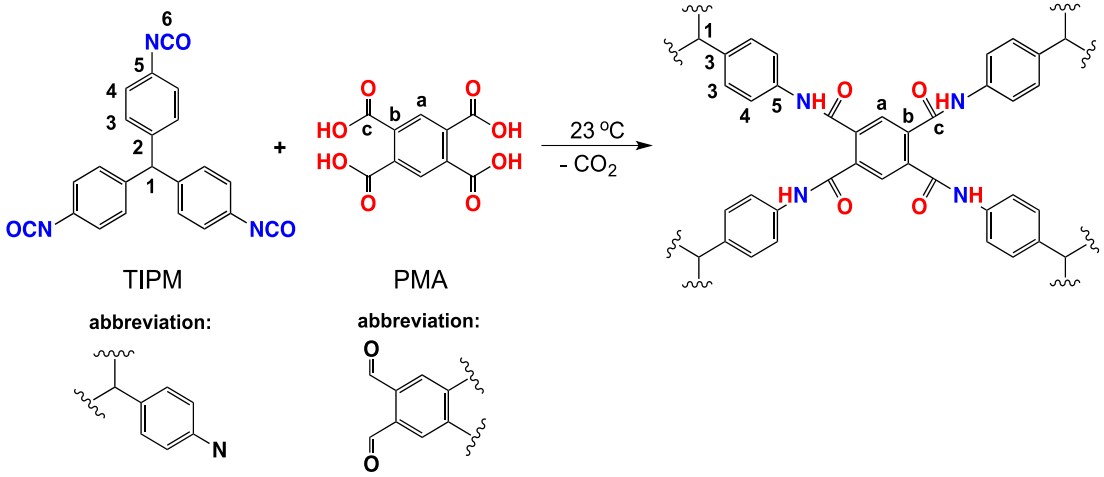

2. RESULTS AND DISCUSSION

This section describes the synthesis and characterization of polymeric aerogels from TIPM and PMA (subsection 2.1), their conversion to carbon aerogels followed by

reactive etching with CO_2 (subsection 2.2), and a comparative evaluation of the resulting carbons in terms of their preference for CO_2 adsorption versus CH_4, H_2 and N_2 (subsection 2.3). The discussion focuses on material properties related to the creation and evolution of microporosity along processing.

2.1. Synthesis and characterization of polymeric aerogels from TIPM and PMA.

2.1a. Synthesis. Our materials design was based on the fact that isocyanates react with carboxylic acids and give amides.[60-62] That reaction has been utilized for the synthesis of polyamide aerogels from TIPM and trimesic acid,[58] and more recently from TIPM and ferrocene dicarboxylic acid.[63] For reasons outlined in the Introduction, here that reaction was implemented with PMA. Scheme 2 summarizes the synthetic protocol towards polymeric aerogels along with subsequent carbonization and reactive etching, and includes a photograph of the resulting materials. In sort, gelation was carried out at room temperature in THF/ethyl acetate (EtOAc) mixtures. THF was chosen because it is a good solvent for PMA. EtOAc was introduced in the reaction mixture with the monomer, TIPM, which is supplied as a 27% w/w solution in anhydrous EtOAc, and was used as received (see Experimental). The two reagents were used in the required stoichiometric ratio of PMA:TIPM=3:4 mol/mol (Scheme 1). The total monomer concentration (TIPM+PMA) was bracketed between 5% and 25% w/w by varying the amount of THF (see Table S.1 of Appendix I in Supporting Information). Below that concentration range sols did not gel at room temperature.[64] The upper limit of that range was set by the fact that PMA is not soluble in EtOAc; above that limit the amount of THF needed for dilution was below what was required in order to keep PMA in solution. Gelation times (included in Table S.1) varied from 15 min to 3 h 15 min, in reverse order to the sol concentration. Wet-gels were

washed with fresh solvent (THF), and were solvent-exchanged with acetone before they were extracted with liquid CO_2, which was removed as a supercritical fluid (SCF). The resulting Polymeric Aerogels are referred to as PA-xx, whereas xx denotes the total monomer (PMA+TIPM) weight percent concentration in the sol. According to the above, $5 \leq xx \leq 25$, and for the purposes of this study, xx was set at 5 levels: 5, 10, 15, 20, 25.

Scheme 2. Synthesis of polymeric aerogels from PMA/TIPM, followed by carbonization and etching.

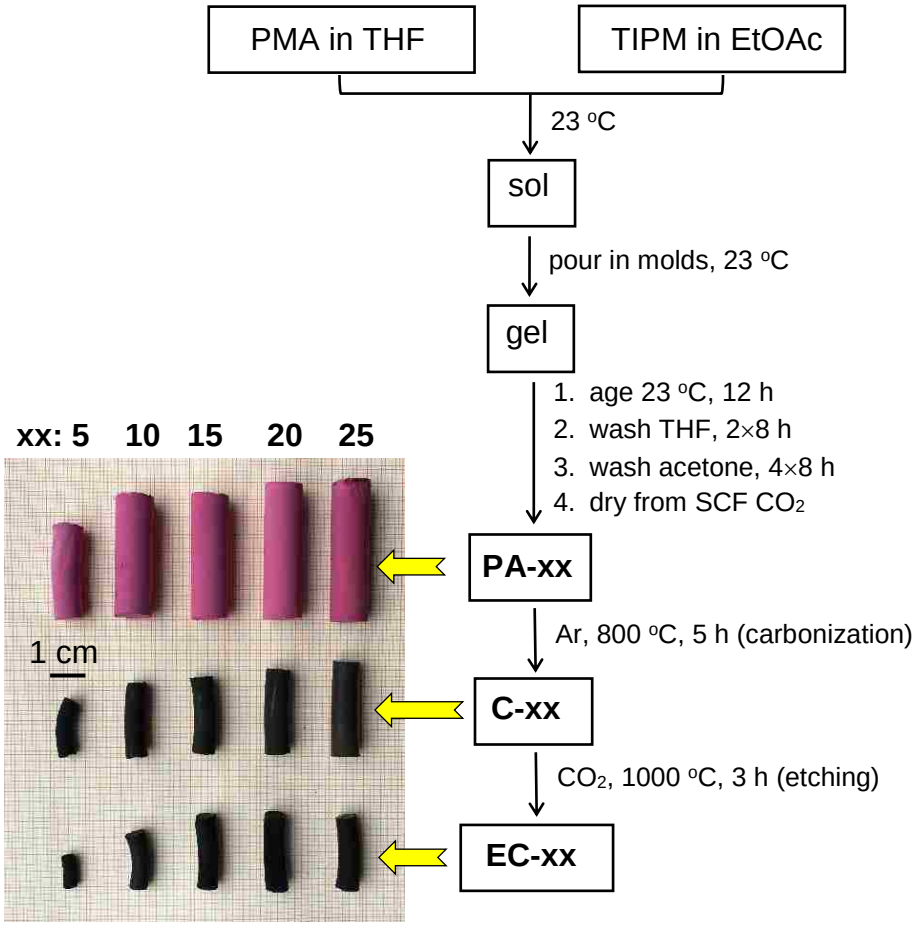

*2.1b. General material properties and the porous structure of PA-xx***.** PA-xx shrunk during drying, in reverse order to the sol-concentration (Scheme 2). Linear shrinkage varied from 35% (xx=5) to 13% (xx=25) relative to the molds. At first approximation, decreasing shrinkage is attributed to more extensive chemical bonding along the skeletal framework as xx increased. Owing to decreasing shrinkage, although sols at xx=25 were five-fold more concentrated than those at xx=5, the resulting PA-25 aerogels were less than 3× as dense as PA-5 (bulk densities: ρ_b=0.330±0.008 g cm^{-3} versus ρb=0.139±0.008 g cm^{-3}, respectively). (Bulk densities, and other data relevant to PA-xx are summarized in Table 1.) Skeletal densities (ρ_s) varied in the 1.31-1.32 g cm^{-3} range in no particular order, and open porosities, Π, calculated as percent of empty space via Π=100×(ρ_s–ρ_b)/ρ_s, varied from 89% v/v (PA-5) to 75% v/v (PA-25). Quantitative evaluation of the pore structures relied on N_2-sorption. All isotherms were similar in shape (Figure 1) with narrow hysteresis loops and no saturation plateaus, both indicative of mostly macroporous materials. Indeed, for all xx the specific pore volume in the 1.7-300 nm range, calculated with the BJH desorption method,[65] was always less than 8% of the total specific pore volume calculated via V_{Total}=(1/ρ_b)-(1/ρ_s) (Table 1). Average pore diameters, calculated via the 4V_{Total}/σ method, were in the 100-200 nm range. Pore size distributions for the low fraction of pores that happened to be in the 1.7-300 nm range were calculated with the BJH equation; they were very broad with maxima in the 27-38 nm range for all xx (see Inset in Figure 1 and Table 1). In terms of BET surface areas, σ, those started higher at low xx (e.g., σ=176 m^2 g^{-1} in PA-5) and decreased by a four-fold as density increased (σ=46 m^2 g^{-1} in PA-25). Interestingly, an 8-14% of the BET surface area was attributed to micropores (calculated with the Harkins and Jura model[66]), in increasing order with xx. Namely, despite that the

surface area of, for example, PA-25 was lower than that of the rest of the samples, the percent of that surface area that was attributed to micropores was higher.

*2.1c. The skeletal framework of PA-xx***.** Scanning electron microscopy (SEM – Figure 2) shows that all skeletal frameworks across the xx domain consisted of random assemblies of seemingly similar-size spherical particles. The presence of large voids supports the macroporous character of the samples, as inferred from N_2-sorption above. A quantitative evaluation of the skeletal framework was obtained from small angle x-ray scattering (SAXS) data analyzed with the Baucage Unified Model[67,68] (see Appendix II in Supporting Information). All scattering profiles could be fitted in four regions: two power-laws and two Guinier knees. From the latter, we calculated the radii of primary and secondary particles (R_1 and R_2, respectively - included in Table 1); the high-Q slope (Q: scattering vector) obeyed Porod's law; the values of the low-Q slopes were always lower than -3, meaning that secondary particles were densely-packed surface-fractal assemblies of primary particles. Secondary particle radii were in the 44-55 nm range, in no particular order. For low-density samples (i.e., at the low-end of the xx range) R_1 values agreed reasonably well with the radii of the smallest building blocks calculated from gas sorption data, $r=3/(\rho_s \times \sigma)$- included in Table 1). For example, for PA-5, R_1=10.2±0.5 nm and r=17 nm. However, at higher xx values, $r>>R_1$. For instance, for PA-25, r=49 nm, while R_1=12.2±0.9 nm. That kind of discrepancy ($r>>R_1$) is not new,[69] and based on results from silica particles deliberately embedded in polymer (case of X-aerogels),[70,71] it has been concluded that when $r>>R_1$, a primary skeletal network is formed fast, and then is coated with a layer of polymer formed by reaction of monomer remaining unreacted in the

Table 1. Characterization of the PA-xx aerogels.

xx	linear shrinkage (%) [a,b]	bulk density, ρ_b (g cm^{-3}) [a]	skeletal density, ρ_s (g cm^{-3}) [c]	Π (% v/v) [d]	specific pore volume (cm^3 g^{-1})			BET surface area, σ (m^2 g^{-1})	average pore diameter (nm)		particle radius (nm)		
					V_{Total} [e]	$V_{1.7\text{-}300\_nm}$ [f]	$V_{>300\ nm}$ [g]		$4V/\sigma$ [h] method	BJH [i] method	r [j]	R_1 [k]	R_2 [l]
5	35.39 ± 0.95	0.139 ± 0.008	1.316 ± 0.073	89	6.43	0.504	5.93	176 (15)	146 [10]	31[52]	13	10.16 ± 0.55	54.95 ± 4.09
10	20.88 ± 0.33	0.169 ± 0.003	1.306 ± 0.008	87	5.15	0.456	4.70	163 (17)	126 [12]	27[47]	14	9.74 ± 0.54	50.37 ± 3.11
15	17.21 ± 0.26	0.246 ± 0.010	1.307 ± 0.004	81	3.30	0.468	2.83	143 (14)	92 [14]	36[66]	16	10.85 ± 0.55	50.98 ± 1.91
20	13.73 ± 1.08	0.285 ± 0.007	1.319 ± 0.004	78	2.75	0.295	2.46	91 (11)	121 [13]	38[68]	25	10.31 ± 1.09	43.57 ± 1.98
25	12.90 ± 0.46	0.330 ± 0.008	1.321 ± 0.002	75	2.27	0.117	2.16	46 (6)	198 [10]	36[65]	49	12.17 ± 0.92	48.45 ± 2.26

[a] Average of 3 samples. [b] Linear shrinkage=100×(mold diameter – sample diameter)/(mold diameter). [c] Single sample, average of 50 measurements. [d] Porosity, Π=100×(ρ_s–ρ_b)/ρ_s. [e] Calculated via V_{Total}=(1/ρ_b)-(1/ρ_s). [f] Cumulative volume of pores between 1.7 nm and 300 nm from N_2-sorption data and the BJH desorption method. [g] $V_{>300\ nm}$ = V_{Total} - $V_{1.7\text{-}300\ nm}$. [h] For the first number, V was taken equal to V_{Total} =(1/ρ_b)-(1/ρ_s); for the number in [brackets], V was set equal to the maximum volume of N_2 absorbed along the isotherm as P/Po→1.0. [i] From the BJH plots: first numbers are peak maxima; numbers in (parentheses) are full widths at half maxima. [j] Particle radius, r=3/(ρ_s×σ); [k] R_1: radius of primary particles from SAXS; [l] R_2: radius of secondary particles from SAXS.

pores with “live” functional groups on the surface of the nanoparticles comprising the primary network. Since we are still able to ‘see’ the primary particles underneath the new polymeric layer, we conclude that the latter had a different –in fact lower– density than that of the nanoparticles of the primary network. This is consistent with the fact that the percent microporosity (actually at this point microporosity is synonymous with free-volume porosity) increased as xx increased. The monomer-to-network growth mechanism is reminiscent of Ostwald ripening,[72] whereas the monomer/surface reaction is most exothermic at the points of negative curvature, i.e., at the contacts between primary particles, thereby new polymer accumulated and eventually filled the empty space between primary particles. Two independent experimental observations support this conclusion: first, as we saw above, the BET surface area decreased with increasing xx; and second, as xx increased r ---> R_2; case in point: PA-25, r ≈ R_2=48.45±2.26 nm (Table 1).

*2.1d. The chemical make-up of PA-xx***.** The chemical makeup of PA-xx was probed mainly with solid-state CPMAS ^{13}C and 15N NMR. All solid-state ^{13}C NMR spectra of PA-xx are shown in Figure S.2 of Appendix III in Supporting Information, and are identical to one another. For the sake of this discussion, a representative spectrum (of PA-15) is shown in Figure 3 along with the liquid ^{13}C NMR spectra of the monomers, and the spectra of TIPM/H_2O-derived polyurea aerogels,[73] and of TIPM/pyromellitic anhydride-derived polyimide aerogels.[74] At first glance, the solid-state ^{13}C NMR spectra of PA-xx seemed deceptively simple: they combined the prominent aliphatic and aromatic ^{13}C-resonances of TIPM and PMA, and the extra peak at 165.0 ppm was assigned to the amide carbonyl (see Scheme 1). In comparison with the spectrum of TIPM/H_2O-derived polyurea, the lower-intensity resonance at around 155 ppm could be assigned to a urea carbonyl. (Upon closer

examination, however, the resonance at 155 ppm had actually two maxima (at 156.3 ppm and at 154.5 ppm), and that observation was consistent throughout all PA-xx – we will return to this point at the end of this section.) The initial reaction product of an isocyanate with a carboxylic acid is a carbamic-anhydride adduct (Scheme 3, Eq 1).61 That adduct either undergoes unimolecular rearrangement to an amide (Eq 2), or disproportionates with another molecule of the same kind towards urea and anhydride. The latter two products may react further with one another (reaction not shown) to yield 2 mol of the same amide that is obtained through the unimolecular route of Eq 2. It is unlikely, however, that polyurea here was the leftover of that bimolecular route. If it were, it should have been accompanied by an equivalent amount of anhydride. In that context, although the peak at 165.0 ppm could indeed include the ^{13}C=O resonance of an anhydride,75 two facts corroborate against this hypothesis: (a) in solid-state NMR, the anhydride ^{13}C=O appears as a pair of resonances[76] (see for example Figure S.3 in Appendix III of the Supporting Information), which are not observed in the spectrum of any PA-xx, and (b) the IR spectrum of PA-xx (see Figure S.4 in Appendix IV of the Supporting Information) does not show the characteristic pair of strong symmetric and asymmetric stretches of an anhydride in the ranges of 1800-1830 cm^{-1} and 1740-1775 cm^{-1}, respectively. Therefore, formation of polyurea should have been balanced out by something other than an anhydride, whose carbonyl resonance had to be included in the 165.0 ppm peak. As shown in Figure 3, one such possibility is TIPM/pyromellitic anhydride-derived polyimide. In IR (Figure S.4), PA-xx does show the imide carbonyl absorptions at 1778 cm^{-1} (w) and 1717 cm^{-1} (s). In order to get a better idea about the number and identity of the N-based polymers in PA-xx, we combined mechanistic reasoning with solid-state ^{15}N NMR data.

In solid-state ^{15}N NMR (Figure 4) the peak at 102.3 ppm is near the resonance of TIPM/H_2O-derived polyurea at 105.3 ppm. The peak at 170.8 ppm was assigned to polyimide derived from TIPM/pyromellitic dianhydride (included in Figure 4),[74] which by itself gave a resonance at 168.8 ppm. The resonance at 132.8 ppm was assigned to

Scheme 3. Mechanism of parallel formation of polyamide, polyurea and polyimide. Part A: Primary reaction step and primary products from the immediate intermediate (a carbamic-anhydride adduct) Part B: Secondary reaction steps, and products from secondary intermediates.

(Part A)

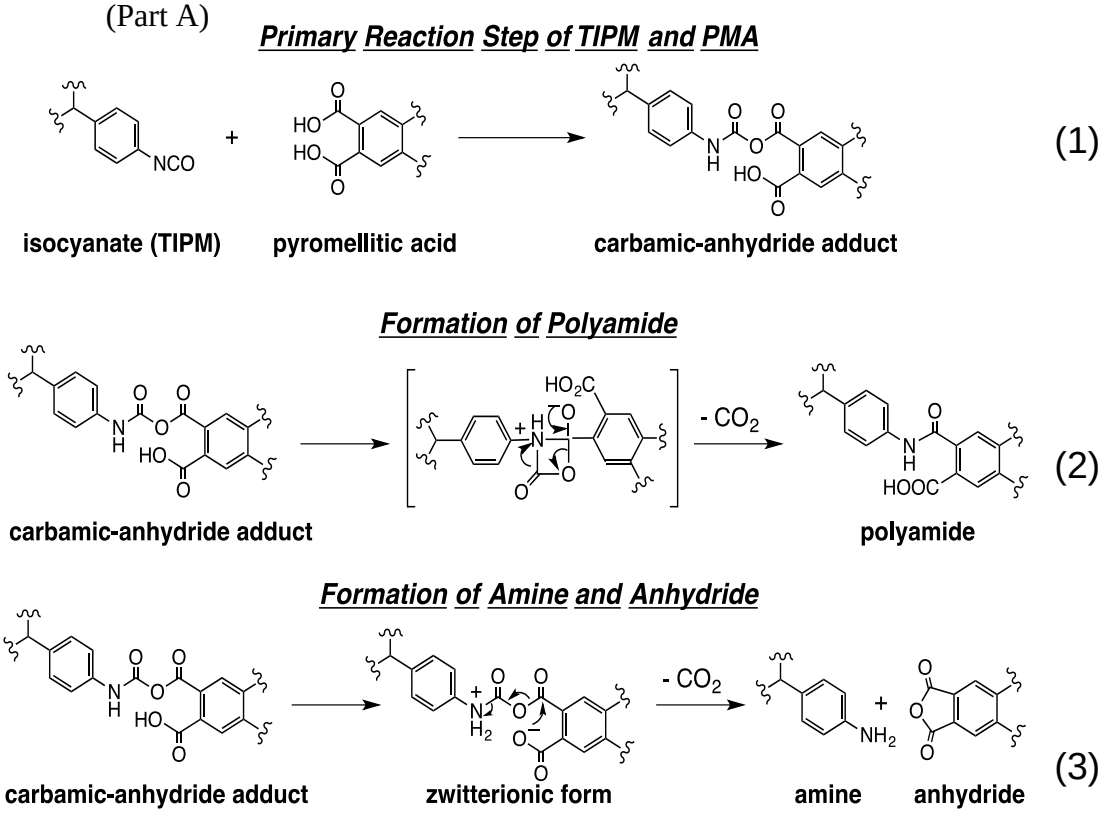

(Continued from previous page)

(Part B)

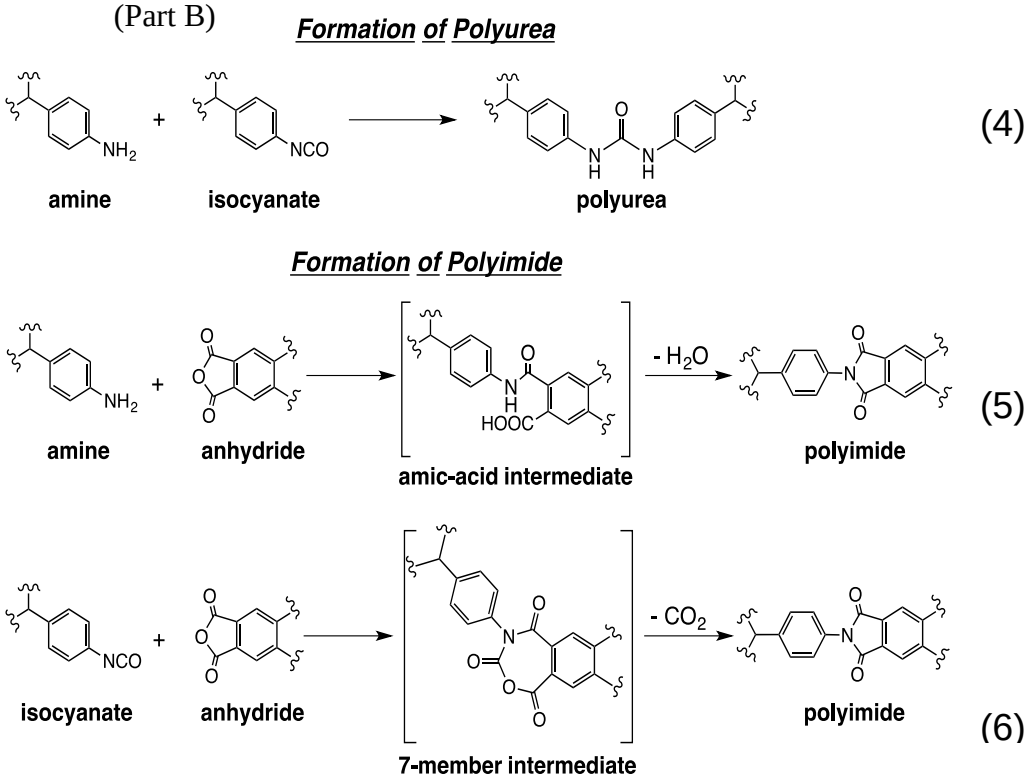

polyamide and the remaining resonance at 54.4 ppm was assigned to dangling free aromatic amines.[77] A mechanistic scheme accounting for: (a) polyimide as a main product; and, (b) formation of polyurea without parallel formation of an equivalent amount of anhydride, is based on that: (a) formation of pyromellitic anhydride from pyromellitic acid is stereochemically favorable; and, (b) pyromellitic anhydride may in turn react towards polyimide either with TIPM-derived free amines,[78-80] or directly with the isocyanate (TIPM).[81-83]

Specifically, it is speculated that the reaction sequence is initiated by an intramolecular acid-base neutralization within the carbamic-anhydride adduct toward its zwitterinic form, which in turn expels CO_2, and yields free aromatic amine and

(pyromellitic) anhydride (Eq 3). Both of those products are highly reactive towards –N=C=O.[84] Thus, newly formed free dangling $–NH_2$ react either with yet unreacted isocyanate to give polyurea (Eq 4), or with newly formed anhydride to polyimide (Eq 5). The latter reaction proceeds via an amic acid intermediate (see Eq 5) that, in a typical imide synthesis, requires a sacrificial dehydrating agent (usually acetic anhydride/pyridine).[85] Without going into further mechanistic details, the role of that dehydrating agent is played here by the isocyanate. Alternatively, polyimide may also be formed via reaction of anhydride groups with isocyanate via a 7-member intermediate that expels CO_2 (Eq 6).[81-83,86]

Data so far show that PA-xx were mixtures of three main components: polyamide, polyimide and polyurea. Upon closer examination, though, we note that the ^{15}N NMR resonances of polyimide and polyurea in PA-xx were near, but not exactly at the resonances of the pure components. This is taken as a strong evidence that PA-xx was a random copolymer of the three components rather than a polymer blend. Furthermore, although ^{15}N NMR data may not be exactly quantitative, we cannot but notice that the resonance at 102.3 ppm was disproportionally intense. Heating of any as-prepared PA-xx sample to 150 ^{o}C: (a) liberates CO_2 (see Movie S.1 in Supporting Information - the chemical identity of the evolving gas was confirmed with mass spectrometry); (b) decreases the intensity of the ^{15}N NMR resonance at 102.3 ppm and moves it closer to the resonance of polyurea (new position at 104.5 ppm); and, (c) increases the relative intensity of the amide resonance. (The post-heating ^{15}N NMR spectrum of PA-xx is included in Figure 4.) More subtle but similar are changes observed in the ^{13}C NMR spectra of PA-xx upon heating (Figure S.2 in Appendix III of the Supporting Information). For example, after heating PA-15 at 150

^{o}C, the feature at 156/154 ppm turned into a single-maximum resonance at 153.6 ppm, and the integrated peak intensity ratio changed in favor of the resonance at 165.0 ppm: from (7.4±0.3): (2.6±0.3) in all PA-xx before heating, to, for example, 8.3:1.7 for PA-15 after heating. Therefore, the feature at 156/154 ppm included again two components, only one of which was polyurea; the second one was convertible to polyamide, whose resonance was under the peak at 165.0 ppm. Finally, after heating at 150 ^{o}C, the carbonyl region of the IR spectrum of PA-xx was simplified by a lot: the strongest, broad absorption at 1670 cm^{-1} was removed and the imide absorptions at 1778 cm^{-1} and 1719 cm^{-1} became sharper (see Figure S.5). All heating experiments (including spectroscopic evidence and evolution of CO_2) support that PA-xx comprised a fourth component: unreacted carbamic-anhydride moieties (Eq 1). This is deemed important in terms of interpreting the evolution of the porous structure upon pyrolysis.

2.2. Pyrolysis of PA-xx aerogels to carbons and reactive etching with CO_2.

2.2a. Preparation of C-xx and EC-xx carbon aerogels. Figure 5 compares the thermogravimetric analysis (TGA) data from PA-xx, TIPM/H2O-derived polyurea[73], and TIPM/pyromellitic anhydride-derived polyimide.[74] Low-temperature (<100 ^{o}C) mass losses in polyurea are attributed to loss of residual solvent – see ^{13}C NMR. According again to solid-state ^{13}C NMR, PA-xx was free of residual solvent; the early mass loss of about 3% was due to loss of CO_2 (Movie S.1) from the carbamic-anhydride aduct (Eq 2, Scheme 3). At higher temperatures, PA-xx showed three main degradation events: one at 605 ^{o}C, which, surprisingly, was higher than the highest decomposition events of either the polyurea (541 ^{o}C), or the polyimide (579 ^{o}C) components; a second degradation event at 350 ^{o}C was close to the first decomposition step of the polyurea component (369 ^{o}C); and,

a third event at 253 ºC was attributed to the polyamide component.[87] PA-xx were then carbonized at 800 ºC under Ar (i.e., at about 200 ºC higher than the highest degradation step in TGA) to materials referred to as C-xx. The latter were etched with CO_2 at 1,000 ºC to materials referred to as EC-xx (Scheme 2).

2.2b. Chemical composition of C-xx and EC-xx aerogels. The (carbonization) yield of PA-xx to C-xx varied in the range of 42-57% w/w. Reactive etching removed less mass than carbonization: yields from C-xx to EC-xx were in the range of 65-78% w/w. CHN analysis of middle-density PA-15 gave (% w/w): C, 62.91; H, 4.40 and N, 7.93. After carbonization, C-15 consisted of: C, 85.95%, H, 1.54%; N, 5.44%. After etching, EC-15 consisted of: C, 80.92%, H, 1.18%; N, 5.61%. Based on those CHN analysis data, together with the carbonization yield of PA-15 (47.82±0.63%), and the etching yield of C-15 (75.11±2.22%), it was calculated that C-15 retained (w/w) 65% of the C, and 33% of the N in the parent PA-15. By the same token, EC-15 retained (w/w) 71% of the C, and 77% of the N present in C-15. Overall, EC-15 retained 25% w/w of the N initially present in PA-15.

Because of the importance of N for sequestration of CO_2,[88,89] the chemical environment of N in C-xx and EC-xx was probed with XPS. The high-resolution spectra of the N1s peak in C-25 and EC-25 are shown in Figure 6. Both spectra were fitted with four Gaussians. In C-25 those curves were centered at 398.62 eV (pyridinic N, 28.49%), at 400.71 eV (pyridonic N, 16.68%), at 401.57 (quaternary N, 22.87%), and at 403.62 eV (pyridine oxide, 31.96%).[90] After etching, those curves were centered at 398.68 eV (pyridinic N, 17.41%), at 400.95 eV (pyridonic N, 29.50%), at 401.51 eV (quaternary N, 28.66%), and at 403.30 eV (pyridine oxide, 24.43%). (Those assignments are supported by

carbon found in C=O and C-N – Figure S.6 of Appendix V in Supporting Information.) Overall, XPS shows that a significant portion of the retained N was situated in pyridinic and pyridonic positions that were most likely to interact with CO_2.

2.2c. General material properties and the nanostructure of C-xx and EC-xx aerogels. Microscopically C-xx and EC-xx looked similar to one another (Figure 2). In comparison with PA-xx it seems that pyrolysis brought about a fusion of particles and made macropores wider. In SAXS (Appendix II), the primary particle radii of C-xx were in the 31-38 nm range, which, accounting for pyrolytic shrinkage (see next paragraph), roughly corresponds to the secondary particle radii in PA-xx (found in the range of 44-55 nm – see Table 1). Particles in SEM matching the SAXS primary particle radii of C-xx are pointed by arrows (Figure 2).

According to the photographs of Scheme 2, C-xx shrunk significantly relative to PA-xx, but did much less so upon etching. Following the same pattern with the parent PA-xx, shrinkage of both C-xx and EC-xx decreased as xx increased. (For shrinkage and other relevant material characterization data for C-xx and EC-xx see Table 2.) Again, following the pattern of PA-xx, bulk densities of C-xx increased monotonically with xx. However, bulk densities of EC-xx *decreased* as xx increased. For instance, for EC-5 ρ_b=0.919±0.037 g cm^{-3}, for EC-10 ρ_b=0.284±0.011 g cm^{-3} and for EC-25 ρ_b=0.247±0.001 g cm^{-3} (Table 2). That trend could not be attributed entirely to the lower shrinkage observed at higher xx. As discussed in section 2.1.3, the polymeric layer accumulating on top of the primary nanoparticle network via the monomer-to network growth mechanism included free-volume porosity, and its density was lower than that of the primary network. It is reasonable then that the secondary layer of polymer leads to somewhat less dense, more reactive

carbon, which was etched faster than carbon from the core network. The thicker that layer, the higher the mass loss, which, in combination with decreasing shrinkage at higher xx values, justifies the downward trend in the bulk densities of EC-xx. This interpretation is supported by skeletal density data: as shown in Table 2, the ρ_s values of C-xx decreased monotonically with xx, from 2.033±0.021 g cm^{-3} (C-5) to 1.870±0.025 g cm^{-3} (C-25), while skeletal densities of EC-xx *did exactly the opposite*: they *increased* from 1.763±0.235 g cm^{-3} (EC-5) to 2.246±0.034 g cm^{-3} (EC-25). The downward trend in the ρ_s values of C-xx implies that those samples included closed porosity. The inverse trend in EC-xx supports that: (a) reactive etching opened access to the closed pores of C-xx (i.e., rendered open pores closed); and, (b) carbon from the primary skeletal network was denser, as argued.

2.2d. The pore structure of C-xx and EC-xx aerogels. Overall, C-xx had pairwise about equal percent porosities with their parent PA-xx (refer to and compare data in Tables 1 and 2), descending from 84/89% v/v (C-5/PA-5) to 76/75% v/v (C-25/PA-25); that trend suggests that, closed pores notwithstanding, pyrolytic mass loss and shrinkage nearly compensated one another. On the other hand, with the exception of EC-5, which underwent excessive shrinkage (Scheme 2), the porosities of all other EC-xx remained high (87-89% v/v). Correspondingly, the total specific pore volume, V_{Total}, of C-xx decreased from 2.6 $cm^3\ g^{-1}$ (C-5) to 1.7 $cm^3\ g^{-1}$ (C-25), while VTotal of EC-xx jumped from 0.52 $cm^3\ g^{-1}$ (EC-5) to 3.1 $cm^3\ g^{-1}$ (EC-10), and kept on increasing slowly afterwards to 3.6 $cm^3\ g^{-1}$ (EC-25) (Table 2). At first, pore structures were probed with N_2 sorption porosimetry at 77 K. The isotherms of both C-xx and EC-xx (Figure 7) were very different from those of the parent PA-xx (Figure 1): they were dominated by an early sharp uptake of N_2 at low partial pressures (P/Po<0.1), followed by extended plateaus and relatively small upwards

Table 2. Characterization of carbon (C-xx) and etched-carbon (EC-xx) aerogels

xx	linear shrinkage (%) [a,b]	bulk density, ρ_b (g cm^{-3}) [a]	skeletal density, ρ_s (g cm^{-3}) [c]	Π (% v/v) [d]	specific pore volume (cm^3 g^{-1})				BET surface area, σ (m^2 g^{-1})	average pore diameter (nm)		micropore width (nm) [j]		particle radius (nm)
					V_{Total} [e]	$V_{1.7\text{-}300\_nm}$ [f]	$V_{micropre}$ [g] N_2	$V_{micropre}$ [g] CO_2		$4V/\sigma$ [h] method	BJH [i] method	cylindrical	slit	r [k]
Carbon Aerogels (C-xx)														
5	63.71 ± 0.28	0.322 ± 0.025	2.033 ± 0.021	84	2.614	0.090	0.130	0.134	429 (337)	24 [2.7]	29 [-]	0.583	0.347	3.44
10	54.92 ± 0.26	0.367 ± 0.006	2.030 ± 0.019	82	2.232	0.078	0.102	0.122	380 (291)	24 [2.8]	28 [17]	0.608	0.365	3.89
15	47.82 ± 0.63	0.404 ± 0.018	1.956 ± 0.017	79	1.964	0.070	0.155	0.125	353 (270)	22 [2.8]	32 [21]	0.577	0.342	4.34
20	43.93 ± 0.10	0.422 ± 0.008	1.954 ± 0.021	78	1.858	0.056	0.192	0.119	365 (301)	20 [2.7]	35 [24]	0.708	0.426	4.21
25	39.80 ± 0.28	0.451 ± 0.013	1.870 ± 0.025	76	1.683	0.068	0.255	0.126	302 (230)	22 [3.0]	36 [26]	0.669	0.403	5.31
Etched Carbon Aerogels (EC-xx)														
5	83.60 ± 0.16	0.919 ± 0.037	1.763 ± 0.235	48	0.521	0.010	0.408	0.191	793 (741)	2.6 [2.1]	22 [13]	0.703	0.423	2.15
10	60.69 ± 0.36	0.284 ± 0.011	2.143 ± 0.126	87	3.054	0.127	0.414	0.189	1561(1148)	7.8 [2.3]	27 [11]	0.698	0.420	0.90
15	59.81 ± 0.27	0.279 ± 0.007	2.169 ± 0.090	87	3.123	0.123	0.454	0.191	1556(1130)	8.0 [2.3]	26 [9]	0.689	0.415	0.89
20	52.43 ± 0.23	0.255 ± 0.006	2.325 ± 0.123	89	3.491	0.120	0.295	0.190	1742(1140)	8.0 [2.3]	28 [10]	0.654	0.394	0.74
25	45.12 ± 0.19	0.247 ± 0.001	2.246 ± 0.034	89	3.603	0.101	0.167	0.190	1394(1122)	10 [2.8]	33 [11]	0.636	0.383	0.96

[a] Average of 3 samples. [b] Linear shrinkage=100×(mold diameter – sample diameter)/(mold diameter). [c] Single sample, average of 50 measurements. [d] Porosity, $\Pi=100\times(\rho_s-\rho_b)/\rho_s$. [e] Calculated via $V_{Total}=(1/\rho_b)-(1/\rho_s)$. [f] Cumulative volume of pores between 1.7 nm and 300 nm from N_2-sorption data and the BJH desorption method. [g] $V_{micropre}$ was calculated either with N_2-sorption at 77 K, or with CO_2-sorption up to 760 torr (relative pressure of 0.03) at 273 K. [h] For the first number, V was taken equal to $V_{Total}=(1/\rho_b)-(1/\rho_s)$; for the number in [brackets], V was set equal to the maximum volume of N_2 absorbed along the isotherm as P/Po→1.0. [i] From the BJH plots: first numbers are peak maxima; numbers in (parentheses) are full widths at half maxima. [j] By applying the Horvath–Kawazoe method on N_2-sorption data under low-pressure dosing (P/Po ≤ 0.1). First column, assuming cylindrical pores; second column, assuming slit pores. [k] Particle radius, $r=3/(\rho_s\times\sigma)$.

inflections at P/Po>0.85. With the exception of EC-5, the plateau positions within each C-xx or EC-xx series of samples were almost independent of xx. Next, we note that the EC-xx plateaus were four to five-fold higher than those of C-xx. Qualitatively, these data signify that the pore structure below 300 nm in both C-xx and EC-xx were dominated by micropores. The fact that isotherms within each one of the two types of materials, C-xx and EC-xx, were practically invariant of xx and clustered together suggests that generation of microporosity in PA-xx was mostly independent of the nanostructure, thereby an innate property of the material. According to this reasoning, microporosity most likely was created by the stepwise decomposition of the PA-xx components (Figure 5), starting from below 200 ^{o}C with liberation of CO_2 from the carbamic-anhydride adduct (Eq 2). The most (thermally) stable component, imide, is also the hardest one, and kept the shape around the newly formed microcavities. That process created both closed and open micropores (based on the ρ_s data of C-xx, as discussed above), and the primary effect of reactive etching was to open access to the closed pores. A secondary effect of reactive etching, as it will be discussed below, was to make micropores slightly wider.

The first profound effect of microporosity was on surface areas (Table 2). The BET surface area of C-xx was in the 300-400 $m^2\ g^{-1}$ range (versus those of the parent PA-xx in the 50-170 $m^2\ g^{-1}$ range – Table 1). A high portion of the surface area of C-xx (76-78% or 230-340 $m^2\ g^{-1}$) was allocated (Harkins and Jura model) to micropores. After etching, the BET surface area of CE-xx ($10 \leq xx < 25$) was catapulted into the 1400-1750 $m^2\ g^{-1}$ range, with 65-80% of that (1120-1150 $m^2\ g^{-1}$) attributed to micropores.

A quantitative evaluation of microporosity was carried out by two methods: from the N_2-sorption isotherms at 77 K (Figure 7) according to the Horvath-Kawazoe model,[91]

and with CO_2 adsorption porosimetry up to 1 bar at 0 ^oC (Figure 8A). Pore size distributions (PSD) within the micropore range were calculated from the CO_2 adsorption isotherms using a DFT model.

Micropore volumes by the two methods (N_2 sorption and CO_2 adsorption) tended to agree for C-xx; for EC-xx, micropore volumes by CO_2 adsorption were in general lower than those obtained by N_2-sorption, therefore not all micropore volume was accessible to CO_2. Within either method, however, micropore volumes of EC-xx were generally higher than those of C-xx. Representative PSD data in the micropore range are shown in Figure 8B (PSD data for all samples are shown in Figure S.7 of Appendix VI in Supporting Information). Clearly, the PSDs of both C-xx and EC-xx were qualitatively similar, and the effect of etching, in addition to opening access to closed pores, was to make micropores somewhat wider, shifting the PSD of EC-xx towards larger values.

The big overall picture is that for all carbon samples the total specific pore volume calculated via $V_{Total}=(1/\rho_b)-(1/\rho_s)$ was many-fold higher (up to 13×) than the sum of pore volumes below 300 nm ($V_{1.7\text{-}300\_nm}+V_{micropore,N2}$). Below 300 nm, porosities were dominated by pore sizes <1.7 nm: in C-xx the $V_{micropore,N2}$ values were 60-70% of ($V_{1.7\text{-}300\_nm}+V_{micropore,N2}$); in EC-xx the percent micropore volume was higher, at 85-90% of the volume of pores with diameters <300 nm. In summary, both C-xx and EC-xx were monolithic, and essentially bimodal macroporous/microporous materials, which is highly desirable from an application perspective (see Introduction). Macroporosity, due mostly to larger, >300 nm pores, dominated over microporosity.

2.3. Comparative gas sorption of CO_2, CH_4, N_2 and H_2 by C-xx and EC-xx.

CCS by nanoporous materials relies on kinetic and thermodynamic considerations related to the pore size, and the surface chemical properties of the adsorber.[52] The microporosity of C-xx and CE-xx (Figure 8B) is commensurate with the kinetic diameter of CO_2 (3.3 Å), and meets the kinetic aspect of the requirements for CCS.[92] On the other hand, the presence of pyridinic and pyridonic nitrogen enhances the thermodynamic aspect of the interaction of both C-xx and EC-xx with acidic CO_2. [88,93] Upon a closer look at the isotherms of Figure 8A, at 1 bar C-xx adsorbed 3.3 mmol of CO_2 per g of adsorber, while EC-xx adsorbed up to 4.9 mmol per g (21% w/w, a 48% increase over C-xx). Using the van der Waals radius of CO_2 (2.57 Å) and considering either the average BET surface area (366±46 m^2 g^{-1}), or the average pore volume of C-xx (0.125±0.006 cm^3 g^{-1} with CO_2 as a probe – Table 2), the theoretical uptake of CO_2 should be at 2.92-2.93 mmol g^{-1}, which is considered close to the experimental value. Things, however, are different for EC-xx: considering the average surface area of those materials (1409±355 m^2 g^{-1}), the theoretical CO_2 uptake (for monolayer coverage) should be 11.3 mmol g^{-1}, namely 2.3× higher than the maximum experimental value; by the same token, considering the average micropore volume of EC-xx (0.190±0.001 cm^3 g^{-1}), it is calculated that filling that volume with CO_2 requires 4.45 mmol g^{-1}, which is within the experimental range. Those data suggest that surface area is not a determining factor for CO_2 adsorption by C-xx and EC-xx. Also, it is considered unlikely that the small pore-size increase in EC-xx over C-xx (Figure 8) would account for the different CO_2 uptake by the two materials, leaving therefore that role to the pore volume. To put those data in perspective, we note that the CO_2 uptake by EC-xx is equal or better than what has been reported for many other carbons,[94,95] and competes favorably

with several porous carbons specifically doped with N from suitable precursors (3.9-6.2 mmol g^{-1}, all at 273-298 K, 1 bar),[88,96-98] or even with certain MOFs specifically doped with amines and pyrimidine moieties (e.g., bio-MOF-11, 6 mmol g^{-1} at 273 K).[99] Furthermore, the fact that neither C-xx nor EC-xx show saturation up to 1 bar (Figure 8A), leaves plenty of scope for further investigation at higher pressures.

Motivated by the promising levels of CO_2 adsorption by C-xx and EC-xx, it was deemed important, from an application perspective, to explore their selectivity towards fuels (CH_4 and H_2 – relevant to pre-combustion gas purification) as well as towards N_2 (relevant to post-combustion CCS). Figure 9 shows the adsorption isotherms of the four gasses up to 1 bar at 273 K. In all cases EC-xx was a stronger adsorber than C-xx. Figure 10A compares the relative gas uptake by C-xx and by EC-xx at 1 bar. (The collective gas sorption data are presented in Table S.3 of Appendix VII in Supporting Information.) Both C-xx and EC-xx took up significant amounts of methane, the later up to 2.16 mmol g^{-1} at 1 bar (3.45% w/w). The uptake of N_2, and particularly of H_2 were much lower. The kinetic diameters of CH_4, N_2 and H_2 are 3.80 Å, 3.64 Å, and 2.89 Å, respectively, therefore their relative magnitude might offer a reason for the relative adsorption trend of those three gasses. Clearly, adsorption of CO_2 (with a kinetic diameter of 3.30 Å) does not follow that trend. By looking at CO_2 and CH_4 closer, it is noted that the van der Waals radii of the two gasses are equal (at 2.57 Å), thereby the higher uptake of CO_2 must be attributed to some sort of special interaction with the cavity that results to pores filled completely with CO_2 as calculated above. It is speculated then that once in the micropores, CO_2 reacts with wall-bound pyridinic and pyridonic N towards pyridinic/pyridonic-N^+–$(C=O)O^-$. Now, since additional CO_2 inside the micropores has already paid an entropic cost,[52] reaction with the

wall-bound monolayer of $–(C=O)O^-$ to form pyridinic/pyridonic-N^+–(C=O)O–$(C=O)O^-$ is practically energy-neutral and may contribute towards filling the micropores with CO_2. (The "energy-neutral" argument is based on the bond energy of C=O, which is 173-181 kcal mol^{-1}, and the bond energy of C-O, which is 85-91 kcal mol^{-1}.[100])

The relative selectivity of C-xx and EC-xx towards the four gasses were calculated using Henry's law,[101] from the low-pressure slopes (<0.1 bar) of the isotherms.[102] The resulting values are plotted in Figure 10B (for the primary data see Table S.3). The highest selectivity was observed in the CO_2/H_2 pair (from 284:1 up to 928:1). The CH_4/H_2 pair showed the second highest selectivity (in the range of 57:1 to 360:1). The lowest selectivity was observed in the CO_2/CH_4 pair (2.6:1 to 3.4:1). The selectivity in the CO_2/N_2 pair (in the range of 17:1 to 31:1) was comparable to what has been reported for several other nanoporous carbons tested under similar conditions of temperature and pressure,[103] yet below other non-carbonaceous microporous CO_2 adsorbers. For example, certain organic cages have shown CO_2/N_2 adsorption selectivity up to 73:1 (1.0 bar, 293 K), however, the absolute amount of CO_2 adsorbed was just 0.20 mmol g^{-1}.[104] Reported CO_2/N_2 selectivities for amide networks based on rigid tetraphenyladamantane were in the 58-74 range, still the CO_2 uptake at 273 K, 1 bar was only 1.47 mmol g^{-1}.[105] Similarly, certain azo-COPs from tetrafunctional monomers have shown remarkable CO_2/N_2 selectivities at 273 K, 1 bar (63.7–109.6), but again a relatively low CO_2 uptake (2.55 mmol g^{-1}).[106] Overall, more often than not, there seems to be a tradeoff in organic CO_2 adsorbers between adsorption capacity and selectivity. (Incidentally, this is the case here as well: PA-xx shows a high selectivity for CO_2 vs. CH_4 (around 10), but low capacities (<1 mmol g^{-1}) – data included in Table S.3.) In that regard, C-xx and EC-xx seem to offer a fair balance between the two. However,

there is more to it: in order to place C-xx and EC-xx in a more global perspective, we need to consider all factors related to practicality. The latter is a tradeoff not only of adsorption capacity and selectivity, but also of physicochemical stability, cost and scalability. In terms of cost and scalability, it is difficult to imagine any kind of scale-up akin to commodity materials with specialty chemicals, thereby C-xx and EC-xx were designed precisely with those factors in mind (see Introduction). In terms of stability, in addition to being insoluble in all common (and less common) organic solvents, in two separate experiments C-xx and EC-xx were placed for 7 days in 12 M HCl, and again for 7 days in water in an autoclave at 200 ^{o}C, with no observable shrinkage, mass loss, or change in density and porosity in either experiment.

3. CONCLUSION

Multiscale monolithic polymeric aerogels may provide a sensible approach to the problem of packaging microporous materials in practical forms. Aerogel synthesis based on the room-temperature reaction of TIPM and PMA produced a statistical co-polymer (PA-xx) of polyamide, polyurea, polyimide that also contained carbamic-anhydride intermediate. Despite use of multifunctional monomers, only a small fraction of the surface area of PA-xx could be associated with micropores. However, successive thermal decomposition of the component polymers created both open and closed microporosity. Reactive etching opened access to closed pores, and the accessible micropore volume increased by four-fold. Such carbon aerogels demonstrated a good balance of adsorption capacity for CO_2 (up to 4.9 mmo g^{-1}) and selectivity towards other gasses. The selectivity towards H_2 in particular (up to 928:1) renders these carbon aerogels reasonable candidates

for pre-combustion fuel purification. Relevant to post-combustion CCS, selectivity towards N_2 varied in the 17:1 to 31:1 range, which in combination with the attractive capacity for CO_2 adsorption, low monomer cost, and physicochemical stability render those materials reasonable candidates for practical consideration.

CO_2 adsorption by PA-xx was not competitive, therefore it was given only cursory reference. Nevertheless, full data are presented in Table S.3, where it can be seen that the CO_2 adsorption capacity of PA-xx varied in the 0.8-0.9 mmol g^{-1} range, lower than that of C-xx (up to 3.3 mmol g^{-1}), and of EC-xx (up to 4.9 mmol g^{-1}). Looking at those data from a different perspective, the adsoption of CO_2 by PA-xx can be considered quite significant given that the micropore surface area of PA-xx was <17 m^2 g^{-1} (Table 1). Therefore, CO_2 adsorption by the materials of this study could not be attributed to surface areas alone. In that context, it was suggested that pyridinic and pyridonic N in C-xx and EC-xx engage CO_2 in an energy-neutral surface reaction in the micropores, which eventually fills them with CO_2.

Creating free volume microporosity from rigid polymers is becoming a mature field. Follow-up carbonization and exploration of the resulting materials in gas separation is a natural extension of those studies, and we perceive plenty of scope in that pursue. As this study has shown, microporosity can be created, or enhanced tremendously, by stepwise pyrolytic decomposition of the polymer. Another approach will be to induce rigidization during pyrolysis by manipulating the carbonization chemistry in the spirit of the well-known carbonization of acrylonitrile,[107] or more recently of polybenzoxazines.[108]

4. EXPERIMENTAL

4.1. Materials. All reagents and solvents were used as received, unless noted otherwise. Anhydrous tetrahydrofuran (THF) and 1,2,4,5-benzenetetracarboxylic acid (pyromellitic acid, PMA, 96%) were purchased from Sigma Aldrich Chemical Co. Deuterated DMSO (DMSO-d_6) and chloroform ($CDCl_3$) were obtained from Cambridge Isotope Laboratories. Tris(4-isocyanatophenyl) methane (TIPM) was donated from Covestro LLC (formerly Bayer Corporation U.S.A.) as a 27% w/w solution in dry ethylacetate under the trade name Desmodur RE. Siphon grade CO_2, argon (99.99999 %), N_2 (99.999%), H_2 (99.999%), CO_2 (99.999%) and CH_4 (99.99%) were purchased from Ozark Gas (Rolla, MO).

4.2. Synthesis of polymeric aerogels (PA-xx). In a typical procedure PMA (1.77 g, 6.96 mmol, re-dried at 120 ^oC for 24 h) was dissolved in variable amounts of anhydrous THF and the solution was added to 13.6 g of Desmodur RE (containing 3.67 g, 10.0 mmol of TIPM). The resulting sol was stirred at room temperature under N_2 for 10 min, and subsequently it was poured in molds (Wheaton 4 mL Polypropylene Omni-Vials 1.04 cm in inner diameter, Fisher part No. 225402), which were then sealed and left for gelation. The total weight percent concentration of monomers (PMA + TIPM) in the sol was varied by varying the amount of solvent (THF), and is denoted by extension –xx in the sample names, which are referred to as PA-xx. (PA: Polymeric Aerogels; xx was varied in the range $5 \leq xx \leq 25$, at 5 levels) All sols gelled at room temperature. (Attempted gelation of a PA-2.5 sol failed at room temperature, but that sol gelled at 60 °C.) All formulations and gelation times are summarized in Table S.1. All gels were aged for 12 h at room temperature in their molds, then they were removed from the molds, washed with THF (2×,

8h each time), acetone (4×, 8h each time), using an amount of solvent equal to 4× the volume of the gel for each wash. Finally, wet-gels were dried with liquid CO_2 in an autoclave taken out as a supercritical fluid (SCF).

4.2a. Conversion of PA-xx aerogels to carbon aerogels (C-xx). PA-xx aerogel monoliths were transferred into a MTI GSL1600X-80 tube furnace (alumina 99.8% pure, 72/80 mm inner/outer diameters, 457 mm heating zone). The temperature was raised to 800 ^oC at 5 ^oC min^{-1} under flowing Ar (150 mL min^{-1}) for 5 h. At the end of the heating period the temperature was returned to room temperature at 5 ^oC min^{-1} under constant flow of Ar.

4.2b. Conversion of C-xx aerogels to etched carbon aerogels (EC-xx). C-xx aerogels were placed in a tube furnace under flowing argon and were heated at 1000 °C. The flowing gas was switched to CO_2 and the temperature was maintained at that level for 3 h. Typically, that process was carried out in tandem with carbonization. Subsequently, the flowing gas was switched back to Ar and the temperature was returned to room temperature at 5 ^oC min^{-1} under constant flow of Ar.

4.3. Methods. Drying of acetone-exchanged wet-gels with supercritical fluid (SCF) CO_2 was carried out in an autoclave (SPIDRY Jumbo Supercritical Point Dryer, SPI Supplies, Inc. West Chester, PA). Samples were loaded into the autoclave and acetone was added till all samples were submerged. The pressure vessel was closed and liquid CO_2 was allowed in at room temperature until it displaced all acetone, which was then drained out. Liquid CO_2 was allowed in the vessel several more times until acetone was extracted out of the pores of the samples completely. The criterion for the latter was that CO_2 released

from the vessel formed powder of dry ice. Finally, the temperature of the autoclave was raised to 40 ^{o}C and SCF CO_2 was vented off as a gas.

Physical Characterization*:* Bulk densities (ρ_b) were calculated from the weight and the physical dimensions of the samples. Skeletal densities (ρ_s) were measured with helium pycnometry using a Micromeritics AccuPyc II 1340 instrument.

Chemical Characterization: CHN elemental analysis was performed by Intertek Pharmacheutical Services (Whitehouse, N.J.).

Infrared (IR) spectra were obtained in KBr pellets, using a Nicolet-FTIR Model 750 spectrometer.

Liquid ^{13}C-NMR spectra of monomers were obtained with a 400 MHz Varian Unity Inova NMR instrument (100 MHz carbon frequency). Solid-state CPMAS ^{13}C-NMR spectra were obtained with samples ground into fine powders on a Bruker Avance III 400 MHz spectrometer with a carbon frequency of 100 MHz, using a 7 mm Bruker MAS probe at a magic angle spinning rate of 5 kHz, with broadband proton suppression, and the CP TOSS pulse sequence. The Total Suppression of Spinning Sidebands (TOSS) pulse sequence was applied by using a series of four properly timed 180º pulses on the carbon channel at different points of a cycle before the acquisition of the FID, after an initial excitation with a 90º pulse on the proton channel. The 90º excitation pulse on the proton and the 180º excitation pulse on carbon were set to 4.2 µs and 10 µs, respectively. A contact time of 2 ms was used for cross polarization. Solid-state ^{13}C NMR spectra were referenced externally to glycine (carbonyl carbon at 176.03 ppm). Chemical shifts are reported versus TMS (0 ppm). Solid-state CPMAS ^{15}N-NMR spectra were also obtained on the same Bruker Avance III 400 MHz Spectrometer with a nitrogen frequency of 40.557 MHz , using

a 7 mm Bruker MAS probe with broadband proton suppression and magic angle spinning rate of 5 kHz. For cross polarization, a 90º proton excitation pulse was set to 4.2 μs with 2 ms contact time. Chemical shifts are reported versus liquid ammonia (0 ppm) and were externally referenced to glycine (amine nitrogen at 33.40 ppm). In all solid-state NMR experiments the relaxation delay was set at 5 s.

XPS data were obtained with a Kratos Axis 165 Photoelectron Spectroscopy System. Flat samples were placed on conductive carbon tape that was then adhered to stainless steel sample holders. Sample were introduced into the analysis chamber one at a time and the chamber was evacuated at 10^{-8} Torr or lower. No ion sputtering was performed on any of the samples. An Al monochromatic source at 150 watts was used for excitation. A charge neutralizer was used to reduce the effects of differential or sample charging. The analysis area was 700×300 microns. Elemental quantification calculations were based on broad survey results from single sweeps at higher sensitivity (Pass Energy=80), and were carried out with the Kratos Axis Vision. Processing software and its appropriate relative sensitivity factors for the particular XPS system. High resolution elemental scans where carried out at a lower sensitivity (Pass Energy=20), using multiple sweeps to improve the signal-to-noise ratios.

Structural Characterization: Scanning electron microscopy (SEM) was conducted with Au-coated samples on a Hitachi Model S-4700 field-emission microscope.

The fundamental building blocks of all aerogels were probed with small angle X-ray scattering (SAXS), using ~2 mm thick disks cut either with a knife (case of PA-xx, very important!), or with a diamond saw (case of C-xx). SAXS was conducted with a PANalytical X'Pert Pro multipurpose diffractometer (MPD) configured for SAXS, using

Cu Kα radiation (wavelength = 1.54 Å), a 1/32° SAXS slit, a 1/16° antiscatter slit on the incident beam side, and a 0.1 mm antiscatter slit together with a Ni 0.125 mm automatic beam attenuator on the diffracted beam side. Samples were placed in circular holders between thin Mylar sheets, and scattering intensities were measured by running 2θ scans from −0.1° to 5° with a point detector in the transmission geometry. All scattering data were reported in arbitrary units as a function of *Q*, the momentum transferred during a scattering event. Data analysis was conducted using the Beaucage Unified Model[67,68] applied with the Irena SAS tool for modeling and analysis of small angle scattering within the Igor Pro application (a commercial scientific graphing, image processing, and data analysis software from Wave Metrics, Portland, OR).

Thermal Characterization: Thermogravimetric analysis (TGA) was conducted under N_2 with a TA Instruments Model TGA Q50 analyzer, using a heating rate of 5 °C min^{-1}.

Porosimetry and gas sorption selectivity study: All samples were degassed at 80 °C for 24 h prior to each gas sorption study. BET surface areas and pore size distributions for pore sizes in the 1.7-300 nm range were determined with N_2-sorption porosimetry at 77 K using a Micromeritics ASAP 2020 surface area and porosity analyzer. Micropore analysis was conducted either with N_2-sorption, at 77 K using a low pressure transducer (0.1 Torr) on the Micromeritics ASAP 2020 surface area and porosity analyzer, or with CO_2-sorption up to 760 torr (0.03 relative pressure) at 273 K (ice-water bath) using a Micromeritics Tristar II 3020 version 3.02. The same instrument was used for a relative adsorption study for N_2, H_2, CH_4 and CO_2 at 273 K.

Adsorption isotherms were obtained up to 1 bar, and the gas sorption selectivities were calculated with Henry's law ($p=k_HC$, p: partial pressure in phase II; C: concentration in phase I; k_H: Henry's law constant),[101] from the ratios of the low-pressure slopes (<0.1 bar) of the corresponding isotherms.[102]

FIGURES

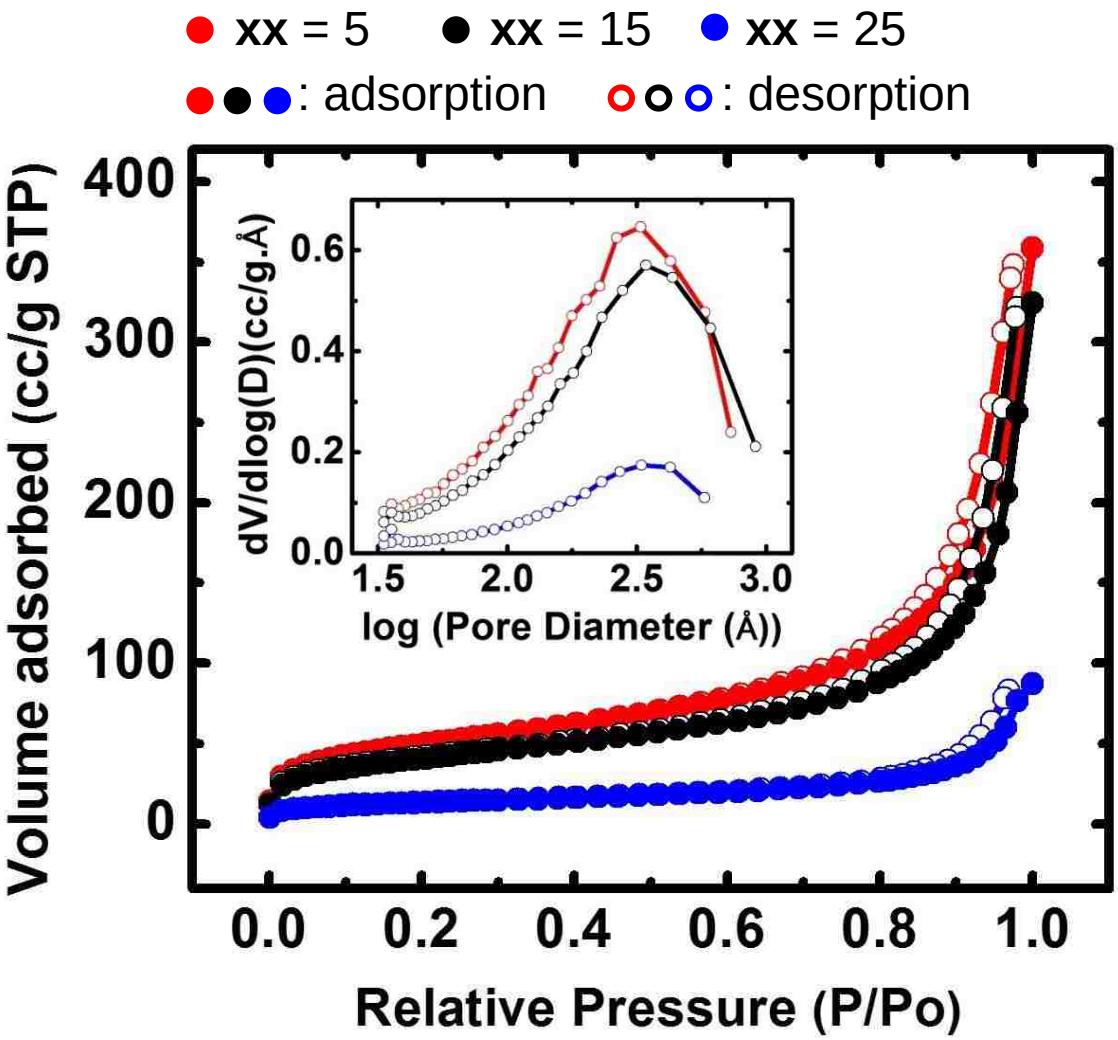

Figure 1. N_2-sorption isotherms at 77 K of three PA-xx aerogels prepared with the lowest (xx=5), middle (xx=15) and highest (xx=25) concentration sols used in this study. Inset: Corresponding pore-size distributions in the 1.7-300 nm range by the BJH desorption method.

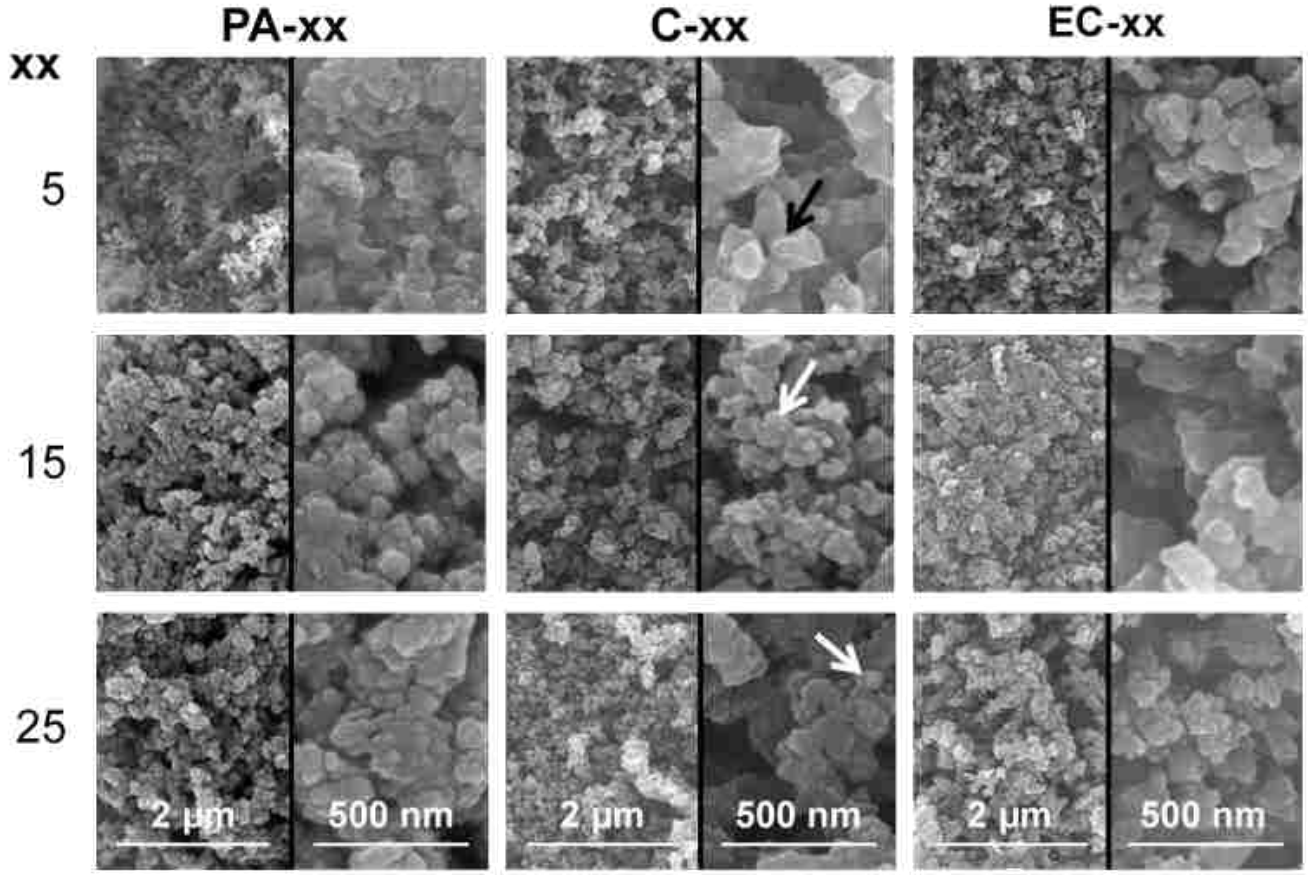

Figure 2. Scanning Electron Microscopy (SEM) at two different magnifications of low (xx=5), middle (xx=15) and high (xx=25) density PA-xx aerogels, the corresponding carbon aerogels (C-xx) and the etched carbon aerogels (EC-xx). Arrows point at particles matching the primary particle sizes as those were identified with SAXS (see Table 2, and Appendix II in Supporting Information).

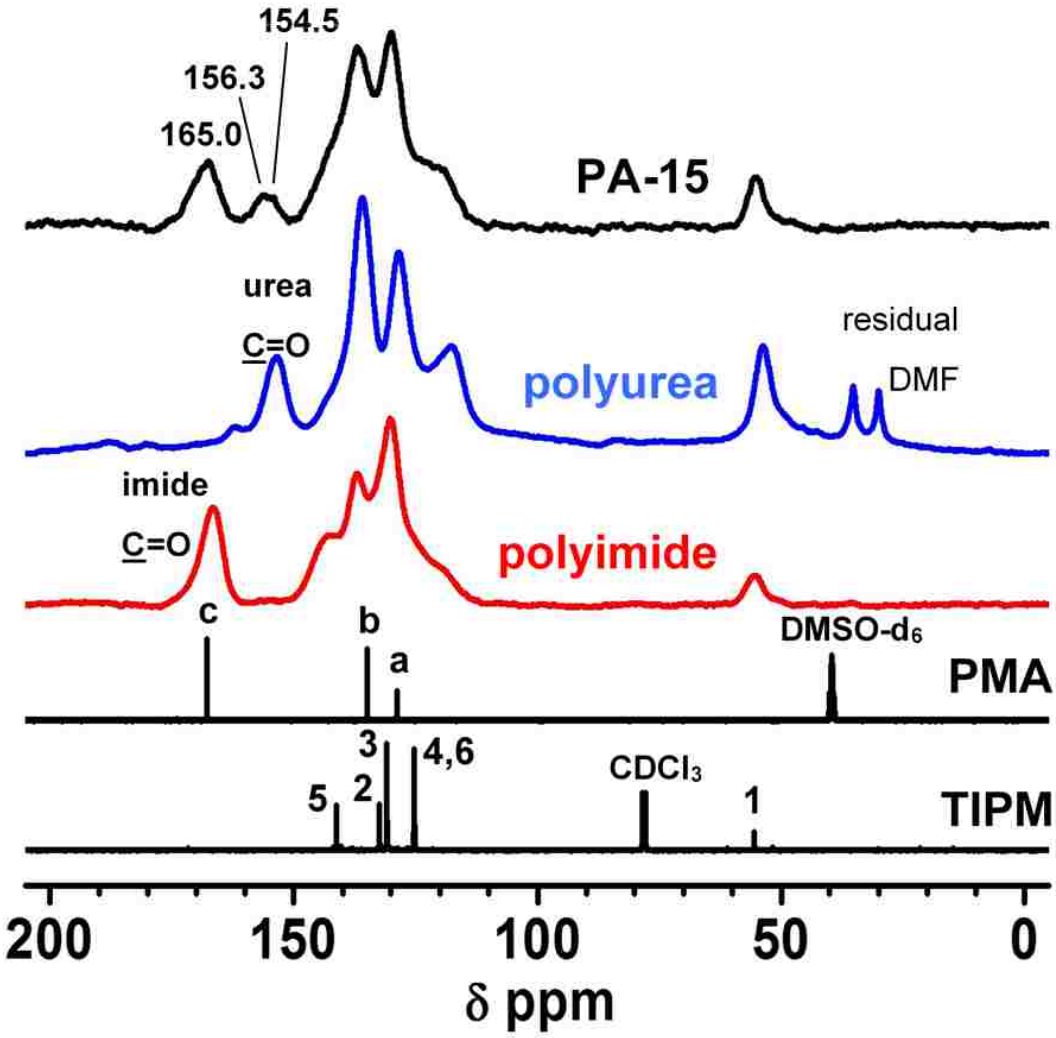

Figure 3. Top three spectra: Solid-state CPMAS ^{13}C NMR spectra of a representative PA-xx aerogel, of a TIPM/H_2O-derived polyurea aerogel, and of a TIPM/pyromellitic anhydride-derived polyimide aerogel, as indicated. (Note, only polyurea contained residual gelation solvent: DMF.) Bottom two spectra: Liquid state ^{13}C NMR of pyromellitic acid (PMA) in DMSO-d_6, and of TIPM in $CDCl_3$. (All spectra are referenced to TMS.)

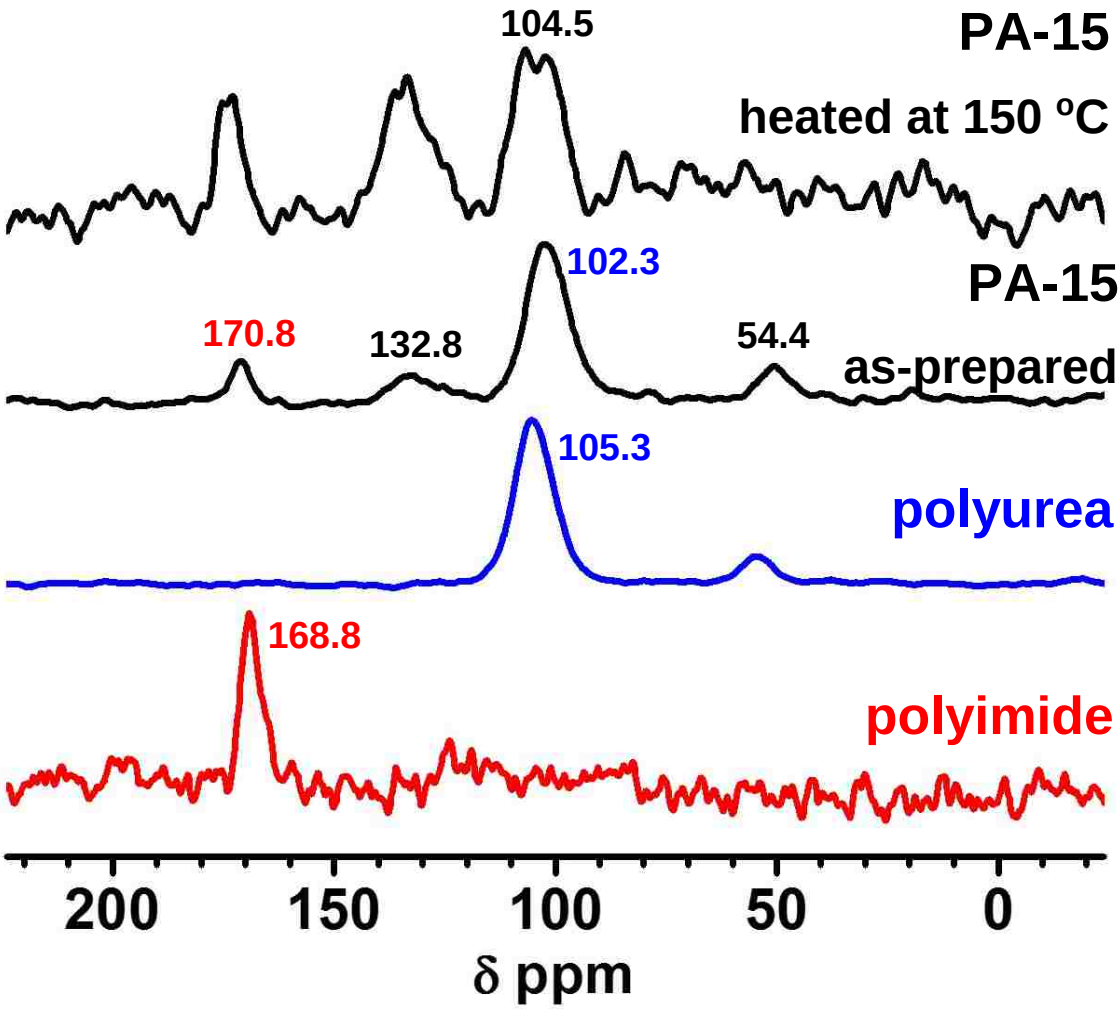

Figure 4. Solid-state CPMAS ^{15}N NMR spectra of a representative as-prepared PA-xx aerogel and after heating at 150 ºC, together with the spectra of a TIPM/H_2O-derived polyurea aerogel, and of a TIPM/pyromellitic anhydride-derived polyimide aerogel, as indicated. (All spectra are referenced to liquid NH_3.)

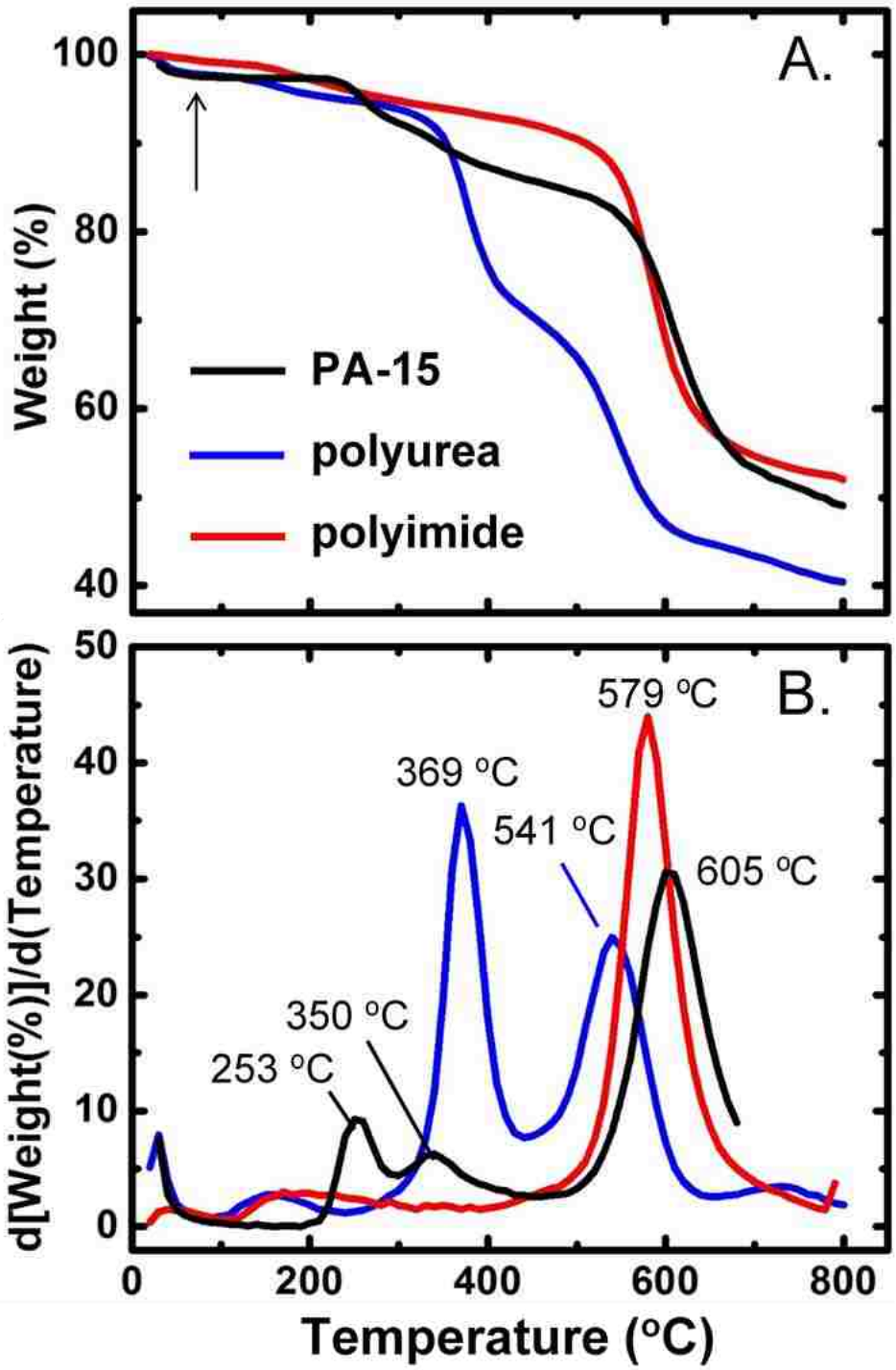

Figure 5. A. Representative thermogravimetric analysis data (TGA) under N_2 at 5 ^oC min^{-1} of samples as shown. (Arrow points at the early mass loss by PA-15 (about 3%), which is due to loss of CO_2. See text and Movie S.1). B. First derivative of the traces in part A.

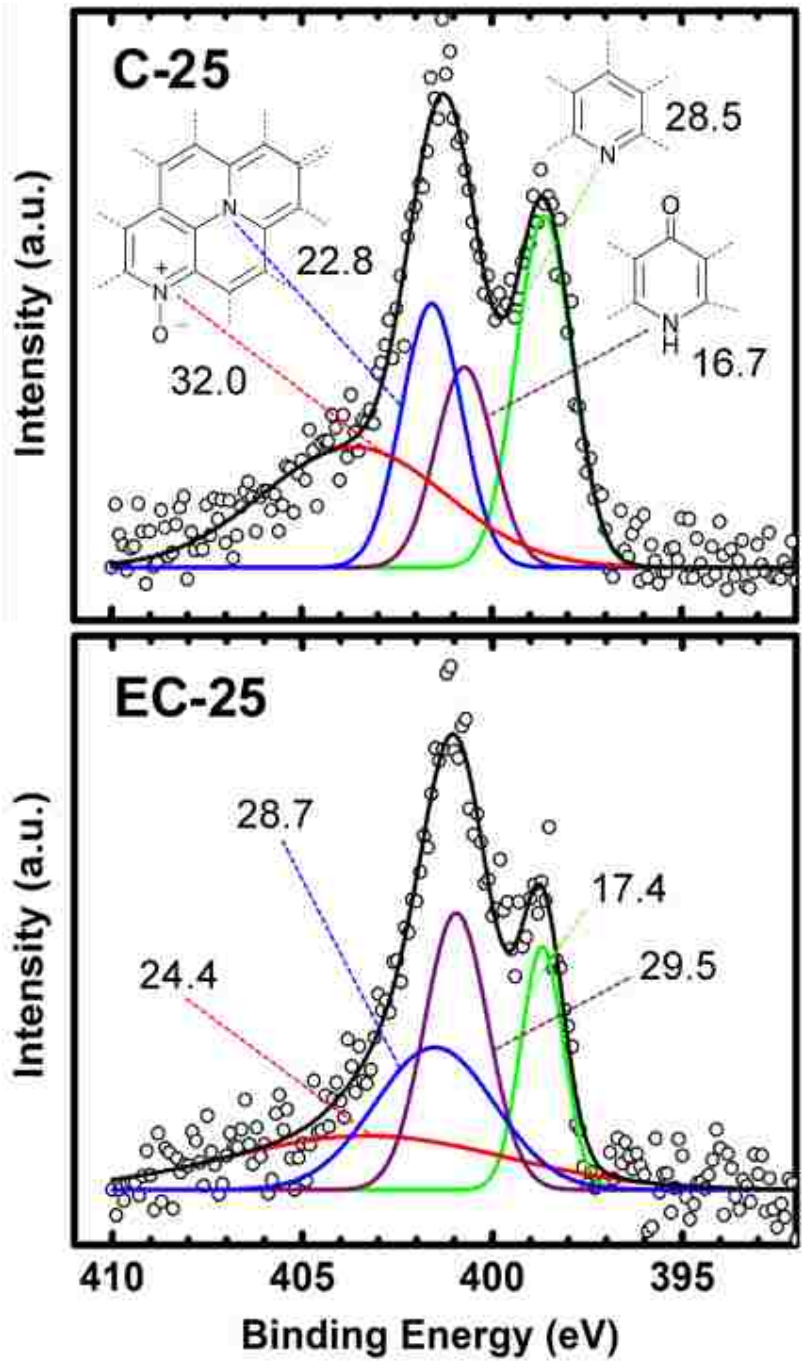

Figure 6. High resolution XPS spectra (circles) of the N1s peak in the two samples as shown. Data were fitted with Gaussians that correspond to the types of N as indicated. (For C-25, R^2=0.969; for EC-25, R^2=0.959).

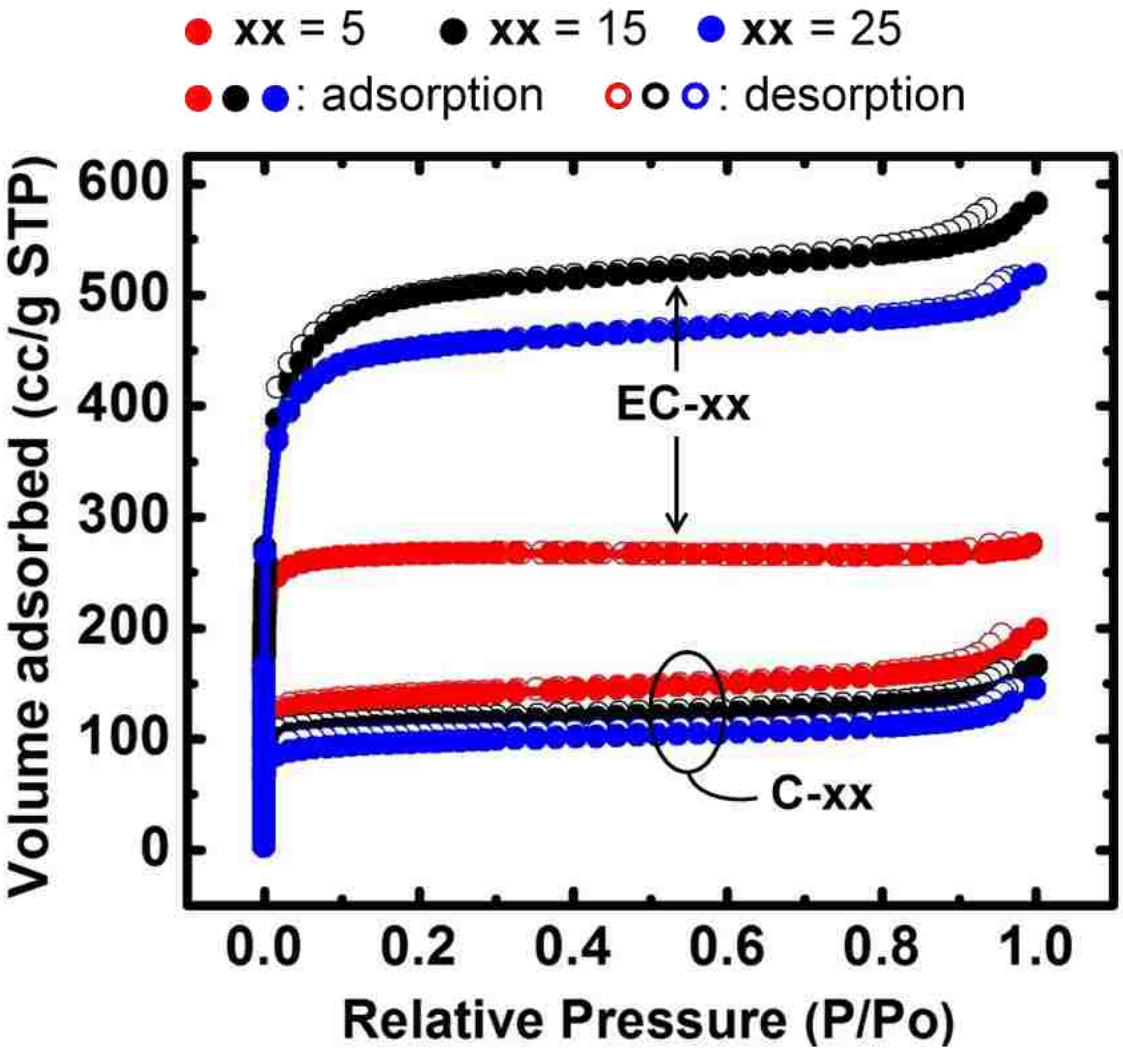

Figure 7. N_2-sorption isotherms at 77 K of three C-xx and three EC-xx aerogels at the lowest (xx=5), middle (xx=15) and highest (xx=25) density levels, as indicated by color-coding. (Each isotherm combines data from two experiments, including one carried out with a low-pressure transducer to follow micropores.)

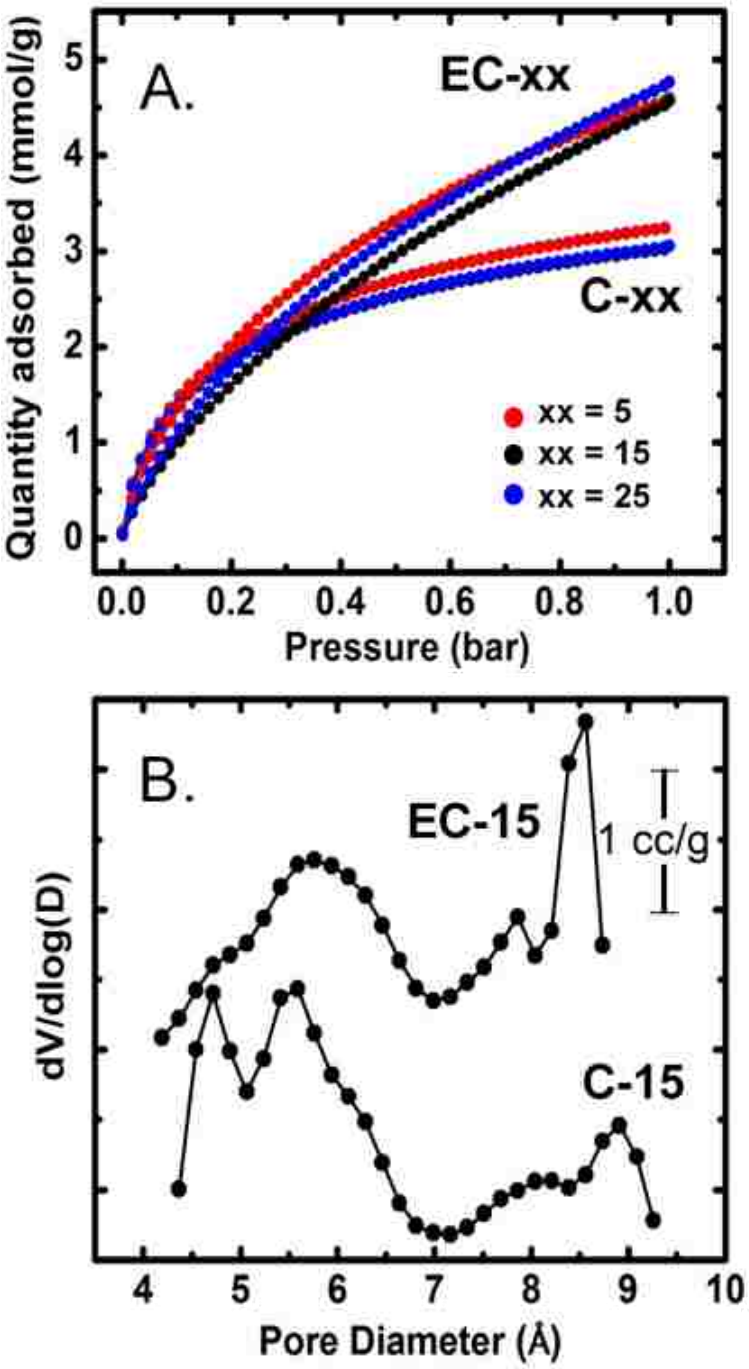

Figure 8. A. CO_2 adsorption isotherms at 0 ^oC (273 K) up to 1 bar of the carbon aerogels samples, as shown. B. Pore size distribution calculated by the CO_2 adsorption data of part A.

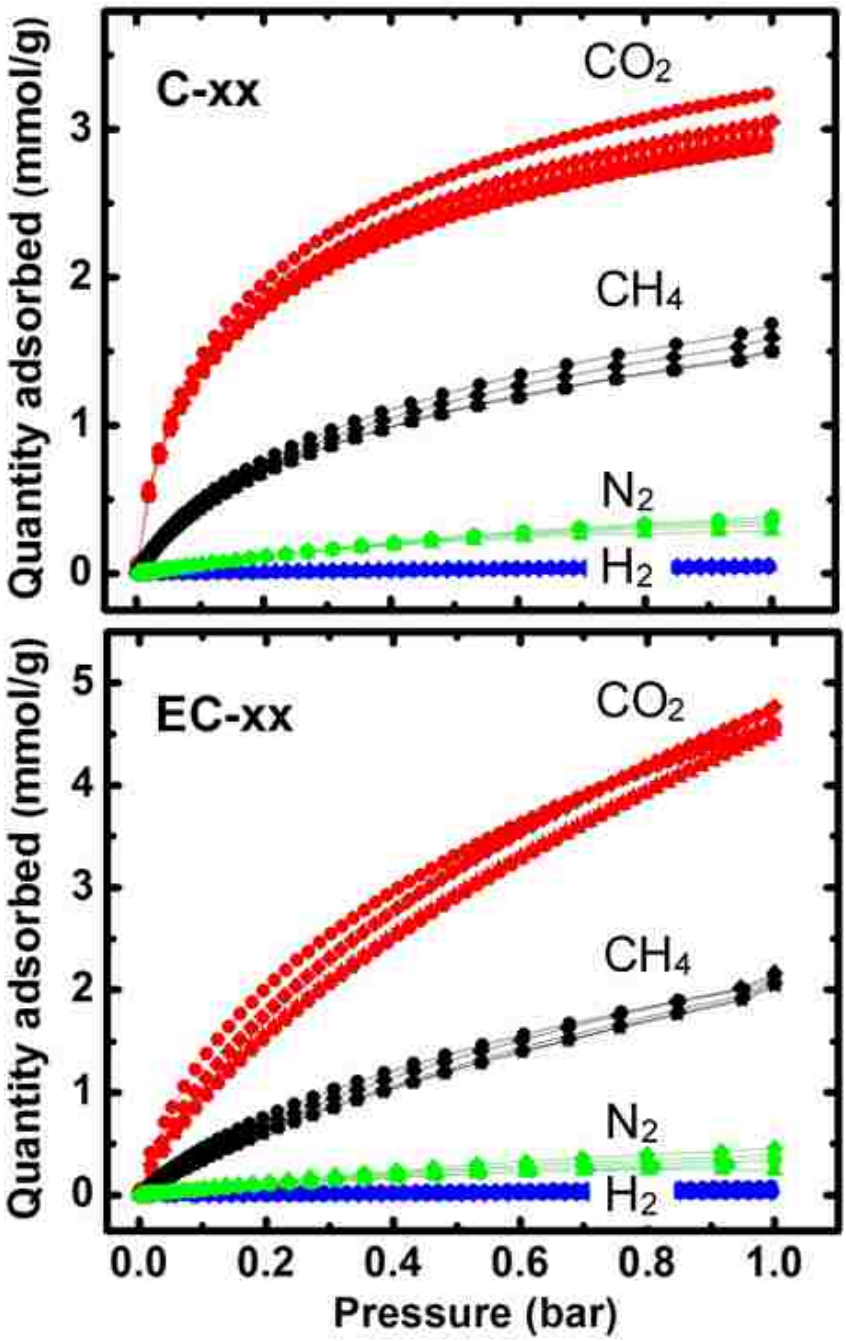

Figure 9. Adsorption isotherms at 0 ºC (273 K) up to 1 bar of the four gasses as shown on C-xx and EC-xx. The plots include samples at all five xx levels considered in this study.

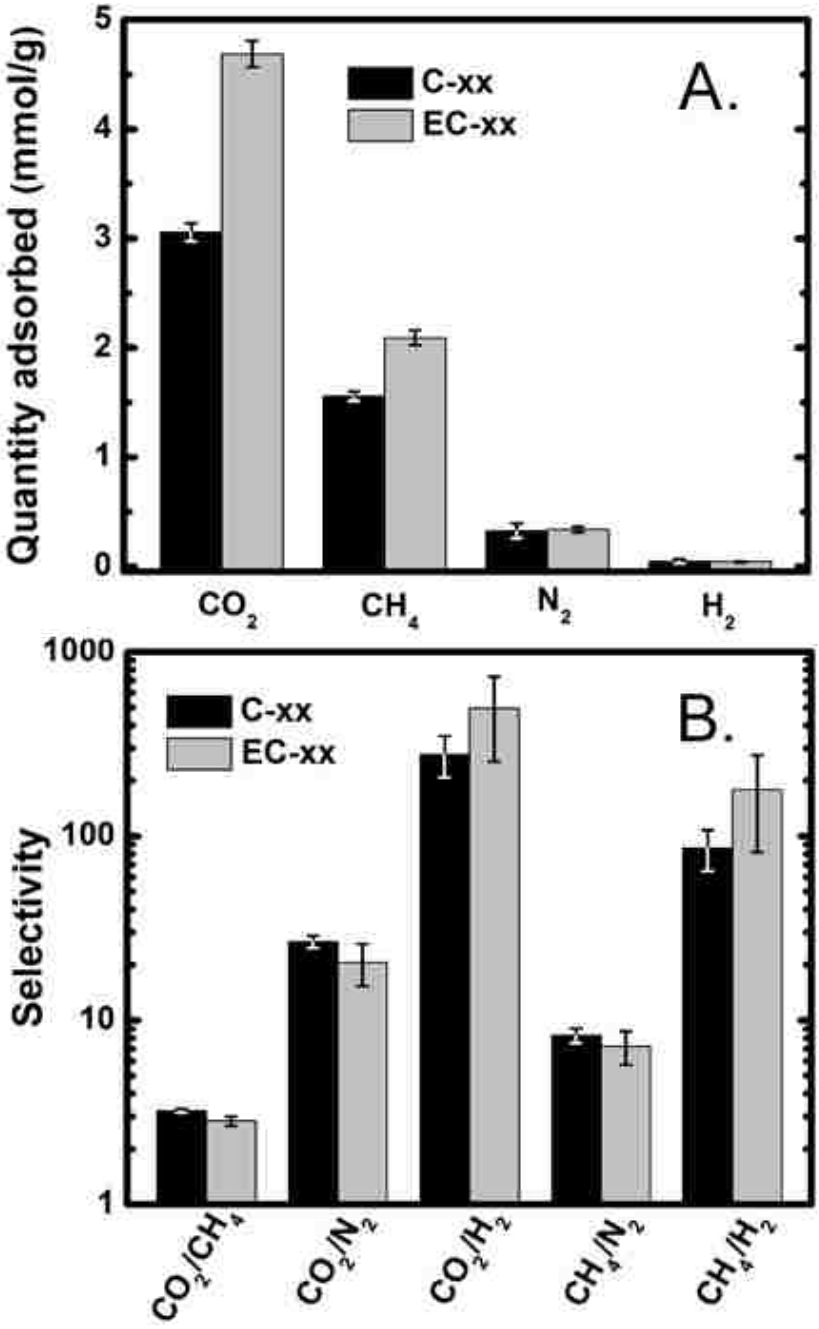

Figure 10. A. Comparison of the total gas uptake at 1 bar by the two carbon aerogels, C-xx and EC-xx (data from Figure 9). B. Selectivities calculated from the low-pressure end of the isotherms of Figure 9 using Henry's law. Data in both parts A and B are average over all the xx levels of C-xx and EC-xx. (For the actual data, refer to Table S.2 of Appendix VII in Supporting Information.

SUPPORTING INFORMATION

Appendix I: Formulations and gelation times of PA-xx aerogels. Appendix II: Small-angle X-ray scattering (SAXS) data for PA-xx and C-xx aerogels. Appendix III: Solid-state CPMAS ^{13}C-NMR spectra of all PA-xx, and of certain anhydrides as controls. Appendix IV: FTIR of PA-xx. Appendix V: High-resolution XPS spectra of the C1s of C-25 and EC-25. Appendix VI: Micropore size distribution of all C-xx and EC-xx. Appendix VII: Gas sorption data for CO_2, CH_4, N_2 and H_2 by C-xx and by EC-xx at 273 K, 1 bar. Movie S.1: CO_2 evolution by heating a PA-xx aerogel at 150 ºC. This material is available free of charge via the Internet at http://pubs.acs.org.

Figure S.5. FTIR of PA-15 aerogel after heating at 150 ^{o}C. In comparison with the previous spectrum, note the sharpening of the imide absorptions at 1778 cm^{-1} and 1719 cm^{-1}, and the absence of the broad absorption at 1670 cm^{-1}.

Appendix V. High resolution XPS spectra of the C1s of C-25 and EC-25

Figure S.6. High resolution XPS data (circles) of the C1s peak in the two samples as shown. Both spectra were fitted with 4 Gaussians as shown. (For both C-25 and EC-25, R^2=0.998.)

Appendix VI. Micropore size distribution of all C-xx and EC-xx

Figure S.7. Pore size distributions in the micropore range of C-xx and EC-xx as shown. Data are based on CO_2 adsorption isotherms at 0 ^{o}C, up to 1 bar absolute pressure (see Figure 8 in the main article) and were calculated using a DFT model.

Appendix VII. Gas sorption data for CO_2, CH_4, N_2 and H_2 by C-xx and by EC-xx at 273 K, 1 bar

Table S.3. Adsorption capacities and selectivities as shown.

Appendix I. Formulations and gelation times of PA-xx aerogels

Table S.1. Formulations and gelation times of PA-xx aerogels.

Sample	PMA				Desmodur RE		TIPM			THF		gelation time [d]
	mass (g)	Volume [a] (mL)	mmol	*C* (M)	Volume (mL)	mass [b] (g)	mass [c] (g)	mmol	*C* (M)	mass (g)	Volume (mL)	
PA-2.5	0.190	0.116	0.75	0.030	1.330	1.359	0.367	1.00	0.040	20.7	23.3	~ 4 h
PA-5	0.190	0.116	0.75	0.061	1.330	1.359	0.367	1.00	0.081	9.59	10.8	3 h 15 min
PA-10	0.190	0.116	0.75	0.125	1.330	1.359	0.367	1.00	0.167	4.02	4.52	2 h 10 min
PA-15	0.190	0.116	0.75	0.193	1.330	1.359	0.367	1.00	0.257	2.16	2.43	1 h 30 min
PA-20	0.190	0.116	0.75	0.264	1.330	1.359	0.365	1.00	0.352	1.23	1.39	45 min
PA-25	0.190	0.116	0.75	0.339	1.330	1.359	0.367	1.00	0.453	0.67	0.76	15 min

[a] The volume of PMA was calculated based on its density measured with helium pycnometry (1.642 g cm^{-3}). [b] The mass of commercial Desmodur RE was calculated based on its density as that was measured in our laboratory (1.022 g cm^{-3}). [c] The mass of TIPM in Desmodur RE was calculated based on the 27% w/w concentration given by the manufacturer. [d] All gelation times, except for PA-2.5, are at room temperature. PA-2.5 gelled at 60 °C.

Appendix II. Small angle x-ray scattering (SAXS) data for PA-xx and C-xx aerogels

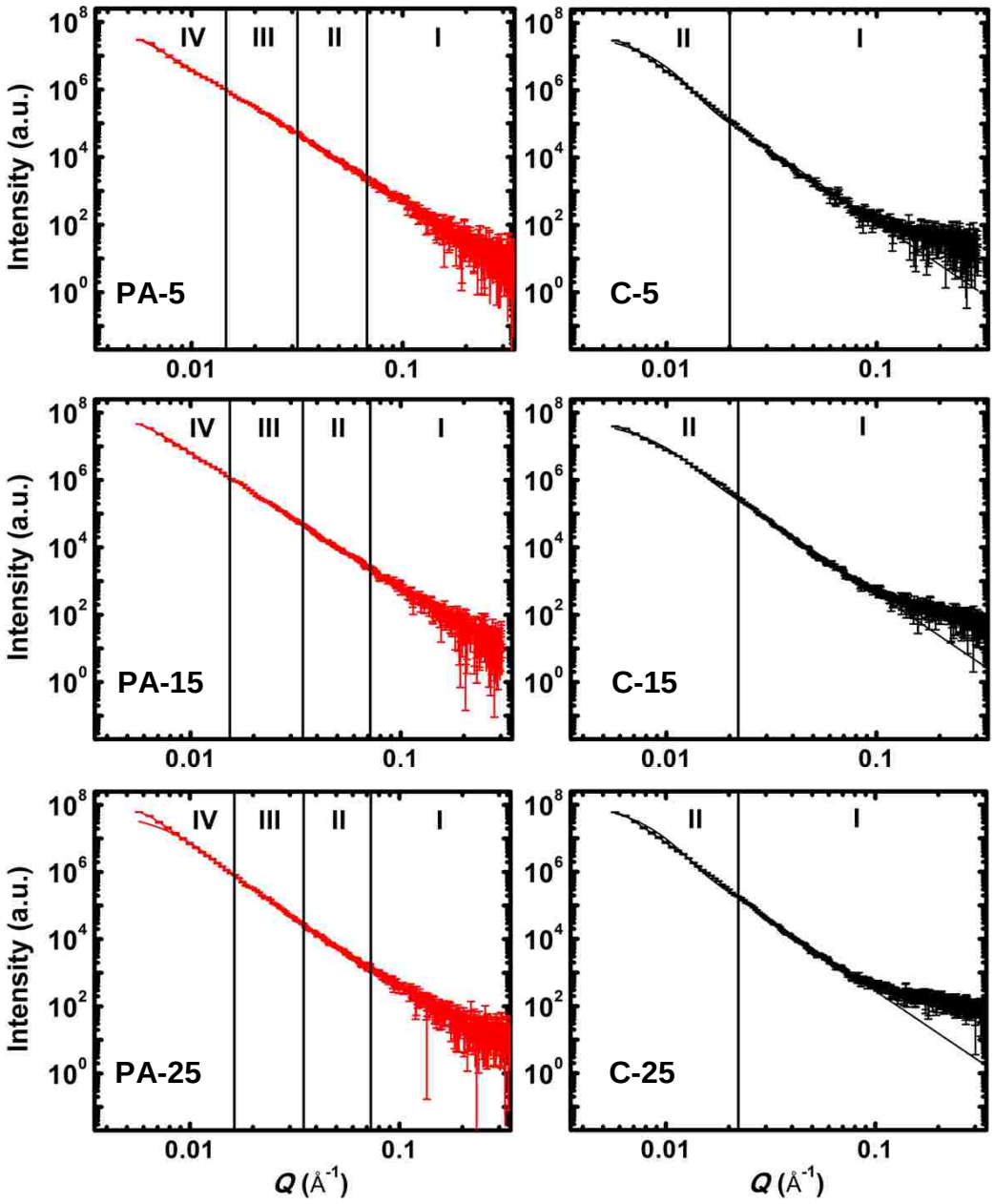

Figure S.1. SAXS profiles from selected polymeric aerogels of this study (PA-xx, for xx=5, 15 and 25), and their respective carbon aerogels (C-xx).

Table S.2. SAXS data obtained by fitting the scattering profiles of Figure S.1 using the Beaucage Unified Model[S.R-1].

Sample	Primary Particles			Secondary Particles		
XX	high-Q slope [a]	R_G(I) [b] (nm)	R_1 [c] (nm)	low-Q slope [d]	R_G(II) [e] (nm)	R_2 [f] (nm)
PA-xx						
5	-4.05 ± 0.02	7.82 ± 0.42	10.16 ± 0.55	-3.51 ± 0.09	42.31 ± 3.15	54.95 ± 4.09
10	-4.23 ± 0.02	7.50 ± 0.41	9.74 ± 0.54	-3.69 ± 0.16	38.79 ± 2.40	50.37 ± 3.11
15	-4.00 ± 0.02	8.35 ± 0.42	10.85 ± 0.55	-3.72 ± 0.11	39.26 ± 1.47	50.98 ± 1.91
20	-4.25 ± 0.05	7.94 ± 0.84	10.31 ± 1.09	-3.96 ± 0.29	33.55 ± 1.53	43.57 ± 1.98
25	-4.22 ± 0.05	9.37 ± 0.71	12.17 ± 0.92	-4.13± 0.30	37.31 ± 1.74	48.45 ± 2.26
C-xx [g]						
5	-4.20 ± 0.01	27.94 ± 1.16	36.28 ± 0.21	-	-	-
10	-4.21 ± 0.01	24.19 ± 0.11	31.42 ± 0.14	-	-	-
15	-4.21 ± 0.01	25.37 ± 0.18	32.95 ± 0.23	-	-	-
20	-4.21 ± 0.01	24.74 ± 0.15	32.13 ± 0.19	-	-	-
25	-4.20 ± 0.01	29.11 ± 0.14	37.80 ± 0.18	-	-	-

Referring to Figure S.1:

[a] From power-law Region I. Slopes <-4.00, signify primary particles with density-gradient boundaries.

[b] Radius of gyration of primary particles, R_G(I), from Region II (first Guinier knee).

[c] Primary particle radii $R_1 = (R_G(I)/0.77)$.

[d] From power-law Region III. All slopes <-3, meaning surface fractal secondary particles; surface fractal dimension, D_s=6-|slope|.

[e] Radius of gyration of secondary particles, R_G(II), from Region IV (second Guinier knee).

[f] Secondary particle radii, $R_2 = (R_G(II)/0.77)$.

[g] Within our accessible range of Q, scattering profiles of C-xx aerogels could be fitted only with a high-Q power law and one Guinier knee.

S.R-1 (a) Beaucage, G. *J. Appl. Crystallogr.* **1995**, *28*, 717-728.

(b) Beaucage, G. *J. Appl. Crystallogr.* **1996**, *29*, 134-146.

Appendix III. Solid-state CPMAS ^{13}C-NMR spectra of all PA-xx and of anhydrides

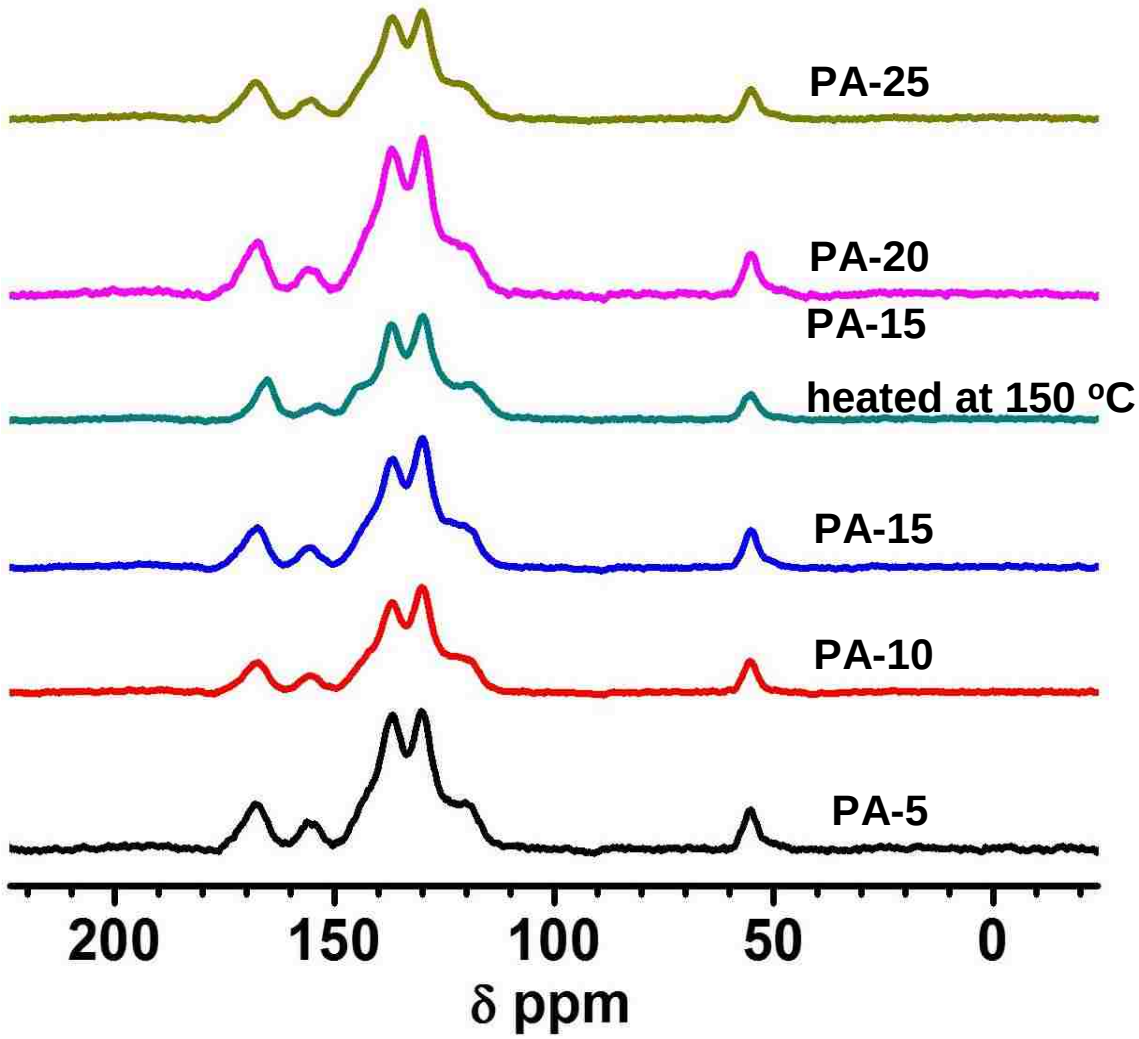

Figure S.2. Solid-state CPMAS ^{13}C NMR spectra of all PA-xx as shown.

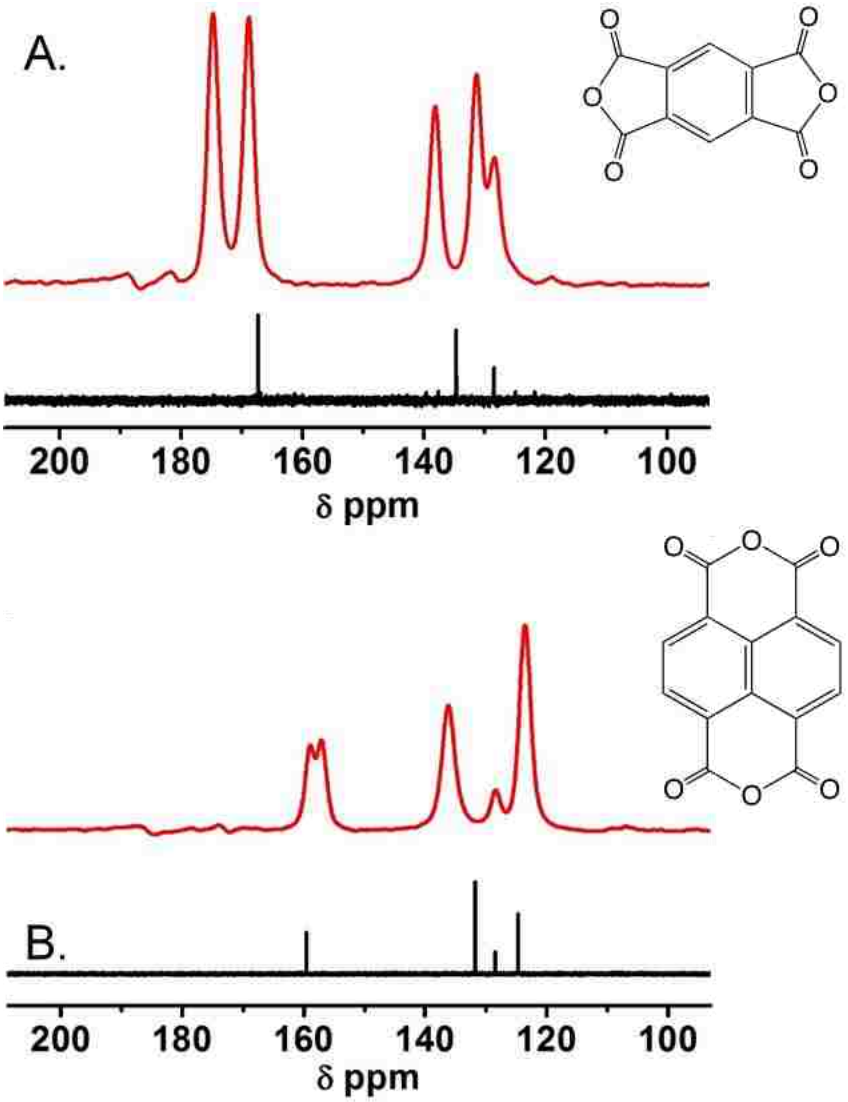

Figure S.3. Comparison of liquid phase (in DMSO-d_6) and solid-state CPMAS ^{13}C NMR spectra of pyromellitic dianhydride (A) and naphthalene tetracarboxylic dianhydride (B), as shown.

Appendix IV. IR spectra of PA-xx

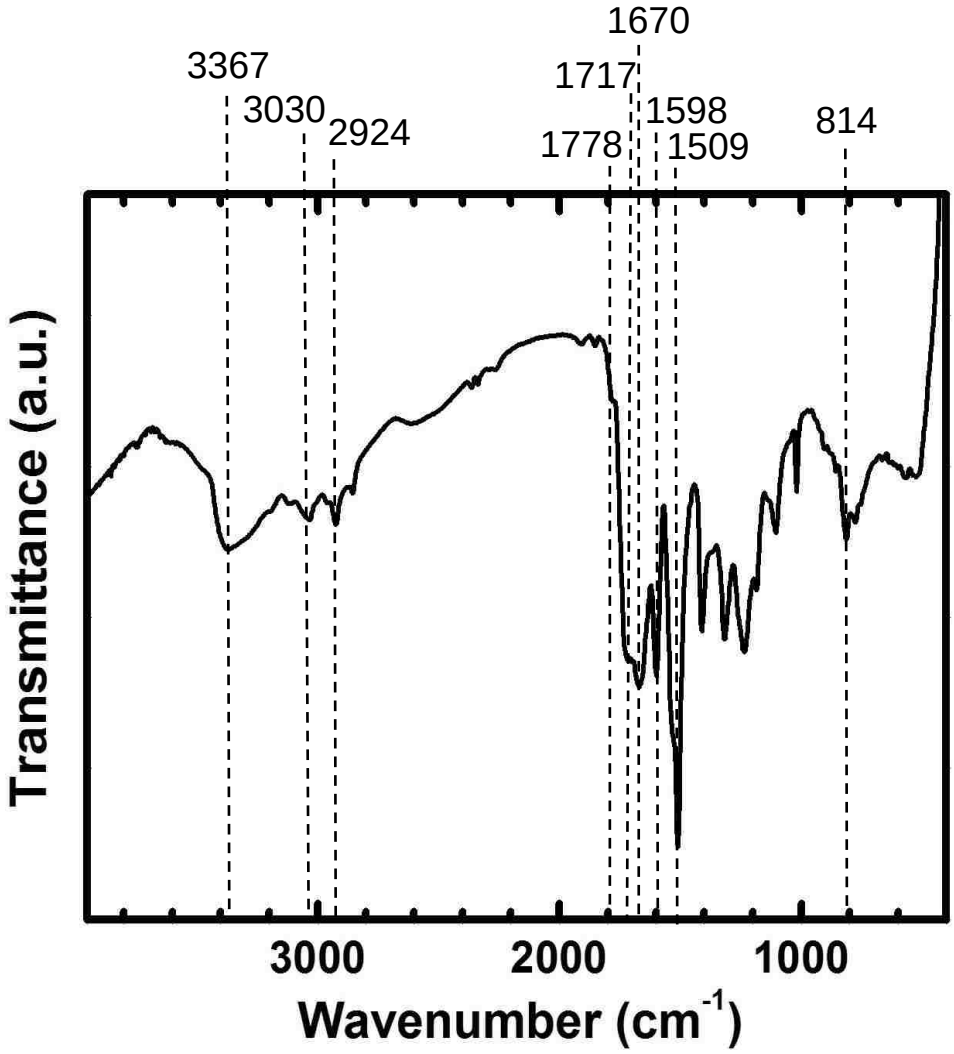

Figure S.4. FTIR spectrum of a representative as-prepared PA-xx aerogel (PA-15).

Peak Assignment:

3367 cm^{-1}: NH stretch.

3030 cm^{-1}: aromatic C-H stretch

2924 cm^{-1}: aliphatic C-H stretch

1717 cm^{-1} and 1778 cm^{-1} (shoulder): symmetric and asymmetric stretches of imide C=O

1670 cm^{-1}: overlapping urea, amide and carbamic-anhydride C=O stretches

1598 cm^{-1}, 1509 cm^{-1}: aromatic C=C stretches

814 cm^{-1}: aromatic CH OOP bending (*para* substituted ring)

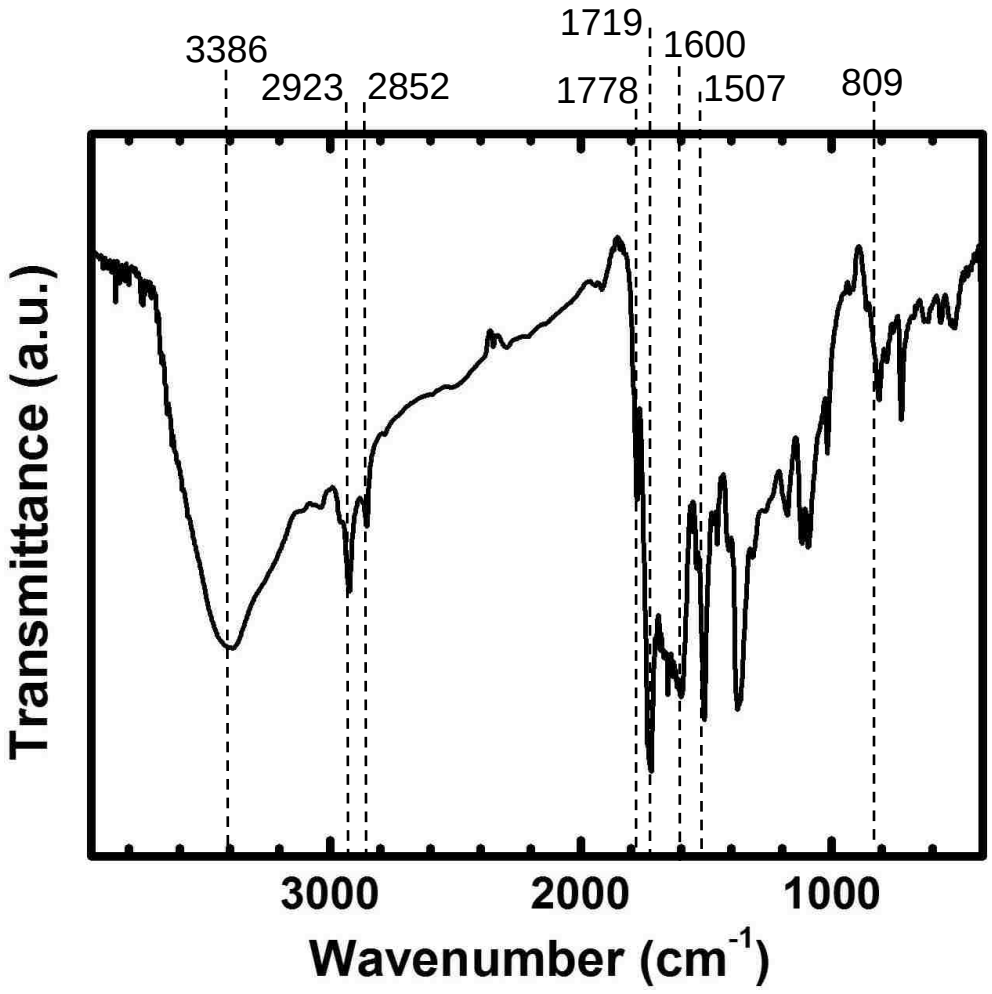

Figure S.5. FTIR of PA-15 aerogel after heating at 150 ºC. In comparison with the previous spectrum, note the sharpening of the imide absorptions at 1778 cm^{-1} and 1719 cm^{-1}, and the absence of the broad absorption at 1670 cm^{-1}.

Appendix V. High-resolution XPS spectra of the C1s of C-25 and EC-25

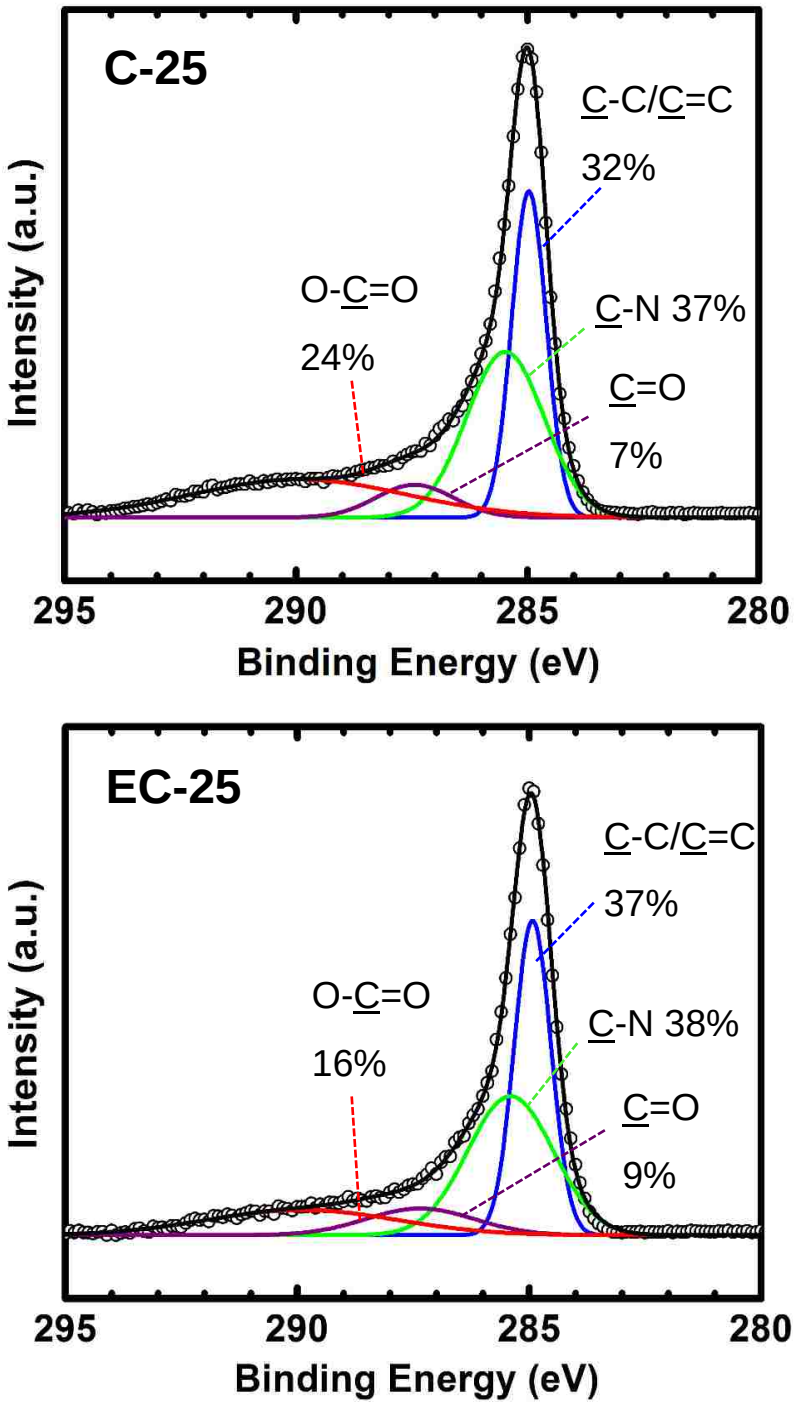

Figure S.6. High resolution XPS data (circles) of the C1s peak in the two samples as shown. Both spectra were fitted with 4 Gaussians as shown. (For both C-25 and EC-25, R^2=0.998).

Appendix VI. Micropore size distribution of all C-xx and EC-xx

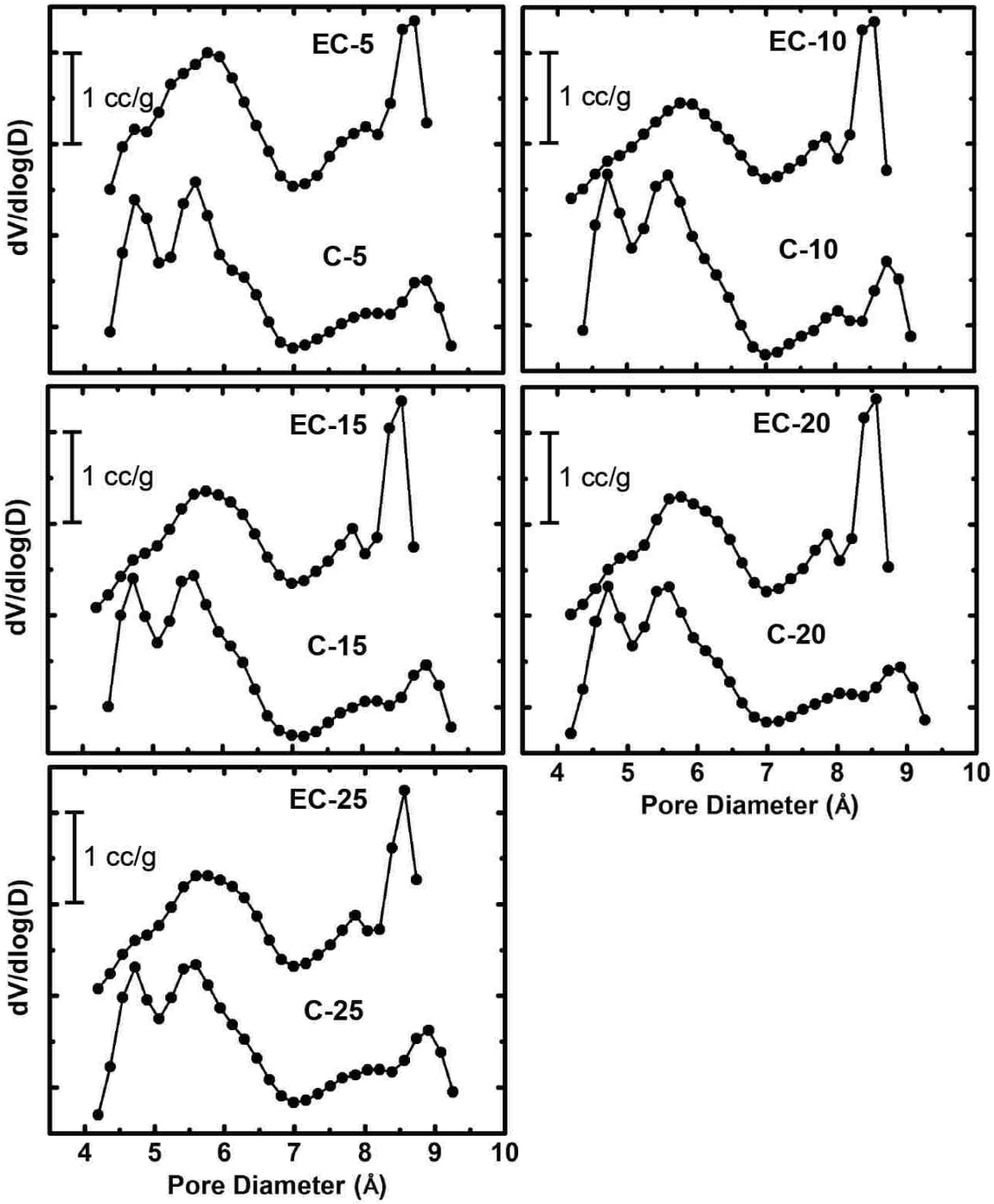

Figure S.7. Pore size distributions in the micropore range of C-xx and EC-xx as shown. Data are based on CO_2 adsorption isotherms at 0 ^oC, up to 1 bar absolute pressure (see Figure 8 in the main article) and were calculated using a DFT model.

Appendix VII. Gas sorption data for CO_2, CH_4, N_2 and H_2 by C-xx and by EC-xx at 273 K, 1 bar

Table S.3. Adsorption capacities and selectivities as shown.

Sample	N_2 adsorption @1 bar (273 K)		CO_2 adsorption @ 1 bar (273 K)		H_2 adsorption @ 1 bar (273 K)		CH_4 adsorption @ 1 bar (273 K)		Selectivity				
	mmol/g	%w/w	mmol/g	%w/w	mmol/g	%w/w	mmol/g	%w/w	CO_2/N_2	CO_2/H_2	CO_2/CH_4	CH_4/N_2	CH_4/H_2
PA-xx													
5	-	-	0.91	4.00	-	-	0.22	0.35	-	-	10.0	-	-
10	-	-	0.85	3.74	-	-	0.17	0.27	-	-	13.0	-	-
15	-	-	0.86	3.78	-	-	0.21	0.33	-	-	9.40	-	-
20	-	-	0.86	3.78	-	-	0.22	0.35	-	-	9.60	-	-
25	-	-	0.80	3.52	-	-	0.19	0.30	-	-	10.5	-	-
C-xx													
5	0.32	0.90	3.27	14.4	0.05	0.01	1.68	2.68	30.6	180	3.18	9.64	56.7
10	0.29	0.81	2.99	13.2	0.05	0.01	1.51	2.41	26.6	380	3.27	8.14	116
15	0.36	1.03	3.05	13.4	0.05	0.01	1.52	2.43	25.5	222	3.36	7.60	66.2
20	0.31	0.87	2.91	12.8	0.05	0.01	1.49	2.38	24.7	301	3.22	7.67	93.6
25	0.35	0.98	3.07	13.5	0.04	0.00_9	1.59	2.54	26.3	310	3.13	8.38	99.0
EC-xx													
5	-	-	4.66	20.5	0.08	0.01	2.12	3.39	30.9	284	3.08	10.0	92.4
10	0.25	0.70	4.62	20.4	0.04	0.00_8	2.09	3.34	20.5	336	2.74	7.51	122
15	0.38	1.06	4.67	20.5	0.04	0.00_8	2.04	3.26	17.1	342	2.94	5.81	116
20	0.33	0.92	4.64	20.4	0.02	0.00_4	2.05	3.28	16.8	928	2.60	6.47	356
25	0.44	1.23	4.85	21.3	0.03	0.00_6	2.16	3.45	17.9	584	2.84	6.32	205

ACKNOWLEDGEMENTS

We thank the Army Research Office for financial support under Award Number W911NF-14-1-0369. We also thank Covestro LLC (formerly Bayer Corporation U.S.A.) for the generous supply of Desmodur RE (TIPM), and the Materials Research Center of the Missouri University of Science and Technology for support with materials characterization.

REFERENCES

(1) Falkowski, P.; Scholes, R. J.; Boyle, E.; Canadell, J.; Canfield, D.; Elser, J.; Gruber, N.; Hibbard, K.; Högberg, P.; Linder, S.; MacKenzie, F. T.; Moore, B.; Pedersen, T.; Rosenthal, Y.; Seitzinger, S.; Smetacek, V.; Steffen, W. The Global Carbon Cycle: A Test of Our Knowledge of Earth as a System. *Science* **2000**, *290*, 291–296.

(2) Junling, H.; McElroy, M. B. The Contemporary and Historical Budget of Atmospheric CO_2. *Can. J. Phys.* **2012**, *90*, 707–716.

(3) Bauer, J. E.; Cai, W. J.; Raymond, P. A.; Bianchi, T. S.; Hopkinson, C. S.; Regnier, P. A. G. The Changing Carbon Cycle of the Coastal Ocean. *Nature* **2013**, *504*, 61–70.

(4) http://earthobservatory.nasa.gov/Features/OceanCarbon (08-03-16).

(5) http://www.grida.no/publications/rr/natural-fix/page/3725.aspx (08-03-16).

(6) https://scripps.ucsd.edu/programs/keelingcurve (05-02-16).

(7) Shakun, J. D.; Clark, P. U.; He, F.; Marcott, S. A.; Mix, A. C.; Liu, Z.; Otto-Bliesner, B.; Schmittner, A.; Bard, E. Global Warming Preceded by Increasing Carbon dioxide Concentrations during the Last Deglaciation. *Nature* **2012** 484, 49–54.

(8) Haszeldine, R. S. Carbon Capture and Storage: How Green Can Black Be? *Science* **2009**, *325*, 1647–1652.

(9) Sahney, S.; Benton, M. J. Recovery from the Most Profound Mass Extinction of All Time. *Proc. R. Soc. B* **2008**, *275*, 759–765.

(10) Chiesa, P.; Consonni, S.; Kreutz, T.; Williams, R. Co-production of Hydrogen, Electricity and CO_2 from Coal with Commercially Ready Technology. Part A: Performance and Emissions. *Int. J. Hydrogen Energy* **2005**, *30*, 747−767.

(11) Nugent, P.; Belmabkhout, Y.; Burd, S. D.; Cairns, A. J.; Luebke, R.; Forrest, K.; Pham, T.; Ma, S.; Space, B.; Wojtas, L.; Eddaoudi, M.; Zaworotko, M. J. Porous Materials with Optimal Adsorption Thermodynamics and Kinetics for CO_2 Separation. *Nature* **2013**, *495*, 80–84.

(12) Luis, P. Use of Monoethanolamine (MEA) for CO_2 Capture in a Global Scenario: Consequences and Alternatives. *Desalination* **2016**, *380*, 93–99.

(13) Wang, J.; Huang, L.; Yang, R.; Zhang, Z.; Wu, J.; Gao, Y.; Wang, Q.; O'Hare, D.; Zhong, Z. Recent Advances in Solid Sorbents for CO_2 Capture and New Development Trends. *Energy Environ. Sci.* **2014**, *7*, 3478–3518.

(14) Lennard-Jones, J. E. Processes of Adsorption and Diffusion on Solid Surfaces. *Trans. Faraday Soc.* **1932**, *28*, 333–359.

(15) Banerjee, R.; Phan, A.; Wang, B.; Knobler, C.; Furukawa, H.; O'Keeffe, M.; Yaghi, O. M. High-Throughput Synthesis of Zeolitic Imidazolate Frameworks and Application to CO_2 Capture. *Science* **2008**, *319*, 939–943.

(16) Su, F.; Lu, C. CO_2 Capture from Gas Stream by Zeolite 13X Using a Dual-column Temperature/Vacuum Swing Adsorption. *Energy Environ. Sci*. **2012**, *5*, 9021–9027.

(17) Himeno, S.; Komatsu, T.; Fujita, S.; High-pressure Adsorption Equilibria of Methane and Carbon dioxide on Several Activated Carbons. *J. Chem. Eng. Data* **2005**, *50*, 369–376.

(18) Lu, C.; Bai, H.; Wu, B.; Su, F.; Hwang, J. F. Comparative Study of CO_2 Capture by Carbon Nanotubes, Activated Carbons, and Zeolites. *Energy Fuels* **2008**, *22*, 3050–3056.

(19) Furukawa, H.; Ko, N.; Go, Y. B.; Aratani, N.; Choi, S. B.; Choi. E.; Yazaydin, A. O.; Snurr, R. Q.; O'Keeffe, M.; Kim, J.; Yaghi, O. M. Ultrahigh Porosity in Metal-Organic Frameworks. *Science* **2010**, *329*, 424–428.

(20) Cote, A. P.; Benin, A. I.; Ockwig, N. W.; O'Keeffe, W.; Matzger, A. J.; Yaghi, O. M. Porous, Crystalline, Covalent Organic Frameworks. *Science* **2005**, *310*, 1166–1170.

(21) McDonald, T. M.; Mason, J. A.; Kong, X.; Bloch, E. D.; Gygi, D.; Dani, A.; Crocellà, V.; Giordanino, F.; Odoh, S. O.; Drisdell, W. S.; Vlaisavljevich, B.; Dzubak, A. L.; Poloni, R.; Schnell, S. K.; Planas, N.; Lee, K.; Pascal, T.; Wan, L. F.; Prendergast, D.; Neaton, J. B.; Smit, B.; Kortright, J. B.; Gagliardi, L.; Bordiga, S.; Reimer, J. A.; Long. J. R. Cooperative Insertion of CO_2 in Diamine-appended Metal-Organic Frameworks. *Nature* **2015**, *519*, 303–308.

(22) Xu, Y.; Jin, S.; Xu, H.; Nagaia, A, Jiang, D. Conjugated Microporous Polymers: Design, Synthesis and Application. *Chem. Soc. Rev.* **2013**, *42*, 8012–8031.

(23) Vilela, F.; Zhang, K.; Antonietti, M. Conjugated Porous Polymers for Energy Applications. *Energy Environ. Sci*. **2012**, *5*, 7819–7832.

(24) Li, B.; Gong, R.; Wang, W.; Huang, X.; Zhang, W.; Li, H.; Hu, C.; Tan. B. A New Strategy to Microporous Polymers: Knitting Rigid Aromatic Building Blocks by External Cross-Linker. *Macromolecules* **2011**, 44, 2410–2414.

(25) Ben, T.; Qiu, S. Porous Aromatic Frameworks: Synthesis, Structure and Functions. *Cryst. Eng. Comm*. **2013**, *15*, 17–26.

(26) El-Kaderi, H. M.; Hunt, J. R.; Medoza-Cortes, J. L.; Cote, A. P.; Taylor, R. E.; O'Keeffe, M.; Yaghi, O. M. Designed Synthesis of 3D Covalent Organic Frameworks. *Science* **2007**, *316*, 268–272.

(27) Xu, H.; Gao, J.; Jiang, D. Stable, Crystalline, Porous, Covalent Organic frameworks as a Platform for Chiral Organocatalysts. *Nature Chemistry* **2015**, *7*, 905–912.

(28) Lua, J.; Zhang, J. Facile Synthesis of Azo-linked Porous Organic Frameworks via Reductive Homocoupling for Selective CO_2 Capture. *J. Mater. Chem. A* **2014**, *2*, 13831–13834.

(29) Xiang, Z.; Cao, D.; Dai, L. Well-defined two Dimensional Covalent Organic Polymers: Rational Design, Controlled Syntheses, and Potential Applications. *Polym. Chem.* **2015**, *6*, 1896–1911.

(30) Islamoglu, T.; Kim, T.; Kahveci, Z.; El-Kadri, O. M.; El-Kaderi. H. M. Systematic Postsynthetic Modification of Nanoporous Organic Frameworks for Enhanced CO_2 Capture from Flue Gas and Landfill Gas. *Phys. Chem. C.* **2016**, *120*, 2592−2599.

(31) Zhu, Y.; Long, H.; Zhang, W. Imine-Linked Porous Polymer Frameworks with High Small Gas (H_2, CO_2, CH_4, C_2H_2) Uptake and CO_2/N_2 Selectivity. *Chem. Mater*. **2013**, *25*, 1630–1635.

(32) Patel, H. A.; Sang, H. J.; Joonho, P.; Dennis, P.; Chen, Y. J.; Cafer, T. Y.; Ali, C. Unprecedented High-temperature CO_2 Selectivity in N_2-phobic Nanoporous Covalent Organic Polymers. *Nature Communications* **2013**, *4*, 1357–1364.

(33) Talapaneni, S. N.; Buyukcakir, O.; Je, S.; Srinivasan, S.; Seo, Y.; Polychropoulou, K.; Coskun, A. Nanoporous Polymers Incorporating Sterically Confined N-Heterocyclic Carbenes for Simultaneous CO_2 Capture and Conversion at Ambient Pressure. *Chem. Mater*. **2015**, *27*, 6818− 6826.

(34) Klumpen, C.; Breunig, M.; Homburg, T.; Stock. N.; Senker. Microporous Organic Polyimides for CO_2 and H_2O Capture and Separation from CH_4 and N_2 Mixtures: Interplay between Porosity and Chemical Function. *Chem. Mater.* **2016**, *28*, 5461–5470.

(35) Torrisi, A.; Bell, R. G.; Mellot-Draznieks, C. Functionalized MOFs for Enhanced CO_2 Capture. *Cryst. Growth Des*. **2010**, *10*, 2839−2841.

(36) Yang, X.; Yao, S. W.; Yu, M.; Jiang, J.-X. Synthesis and Gas Adsorption Properties of Tetra-Armed Microporous Organic Polymer Networks Based on Triphenylamine. *Macromol. Rapid Commun.* **2014**, *35*, 834−839.

(37) Dutta, S.; Bhaumik, A.; Wu, K. C.-W. Hierarchically Porous Carbon Derived from Polymers and Biomass: Effect of Interconnected Pores on Energy Applications. *Energy Environ. Sci*. **2014**, *7*, 3574–3592.

(38) Ma, T. Y.; Liu, L.; Yuan, Z. Y. Direct Synthesis of Ordered Mesoporous Carbons. *Chem. Soc. Rev.* **2013**, *42*, 3977–4003.

(39) Hoekman, S. K.; Broch, A.; Robbins, C. Hydrothermal Carbonization (HTC) of Lignocellulosic Biomass. *Energy Fuels* **2011**, *25*, 1802−1810.

(40) Hu, B.; Yu, S. H.; Wang, K.; Liu, L.; Xu, X. W. Functional Carbonaceous Materials from Hydrothermal Carbonization of Biomass: An Effective Chemical Process. *Dalton T.* **2008**, *40*, 5414−5423.

(41) Titirici, M. M.; Thomas, A.; Antonietti, M. Back in the Black: Hydrothermal Carbonization of Plant Material as an Efficient Chemical Process to Treat the CO_2 Problem? *New J. Chem.* **2007**, *31*, 787−789.

(42) An-Hui, L.; Hao, G. P.; Zhang, X. Q. "Porous Carbons for Carbon Dioxide Capture" In Porous Materials for Carbon Dioxide Capture, Green Chemistry and Sustainable Technology. An-Hui, L.; Sheng, D. Eds, Springer: New York, N.Y. 2014, pp 15-77.

(43) Xing, W.; Liu, C.; Zhou, Z.; Zhang, L.; Zhou, J.; Zhuo, S.; Yan, Z.; Gao, H.; Wang, G.; Qiao, S. Z. Superior CO_2 Uptake of N-doped Activated Carbon through Hydrogen-bonding Interaction. *Energy Environ. Sci.* **2012**, *5*, 7323–7327.

(44) Thote, J. A.; Iyer, K. S.; Chatti, R., Labhsetwar, N. K.; Biniwale, R. B.; Rayalu, S. S. In situ Nitrogen Enriched Carbon for Carbon dioxide Capture. *Carbon* **2010**, *48*, 396–402.

(45) Davis, M. E. Ordered Porous Materials for Emerging Applications. *Nature* **2002**, *417*, 813–821.

(46) McKeown, N. B.; Budd, P. M. Polymers of Intrinsic Microporosity (PIMs): Organic Materials for Membrane Separations, Heterogeneous Catalysis and Hydrogen Storage. *Chem. Soc. Rev.* **2006**, *35*, 675–683.

(47) McKeown, N. B.; Budd, P. M.; Msayib, K. J.; Ghanem, B. S.; Kingston, H. J.; Tattershall, C. E.; Makhseed, S.; Reynolds, K. J. D. Fritsch. Polymers of Intrinsic Microporosity (PIMs): Bridging the Void between Microporous and Polymeric Materials. *Chem. Eur. J.* **2005**, *11*, 2610–2620.

(48) Svec F.; Huber, C. G. Monolithic Materials: Promises, Challenges, Achievements. *Anal. Chem.* **2006**, *78*, 2100–2107.

(49) Debe, M. K. Electrocatalyst Approaches and Challenges for Automotive Fuel Cells. *Nature* **2012**, *486*, 43−51.

(50) Tomasic, V.; Jovic, F. State-of-the-art in the Monolithic Catalysts/Reactors. *Appl. Catal. A* **2006**, *311*, 112−121.

(51) Twigg, M. V. Catalytic Control of Emissions from Cars. *Catal. Today* **2011**, *163*, 33−41.

(52) Smit, B; Reimer, J. A.; Oldenburg, C. M.; Bourg, I. C. "Membranes" In Introduction to Carbon Capture and Sequestration. Imperial College Press, London, **2014**, Chapter 7, pp 281-354.

(53) Pierre, A. C.; Pajonk, G. M. Chemistry of Aerogels and Their Applications. *Chem. Rev*. **2002**, *102*, 4243−4265.

(54) Hüsing, N.; Schubert, U.; Aerogels−Airy Materials: Chemistry, Structure, and Properties. *Angew. Chem. Int. Ed.* **1998**, *37*, 22−45.

(55) Pekala, R. W. Organic Aerogels from the Polycondensation of Resorcinol with Formaldehyde. *J. Mater. Sci.* **1989**, *24*, 3221–3227.

(56) Baumann, T.F.; Worsley, M.A.; Han, T. J.; Satcher Jr. J. H. High Surface Area Carbon Aerogel Monoliths with Hierarchical Porosity. *J. Non-Cryst. Solids* **2008**, *354*, 3513–3515.

(57) Antonietti, M.; Fechler, N.; Fellinger, P. Carbon Aerogels and Monoliths: Control of Porosity and Nanoarchitecture via Sol−Gel Routes. *Chem. Mater*. **2014**, *26*, 196−210.

(58) Leventis, N.; Chidambareswarapattar, C.; Mohite, D. P.; Larimore, Z. J.; Lu, H.; Sotiriou-Leventis, C. Multifunctional Porous Aramids (aerogels) by Efficient Reaction of Carboxylic acids and Isocyanates. *J. Mater. Chem.* **2011**, *21*, 11981−11986.

(59) Williams, J. C.; Meador, M. A.; McCorkle, L.; Mueller, C.; Wilmoth, N. Synthesis and Properties of Step-Growth Polyamide Aerogels Crosslinked with Triacid Chlorides. *Chem. Mater*. **2014**, *26*, 4163−4171.

(60) Blagbrough, I. S.; Mackenzie, N. E.; Ortiz, C.; Scott, A. I. The Condensation Reaction Between Isocyanates and Carboxylic Acids. A Practical Synthesis of Substituted Amides and Anilides. *Tetrahedron Lett*. **1986**, *27*, 1251–1254.

(61) Sorensen, W. R. Reaction of An Isocyanate and A Carboxylic Acid in Dimethyl Sulfoxide. *J. Org. Chem*. **1959**, *24*, 978–980.

(62) Rogers, M. E.; Long, T. E. *Synthetic Methods in Step-Growth Polymers*. Wiley-Interscience: New York, NY, **2003**; p 225.

(63) Saeed, A. M.; Wisner, C. A.; Donthula, S.; Far, H. M.; Sotiriou-Leventis, C.; Leventis, N. Reuseable Monolithic Nanoporous Graphite-Supported Nanocatalysts (Fe, Au, Pt, Pd, Ni, and Rh) from Pyrolysis and Galvanic Transmetalation of Ferrocene-Based Polyamide Aerogels. *Chem. Mater*. **2016**, *28*, 4867−4877.

(64) For example, 2.5% sols gelled at 60 ^{o}C after prolonged incubation, however after pyrolysis of the resulting aerogels we saw evidence of internal structural collapse.

(65) Barrettl, E.; Joyner, E.; Halendra, P. The Determination of Pore Volume and Area Distributions in Porous Substances. I. Computations from Nitrogen Isotherms. *J. Am. Chem. Soc*. **1951**, *73*, 373–380.

(66) Webb, P. A.; Orr, C. Analytical Methods in Fine Particle Technology; Micromeritics Instrument Corporation: Norcross, GA, U.S.A, **1997**, 67 − 68.

(67) Beaucage, G. Approximations Leading to a Unified Exponential/Power-Law Approach to Small-Angle Scattering. *J. Appl. Crystallogr.* **1995**, *28*, 717-728.

(68) Beaucage, G. Small-Angle Scattering from Polymeric Mass Fractals of Arbitrary Mass-Fractal Dimension. *J. Appl. Crystallogr.* **1996**, *29*, 134-146.

(69) Chidambareswarapattar, C.; McCarver, P. M.; Luo, H.; Lu, H.; Sotiriou-Leventis, C.; Leventis, N. Fractal Multiscale Nanoporous Polyurethanes: Flexible to Extremely Rigid Aerogels from Multifunctional Small Molecules. *Chem. Mater*. **2013**, *25*, 3205-3224.

(70) Mohite, D. P.; Larimore, Z. J.; Lu, H.; Mang, J. T.; Sotiriou-Leventis, C.; Leventis, N. Monolithic Hierarchical Fractal Assemblies of Silica Nanoparticles Cross-Linked with Polynorbornene via ROMP: A Structure-Property Correlation from Molecular to Bulk through Nano. *Chem. Mater.* **2012**, *24*, 3434-3448.

(71) Leventis, N. Three Dimensional Core-Shell Superstructures: Mechanically Strong Aerogels. *Acc. Chem. Res.* **2007**, *40*, 874-884.

(72) Gupta, A.; Eral, H. B.; Hatton, T. A.; Doyle, P. S. Nanoemulsions: Formation, Properties and Applications. *Soft Matter* **2016**, *12*, 2826-2841.

(73) Leventis, N.; Sotiriou-Leventis, C.; Chandrasekaran, N.; Mulik, S.; Larimore, Z. J.; Lu, H.; Churu, G.; Mang, J. T. Multifunctional Polyurea Aerogels from Isocyanates and Water. A Structure-Property Case Study. *Chem. Mater.* **2010**, *22*, 6692-6710.

(74) Chidambareswarapattar, C.; Xu, L.; Sotiriou-Leventis, C.; Leventis, N. Robust Monolithic Multiscale Nanoporous Polyimides and Conversion to Isomorphic Carbons. *RSC Adv.* **2013**, *3*, 26459-26469.

(75) Schneider, B.; Schmidt, P.; Marek, M. Jr.; Straka, J.; Bednář, B.; Králíček. I.r. and ^{13}C-CP-MAS-NMR Spectra of Pyromellitide and of its Precursor Based on 4,4'-Diaminodiphenymethane. *Eur. Polym. J.* **1990**, *26*, 941-945.

(76) Wolfe, R. A.; Schwartz, W. T.; Dinan, F. J. Correlation of the Crystal Structure and Solid-state ^{13}C NMR Spectrum of Pyromellitic Dianhydride. *Magn. Reson. Chem*. **1991**, *29*, 440−443.

(77) Leventis, N.; Sotiriou-Leventis, C.; Saeed, A. M.; Donthula, S.; Majedi Far, H.; Rewatkar, P. M.; Kaiser, H.; Robertson, J. D.; Lu, H.; Churu, G. Nanoporous Polyurea from a Triisocyanate and Boric Acid: A Paradigm of a General Reaction Pathway for Isocyanates and Mineral Acids. *Chem. Mater.* **2016**, *28*, 67−78.

(78) Edwards, W. E.; Robinson, I. M. Polyimides of Pyromellitic Acid. U.S. Patent No. 2,710,853 (**1955**).

(79) Edwards, W. E.; Robinson, I. M. Preparation of Pyromellitimides. U.S. Patent No. 2,867,609 (**1959**).

(80) Sroog, C. E. Polyimides. *Prog. Polym. Sci*. **1991**, *16*, 561–694.

(81) Meyers, R. A. The polymerization of Pyromellitic Dianhydride with Diphenylmethane Diisocyanate. *J. Polym. Sci., Part A1* **1969**, *7*, 2757–2762.

(82) Barikani, M.; Mehdipour-Ataei, S. Preparation and Properties of Polyimides and Polyamide-Imides from Diisocyanates. *J. Polym. Sci., Part A: Polym. Chem*. **1999**, *37*, 2245–2250.

(83) Yeganeh, H.; Mehdipour-Ataei, S. Preparation and Properties of Novel Processable Polyimides Derived from a New Diisocyanate. *J. Polym. Sci., Part A: Polym. Chem*. **2000**, *38*, 1528–1532.

(84) It is noted in passing that the sequence of Eq 1 and Eq 3 is effectively equivalent to dehydration of PMA, whereas an isocyanate (TIPM in this case) acts as the dehydrating agent. Entropic terms notwithstanding, that dehydration process is favorable by about 4 kcal mol^{-1}.

(85) Rhine, W.; Wang, J.; Begag, R. Polyimide Aerogels, Carbon Aerogels, and Metal Carbide Aerogels and Methods of Making Same. U.S. Patent No. 7,074,880 (**2006**).

(86) Chidambareswarapattar, C.; Larimore, Z.; Sotiriou-Leventis, C.; Mang, J. T.; Leventis, N. One-step Room-Temperature Synthesis of Fibrous Polyimide Aerogels from Anhydrides and Isocyanates and Conversion to Isomorphic Carbons. *J. Mater. Chem*. **2010**, *20*, 9666–9678.

(87) A similar lower-temperature degradation event, at about 310 ^{o}C, was reported recently for polyamide aerogels derived from TIPM and ferrocene dicarboxylic acid.[63]

(88) Wang, M.; Wang, J.; Qiao, W.; Ling, L.; Long, D. Scalable Preparation of Nitrogen-enriched Carbon Microspheres for Efficient CO_2 Capture. *RSC Adv*. **2014**, *4*, 61456−61464.

(89) Zhong, M.; Kim, E. K.; McGann, J. P.; Chun, S-E.; Whitacre. J. F.; Jaroniec, M.; Matyjaszewski, K.; Kowalewski, T. Electrochemically Active Nitrogen-Enriched Nanocarbons with Well- Defined Morphology Synthesized by Pyrolysis of Self-Assembled Block Copolymer. *J. Am. Chem. Soc*. **2012**, *134*, 14846−14857.

(90) Peak assignment according to: Pels, J. R.; Kapteijn, F.; Moulijn, J. A.; Zhu, Q.; Thomas, K. M. Evolution of Nitrogen Functionalities in Carbonaceous Materials During Pyrolysis. *Carbon* **1995**, *33*, 1641 − 1653, and references therewith.

(91) Horváth, G.; Kawazoe, K. Distribution in Molecular Sieve Carbon. *J. Chem. Eng. Jpn*. **1983**, *16*, 470-475.

(92) Ben, T.; Ren, H.; Ma, S.; Cao, D.; Lan, J.; Jing, X.; Wang, W.; Xu, J.; Deng, F.; Simmons, J. M.; Qiu, S.; Zhu, G. Targeted Synthesis of a Porous Aromatic Framework with High Stability and Exceptionally High Surface Area. *Angew. Chem. Int. Ed.* **2009**, *48*, 9457−9460.

(93) Sethia, G.; Sayari, A. Nitrogen-Doped Carbons: Remarkably Stable Materials for CO_2 Capture. *Energy Fuels* **2014**, *28*, 2727−2731.

(94) Himeno, S.; Komatsu, T.; Fujita, S. High-Pressure Adsorption Equilibria of Methane and Carbon Dioxide on Several Activated Carbons. *J. Chem. Eng. Data* **2005**, *50*, 369−376.

(95) Ben, T.; Li, Y.; Zhu, L.; Zhang, D.; Cao, D.; Xiang, Z.; Yaoc, X.; Qiu, S. Selective Adsorption of Carbon Dioxide by Carbonized Porous Aromatic Framework (PAF). *Energy Environ. Sci.* **2012**, *5*, 8370–8376.

(96) Sevilla, M.; Valle-Vigón, P.; Fuertes, A. B. N-Doped Polypyrrole-Based Porous Carbons for CO_2 Capture. *Adv. Funct. Mater.* **2011**, *21*, 2781–2787.

(97) Hao, G.-P.; Li, W.-C.; Qian, D.; Lu, A.-H. Rapid Synthesis of Nitrogen-Doped Porous Carbon Monolith for CO_2 Capture. *Adv. Mater.* **2010**, *22*, 853–857.

(98) Zhou, J.; Li, W.; Zhang, Z.; Xing, W.; Zhuo, S. Carbon Dioxide Adsorption Performance of N-Doped Zeolite Y Templated Carbons. *RSC Adv.* **2012**, *2*, 161–167.

(99) An, J.; Geib, S. J.; Rosi, N. L. High and Selective CO_2 Uptake in a Cobalt Adeninate Metal−Organic Framework Exhibiting Pyrimidine- and Amino-Decorated Pores. *J. Am. Chem. Soc.* **2010**, *132*,38−39.

(100) March's Advanced Organic Chemistry. Sixth Edition. Smith. M. B.; March, J. Eds, John Wiley & Sons, Inc., Hoboken, New Jersey. **2007**, p 3-31.

(101) Perry's Chemical Engineer's Handbook, 6th Edition, Green, D. W.; Perry, R. H, Eds, McGraw-Hill, **1984**, pp 9-14, ISBN 0-07-049479-7.

(102) Kim, H.; Kim, Y.; Yoon, M.; Lim, S.; Park, S. M.; Seo, G.; Kim, K. Highly Selective Carbon Dioxide Sorption in an Organic Molecular Porous Materials. *J. Am. Chem. Soc.* **2010**, *132*, 12200-12202.

(103) Jin, Y.; Hawkins, S. C.; Huynh, C. P.; Su, S. Carbon Nanotube Modified Carbon Composite Monoliths as Superior Adsorbents for Carbon Dioxide Capture. *Energy Environ. Sci.* **2013**, *6*, 2591–2596.

(104) Jin, Y.; Voss, B. A.; Noble, R. D.; Zhang, W. A Shape-Persistent Organic Molecular Cage with High Selectivity for the Adsorption of CO_2 over N_2. *Angew. Chem. Int. Ed.* **2010**, *49*, 6348−6351.

(105) Zulfiqar, S.; Mantione, D.; Tall, O. E.; Sarwar, M. I.; Ruipérez, F.; Rothenbergere, A.; Mecerreyes, D. Nanoporous Amide Networks Based on Tetraphenyladamantane for Selective CO_2 Capture. *J. Mater. Chem. A.* **2016**, *4*, 8190−8197.

(106) Patel, H. A.; Je, S. H.; Park, J.; Jung, Y.; Coskun, A.; Yavuz, C. T. Directing the Structural Features of N_2-Phobic Nanoporous Covalent Organic Polymers for CO_2 Capture and Separation. *Chem. Eur. J.* **2014**, *20*, 772−780.

(107) Rahaman, M. S. A.; Ismail, A. F.; Mustafa, A. A Review of Heat Treatment on Polyacrylonitrile Fiber. *Polym. Degrad. Stab.* **2007**, *92*, 1421–1432.

(108) Mahadik-Khanolkar, S.; Donthula, S.; Sotiriou-Leventis, C.; Leventis, N. Polybenzoxazine Aerogels. 1. High-Yield Room-Temperature Acid-Catalyzed Synthesis of Robust Monoliths, Oxidative Aromatization and Conversion to Microporous Carbons. *Chem. Mater.* **2014**, *26*, 1303-1317.

II. Reuseable Monolithic Nanoporous Graphite-supported Nanocatalysts (Fe, Au, Pt, Pd, Ni and Rh) from Pyrolysis and Galvanic Transmetalation of Ferrocene-Based Polyamide Aerogels

Adnan M. Saeed, Clarissa A. Wisner, Suraj Donthula, Hojat Majedi Far, Chariklia Sotiriou-Leventis,* and Nicholas Leventis*

Department of Chemistry, Missouri University of Science and Technology, Rolla, MO 65409, U.S.A. E-mail addresses: leventis@mst.edu; cslevent@mst.edu

Published in *Chemistry of Materials* **2016**, *28,* 4867−4877

TOC Graphic

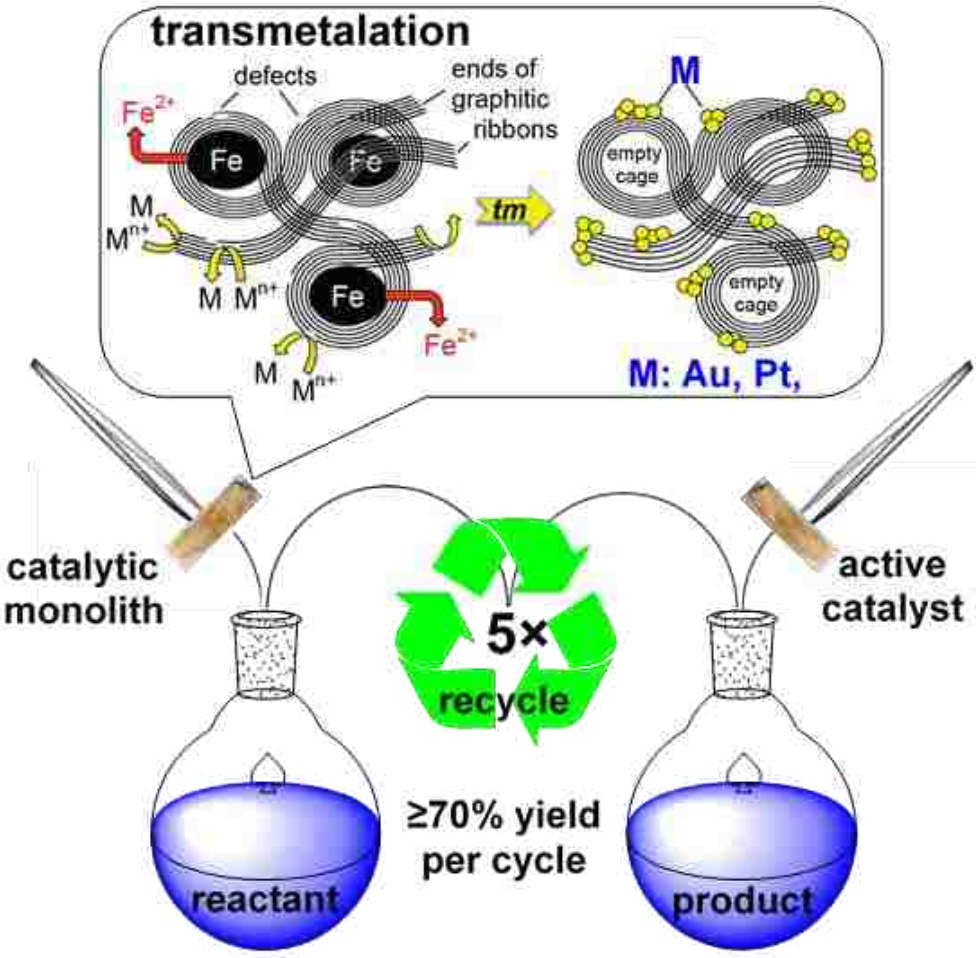

ABSTRACT: Polyamide aerogels with ferrocene as a monomer repeat unit were prepared in one-step from ferrocene dicarboxylic acid and tris(4-isocyanatophenyl)methane. Pyrolysis at ≥800 ºC yielded nanoporous carbons doped throughout with crystallites of α-Fe (about 50 nm in diameter), which in turn were shrouded in graphitic ribbons (<30 graphene layers thick). Transmetalation was carried out with aqueous solutions of Au, Pt, Pd, Rh and Ni salts, via a path akin to galvanic corrosion, whereas graphitic ribbons separated anodes (α-Fe particles) from cathodes (defects along the ribbons). The new metallic phases formed clusters of smaller crystallites (10-20 nm in diameter) on the graphitic ribbons, leaving behind empty cage-like formations previously occupied by the Fe(0) nanoparticles. All metal-doped carbons were monolithic and over 85% porous. Catalytic activity was demonstrated with the oxidation of benzyl alcohol to benzaldehyde catalyzed with carbon-supported Au or Pt, the reduction of nitrobenzene by hydrazine to aniline catalyzed with carbon-supported Fe, and two Heck coupling reactions of iodobenzene with styrene or butyl acrylate, catalyzed with carbon-supported Pd. The distinguishing feature of those catalysts was that they could be just picked up, for example with a pair of tweezers, and re-deployed in a new reaction mixture immediately, thus bypassing less efficient recovery processes like filtration.

1. INTRODUCTION

Heterogeneous catalysis is a surface phenomenon,[1,2] thereby heterogeneous catalysts consist of high surface-to-volume catalytic particles on inert supports. The latter include mostly oxides, carbides, nitrides and activated carbon.[3,4] Supports, typically in particulate/coarse-powder form, provide high surface area for the smaller catalytic particles

to latch on, and pack in a way that ensures low mass transfer resistance to and from the catalytic sites. Recovery of the catalyst at the end of a catalytic cycle is typically carried out by filtration,[5] which is time-consuming and may lead to catalyst loss. At the other extreme, industrial, continuously recyclable heterogeneous catalysts, like those employed in fuel cells,[6] or in catalytic converters,[7,8] operate with gas-phase reagents and are 3-level structures, in which the two lower levels incorporate the general principles set forth above, while, out of engineering necessity, the top level adds their key macroscopic feature: monolithicity. Transferring that feature to any other system is conceptually and practically equivalent to having monolithic catalysts that could be picked up and redeployed immediately in any suitable situation. Clearly, such catalysts will have to be based on porous supports, and in that regard oxide or ceramic aerogels[9,10] doped with metallic nanoparticles[11] could comprise a reasonable option. However, in general those types of aerogels are delicate materials that would not survive harsh reaction environments. Thus, we opted for sturdier carbon aerogels,[12-15] and at that point our attention shifted towards a better dispersion of the metallic nanoparticles in the carbon matrix. For this, a sensible approach is to incorporate a precursor of metallic nanoparticles into every monomer repeat unit of a carbonizable polymer. In that regard, we chose ferrocene, a known precursor of iron nanoparticles.[16]

At the implementation level, that system design was carried out with a hyperbranched polyamide aerogel prepared from ferrocene dicarboxylic acid ($Fc(COOH)_2$), and tris(4-isocyanatophenyl)methane (TIPM) as shown in Scheme 1. TIPM is an inexpensive monomer, and it was chosen because it is also a known precursor of several carbonizable polymeric aerogels,[17,18] including polyamides.[19]

Indeed, pyrolysis of ferrocene-based polyamide aerogels gave monolithic carbon aerogels bearing Fe(0) nanoparticles dispersed throughout their volume. Apart from their own catalytic activity, those materials were transmetalated with selected metal ions, replacing Fe(0) nanoparticles with Au, Pt, Pd, Ni and Rh. All materials were characterized along all processing steps in terms of their chemical composition, and their micro/nanomorphology. Catalytic activity was demonstrated with selected reactions catalyzed by the corresponding metal nanoparticles.

Scheme 1. Reaction of a triisocyanate (TIPM) with ferrocene dicarboxylic acid towards a polyamide (atom labeling is used for NMR peak assignment)

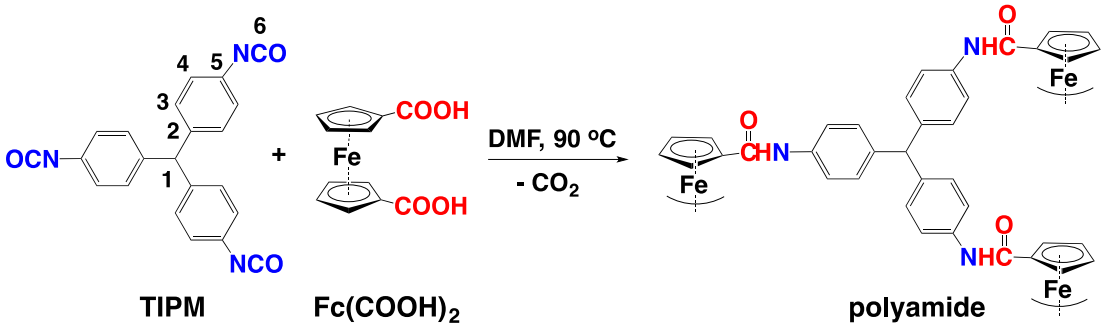

2. RESULTS AND DISCUSSION

This section moves from the synthesis and characterization of ferrocene-based polyamide aerogels (sub-section 2.1), to their pyrolytic conversion to Fe(0)-doped carbon (sub-section 2.2), to transmetalation (sub-section 2.3) and finally to a demonstration of

catalytic activity as set forth above (sub-section 2.4). Emphasis is placed on the metal content, particle size and pore structure.

2.1. Synthesis and characterization of ferrocene-based polyamide aerogels (FcPA-xx). The reaction of Scheme 1 was implemented according to Scheme 2. $Fc(COOH)_2$ was prepared following literature procedures,[20-22] and was co-dissolved at room temperature in a 1.5:1 mol/mol ratio with TIPM in variable amounts of DMF/ethyl acetate (see Experimental). All formulations are provided in Table S.1 of Appendix I in Supporting Information. Gelation was carried out at 90 ^oC, and gelation times (included in Table S.1) varied from 95 min to approximately 3 h, depending on the monomer concentration. Wet-gels were aged in their molds at 90 ^oC for 24 h, solvent-exchanged with acetone and dried with liquid CO_2, vented off at the end as a supercritical fluid (SCF). The resulting aerogels were sturdy monoliths and are referred to as FcPA-xx, where xx stands for the total weight percent concentration of the monomers in the sol, and was varied in the range $05 \leq xx \leq 25$. Materials characterization data for all xx are summarized in Table S.2 of Appendix II in Supporting Information. A typical monolith is shown in Figure 1, along with materials from further processing.

In brief, FcPA-xx shrunk 35-41% in linear dimensions relative to the molds, and in reverse order with xx. Skeletal densities (ρ_s) did not vary in any systematic way that could imply closed porosity. Bulk densities (ρ_b) and porosities ($\Pi = 100 \times (\rho_s - \rho_b)/\rho_s$) varied from 0.12 g cm^{-3} and 92% v/v (xx=05) to 0.49 g cm^{-3} and 63% v/v (xx=25). The porous structure was probed with N_2-sorption porosimetry (Appendix III in Supporting Information).

Scheme 2. Implementation of the reaction of Scheme 1 in the synthesis of ferrocene-based polyamide aerogels.

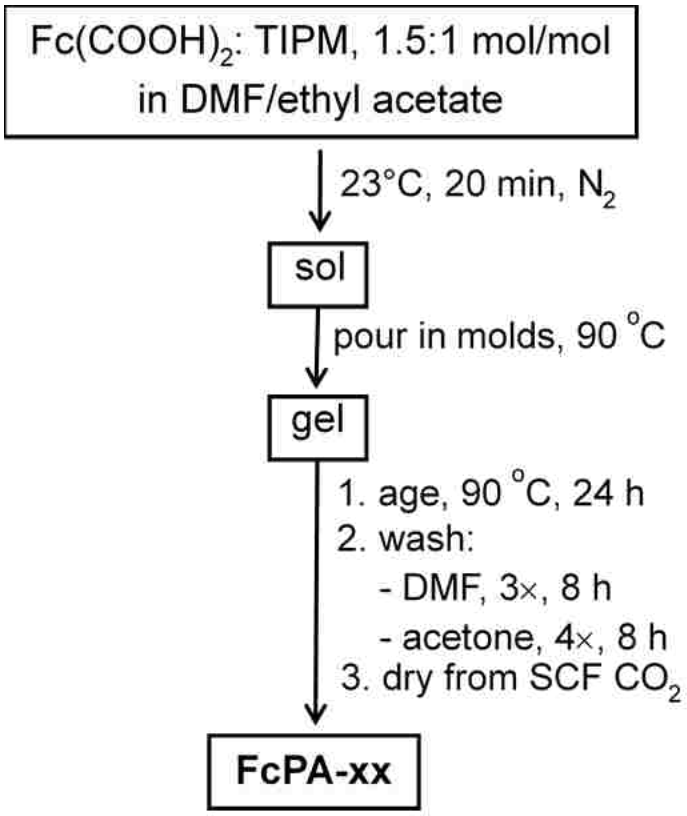

Isotherms started off (at xx=05) with very narrow hysteresis loops, becoming wider at higher densities with well-defined saturation plateaus at xx≥15. Accordingly, lower-density samples were dominated by larger macropores, shifting to smaller macropores and mesopores as density increased (volume ratio, $V_{>300\_nm}/V_{1.7\text{-}300\_nm}$=4.2 for FcPA-05, versus 0.8 for FcPA-25 – see Table S.2). BET surface areas, σ, were in the 460-260 $m^2\ g^{-1}$ range, in descending order with xx. Microscopically, the skeletal framework of all FcPA-xx consisted of random assemblies of nanoparticles (Figure 2A). Particle radii calculated from N_2-soprtion data via $r=3/(\rho_s \times \sigma)$ were in the 4.5-8.7 nm range and agreed well with primary

particle radii calculated from small angle x-ray scattering data (SAXS: 2.9-6.5 nm – see Appendix IV in Supporting Information). SAXS further showed that primary particles aggregated into surface fractal secondary particles with diameters in the range of 35-60 nm (white circles in Figure 2A).

Solid-state CPMAS ^{13}C NMR spectra (Figure 3) showed the aliphatic carbon from TIPM at 55 ppm, the cyclopentadienyl carbons from $Fc(COOH)_2$ as a broad resonance centered at 71 ppm, and the aromatic carbons of TIPM in the 110-140 ppm range. The peak at 167 ppm was assigned to the amide C=O, and the peak at 154 ppm was assigned to the C=O resonance of TIPM-derived polyurea. The latter has been prepared independently by reacting TIPM either with water,[18] or with boric acid[23] and its spectrum is included in Figure 3 as reference.

The reaction of a carboxylic acid with an isocyanate towards an amide starts with a condensation step to a mixed carbamic-carboxylic anhydride (–NH-CO-O-CO–), which either rearranges intramolecularly to the amide ($+CO_2$), or reacts intermolecularly with another molecule of carbamic-carboxylic anhydride towards urea and anhydride,[24-25] the latter two products may also react with one another towards the same amide obtained via the intramolecular route.[26] As confirmed from FTIR (Figure S.6 of Appendix V in Supporting Information), the FcPA-xx does not include an anhydride. On the other hand, based on ^{13}C NMR data obtained during gelation, the solution in the pores of freshly made wet-gels contains a soluble product, which is also observed by adding P_2O_5 (as a dehydrating agent) in a solution of $Fc(COOH)_2$ in DMSO-d_6. The ^{13}C NMR spectrum of that product is consistent with the strained intramolecular anhydride $(FcCO)_2O$, which, however, was unstable and could not be isolated easily for further characterization. Thus,

it is speculated that owing to the favorable topology of the second –COOH group of $Fc(COOH)_2$ relative to the primary condensation product (the carbamic-carboxylic anhydride), the two groups (-COOH and –NH-CO-O-CO–) may react intramolecularly expelling $Fc(CO)_2O$, a free amine and CO_2. In other words, the isocyanate acts as a dehydrating agent of $Fc(COOH)_2$. The free amine reacts with yet unreacted –NCO groups towards urea. At any rate, TIPM-derived polyurea is a high-yield (56% w/w) carbonizable polymer in its own right,[18] thereby is expected to contribute towards the carbon matrix. Integration of the two C=O resonances in the solid-state ^{13}C NMR spectra of FcPA-xx gives a ratio of ferrocene-based polyamide and TIPM-derived polyurea equal to 1:1 mol/mol. Based on (a) that mol ratio, (b) application twice (once for the polyamide, and once for the polyurea) of Eq 1 that gives the molecular mass (G_n) of hyperbranched polymers from di- (*D*)

$$G_n = T - 3\,(1-2^n)\,(D+T) + 3 \times 2^n \times (end\text{-}cap) \qquad (1)$$

and tri- (*T*) functional building blocks ($n \geq 0$: the generation number of the hyperbranched polymer),[27] (c) assuming one bidentate $Fc(CO-)_2$ *end-cap* for every two tips of the hyperbranched polyamide (see also section 2.2b below), and (d) considering the limit of Eq 1 for n--->∞, the expected iron content in FcPA-xx was 8.7 % w/w. (Ii is noted in passing that if FcPA-xx consisted exclusively of ferrocene-derived polyamide, the expected iron content would have been 13.0 % w/w.) The expected iron content in FcPA-xx agrees well with the experimental value ($9._5 \pm 1._1$% w/w) that was calculated from data obtained with thermogravimetric analysis (TGA) in O_2 (Figure 4). In that regard, the TGA residue of FcPA-xx at 1000 ^oC was identified by using powder x-ray diffraction (PXRD)

as Fe_2O_3, and it was found equal to $13._6 \pm 1._5$ % w/w (average of 8 samples from different batches). Then, the weight percent of iron in FcPA-xx was calculated via Eq 2:

$$\text{Fe \% w/w} = [2 \times MW_{Fe} / MW_{Fe2O3}] \times (\text{TGA Residue \% w/w at 1000 } ^oC) \quad (2)$$

2.2. Pyrolytic conversion of FcPA-xx to Fe(0)-doped carbon.

2.2a. Pilot runs. Our first objective was to find out whether and under what conditions FcPA-xx could be converted to carbon-supported Fe(0). For this, mid-density FcPA-15 samples (ρ_b=0.34 g cm^{-3}) were pyrolyzed under flowing H_2 at various temperatures in the range of 400 ^oC to 1400 ^oC. Samples shrunk uniformly, e.g., 68% at 800 ^oC, up to 86% at 1400 ^oC, but remained monolithic. Relevant material properties at various pyrolytic temperatures are given in Table S.3 of Appendix II in Supporting Information. Screening for metallic iron was carried out with powder x-ray diffraction (PXRD – Figure 5). Scheme 3 summarizes the results in terms of chemical composition of the products, and their behavior towards transmetalation (refer to section 2.3 below).

It is noted that our initial attempts focused on producing Fe(0)-doped carbons carbothermally,[28-31] and accordingly pyrolysis was carried out under flowing Ar. However, the only crystalline phase that was observed at ≤1100 ^oC was Fe_3C; some α-Fe was noted only at 1200 ^oC. Under H_2, on the other hand, the main crystalline phase was always α-Fe. In fact, at 400/500 ^oC α-Fe was the only crystalline phase present. Some cementite (Fe_3C) started showing up at ≥600 ^oC, along with some martensite ($Fe_{1.91}C_{0.09}$) at 1400 ^oC (Figure 5). Based on the above, it is reasonable to speculate that under H_2, carbides were produced in a parallel carbothermal process. As summarized in Scheme 3, at ≥800 $^oC/H_2$ samples were electrically conducting, Fe(0) became chemically accessible (e.g., they would start reacting with ions in solution filling the pores – see Figure S.7 of Appendix VI in

Supporting Information), and PXRD included the (002) reflection of graphite at 2θ=26.44º (Figure 5), consistent with iron being a low-temperature graphitization catalyst.[32-34] At ≥1000 ºC the (002) reflection of graphite dominated the PXRD spectra. Samples at the onset of those properties, namely those obtained at 800 ºC, comprised the basis for further study and are referred to as Fe@C.

Scheme 3. Properties at a glance: Chemical composition, electrical conductivity (+), and ability for transmetalation via reaction with metal ions, $[M]^{n+}$, of the product from pyrolysis of FcPA-15 at different temperatures.

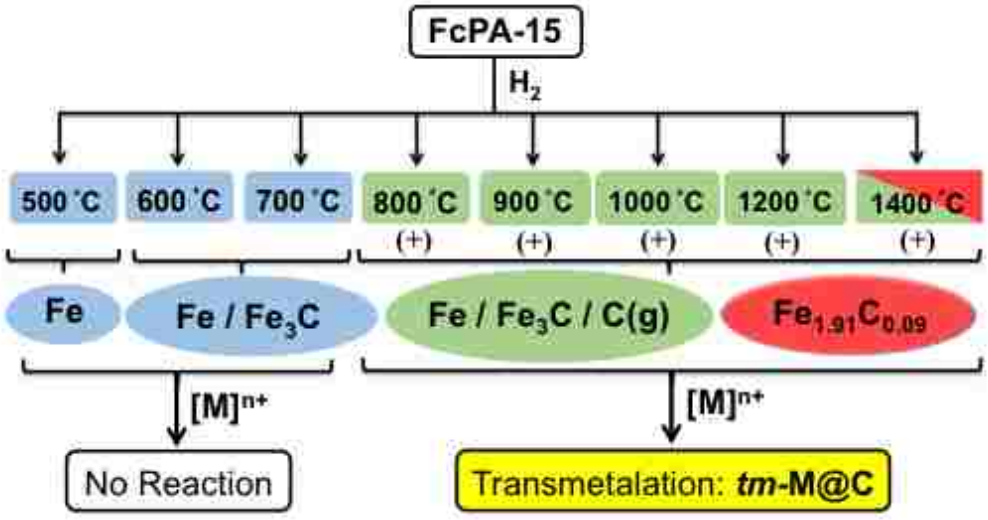

2.2b. Characterization of Fe@C and chemical accessibility of Fe(0). The pyrolytic (char) yield of FcPA-15 to Fe@C was 37.3±1.9 % w/w. Material properties of Fe@C and its derivatives from further processing (transmetalation) are compared with those of FcPA-15 in Table 1. As shown in Figure 1, Fe@C shrunk (49%) relative to their parent FcPA-15, for a 68% of total linear shrinkage relative to the molds. Evidently, however, mass loss

compensated for additional shrinkage, and Fe@C monoliths were less dense (0.286±0.004 g cm^{-3} versus 0.340±0.004 g cm^{-3}) and more porous (88% v/v versus 74% v/v) than FcPA-15 (Table 1.) Microscopically, the framework of Fe@C consisted of finer, fused-together-like particles (Figure 2B). N_2-sorption porosimetry (Appendix III in Supporting Information) showed that the balance of pores shifted to larger macropores relative to FcPA-15 ($V_{>300\_nm}/V_{1.7\text{-}300\_nm}$=3.4, vs. 1.2 in FcPA-15). In short, despite that Fe@C were significantly smaller in size than FcPA-15, they had a higher percentage of internal empty space, and their pores were larger than those of the latter. The BET surface area of Fe@C (about 370 m^2 g^{-1}) was also somewhat higher than that of FcPA-15 (about 310 m^2 g^{-1}), but the distinguishing feature here was that a significant portion of the total BET surface area (175 m^2 g^{-1}, 48%) was assigned (via *t*-plot analysis, Harkins and Jura Model[35]) to newly formed (open) micropores. The apparent particle radius in Fe@C (based on gas sorption data) was smaller (3.4 nm) than that of FcPA-xx (7.3 nm).

However, owing to the lack of well-defined nanoparticles (refer to the network morphology in Figure 2B), this value for the particle radius in Fe@C should be taken only as an estimator of the overall feature size we are dealing with.

The iron content of Fe@C ($11._5$±$2._1$% w/w, via TGA in O_2 – Figure 4) was 40-50% w/w of the expected value ($25._5$±$3._2$%) should all iron in FePA-15 ($9._5$±$1._1$ % w/w) had been retained. That loss of iron is consistent with an early loss of the $Fc(CO\text{-})_2$ end-caps of the ferrocene-based polyamide during pyrolysis: indeed, based on Eq 1, those end-caps contribute 14.3% w/w to the mass of FcPA-xx, which in turn is consistent with the mass loss of about 16% at 310 ºC noted in TGA (Figure 4).

The skeletal density of Fe@C (ρ_s=2.4 g cm^{-3}) was the exact weighted average of iron (7.86 g cm^{-3} at 11.5 % w/w – the TGA-derived value from above) and the experimental skeletal density of the matrix (1.7 g cm^{-3}) after removing Fe with HCl. (The matrix comprised 88.5 % w/w of the total mass of Fe@C.) Despite graphitization, the skeletal density of Fe@C was lower even than the density of sp^2-rich amorphous carbon (1.8-2.0 g cm^{-3}),[36] suggesting that the skeletal framework included closed pores; this is very likely considering that along the newly formed open micropores, some may have been actually closed. (Assuming that all closed pores were confined within the matrix (carbon), the volumetric percent of closed pores on the skeletal backbone varies in the 5-15% v/v range – depending on the density of the skeletal carbon - in the 1.8-2.0 g cm^{-3} range.)

A closer topological view of Fe(0) within Fe@C, which turns out to be important for rationalizing the transmetalation process (Scheme 3 and sub-section 2.3), was obtained with TEM (Figure 6 and S.10 of Appendix VII in Supporting Information). Fe(0) particles were embedded evenly throughout the surrounding matrix (Figure 6A). Their size distribution was broad with a maximum at 52 nm and FWHM=31 nm. The average crystallite size (via the Scherrer equation applied to the (110) peak of Fe(0) – see Figure 5 above) was also equal to 52±1 nm. Under higher magnification (Figure 6B), Fe(0) particles were shrouded in layered ribbons fading away into the surrounding matrix, presumably amorphous carbon. As ribbons faded away, they swirled around *occasionally* forming pockets similar to those encapsulating Fe(0) (see Figure S.10), however, the key observation was that Fe(0) particles were *always* encased in layered ribbons.

Table 1. Materials Characterization data after various stages of processing.

Sample	linear shrinkage (%) [a,b]	bulk density, ρ_b (g cm^{-3}) [a]	skeletal density, ρ_s (g cm^{-3}) [c]	Π [d]	specific pore volume (cm^3 g^{-1}) V_{Total} [e]	$V_{1.7\text{-}300\_nm}$ [f]	$V_{>300\ nm}$ [g]	BET surface area, σ (m^2 g^{-1}) [h]	Av. pore diam. (nm) $4V/\sigma$ [i]	particle radius (nm) r [j]	Metal % w/w expected [k]	found
FcPA-15	38.11 ± 0.03	0.340 ± 0.004	1.333 ± 0.005	74	2.191	0.983	1.214	308 (10.6)	14 [29]	7.31	8.7	$9_{.5} \pm 1_{.1}$
Fe@C	68.24 ± 0.50	0.286 ± 0.004	2.400 ± 0.004	88	3.080	0.705	2.375	369 (176)	9 [33]	3.38	$25_{.5} \pm 3_{.2}$	$11_{.5} \pm 2_{.1}$
Fe@C HCl	68.33 ± 0.16	0.263 ± 0.010	1.704 ± 0.006	85	3.221	0.769	2.452	282 (113)	9 [45]	6.24	-	-
***tm*-Au@C**	69.10 ± 0.02	0.190 ± 0.003	1.964 ± 0.038	90	4.753	0.354	4.399	101 (14.7)	14 [188]	15.2	$31_{.4} \pm 4_{.4}$	$33_{.6} \pm 8_{.8}$
***tm*-Pt@C**	70.04 ± 0.02	0.191 ± 0.004	1.875 ± 0.016	89	4.701	0.284	4.417	100 (1.94)	11 [188]	16.0	$31_{.2} \pm 4_{.4}$	34.5 ± 0.8
***tm*-Pd@C**	70.13 ± 0.05	0.216 ± 0.008	1.981 ± 0.018	89	4.124	0.533	3.591	133 (4.55)	16 [124]	11.4	$19_{.9} \pm 2_{.1}$	$19_{.8} \pm 1_{.8}$

[a] Average of 3 samples. [b] Linear shrinkage=100×(mold diameter – sample diameter)/(mold diameter). [c] Single sample, average of 50 measurements. [d] Porosity (percent of empty space): Π=100×(ρ_s–ρ_b)/ρ_s. [e] Calculated via $V_{Total} = (1/\rho_b) - (1/\rho_s)$. [f] Cumulative volume of pores between 1.7 nm and 300 nm from N_2-sorption data and the BJH desorption method. [g] $V_{>300\ nm} = V_{Total} - V_{1.7\text{-}300\ nm}$. [h] Numbers in brackets correspond to the surface area allocated to micropores. (Calculated using the Harkins and Jura Model.[35]) [i] For the first number (outside the brackets), V was set equal to the maximum volume of N_2 absorbed along the isotherm at P/Po→1.0; for the number in [brackets], V was taken equal to $V_{Total} = (1/\rho_b) - (1/\rho_s)$. (The greater the discrepancy between the two numbers is, the more macroporous the material.) [j] Particle radius, r=3/(ρ_s×σ). [k] For *tm*-M@C (M: Au, Pt, Pd,) expected values were calculated based on replacement of Fe at 11.5% w/w.

The ribbon around the particle of Figure 6B is 9.48 nm thick and consists of 28 graphene layers, giving an interlayer spacing of 3.39 Å, which is close to that of graphite (3.35 Å).[37] That graphene layer stack height is consistent with the value (L_a =16.9 nm) calculated from Raman data using Knight's empirical formula[38] and the ratio of the areas under the characteristic D and G bands of disordered graphite (at 1326 cm^{-1} and 1592 cm^{-1}, respectively; I_D/I_G=2.27 – see Figure S.11 of Appendix VIII in Supporting Information). The agreement between the graphene layer stuck height via TEM and Raman renders graphitic ribbons and cages like those in Figure 6B a general structural property of the entire sample.

Graphitic ribbons is a rather common occurrence in low-temperature Fe(0)-catalyzed graphitization.[39-41] In many cases, shrouding Fe(0) particles in such ribbons (as in Figure 6B) isolates the metal from its environment.[42,43] In Fe@C, however, Fe(0) particles were chemically accessible and were removed with concentrated aqueous HCl (see Experimental), as confirmed by Figure S.8 of Appendix VI that compares PXRD spectra of Fe@C before and after HCl-treatment. In addition, upon general inspection with TEM of HCl-treated samples (Figure S.10) shows an absence of Fe(0) particles, while cage-like structures like those previously shrouding Fe(0) particles abound (Figure 6C). Macroscopically, HCl treatment caused no further shrinkage, but BET surface areas were somewhat compromised (about 280 vs 370 $m^2\ g^{-1}$ before HCl-treatment); yet, 40% of that area (about 110 $m^2\ g^{-1}$) was still assigned to open micropores. (Material properties of HCl-treated samples are included in Table 1.)

2.3. Transmetalation of Fe@C to *tm*-M@C. The chemical accessibility of Fe(0) in Fe@C, as magnifested by our ability to dissolve Fe(0) away with aq. HCl, made

possible to replace Fe(0) with Au, Pt or Pd (M) via reaction with ions of the corresponding metals, $[M]^{n+}$,[44,45] according to Eq 3. In all three cases, the corresponding reactions are highly

$$n\ Fe(0) + 2\ [M]^{n+} \text{---> } n\ Fe^{2+} + 2\ M(0) \quad (3)$$

exothermic with standard redox potentials of over 1.0 V. Experimentally, Fe@C monoliths were infiltrated quickly with aqueous solutions of $[M]^{n+}$ using capillary action under reduced pressure. Transmetalated monoliths (referred to as *tm*-M@C) were washed with water, acetone and were dried under ambient pressure without noticeable changes in their size relative to their Fe@C precursors (Figure 1). Microscopically, *tm*-M@C appeared very similar to Fe@C, although voids seemed to be larger (Figure 2C). Quantitative materials characterization data of the three *tm*-M@C are included in Table 1. Thus, porosities (86-90% v/v) remained in the same range as Fe@C (88% v/v), but pore sizes shifted to even larger macropores (the $V_{>300\_nm}/V_{1.7\text{-}300\_nm}$ ratio moved from 3.4 in Fe@C up to 6.7 in *tm*-Pd@C, 12.4 in *tm*-Au@C, and 15.6 in *tm*-Pt@C). The BET surface areas were reduced from about 370 $m^2\ g^{-1}$ in Fe@C (and 282 $m^2\ g^{-1}$ in HCl-treated Fe@C) to 100-130 $m^2\ g^{-1}$ in *tm*-M@C, with an even greater reduction in the surface area assigned to micropores (from about 170 $m^2\ g^{-1}$ in Fe@C, and about 110 $m^2\ g^{-1}$ in HCl-treated Fe@C, to 5-15 $m^2\ g^{-1}$ in *tm*-M@C). According to the pore volume data, surface-tension-driven nanoscopic contraction cannot be ruled out as a mechanism for the observed changes in the pore structure. On the other hand, however, surface area data suggest that transmetalation, as opposed to removing Fe(0) with HCl, blocked access to micropores. That would increase closed porosity and would decrease the apparent skeletal densities. Indeed, the skeletal densities of all three *tm*-samples were found lower than that of Fe@C, despite quantitative

replacement of Fe(0) with heavier metals; as summarized in Table 1, the skeletal densities of the three *tm*-M@C were in the 1.88-1.98 g cm^{-3} range, versus ρ_s =2.40 g cm^{-3} for Fe@C.

The PXRD spectra of *tm*-M@C were dominated by the new metallic phases (Figure 7). No residual Fe(0) was detected in any of the transmetalated samples, and minor additional reflections were assigned to Fe_3C. TGA-in-O_2 (Figure 4) supported quantitative replacement of Fe(0) by M; that is, starting with $11._5$±$2._1$% w/w of Fe(0) in the parent Fe@C, the expected/found values of M were (% w/w): Au, $31._4$±$4._4$/$33._6$±$8._8$; Pt, $31._2$±$4._4$/34.5±0.8, and Pd, $19._9$±$2._1$/$19._8$±$1._8$ (Table 1). The average crystallite sizes (via the Scherer equation applied to the (111) reflections) were: Au, 15.2±0.5 nm; Pt, 20.9 ±0.7 nm; Pd, 21.4±0.7 nm), namely significantly smaller than those of Fe(0) in Fe@C (52±1 nm). According to TEM (Figure 6D), the graphitic pockets shrouding the parent iron particles in Fe@C were now empty (like after treatment with HCl – compare with Figure 6C), and the new metallic particles clustered on the graphitic ribbons. In no occasion (see also Figure S.10) new metallic nanoparticles were formed inside cages previously occupied by Fe(0). Macroscopically, bulk iron dipped in gold platting solutions is passivated by a layer of Au(0).[46] Microscopically, redox transmetalation typically yields core-shell,[45] or hollow particles.[47] Here, complete consumption of Fe(0) nanoparticles, together with (a) the location of the new metallic particles (on the ribbons rather than in the pockets), and (b) their smaller size relative to the parent Fe(0), points to a galvanic corrosion mechanism (Scheme 4),[48] in which graphitic ribbons separated physically, and connected electrically anodes and cathodes. The former were the Fe(0) nanoparticles; the latter were end-points and defects on ribbons serving as concentrators of the electric field, accelerating electrode

Scheme 4. Galvanic transmetalation mechanism of Fe@C to *tm*-M@C (e.g., M=Au).

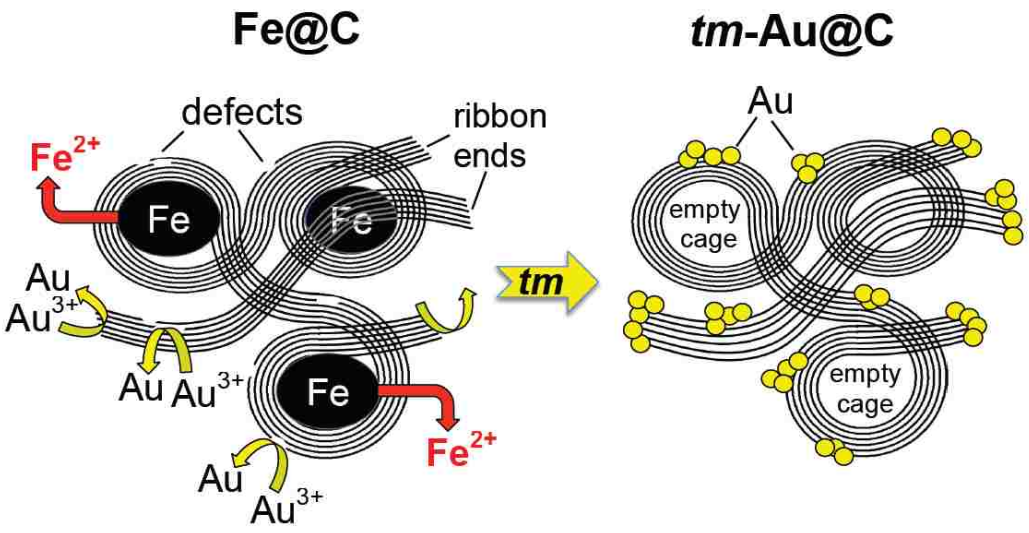

kinetics. Statistically, there are more such defects than Fe(0) particles, therefore we expect clusters of smaller Au, Pt or Pd crystallites than those of the parent Fe(0), as observed. This galvanic mechanism also explains the curious formation of a yellow gold layer on the outer geometric surface of all *tm-Au@C* monoliths (see Figure 1): while reduction of ions infiltrated quickly within the monolith still goes on, namely while there is still unreacted Fe(0), ions diffusing from the surrounding solution towards the monolith get reduced at the point of their first encounter with the conducting carbon network. In further support of the galvanic reduction mechanism, initial transmetalation attempts of Fe@C with nickel were unsuccessful, despite that the standard redox potentials of the reaction Ni^{2+} + Fe(0) ---> Ni(0) + Fe^{2+} is positive (but low: 0.183 V). Meanwhile, Raman (Figure S.11) on one hand shows that at higher processing temperatures the grapheme layer stack high does not change much (L_α=21 nm at 1400 ºC, versus L_α=17 nm in Fe@C), but PXRD on the other (Figure 5) shows that higher-temperature samples contain more graphite. Reasoning that

the internal ohmic drop along the skeletal framework in samples with higher graphite content would be lower, FcPA-15 processed at 1200 ºC were transmetalated successfully with Ni^{2+}, and also with another precious metal, Rh, in which case the crystallite size was found even smaller (9±1 nm) than that of all other metals in *tm*-M@C. (For PXRD data of *tm*-Rh@C and *tm*-Ni@C see Figure S.9 of Appendix VI in Supporting Information.) The ability of galvanic transmetalation to step particle size down is particularly relevant to catalysis as, for example, only nanosized Au is catalytic.[49-51]

2.4. Evaluation of Fe@C and *tm*-M@C as catalysts. Fe@C and *tm*-M@C monoliths similar to those shown in Figure 1, were dipped under vigorous magnetic stirring in reaction mixtures that could be catalyzed by the respective metals.[52-54] Reactions, run times, and results are summarized in Table 2. Based on the weight of each monolith and its metal content (Table 1), the metal-to-limiting reagent ratio was adjusted at 5% mol/mol. Aliquots were taken in regular intervals and were analyzed using gas chromatography (GC - see Experimental; for the raw data see Appendix IX in Supporting Information). Reactions were stopped by removing the catalyst shortly after their limiting reagents had disappeared from the GC traces (see Figures S.12-S.20; typically, 24 h, except Heck coupling of iodobenzene with butyl acrylate that proceeded much faster – Table 2). In order to remove them, catalytic monoliths were picked up with a pair of tweezers, were rinsed briefly with the reaction solvent and were transferred immediately into new reaction mixtures to continue catalysis. The procedure was repeated five times with each catalyst. All monoliths were robust and survived the prolonged "beating" by the magnetic stirrer. Yields remained ≥70% for all catalysts, all cycles (Table 2). No product was observed in any of the controls that included swapping *tm*-M@C with Fe@C, or with Fe@C monoliths

after HCl-treatment. In the case of *tm*-Au@C, catalysis was also attempted with a 1 in^2 gold foil left in the reaction mixture for several days – no reaction was observed. Optimization of catalytic activity, e.g., in terms of turn over numbers (TON), was beyond the scope of this work. Nevertheless, TON were found in the range of 70-100, and compare favorably with C-supported catalysts in powder form.[53] Oxidation of benzyl alcohol with either *tm*-Au@C or *tm*-Pt@C gave practically identical results, pointing to the effectiveness of galvanic replacement to furnish catalytically active nanosized Au.

Finally, because of the way the catalytic experiments were designed and executed, namely: (a) in all catalytic runs the (metal inside the catalyst): (limiting regent) ratio was fixed at 5% mol/mol, and (b) all reactions were monitored and stopped shortly after the limiting reagent had been consumed, it was deemed reasonable to average the yields of the five reactions after each catalytic cycle, and plot them against the latter (Figure 8). According to Figure 8, all catalysts in the family of catalysts of this report behave similarly, namely independent of reaction and catalytic metal. Therefore, the common catalyst "fatigue" observed in Figure 8 is attributed to the matrix, which, owing to its open porous structure may have allowed for catalyst loss. This subject goes beyond the immediate scope of this report, but certainly warrants further investigation.

3. CONCLUSION

Although it is known that pyrolysis of mixtures of carbon or carbon-precursors with iron salts yields similar nanostructures to those described here,[39-43] the key feature of this work is that macroscopically the resulting porous materials are robust monoliths, a key requirement for easily re-deployable catalysts. The conceptual point of departure for this

configuration was the structure of catalytic converters. In that regard, it is conceivably possible to transfer back and apply our findings to our point of departure, but that requires supports inert towards O_2 at high temperatures (e.g., SiC aerogels[55]). With regards to the C-supported catalysts at hand, it is rather straightforward to expand the present approach to other metallocenes. However, loss of ferrocene at two stages during processing (i.e., during gelation and during the early stages of pyrolysis) renders that route less attractive for expensive metals. On the other hand, galvanic replacement is evidently atom-efficient, steps-down the particle size, and is a room-temperature process, which removes any possibility for sintering. Our current attention is focusing on carbide-free materials, like those obtained at 400/500 ^{o}C, and in order to render Fe(0) nanoparticles accessible, we are exploring how to deconvolute reduction and carbonization via, for example, stepwise processing.

4. EXPERIMENTAL

4.1. Materials. All reagents and solvents were used as received, unless noted otherwise. Ferrocene, aluminum chloride, acetyl chloride, lithium aluminum hydride, sodium hydroxide, dichloromethane, hexane, anhydrous *N*,*N*-dimethylformamide (DMF), butyl acrylate, styrene (inhibitor was removed by extraction with 5 M solution of NaOH followed by drying with anhydrous sodium sulphate), acetophenone, hexadecane, benzaldehyde, iodobenzene, benzyl alcohol, butyl cinnamate, triethyl amine, *cis*- and *trans*-stilbene, chloroplatinic acid hydrate, palladium chloride, nickel (II) chloride hexahydrate and concentrated HCl (12.1 N) were purchased from Sigma Aldrich Chemical Co. A gold plating solution (catalog number: 42307) and rhodium (III) chloride trihydrate

were purchased from Alfa Aesar. Tris(4-isocyanatophenyl)methane (TIPM) was donated from Covestro LLC as a 27% w/w solution in dry ethylacetate under the trade name of Desmodur RE. Desmodur RE was also purchased independently from M.F. Cachat (Lakewood, OH, www.mfcachat.com). Deuterated DMSO (DMSO-d_6) and $CDCl_3$ were obtained from Cambridge Isotope Laboratories Inc. Argon (99.99999 %) and H_2 (99.999 %) were purchased from Ozark Gas (Rolla, MO).

Table 2. Use of Fe@C and tm-M@C (M: Au, Pt, Pd) in catalysis: Yields as a function of catalytic cycle (In all cases (catalytic metal):(limiting reagent) = 5% mol/mol - see Experimental; for the raw data, and data analysis see Appendix IX in Supporting Information).

Catalyst	RXN (t) [a]	Yield % mol/mol				
		1st	2nd	3rd	4th	5th
Fe@C	1 (24 h)	89	84	75	83	86
***tm*-Au@C**	2 (24 h)	98	89	75	71	70
***tm*-Pt@C**	2 (24 h)	85	84	79	80	71
***tm*-Pd@C**	3 (24 h)	98	84	74	62	75
***tm*-Pd@C**	4 (2 h)	91	92	79	73	71

[a] RXN (t): Reaction (run time):
1. nitrobenzene + hydrazine ⟶ aniline
2. benzyl alcohol + O_2 ⟶ benzaldehyde
3. iodobenzene + styrene ⟶ *cis*- + *trans*-stilbene
4. iodobenzene + butyl acrylate ⟶ butyl cinnamate

1,1'-Ferrocene dicarboxylic acid ($Fc(COOH)_2$) was prepared in two steps from ferrocene according to literature procedures (Scheme 5).[20-22] Yield: 63 %; mp >250 °C. ^{1}H NMR (400 MHz, DMSO-d_6) δ 4.47 (d, 4H), 4.72 (d, 4H), 12.34 (s, 2H). ^{13}C NMR (400 MHz, DMSO-d_6) δ 171, 73, 72, 71. IR (KBr) 3429, 1687, 1495, 1301, 514 cm^{-1}. Elemental

Analysis, (CHN): Theoretical % w/w for $C_{12}H_{10}O_4Fe$: C, 52.55; H, 4.38. Found: C, 51.83; H, 4.13.

Scheme 5. Synthesis of 1,1'-ferrocene dicarboxylic acid ($Fc(COOH)_2$).

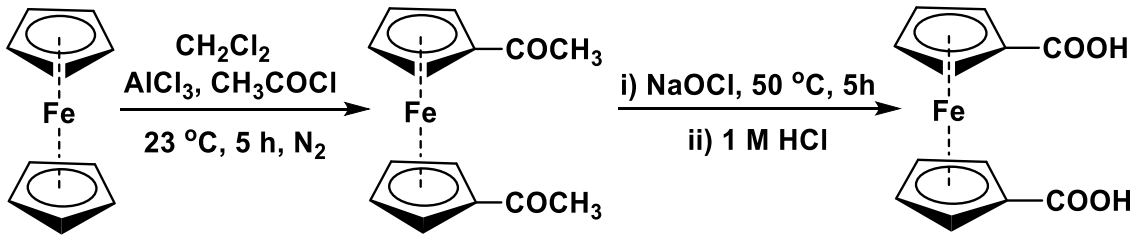

4.2. Synthesis of ferrocene polyamide aerogels (FcPA-xx). In a typical procedure, $Fc(COOH)_2$ (4.11 g, 0.015 mol) was dissolved in anhydrous DMF and the solution was added to 13.6 g of Desmodur RE (containing 3.67 g, 0.01 mol of TIPM). The resulting sol was stirred at room temperature under N_2 for 20 min, and was poured in molds (Wheaton 4 mL Polypropylene Omni-Vials 1.04 cm in inner diameter, Fisher part No. 225402), which were then sealed and left for gelation at 90 ^oC. The total weight percent of monomers (TIPM + $Fc(COOH)_2$) in the sol was varied by varying the amount of solvent (DMF), and is denoted by extension –xx in the sample names. All formulations and gelation times are summarized in Table S.1 of Appendix I in Supporting Information. Gels were aged for 24 h at 90 ^oC in their molds. Subsequently, wet gels were removed from their molds, washed with DMF (3×, 8 h each time), acetone (4×, 8 h each time, using 4× the volume of the gel for each wash) and were dried in an autoclave with liquid CO_2, which

was taken out at the end as a supercritical fluid (SCF). Elemental Analysis, (CHN): Found % w/w: C, 64.34; H, 4.86; N, 8.57.

4.2a. Preparation of Fe(0)-doped nanoporous carbons. FcPA-15 aerogel monoliths were transferred into a MTI GSL1600X-80 tube furnace (alumina 99.8% pure, 72/80 mm inner/outer diameters, 457 mm heating zone). The temperature of the furnace was raised to the desired temperature (400-1400 ^{o}C) at 5 ^{o}C min^{-1} under flowing H_2 (150 mL min^{-1}). Samples were heated at the prescribed temperature for 5 h. At the end of the heating period the temperature returned to room temperature at 5 ^{o}C min^{-1} under constant flow of H_2. FcPA-15 samples processed at 800 ^{o}C/H_2 comprised the basis for further study and are referred to as Fe@C. For control purposes, FcPA-15 samples were also treated at 800 ^{o}C and 1200 ^{o}C under flowing Ar (150 mL min^{-1}) for 5 h. Fe(0) was leached out of Fe@C by dipping monoliths in concentrated HCl under vacuum for 24 h. The HCl solution was changed every 6 h, and after the second wash it was noted that it remained colorless. Subsequently, samples were washed with water and acetone (2× with each solvent, 6 h each time) and were air-dried.

4.2b. Transmetalation of Fe@C to noble-metal (M)-doped nanoporous carbons (tm-M@C). Fe@C monoliths were transmetalated with noble metals (*tm*-M@C, M: Au, Pt, Pd) by dipping in the corresponding metal ion solutions ([Au^{3+}] = 0.018 M; [H_2PtCl_6] = 0.035 M; [$PdCl_2$] = 0.035 M) under reduced pressure, right after they came out of the furnace. The volume of each precious metal solution was adjusted based on the expected amount of Fe(0) in each Fe@C monolith (11.5 ± 2.1 % w/w); in general, in all cases the (volume of metal ion solution):(volume of the Fe@C monolith) ratio was equal to about 80. After 5 h in the respective transmetalation bath, monoliths were placed in a water bath

and were heated at around 50 °C for 5 h still under reduced pressure. Subsequently, they were washed with water (2×, 8 h each time) followed by acetone (2×, 8 h each time) and were vacuum-dried overnight at 80 ^{o}C.

4.3. Methods.

Drying Procedure: Drying of wet-gels with supercritical fluid (SCF) CO_2 was carried out in an autoclave (SPIDRY Jumbo Supercritical Point Dryer, SPI Supplies, Inc. West Chester, PA, or in a Spe-edSFE system, Applied Separations, Allentown, PA). Samples were loaded into the autoclave and acetone was added until all samples were submerged. The pressure vessel was closed and liquid CO_2 was allowed in at room temperature. Acetone was drained out from the pressure vessel as it was being displaced by liquid CO_2. Subsequently, more liquid CO_2 was allowed into the vessel and was drained out several more times until all acetone was extracted out of the pores of the samples. The criterion for that was that vented-out CO_2 started forming dry ice. Subsequently, the temperature of the autoclave was raised to 40 ^{o}C and SCF CO_2 was vented off as a gas.

Physical Characterization: Bulk densities (ρ_b) were calculated from the weight and the physical dimensions of the samples. Skeletal densities (ρ_s) were determined with helium pycnometry using a Micromeritics AccuPyc II 1340 instrument. Porosities, Π, as percent of open empty space were calculated from ρ_b and ρ_s via: $\Pi=100\times[\rho_s - \rho_b]/\rho_s$.

Chemical Characterization: Elemental analysis (CHN) was conducted with a PerkinElmer elemental analyzer (Model 2400 CHN).

Infrared (IR) spectra were obtained in KBr pellets, using a Nicolet-FTIR Model 750 spectrometer. Raman spectroscopy of carbon samples was conducted with a Jobin-Yvon micro-Raman spectrometer with a 632.8 nm He-Ne laser as the excitation source.

Liquid ^{1}H and ^{13}C-NMR spectra were recorded in deuterated solvents using a 400 MHz Varian Unity Inova NMR instrument (100 MHz carbon frequency). Solid-state ^{13}C-NMR spectra were obtained with samples ground into fine powders on a Bruker Avance III 400 MHz spectrometer with a carbon frequency of 100 MHz, using magic-angle spinning (at 5 kHz) with broadband proton suppression and the CPMAS TOSS pulse sequence for spin sideband suppression. Solid-state ^{13}C NMR spectra were referenced externally to glycine (C=O: 176.03 ppm).

Powder X-ray diffraction (PXRD) was conducted with a PANalytical X'Pert Pro multipurpose diffractometer (MPD) with Cu Kα radiation (λ = 1.54 Å) and a proportional counter detector equipped with a flat graphite monochromator. Phase composition was estimated via Rietveld refinement of the x-ray diffraction patterns utilizing RIQAS software (Materials Data, Inc., version 4.0.0.26). Structural information for crystalline phases was obtained from the ICSD database version 2.01. Crystallite sizes were calculated using the Scherrer equation and the FWHM of the lowest-angle diffractions. A Gaussian correction was applied utilizing NIST SRM 660a LaB_6 to determine the instrumental broadening.

Thermogravimetric analysis (TGA) was conducted under O_2 at 5 °C min^{-1} using a TA Instruments Model TGA Q50 thermogravimetric analyzer. The residue from Fe@C after TGA analysis was collected and was analyzed with XRD. The only crystalline phase found was Fe_2O_3.

Gas chromatography (GC) was carried out with a Hewlett Packard, 5890 Series II gas chromatograph equipped with a DB-5 capillary column (30 m/0.25 mm) and a flame ionization detector (FID).

Characterization of the porous structure: Brunauer–Emmett–Teller (BET) surface areas, pore volumes and pore size distributions for pores in the 1.7-300 nm range were determined with N_2-sorption porosimetry at 77 K using a Micromeritics ASAP 2020 surface area and porosity analyzer. Pore size distributions were calculated by applying the Barrett-Joyner-Halenda (BJH) equation to the desorption branch of the isotherms.

Characterization of the skeletal framework: Scanning electron microscopy (SEM) was conducted with Au-coated samples on a Hitachi Model S-4700 field-emission microscope. Transmission Electron Microscopy (TEM) was conducted with an FEI Tecnai F20 instrument employing a Schottky field emission filament operating at a 200 kV accelerating voltage. The samples were finely ground by hand in a mortar with a pestle and the powder was mixed with isopropanol in 5 mL glass vials, which were ultrasonicated for 20 min to disperse the smallest particles in the solvent. Immediately afterwards, and just before particle settling was complete, a single drop was taken and placed on a 200 mesh copper grid bearing a lacey Formvar/carbon film. The grid was allowed to air-dry overnight before microscopy. At least 6 different areas/particles were examined to ensure that the results were uniform over the entire sample.

The fundamental building blocks of the FcPA-xx aerogels were also probed with small angle X-ray scattering (SAXS), using ~2 mm thick disks cut dry with a diamond saw. SAXS analysis was carried out with the same PANalytical X'Pert Pro multipurpose diffractometer (MPD) described above configured for scattering, using a 1/32° SAXS slit, a 1/16° antiscatter slit on the incident beam side, and a 0.1 mm antiscatter slit together with a Ni 0.125 mm automatic beam attenuator on the scattered beam side. Samples were placed in circular holders between thin Mylar sheets, and scattering intensities were measured by

running 2θ scans from −0.1° to 5° with a point detector in the transmission geometry. All scattering data were reported in arbitrary units as a function of *Q*, the momentum transferred during a scattering event. Data analysis was conducted using the Beaucage Unified Model[56-57] applied with the Irena SAS tool for modeling and analysis of small angle scattering within the Igor Pro application (a commercial scientific graphing, image processing, and data analysis software from Wave Metrics, Portland, OR).

Evaluation of Fe@C and tm-M@C as catalysts. All four catalysts (Fe@C, *tm*-Au@C, *tm*-Pt@C, *tm*-Pd@C) were used at a 5 % mol/mol ratio relative to the limiting reagent in the corresponding reaction mixture. Starting materials and products were quantified using gas chromatography and internal standards. Response factors were equal to the slopes of calibration curves that were constructed with a series of samples containing known concentrations of each reactant, product and internal standard.

Reduction of nitrobenzene[52] was catalyzed with Fe@C and was carried out in a thick-jacketed round bottom pressure flask with a Teflon screw-cap. Nitrobenzene (0.984 g, 8 mmol) was dissolved in THF (50 mL). Hydrazine hydrate (0.641 g, 20 mmol) was added as a reducing agent, and hexadecane (1000 µL, 3 mmol) as an internal standard. The flask was sealed and the reaction mixture was stirred for 24 h at 100 °C. Aliquots (100 µL) were taken every 2 h by cooling the flask temporarily to 40 °C, and were analyzed immediately with GC. After 24 h the reaction mixture was cooled down to room temperature, the Fe@C monolith was picked up with a pair of tweezers, rinsed briefly with THF and was transferred immediately to a new reaction mixture for the next cycle. The whole process was repeated five times.

Oxidation of benzyl alcohol[53] was catalyzed either with *tm*-Au@C or *tm*-Pt@C. Benzyl alcohol (0.864 g, 8 mmol) was dissolved in distilled water (50 mL), and acetophenone (1000 µL, 8 mmol) was added as an internal standard. The reaction mixture was heated with an oil bath to 60 °C under constant bubbling of oxygen and vigorous magnetic stirring. Aliquots (100 µL) were taken every 2 h, extracted with diethyl ether (2 mL) and were analyzed immediately with GC. After 24 h the reaction mixture was cooled down to room temperature, the *tm*-Au@C and *tm*-Pt@C monoliths were harvested out as above, rinsed briefly with water and were transferred to new reaction mixture for the next cycle. The whole process was repeated five times.

Heck coupling reactions[54] were catalyzed with *tm*-Pd@C at 80 ^{o}C, with constant magnetic stirring under N_2 in DMF (5 mL) using a mixture of iodobenzene (1.632 g, 8 mmol), triethyl amine (0.809 g, 8 mmol) and butyl acrylate (1.28 g, 10 mmol) or styrene (1.04 g, 10 mmol). In both cases, hexadecane was added as an internal standard (1000 µL, 3 mmol). The same protocol as above was observed for GC analysis and recycling of the catalyst.

FIGURES

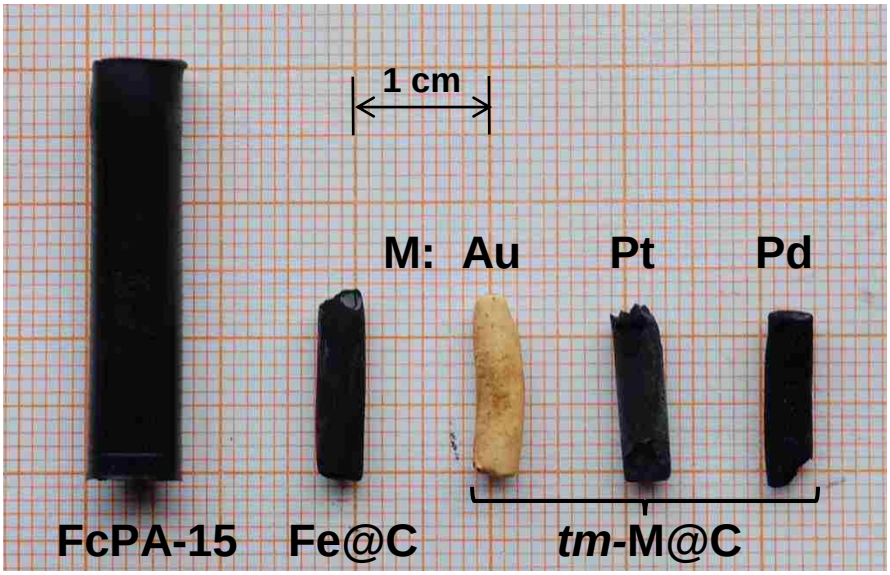

Figure 1. Photograph of samples after different stages of processing as shown. For relevant data refer to Table 1.

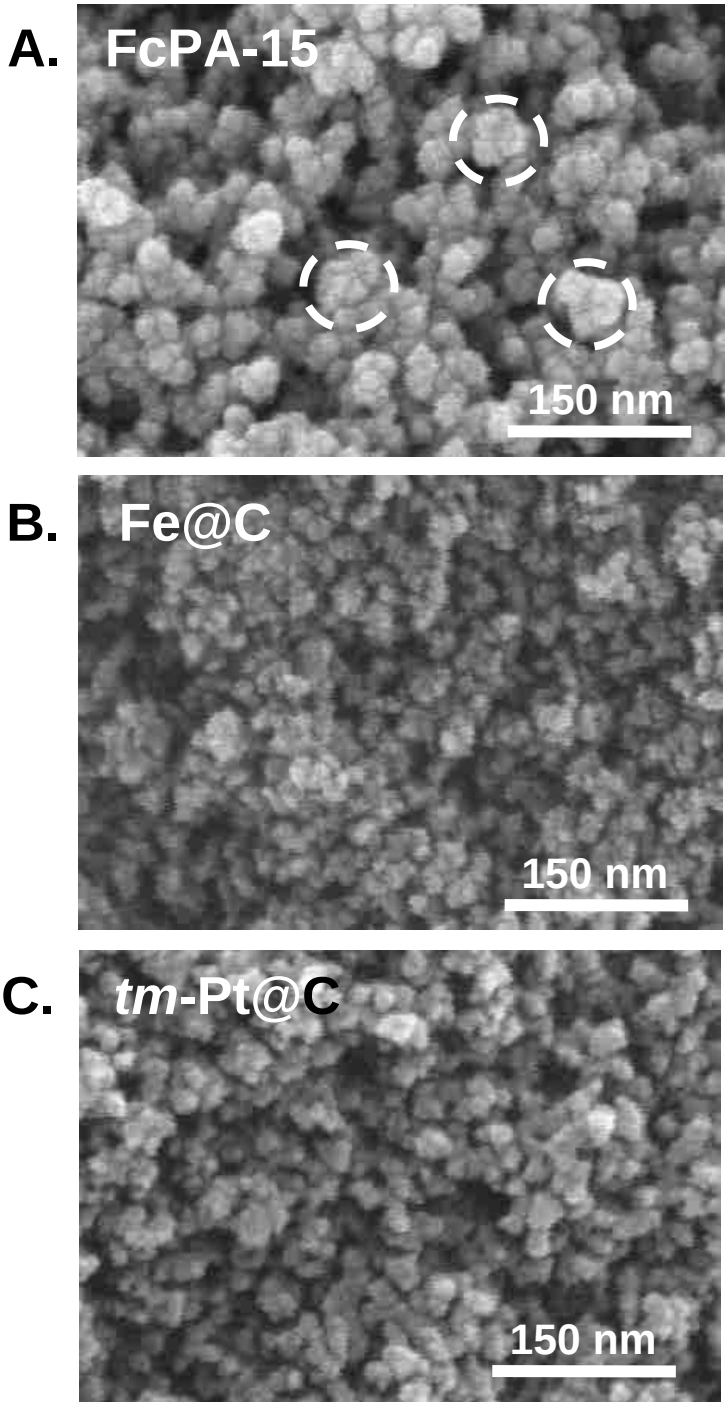

Figure 2. Scanning Electron Microscopy (SEM) of representative samples along processing. White circles in FcPA-15 denote secondary particles as identified via SAXS (see Appendix IV in Supporting Information).

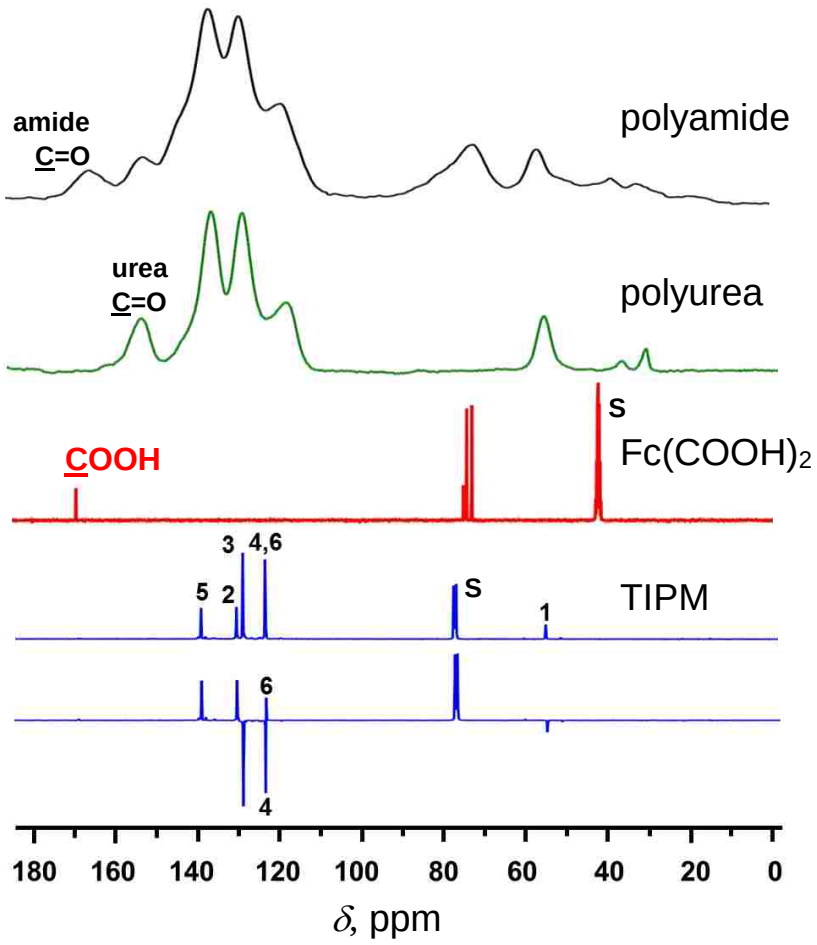

Figure 3. Solid-state CPMAS ^{13}C NMR of FcPA-xx (top) and of TIPM-derived polyurea (second from top). Liquid state ^{13}C NMR of $Fc(COOH)_2$ in DMSO-d_6 (third from the top) and of TIPM in $CDCl_3$ (bottom two spectra). The APT (Attached Proton Test) spectrum of TIPM confirms that C-4 and C-6 overlap. (S: solvent peak).

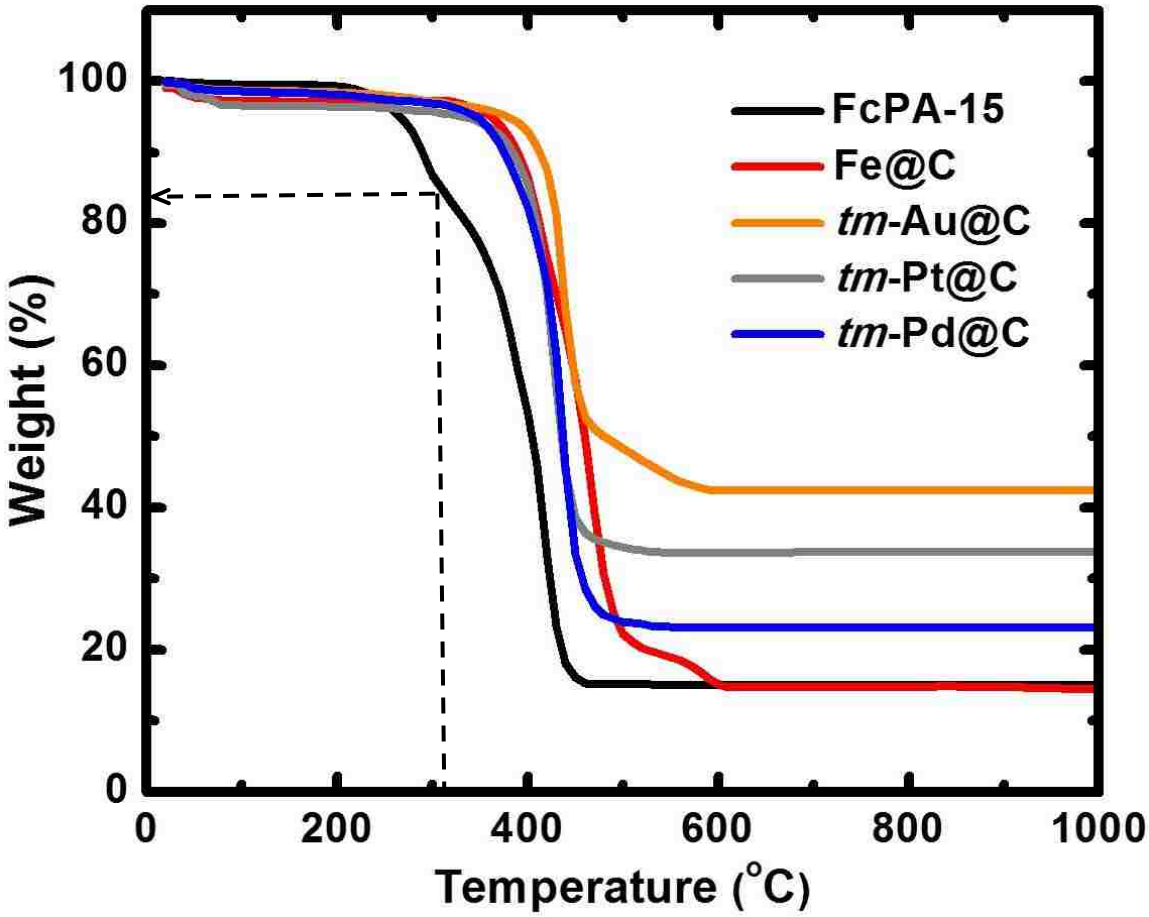

Figure 4. Representative thermogravimetric analysis (TGA) data under O_2 at 5 ^oC min^{-1} of samples as shown. (TGA was repeated several times with samples from different batches and results were used to derive the metal content of various samples as shown in Table 1). The dashed lines and arrow point to the first step of mass loss by FcPA-15 (about 16% w/w at around 310 ^oC). (Via Eq 1, bidentate $Fc(CO-)_2$ end-caps contribute 14.3% w/w to the total mass of FcPA-15.).

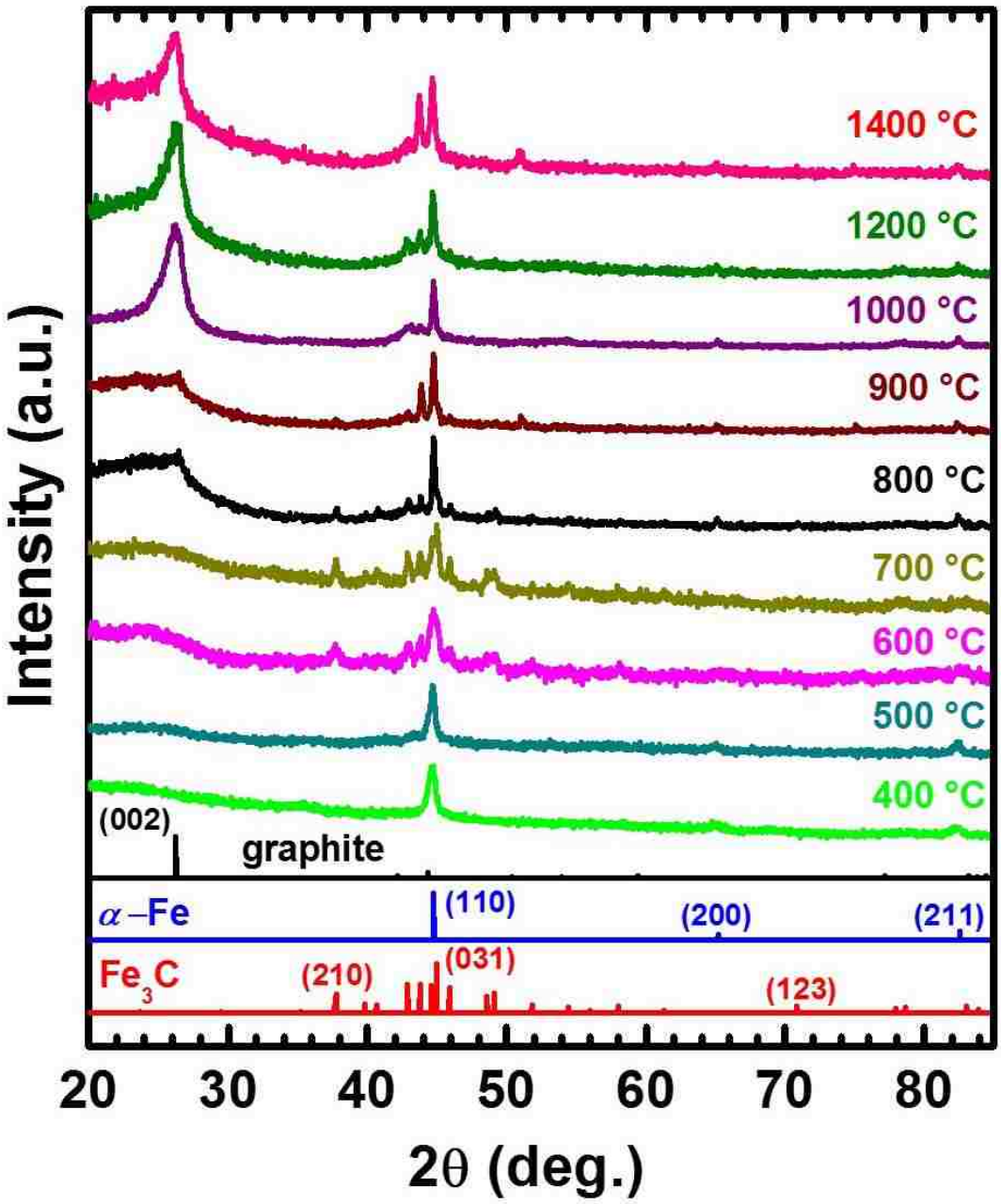

Figure 5. Powder X-ray diffraction (PXRD) data after pyrolysis of FcPA-15 at different temperatures. The (002) reflection of graphite at $2\Theta=26.44^{o}$ first shows up after pyrolysis at 800 ^{o}C and dominates the diffraction pattern above 1000 ^{o}C. (Line spectra are included at the bottom for identification.)

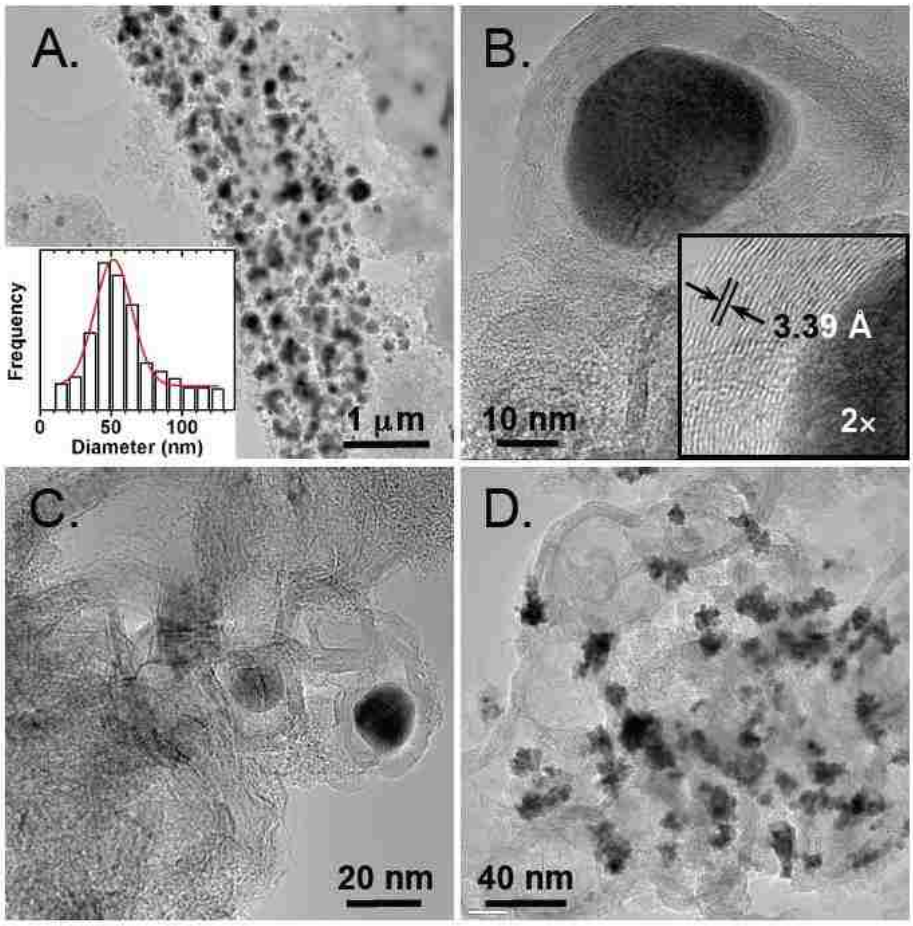

Figure 6. Transmission electron microscopy (TEM). A,B: Fe@C at two different magnifications. Inset in A: Patricle size distribution. C. Fe@C after HCl-treatment. D. *tm*-Pt@C. Arrows point at empty graphitic cages after removing Fe(0). (Additional TEM data are shown in Appendix VII in Supporting Information.)

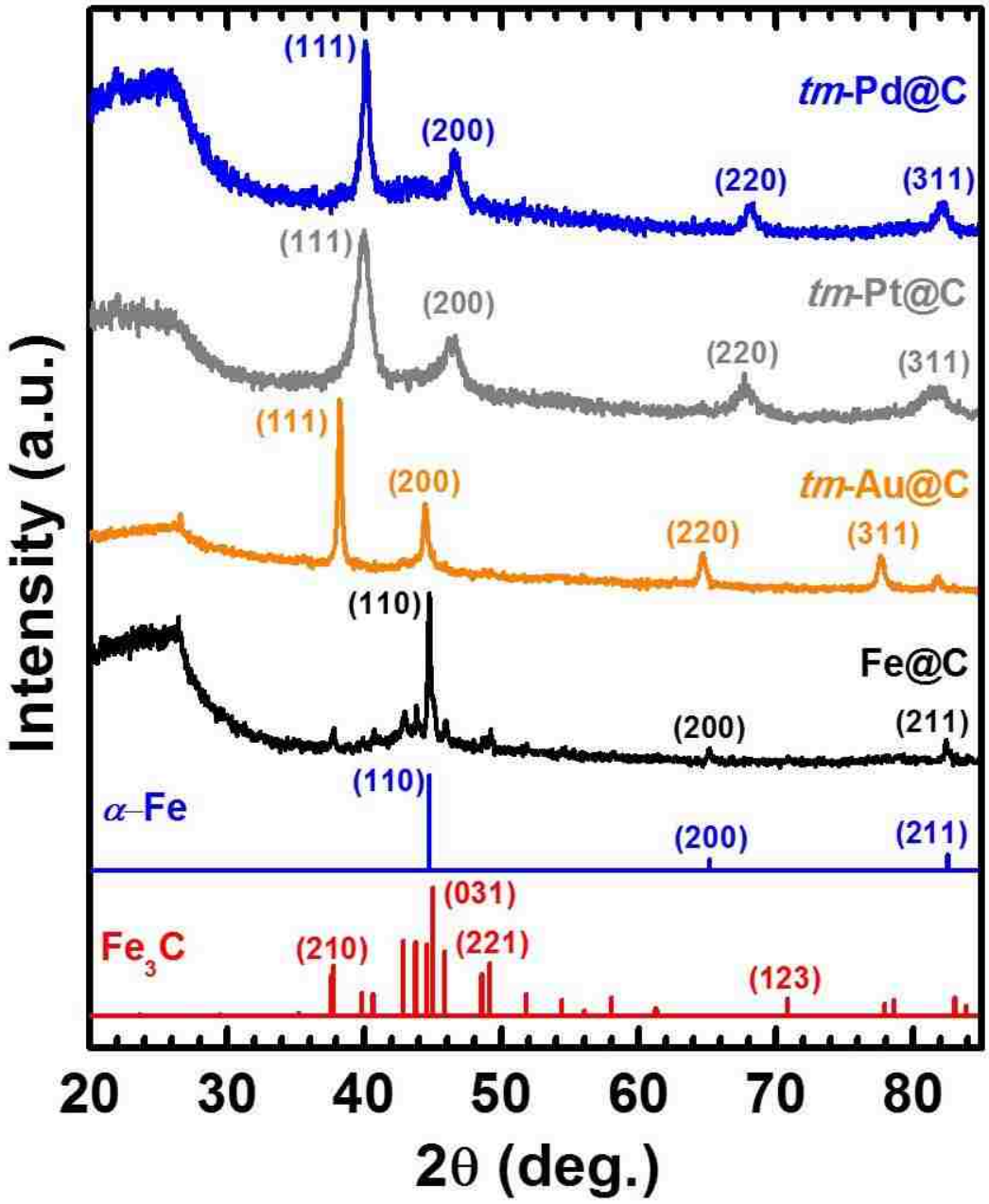

Figure 7. Powder X-ray diffraction (PXRD) data of Fe@C samples transmetalated with Au, Pt and Pd, as shown. The PXRD spectrum of Fe@C is included for comparison. All samples retain the small amount of Fe_3C present in the original Fe@C.

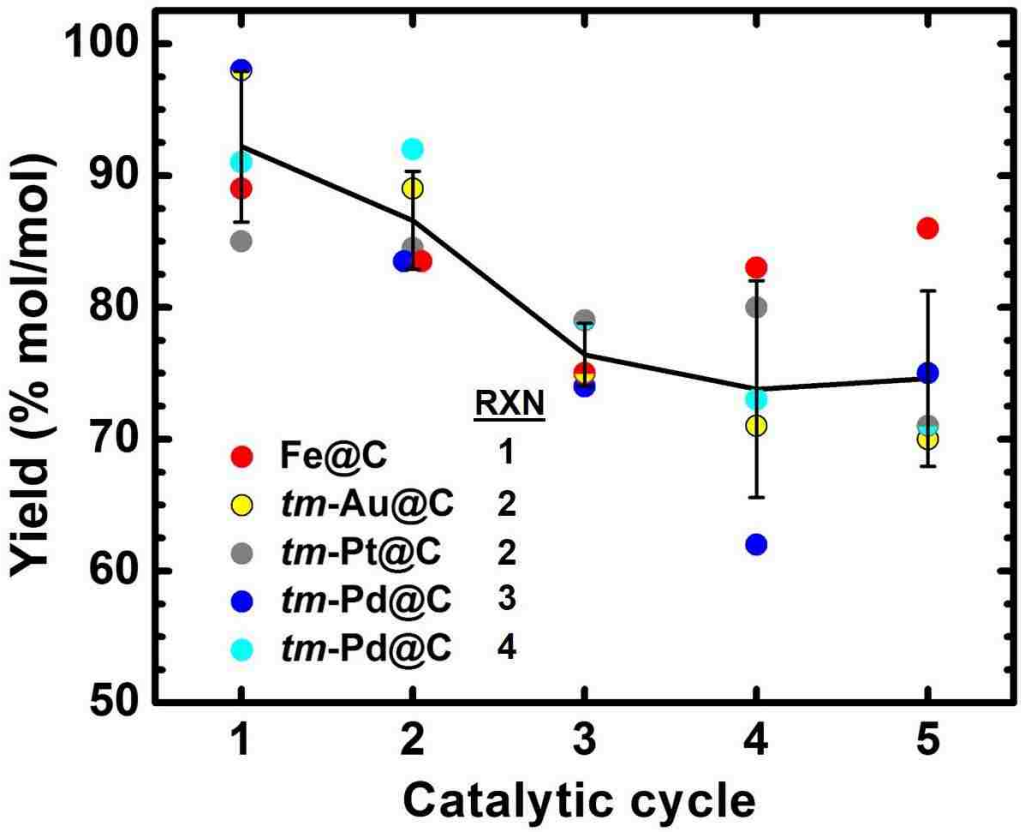

Figure 8. Cumulative graph of % Yield versus Catalytic cycle for all catalysts used in this study (data from Table 2). The solid black line connects the average % yields after each cycle. Error bars are one standard deviation from the average % yields.

SUPPORTING INFORMATION

Appendix I: Formulations of FcPA-xx aerogels. Appendix II: Materials characterization data for FcPA-xx, Fe@C and *tm*-M@C. Appendix III: N_2-sorption data. Appendix IV: Small-angle X-ray scattering (SAXS) data for FcPA-xx. Appendix V: FTIR data for FcPA-xx. Appendix VI: Additional PXRD data related to transmetalation and removal of Fe(0) with HCl. Appendix VII: Additional TEM of Fe@C and *tm*-M@C. Appendix VIII: Raman data for FcPA-15 after pyrolysis at different temperatures. Appendix IX: Data from catalysis using Fe@C and *tm*-M@C as catalysts. This material is available free of charge via the Internet at http://pubs.acs.org.

Figure S.4. N_2-sorption isotherms and pore size distributions by the BJH method of transmetalated samples as shown. Results are summarized in Table S.4.

Appendix IV. Analysis of the FcPA-xx skeletal frameworks: SAXS data

Figure S.5. Small angle X-ray scattering (SAXS) data of FcPA-xx. All data were fitted with two exponentials (Regions I and III) and two Guinier knees (Regions II and IV). Data pertinent to the nanostructures are gathered in Table S.5 below.

Table S.5. Results from analysis of the SAXS data in Figure S.5 using the Beaucage Unified Model

Appendix V. FTIR data for of FcPA-xx

Figure S.6. FTIR of FcPA-xx, TIPM-derived polyurea (PUA) and $Fc(COOH)_2$.

Appendix VI. Additional PXRD data related to transmetalation, and removal of Fe(0) from Fe@C with HCl

Figure S.7. Powder XRD after attempted transmetalation with a Au plating solution of FcPA-15 pyrolyzed at different temperatures, as shown. Note that Fe(0) is removed completely only from samples pyrolyzed at 800 ^oC (referred to as Fe@C). As noted here buy also in Figure 5 of the main article, Fe_3C was produced at $\geq$600 ^oC, and according to this Figure here, it survived the transmetalation process.

Figure S.8. Comparison of powder XRD data (PXRD) of as-prepared Fe@C and after treatment with a concentrated solution of HCl (see Experimental). The reflection designated by the dashed vertical line is attributed to surviving Fe_3C.

Figure S.9. Powder XRD data after transmetalation with Ni and Rh of FcPA-15 samples pyrolyzed at 1200 ^oC under H_2, as shown. Both spectra are dominated by the (002) reflection of graphite and contain small amounts of Fe_3C. Owing to the overlap of the (111) reflection of Ni with the reflections from Fe_3C, reliable application of the Scherrer equation was possible only with the (111) diffraction of Rh, whose crystallite size was calculated equal to 9±1 nm.

Appendix VII. Additional TEM of Fe@C and *tm*-M@C

Figure S.10. TEM of samples as shown. Left: Fe@C. Left column top: Occasionally, ribbons swirl around and form pockets like those shrouding Fe(0) particles. Left Column bottom: Always Fe(0) particles are encased in ribbons. Right: Fe@C after treatment with concentrated

aq. HCl at two magnifications. Consider these data together with the PXRD spectra of Fe@C before and after HCl treatment, shown in Figure S.8. (Continued on the next page.)

Figure S.10 (Continued). TEM of samples as shown. Nowhere in these post-transmetalation sample, new metallic nanoparticles could be associated with the interior of cages that contained Fe(0) in the Fe@C precursor.

Appendix VIII. Raman of FcPA-15 after pyrolysis at different temperatures

Figure S.11. Raman spectra after pyrolysis of FcPA-15 at different temperatures, as shown. All peak assignment according to Dresselhaus, M. S.; Dresselhaus, G.; Saito, R.; Jorio, A. "Raman spectroscopy of carbon nanotubes." *Physics Reports* **2005**, *409*, 47-99. The maxima of the peaks of interest are: D, 1326 cm^{-1}; G, 1592 cm^{-1}. At higher resolution, the D´ peak appears as a shoulder at 1610 cm^{-1} in all spectra. The low-intensity, broad band at around 2150 cm^{-1} could not be assigned. The graphene layer stack height (L_α) was calculated using Knight's formula ($L_a(nm) = (2.4\times10^{-10})\lambda_{exc}^4\left(\frac{A_D}{A_G}\right)^{-1}$) from the ratio of the peak areas (cited on the right). Peak areas were calculated using deconvolution and Laurentian fit. λ_{exc} is the wavelength of the laser, in our case 514.5 nm (2.41 eV).

Appendix IX. Data from catalysis using Fe@C and *tm*-M@C as catalysts

Figure S.12. GC analysis of aliquots taken out during the 1st Cycle of the reduction of nitrobenzene to aniline using a Fe@C monolith as a catalyst. Results are plotted in Figure S.13.

Figure S.13. Reduction of nitrobenzene to aniline using a Fe@C monolith as a catalyst. Inset: Evolution of reactant and product concentrations in a 24 h period (1st Cycle). Data from Figure S.12.

Figure S.14. GC analysis of aliquots taken out during the 1st Cycle of the oxidation of benzyl alcohol to benzaldehyde using a *tm*-Au@C monolith as catalyst. Results are plotted in Figure S.15.

Figure S.15. Oxidation of benzyl alcohol to benzaldehyde using a *tm*-Au@C monolith as a catalyst. Inset: Evolution of reactant and product concentrations in a 24 h period (1st Cycle). Data from Figure S.14.

Figure S.16. GC analysis of aliquots taken out during the 1st Cycle of the oxidation of benzyl alcohol to benzaldehyde using a *tm*-Pt@C monolith as catalyst. Results are plotted in Figure S.17.

Figure S.17. Oxidation of benzyl alcohol to benzaldehyde using a *tm*-Pt@C monolith as catalyst. Inset: Evolution of reactant and product concentrations in a 24 h period (1st Cycle). Data from Figure S.16. (Note the similarity of the data with using *tm*-Au@C as a catalyst in Figure S.15.)

Figure S.18. GC analysis of aliquots taken out during the 1st Cycle of the Heck coupling of iodobenzene and butyl acrylate towards butyl cinnamate using a *tm*-Pd@C monolith as a catalyst. Results are plotted in Figure S.19.

Figure S.19. Heck coupling of iodobenzene and butyl acrylate towards butyl cinnamate using a *tm*-Pd@C monolith as a catalyst. Inset: Evolution of reactant and product concentrations in a 2 h period (1st Cycle). Data from Figure S.18.

Figure S.20. GC analysis of aliquots taken out during the 1st Cycle of the Heck coupling of iodobenzene and styrene towards *cis*- and *trans*-stilbene using a *tm*-Pd@C monolith as a catalyst. Results are plotted in Figure S.21.

Figure S.21. Heck coupling of iodobenzene and styrene towards *cis*- and *trans*-stilbene using a *tm*-Pd@C monolith as a catalyst. Inset: Evolution of reactant and product concentrations in a 24 h period (1st Cycle). Data from Figure S.20.

Appendix I. Formulations of FcPA-xx

Table S.1. Formulations and gelation times of FcPA-xx aerogels.

Sample [a]	$Fc(COOH)_2$				Desmodur RE		TIPM			DMF		gelation time
	mass (g)	volume [b] (mL)	mmol	*C* (M)	volume (mL)	mass [c] (g)	mass [d] (g)	mmol	*C* (M)	mass (g)	volume (mL)	90 ºC
FcPA-05	0.411	0.244	1.5	0.093	1.33	1.359	0.367	1.00	0.062	13.79	14.52	~ 3 h
FcPA-10	0.411	0.244	1.5	0.190	1.33	1.359	0.367	1.00	0.126	6.01	6.32	2 h 30 min
FcPA-15	0.411	0.244	1.5	0.289	1.33	1.359	0.367	1.00	0.193	3.41	3.60	2 h 15 min
FcPA-20	0.411	0.244	1.5	0.394	1.33	1.359	0.367	1.00	0.262	2.12	2.23	~ 2 h
FcPA-25	0.411	0.244	1.5	0.502	1.33	1.359	0.367	1.00	0.335	1.34	1.41	1 h 45 min

[a] Numerical extensions in the sample names designate the weight percent of total monomer ($Fc(COOH)_2$+TIPM) in the sol. [b] The volume of $Fc(COOH)_2$ was calculated based on its density measured with helium pycnometry (1.685 g cm^{-3}). [c] The mass of commercial Desmodur RE was calculated based on its density that in turn was measured in our laboratory (1.022 g cm^{-3}). [d] The mass of TIPM in Desmodur RE was calculated based on the weight percent of monomer (27%) given by the manufacturer.

Appendix II. Materials characterization data for: FcPA-xx; FcPA-15 after pyrolysis; and, *tm*-M@C (M: Au, Pt, Pd)

Table S.2. Characterization of FcPA-xx aerogels.

xx	linear shrinkage (%) [a,b]	bulk density, ρ_b (g cm^{-3}) [a]	skeletal density, ρ_s (g cm^{-3}) [c]	Π [d]	specific pore volume (cm^3 g^{-1})			BET surface area, σ (m^2 g^{-1})	average pore diameter (nm)		particle radius (nm)		
					V_{Total} [e]	$V_{1.7\text{-}300\_nm}$ [f]	$V_{>300\ nm}$ [g]		$4V/\sigma$ [h] method	BJH [I] method	r [j]	R_1 [k]	R_2 [l]
05	41.21 ± 0.50	0.123 ± 0.006	1.472 ± 0.004	92	7.451	1.448	6.003	456	14 [65]	42 [63]	4.47	4.98 ± 0.45	29.11 ± 0.96
10	39.32 ± 0.09	0.202 ± 0.008	1.342 ± 0.006	85	4.205	2.360	1.845	381	25 [44]	32 [14]	5.87	6.57 ± 0.32	25.03 ± 0.37
15	38.11 ± 0.03	0.340 ± 0.004	1.333 ± 0.005	74	2.191	0.983	1.213	308	14 [29]	20 [12]	7.31	3.94 ± 0.45	21.97 ± 0.45
20	37.52 ± 0.70	0.401 ± 0.003	1.363 ± 0.003	70	1.760	0.829	0.931	276	12 [26]	16 [4.8]	7.97	2.85 ± 0.15	19.13 ± 0.19
25	35.44 ± 0.10	0.490 ± 0.007	1.341 ± 0.005	63	1.295	0.719	0.576	258	11 [20]	13 [4.7]	8.67	5.66 ± 1.44	17.48 ± 0.37

[a] Average of 3 samples. [b] Linear shrinkage=100×(mold diameter – sample diameter)/(mold diameter). [c] Single sample, average of 50 measurements. [d] Porosity (percent of empty space): Π=100×(ρ_s–ρ_b)/ρ_s. [e] Calculated via $V_{Total} = (1/\rho_b) - (1/\rho_s)$. [f] Cumulative volume of pores between 1.7 nm and 300 nm from N_2-sorption data and the BJH desorption method. [g] $V_{>300\ nm} = V_{Total} - V_{1.7\text{-}300\ nm}$. [h] For the first number (outside the brackets), V was set equal to the maximum volume of N_2 absorbed along the isotherm at P/Po→1.0; for the number in [brackets], V was taken equal to $V_{Total} = (1/\rho_b) - (1/\rho_s)$. [i] From the BJH plots: first numbers are peak maxima; numbers in (parentheses) are full widths at half maxima. [j] Particle radius, r=3/(ρ_s×σ); [k] R_1: radius of primary particles from SAXS; [l] R_2: radius of secondary particles from SAXS.

Table S.3. Characterization of the product from pyrolysis of FcPA-15 at different temperatures.

Pyrolysis temperature of **FcPA-15** (°C)	linear shrinkage (%) [a,b]	bulk density, ρ_b (g cm^{-3}) [a]	skeletal density, ρ_s (g cm^{-3}) [c]	Π [d]	specific pore volume (cm^3 g^{-1})			BET surface area, σ (m^2 g^{-1})	average pore diameter (nm)		particle radius (nm)
					V_{Total} [e]	$V_{1.7\text{-}300\_nm}$ [f]	$V_{>300\ nm}$ [g]		$4V/\sigma$ [h] method	BJH [i] method	r [j]
800 (**Fe@C**)	68.24 ± 0.50	0.286 ± 0.004	2.400 ± 0.004	88	3.080	0.705	2.375	369	9 [33]	18 [10]	3.38
Fe@C HCl treated	68.33 ± 0.16	0.263 ± 0.010	1.704 ± 0.006	85	3.221	0.769	2.452	282	9 [45]	16 [9.5]	6.24
1000	69.10 ± 0.02	0.812 ± 0.008	1.890 ± 0.006	53	0.702	0.238	0.464	235	5 [12]	4 [0.28]	6.75
1200	83.42 ± 0.50	0.720 ± 0.004	1.491 ± 0.005	51	0.718	0.562	0.156	234	10 [13]	16 [1.88]	8.60
1400	86.02 ± 0.50	0.981 ± 0.003	2.149 ± 0.030	54	0.554	0.227	0.327	84	11 [26]	13 [2.63]	16.6

[a] Average of 3 samples. [b] Linear shrinkage=100×(mold diameter – sample diameter)/(mold diameter). [c] Single sample, average of 50 measurements. [d] Porosity (percent of empty space): Π=100×(ρ_s–ρ_b)/ρ_s. [e] Calculated via $V_{Total} = (1/\rho_b) - (1/\rho_s)$. [f] Cumulative volume of pores between 1.7 nm and 300 nm from N_2-sorption data and the BJH desorption method. [g] $V_{>300\ nm} = V_{Total} - V_{1.7\text{-}300\ nm}$. [h] For the first number (outside the brackets), V was set equal to the maximum volume of N_2 absorbed along the isotherm at P/Po→1.0; for the number in [brackets], V was taken equal to $V_{Total} = (1/\rho_b) - (1/\rho_s)$. (The greater the discrepancy between the two numbers is, the more macroporous the material.) [i] From the BJH plots: first numbers are peak maxima; numbers in (parentheses) are full widths at half maxima. [j] Particle radius, r=3/(ρ_s×σ).

Table S. 4. Characterization of the transmetalation products from Fe@C.

***tm*-M@C M**	linear shrinkage (%) [a,b]	bulk density, ρ_b (g cm^{-3}) [a]	skeletal density, ρ_s (g cm^{-3}) [c]	Π [d]	specific pore volume (cm^3 g^{-1})			BET surface area, σ (m^2 g^{-1})	average pore diameter (nm)		particle radius (nm)
					V_{Total} [e]	$V_{1.7\text{-}300\_nm}$ [f]	$V_{>300\ nm}$ [g]		$4V/\sigma$ [h] method	BJH [i] method	r [j]
Au	69.10 ± 0.02	0.190± 0.003	1.964± 0.038	90	4.753	0.354	4.399	101	14 [188]	17 [7.86]	15.2
Pt	70.04 ± 0.02	0.191± 0.004	1.875± 0.016	89	4.701	0.284	4.417	100	11 [188]	10 [1.69]	16.0
Pd	70.13 ± 0.05	0.216± 0.008	1.981± 0.018	89	4.124	0.533	3.591	133	16 [124]	17 [5.07]	11.4

[a] Average of 3 samples. [b] Linear shrinkage=100×(mold diameter – sample diameter)/(mold diameter). [c] Single sample, average of 50 measurements. [d] Porosity (percent of empty space): Π=100×(ρ_s–ρ_b)/ρ_s. [e] Calculated via $V_{Total} = (1/\rho_b) - (1/\rho_s)$. [f] Cumulative volume of pores between 1.7 nm and 300 nm from N_2-sorption data and the BJH desorption method. [g] $V_{>300\ nm} = V_{Total} - V_{1.7\text{-}300\ nm}$. [h] For the first number (outside the brackets), V was set equal to the maximum volume of N_2 absorbed along the isotherm at P/Po→1.0; for the number in [brackets], V was taken equal to $V_{Total} = (1/\rho_b) - (1/\rho_s)$. (The greater the discrepancy between the two numbers is, the more macroporous the material. Compare with Fe@C in Table S.3.) [i] From the BJH plots: first numbers are peak maxima; numbers in (parentheses) are full widths at half maxima. [j] Particle radius, r=3/(ρ_s×σ).

Appendix III. Porous structure analysis of all samples: N_2 sorption data

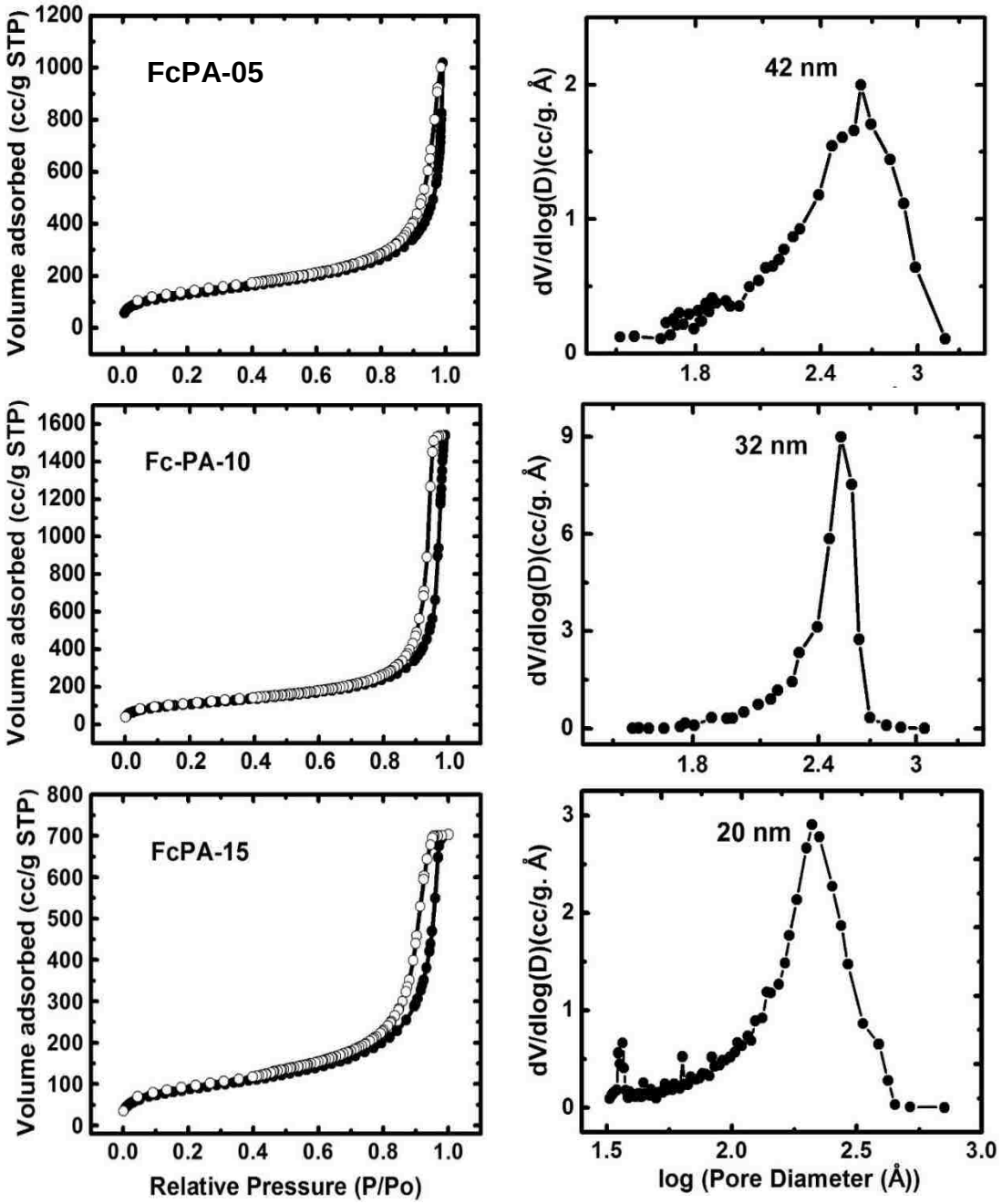

Figure S.1. N_2-sorption isotherms and pore size distributions by the BJH method of FcPA-xx aerogels as shown (continued on next page).

(Continued from previous page)

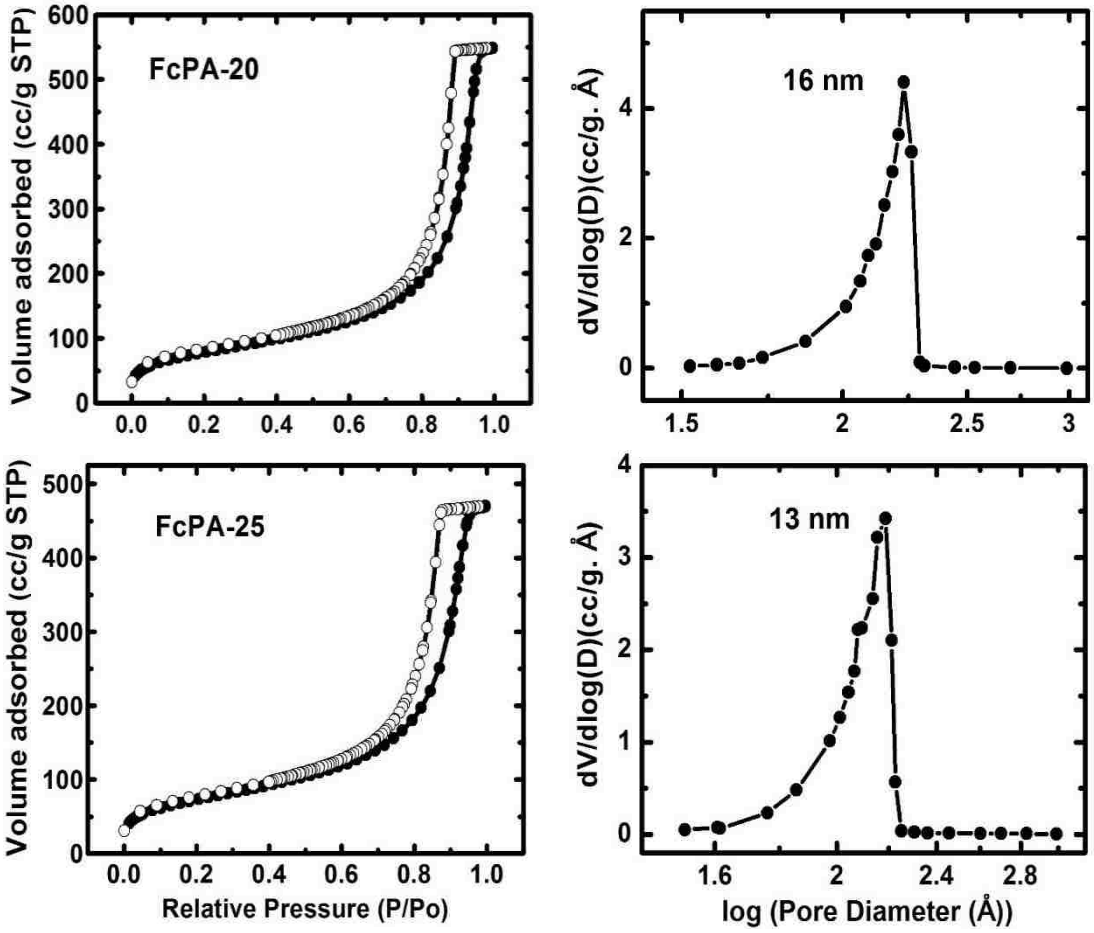

Figure S.1. (Continued). N_2-sorption isotherms and pore size distributions by the BJH method of FcPA-xx aerogels as shown. Results are summarized in Table S.2.

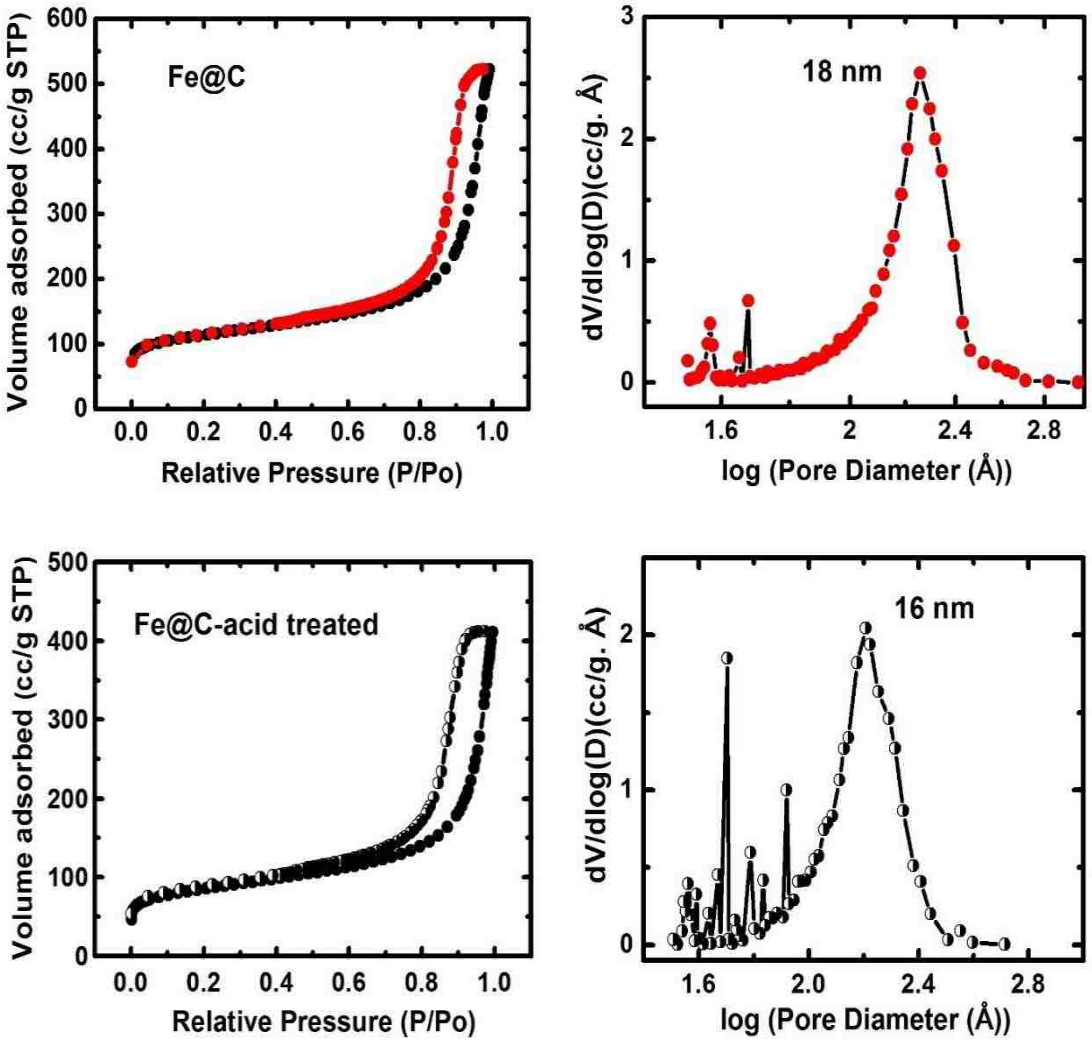

Figure S.2. N_2-sorption isotherms and pore size distributions by the BJH method of Fe@C (i.e., FcPA-xx aerogels pyrolyzed at 800 $^oC/H_2$) and of Fe@C after treatment with aq. HCl to remove Fe nanoparticles. Results are summarized in Table S.3, and in Table 1 of the main article.

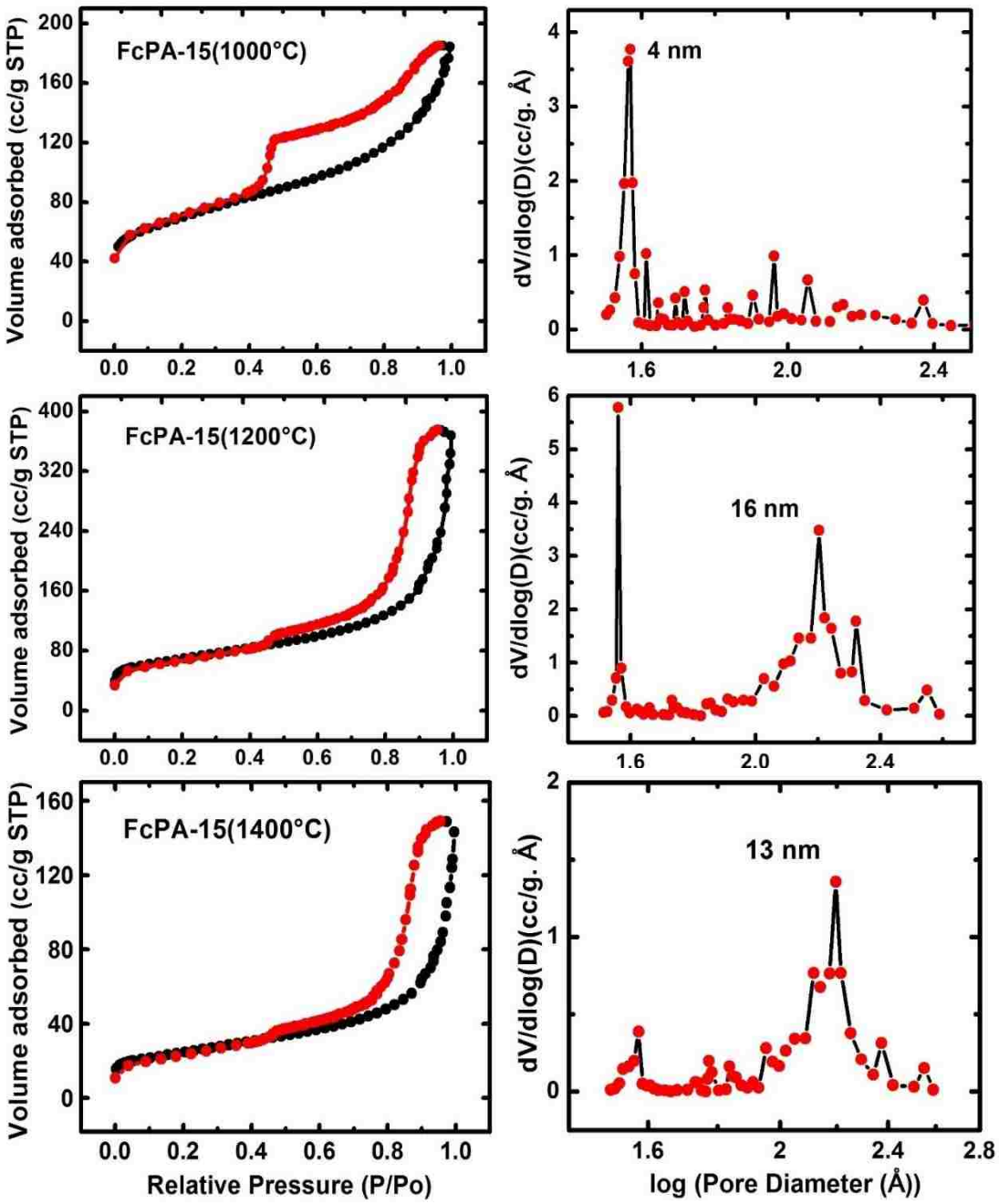

Figure S.3. N_2-sorption isotherms and pore size distributions by the BJH method of FcPA-xx aerogels pyrolyzed under /H_2 at the temperatures shown. Results are summarized in Table S.3.

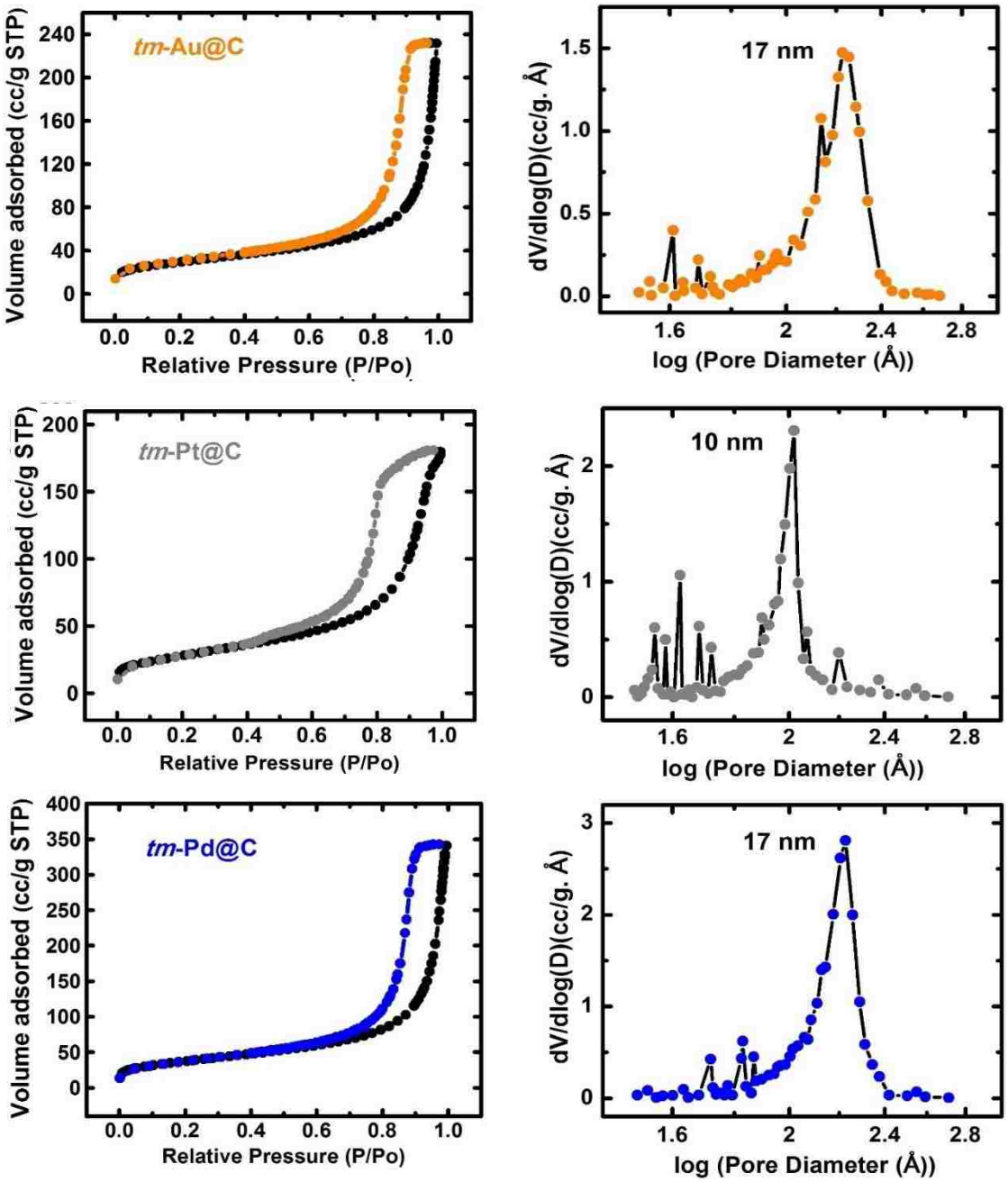

Figure S.4. N_2-sorption isotherms and pore size distributions by the BJH method of transmetalated samples as shown. Results are summarized in Table S.4.

Appendix IV. Analysis of the FcPA-xx skeletal frameworks: SAXS data

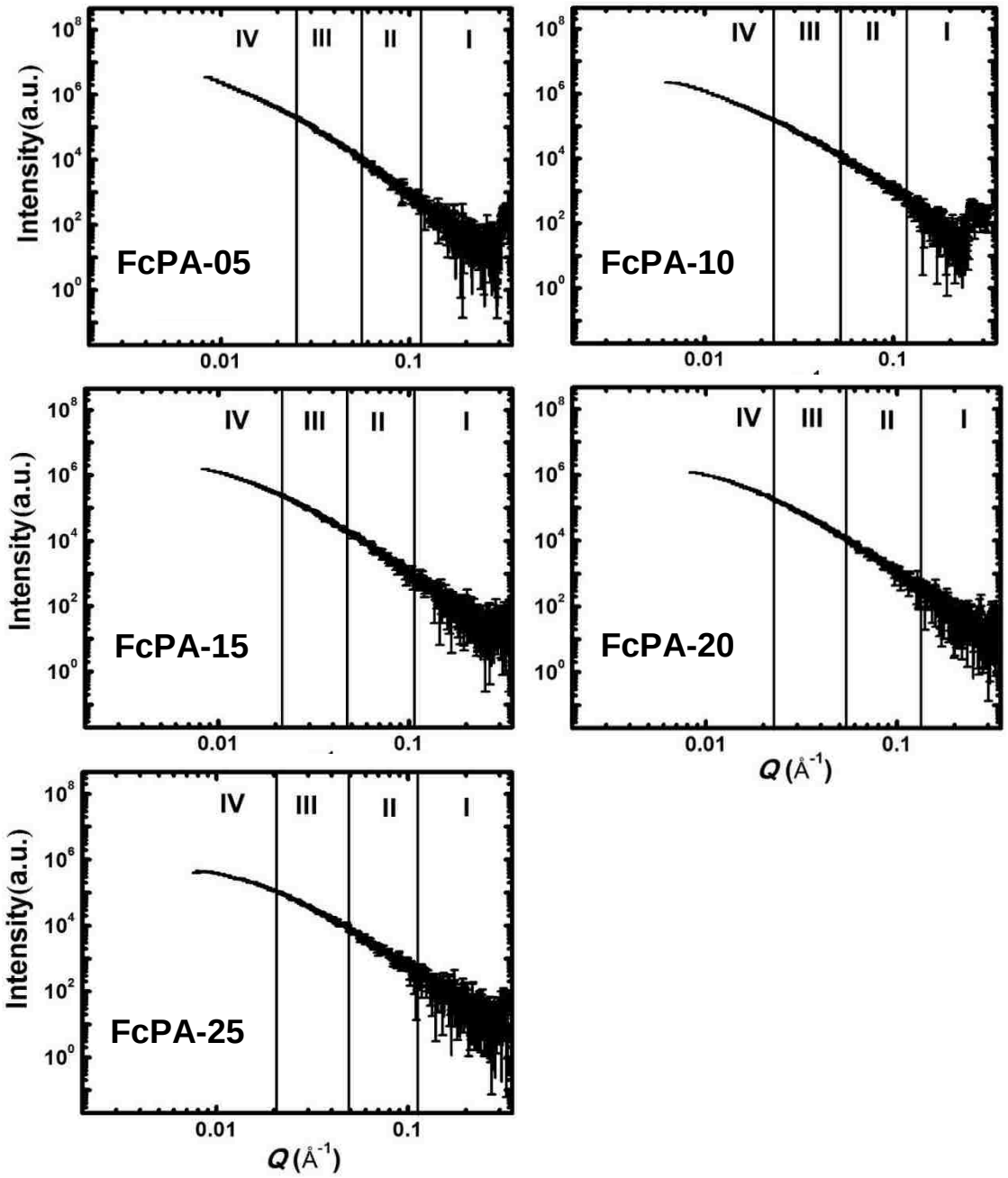

Figure S.5. Small angle X-ray scattering (SAXS) data of FcPA-xx. All data were fitted with two exponentials (Regions I and III) and two Guinier knees (Regions II and IV). Data pertinent to the nanostructures are gathered in Table S.5 below.

Table S.5. Results from analysis of the SAXS data in Figure S.5 using the Beaucage Unified Model.

Sample	Primary Particles			Secondary Particles		
	high-*Q* slope [a]	R_G(I) [b] (nm)	diameter [c] (nm)	low-*Q* slope [d]	R_G(II) [e] (nm)	diameter [f] (nm)
FcPA-05	-4.22 ± 0.14	3.84 ± 0.35	9.97 ± 0.91	-3.14 ± 0.03	22.42 ± 0.74	58.23 ± 1.92
FcPA-10	-4.56 ± 0.08	5.06 ± 0.25	13.14 ± 0.64	-2.95 ± 0.09	20.43 ± 0.29	50.06 ± 0.75
FcPA-15	-4.40 ± 0.10	3.03 ± 0.35	7.88 ± 0.91	-3.03 ± 0.08	16.92 ± 0.35	43.94 ± 0.91
FcPA-20	-4.24 ± 0.29	2.20 ± 0.12	5.71 ± 0.31	-3.24 ± 0.04	14.73 ± 0.15	38.26 ± 0.39
FcPA-25	-4.43 ± 0.14	4.36 ± 0.88	11.32 ± 2.28	-3.01 ± 0.28	13.46 ± 0.29	34.96 ± 0.75

[a] From power-law Region I. Slopes <-4.0 signify primary particles with density-gradient boundaries.

[b] Radius of gyration of primary particles, R_G(I), from Region II (first Guinier knee).

[c] Primary particle diameter = 2(R_G(I)/0.77). *It is noted that there is a good match of primary particle sizes from SAXS and those calculated from N_2-soprtion data. For a quick comparison, both values are cited in Table S.2.*

[d] From power-law Region III. If slope>-3, mass fractal dimension of secondary particles, D_M=|slope|; if slope<-3 (as in this case), surface fractal dimension of secondary particles, D_s=6-|slope|.

[e] Radius of gyration of secondary particles, R_G(II), from Region IV (second Guinier knee).

[f] Secondary particle diameter = 2(R_G(II)/0.77).

Appendix V. FTIR of FcPA-xx

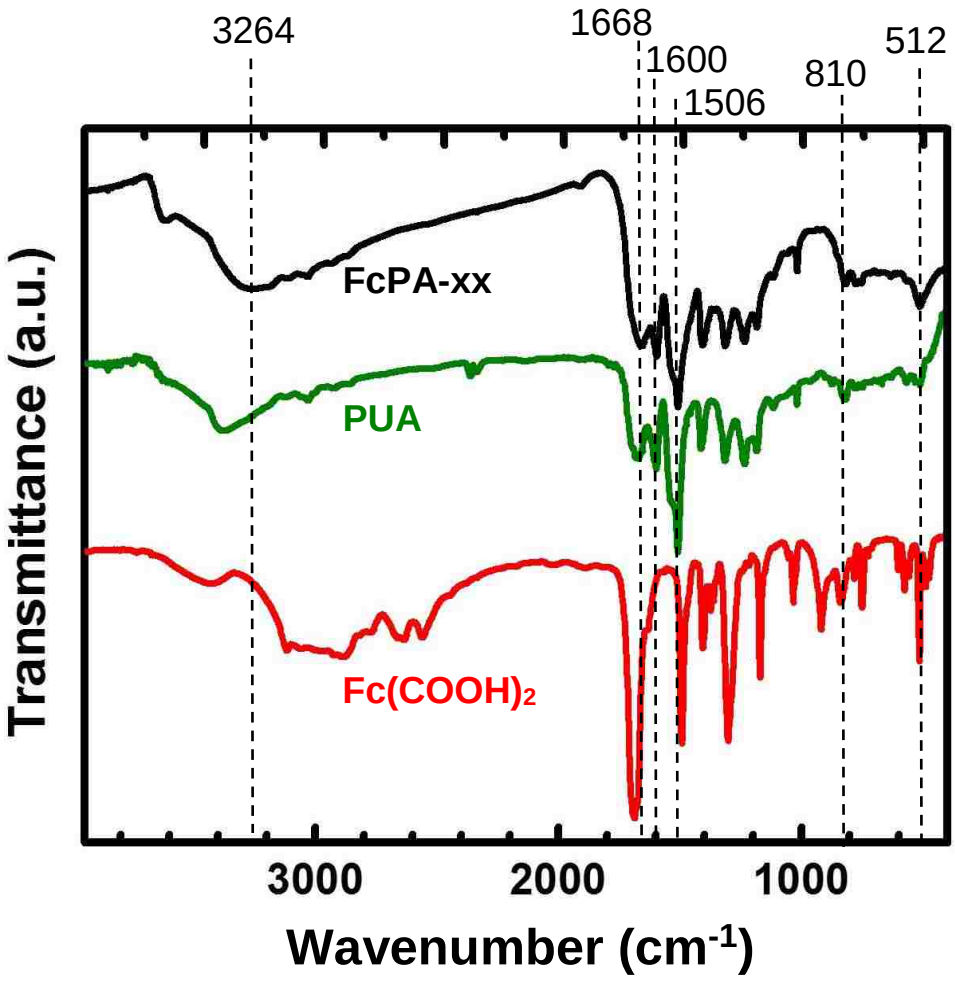

Figure S.6. FTIR of FcPA-xx, TIPM-derived polyurea (PUA) and $Fc(COOH)_2$.

Peak assignment:
NH stretch: 3264 cm^{-1}
CH stretches: weak absorptions around 3000 cm^{-1}
C=O stretch: 1668 cm^{-1}
Aromatic C=C stretch: 1600 cm^{-1} and 1506 cm^{-1}
NH bending: shoulder at around 1530 cm^{-1}
Aromatic CH OOP bending (*para* substituted ring): 810 cm^{-1}
Fe-Cp stretch: 512 cm^{-1}
No characteristic double anhydride band (in the ranges of 1800-1830 cm^{-1} and 1740-1775 cm^{-1}) is observed in the spectrum of FcPA-xx.

Appendix VI. Additional PXRD data related to transmetalation, and removal of Fe(0) from Fe@C with HCl

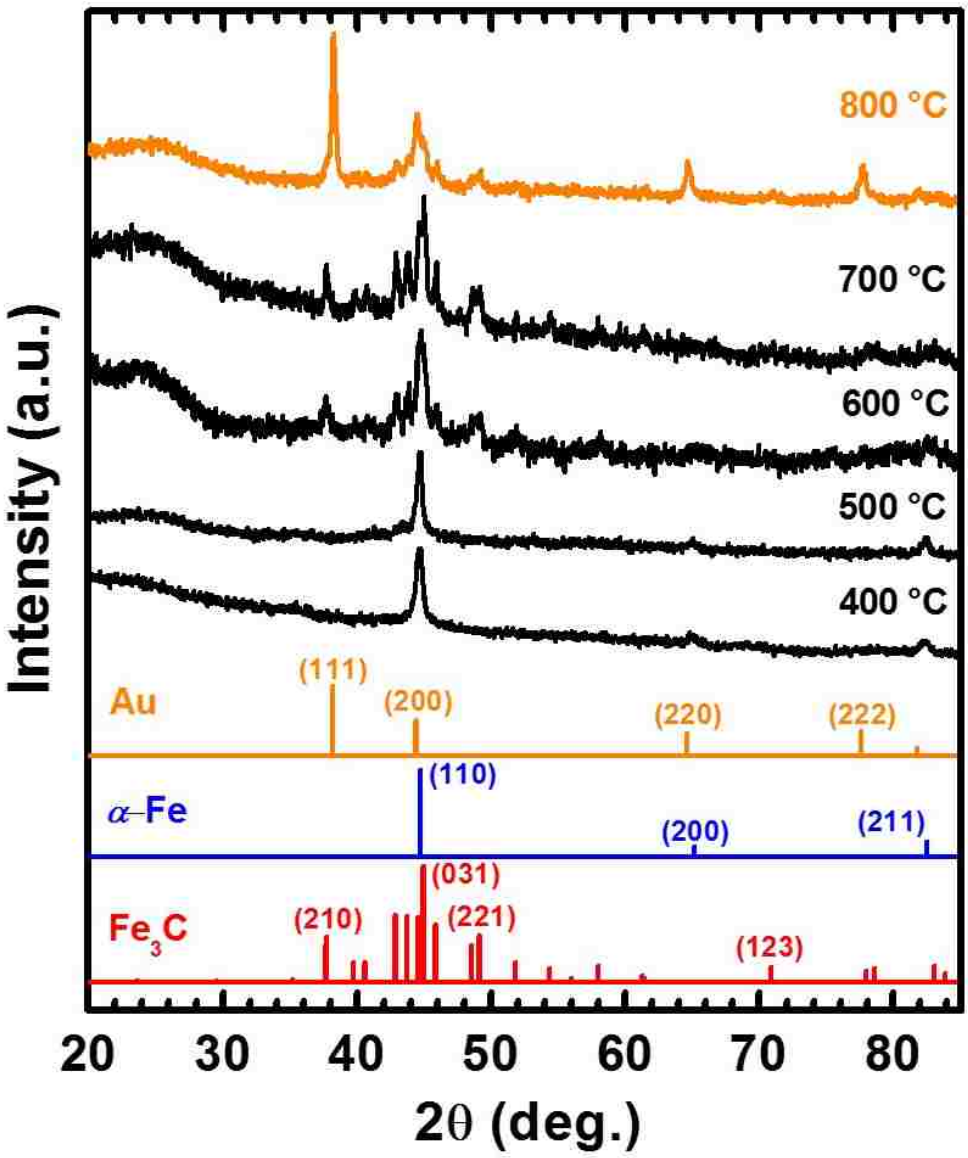

Figure S. 7. Powder XRD after attempted transmetalation with a Au plating solution of FcPA-15 pyrolyzed at different temperatures, as shown. Note that Fe(0) is removed completely only from samples pyrolyzed at 800 ^{o}C (referred to as Fe@C). As noted here buy also in Figure 5 of the main article, Fe_3C was produced at ≥600 ^{o}C, and according to this Figure here, it survived the transmetalation process.

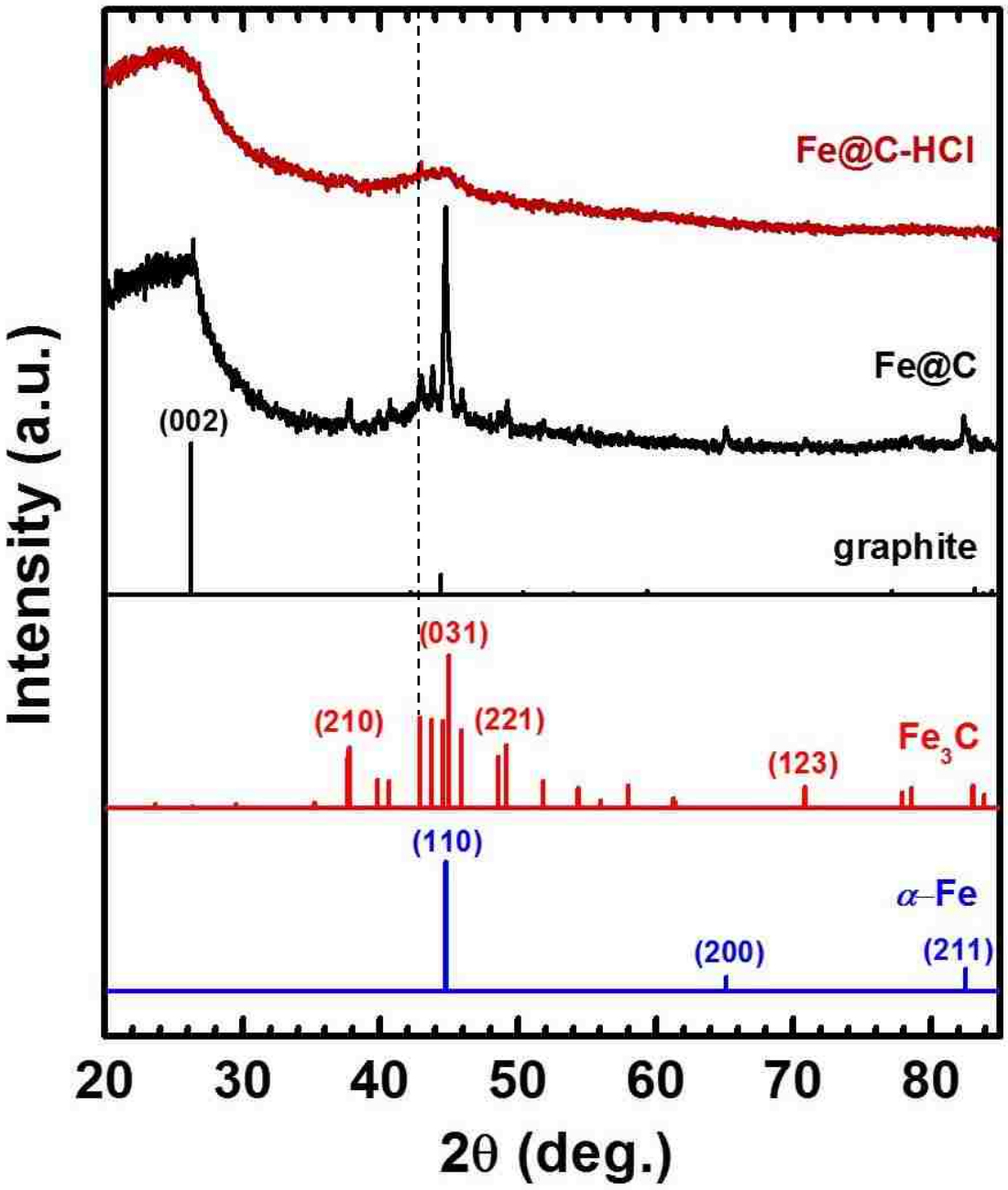

Figure S.8. Comparison of powder XRD data (PXRD) of as-prepared Fe@C and after treatment with a concentrated solution of HCl (see Experimental). The reflection designated by the dashed vertical line is attributed to surviving Fe_3C.

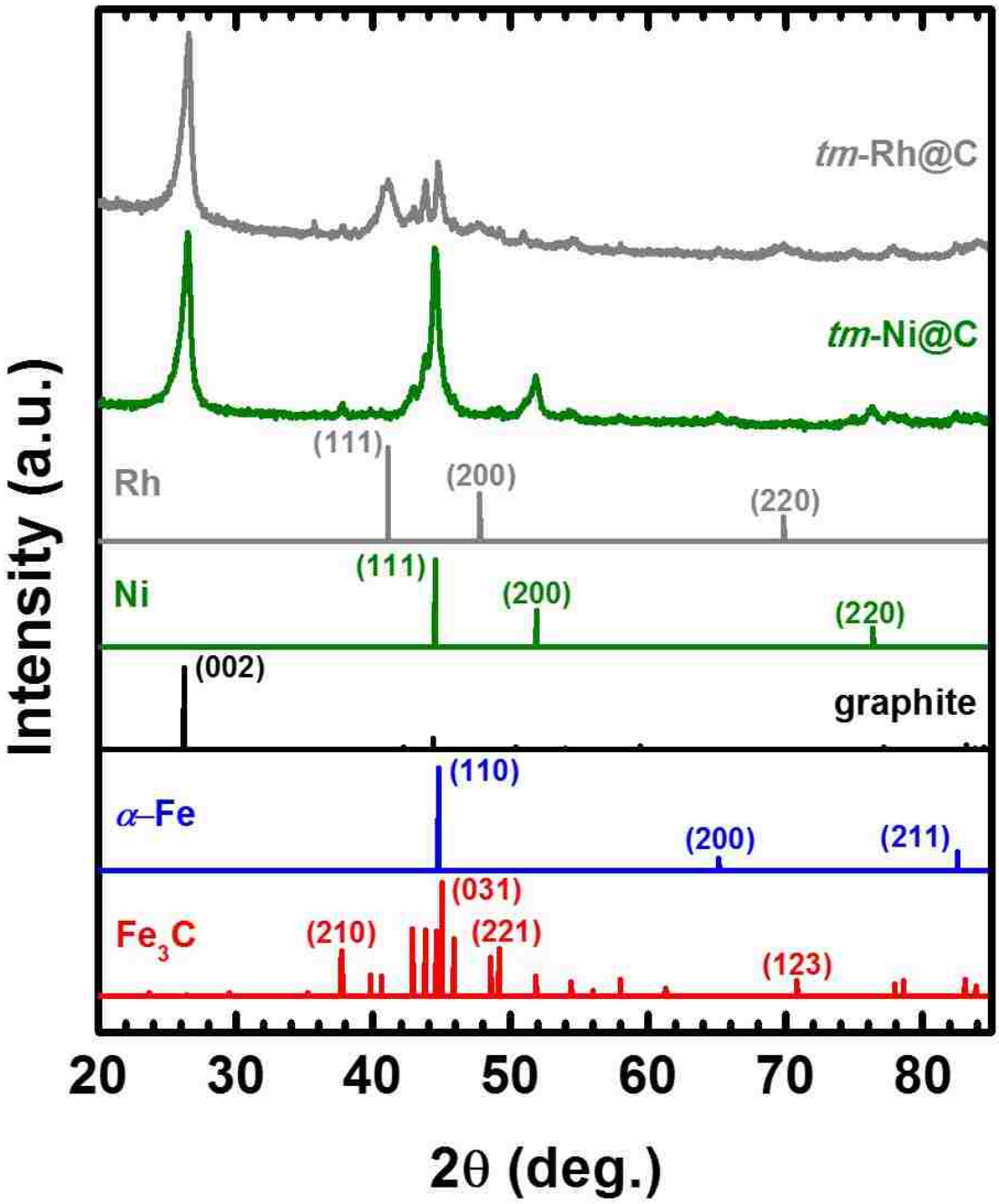

Figure S.9. Powder XRD data after transmetalation with Ni and Rh of FcPA-15 samples pyrolyzed at 1200 °C under H_2, as shown. Both spectra are dominated by the (002) reflection of graphite and contain small amounts of Fe_3C. Owing to the overlap of the (111) reflection of Ni with the reflections from Fe_3C, reliable application of the Scherrer equation was possible only with the (111) diffraction of Rh, whose crystallite size was calculated equal to 9±1 nm.

Appendix VII. Additional TEM of Fe@C and *tm*-M@C

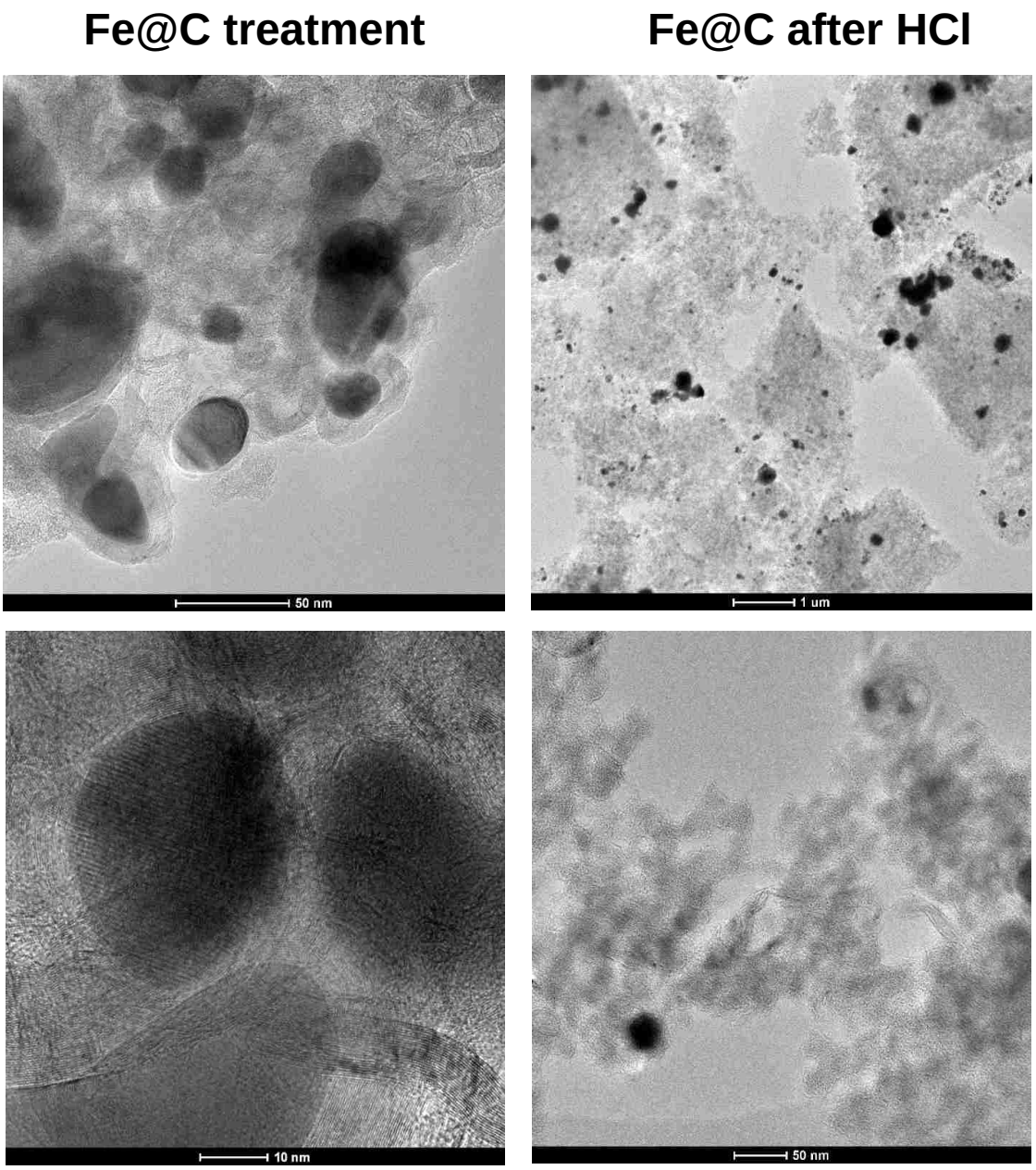

Figure S.10. TEM of samples as shown. Left: Fe@C. Left column top: Occasionally, ribbons swirl around and form pockets like those shrouding Fe(0) particles. Left Column bottom: Always Fe(0) particles are encased in ribbons. Right: Fe@C after treatment with concentrated aq. HCl at two magnifications. Consider these data together with the PXRD spectra of Fe@C before and after HCl treatment, shown in Figure S.8. **(Continued on the next page.)**

(Continued from previous page)

***tm*-Au@C** ***tm*-Pd@C**

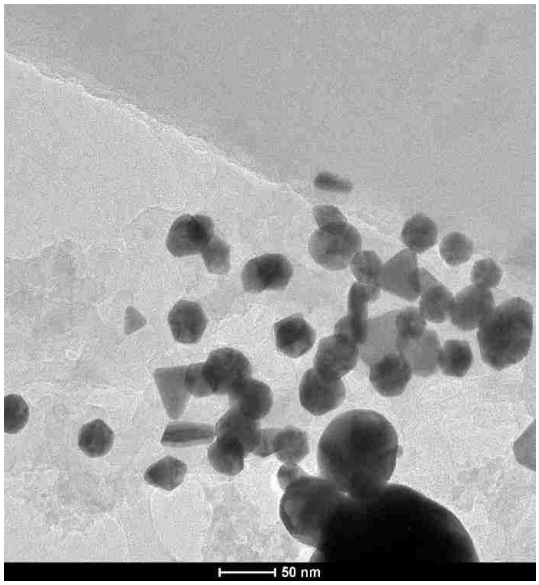

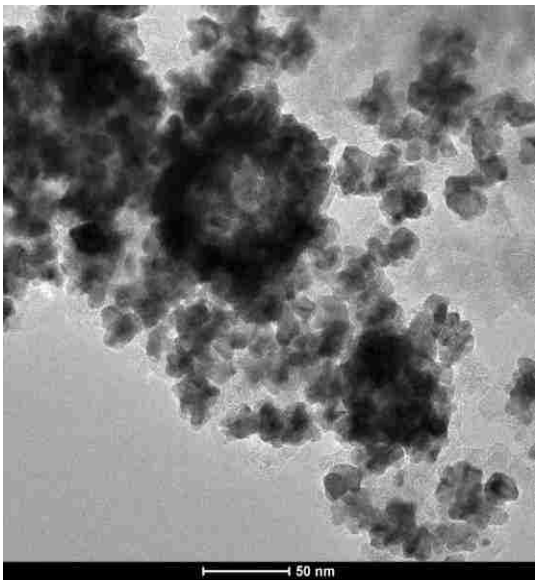

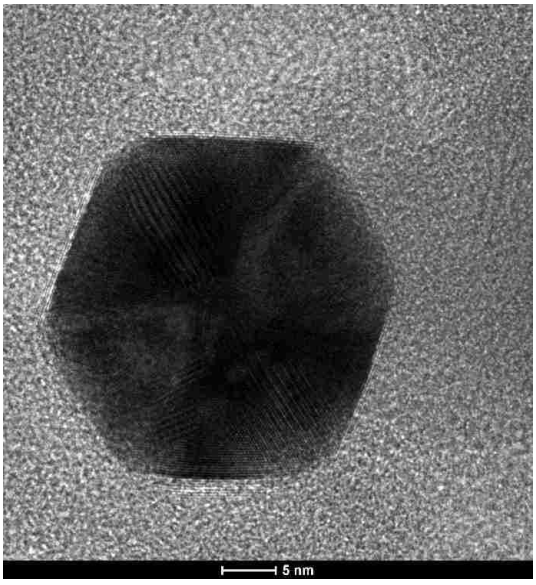

Figure S.10 (Continued). TEM of samples as shown. Nowhere in these post-transmetalation sample, new metallic nanoparticles could be associated with the interior of cages that contained Fe(0) in the Fe@C precursor.

Appendix VIII. Raman of FcPA-15 after pyrolysis at different temperatures

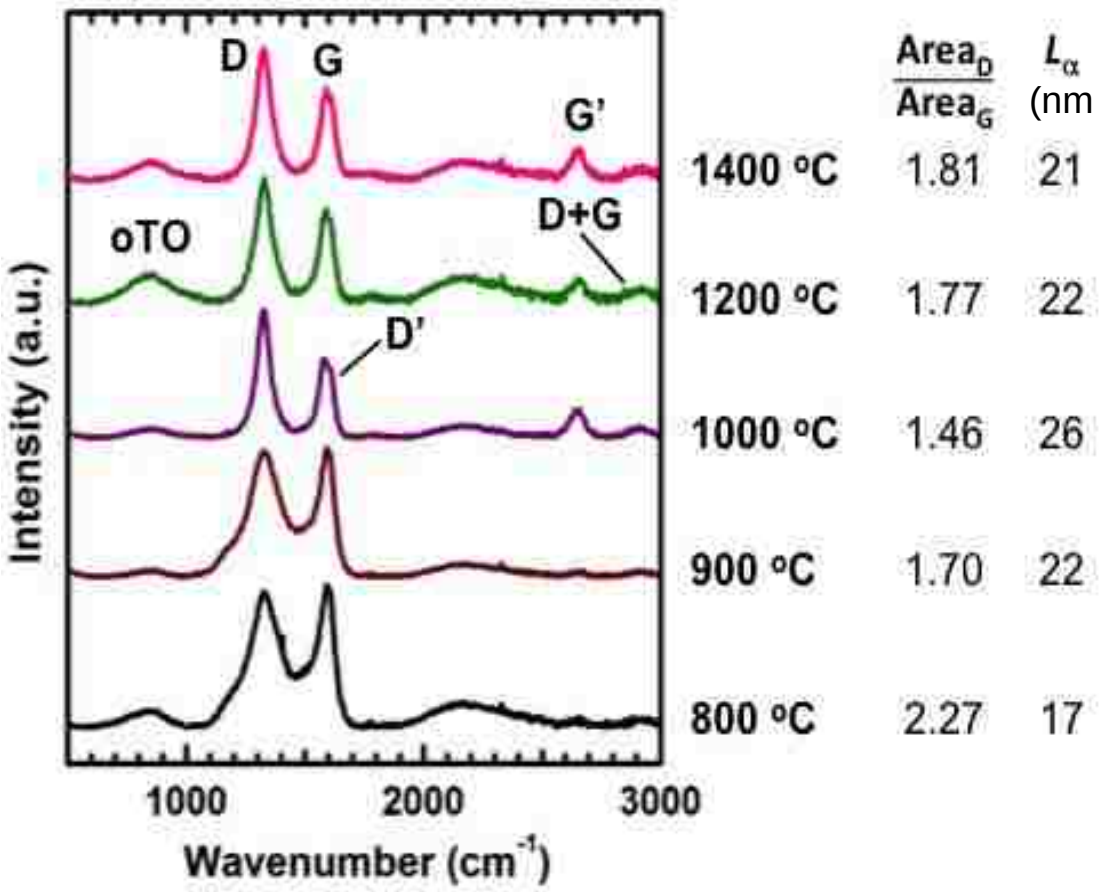

Figure S.11. Raman spectra after pyrolysis of FcPA-15 at different temperatures, as shown. All peak assignment according to Dresselhaus, M. S.; Dresselhaus, G.; Saito, R.; Jorio, A. "Raman spectroscopy of carbon nanotubes." Physics Reports **2005**, *409*, 47-99. The maxima of the peaks of interest are: D, 1326 cm^{-1}; G, 1592 cm^{-1}. At higher resolution, the D´ peak appears as a shoulder at 1610 cm^{-1} in all spectra. The low-intensity, broad band at around 2150 cm^{-1} could not be assigned. The graphene layer stack height (L_α) was calculated using Knight's formula ($L_a(nm) = (2.4\times10^{-10})\lambda_{exc}^4 \left(\frac{A_D}{A_G}\right)^{-1}$) from the ratio of the peak areas (cited on the right). Peak areas were calculated using deconvolution and Laurentian fit. λ_{exc} is the wavelength of the laser, in our case 514.5 nm (2.41 eV).

Appendix IX. Data from catalysis using Fe@C and *tm*-M@C as catalysts

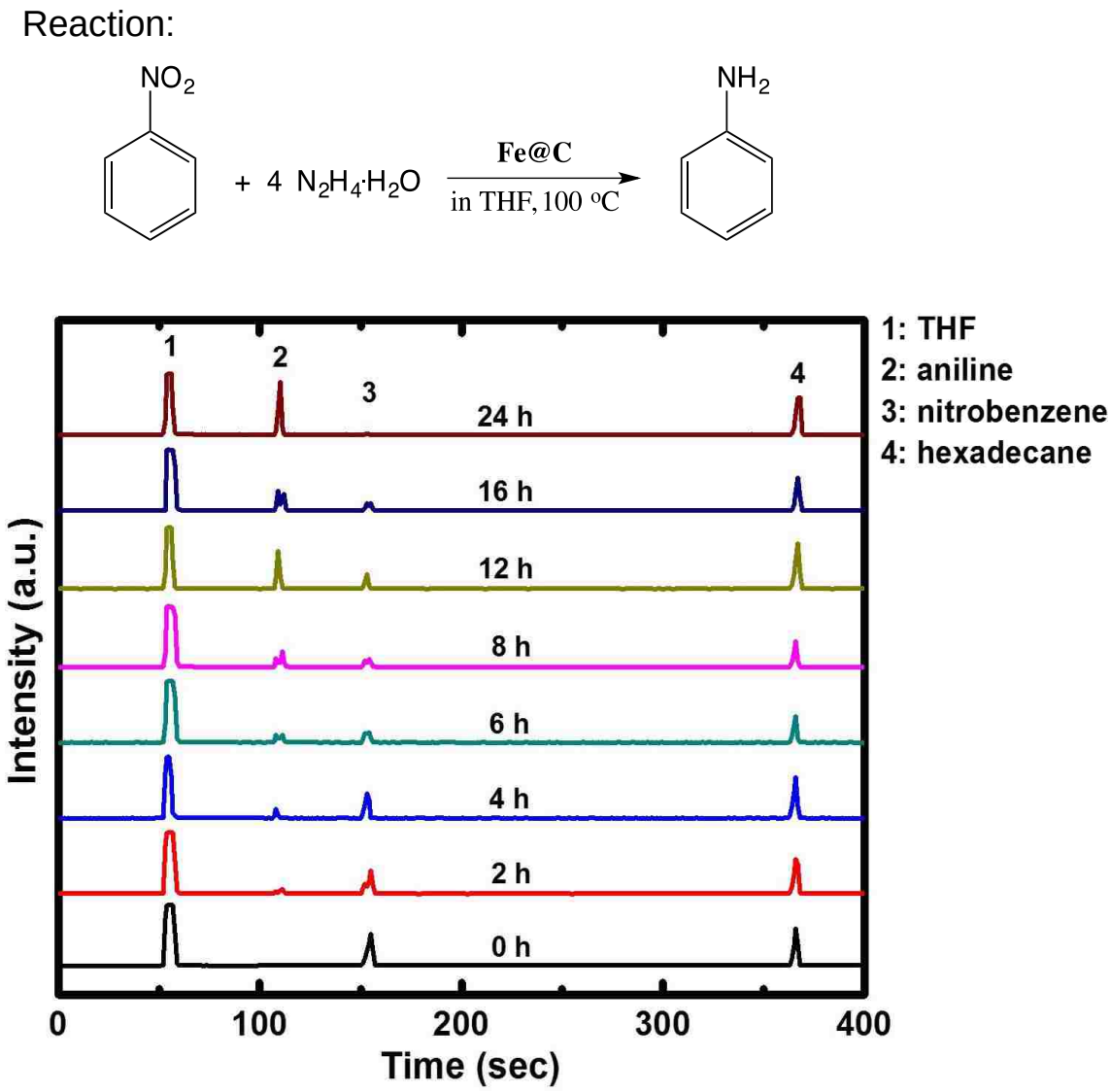

Figure S.12. GC analysis of aliquots taken out during the 1st Cycle of the reduction of nitrobenzene to aniline using a Fe@C monolith as a catalyst. Results are plotted in Figure S.13.

Reaction:

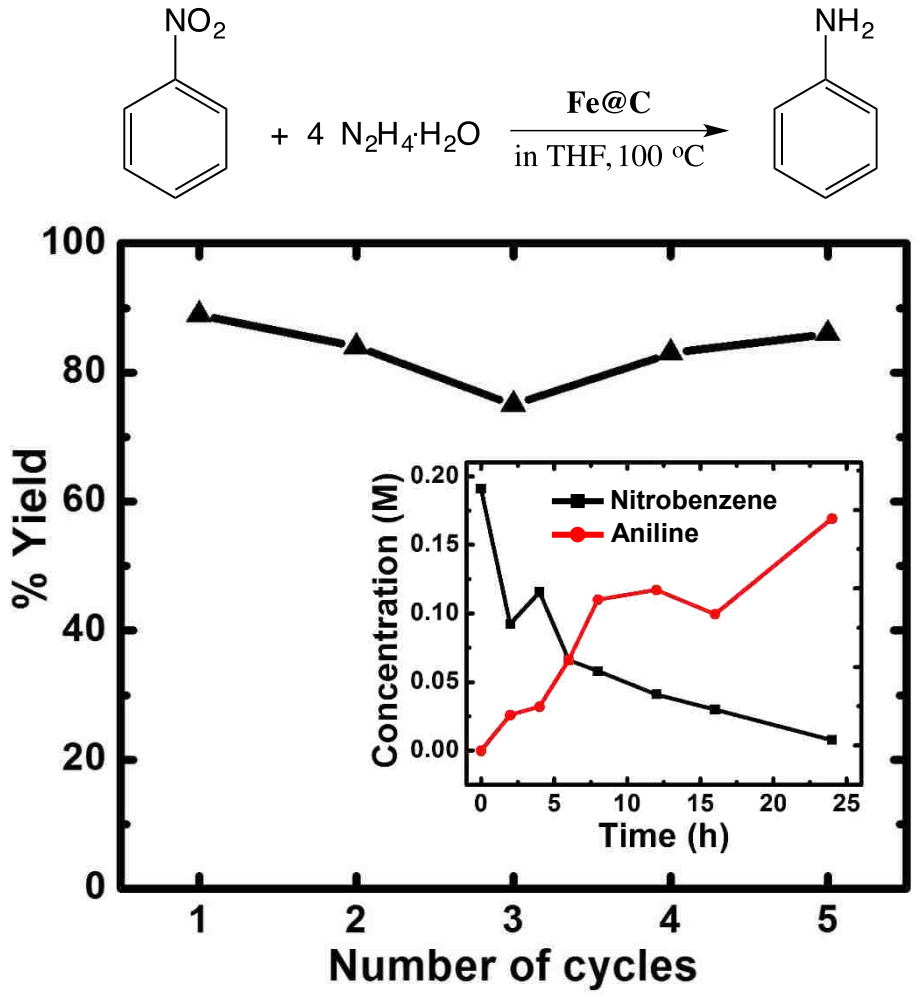

Figure S.13. Reduction of nitrobenzene to aniline using a Fe@C monolith as a catalyst. Inset: Evolution of reactant and product concentrations in a 24 h period (1st Cycle). Data from Figure S.12.

Reaction:

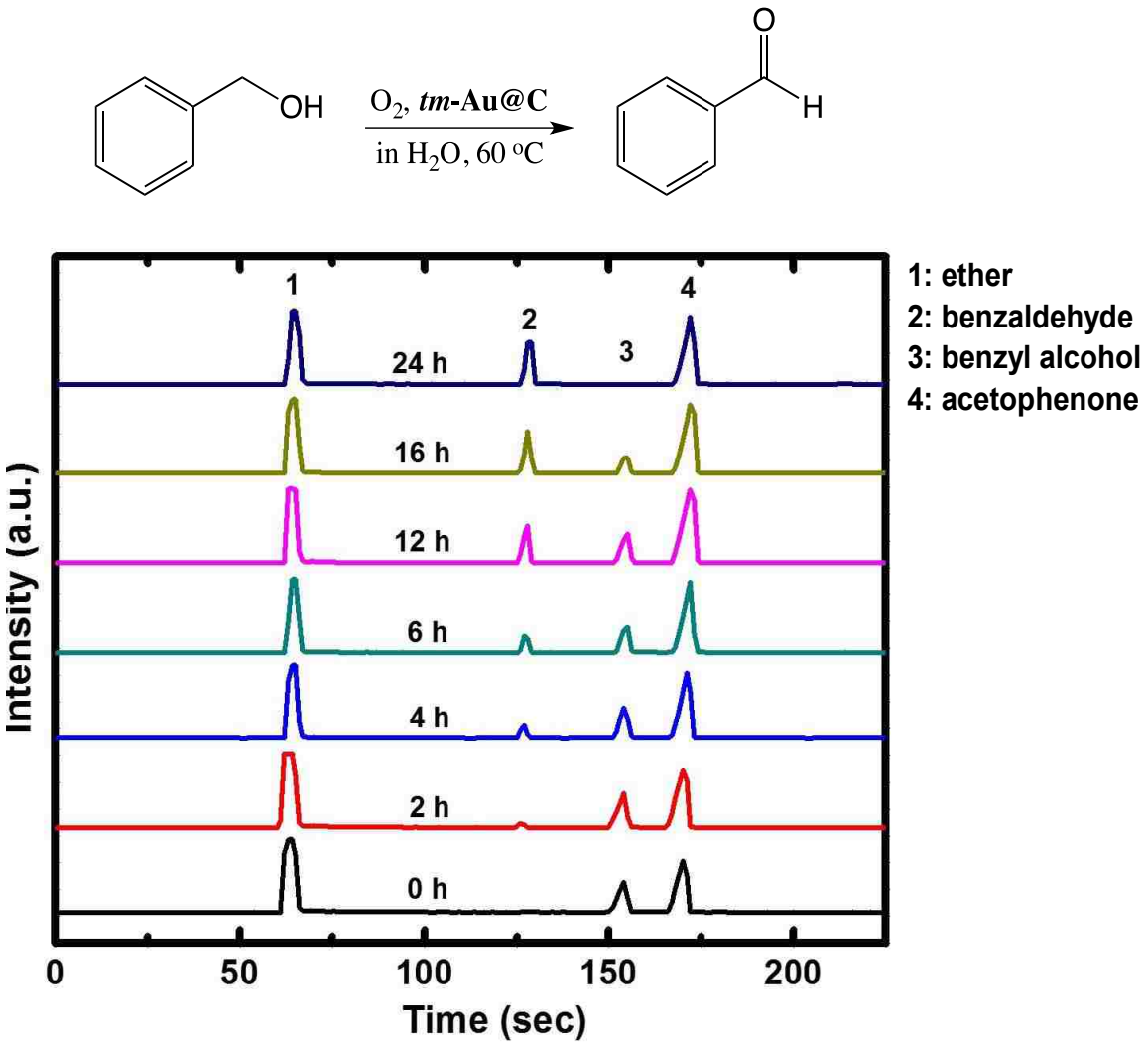

Figure S.14. GC analysis of aliquots taken out during the 1st Cycle of the oxidation of benzyl alcohol to benzaldehyde using a tm-Au@C monolith as catalyst. Results are plotted in Figure S.15.

Reaction:

.

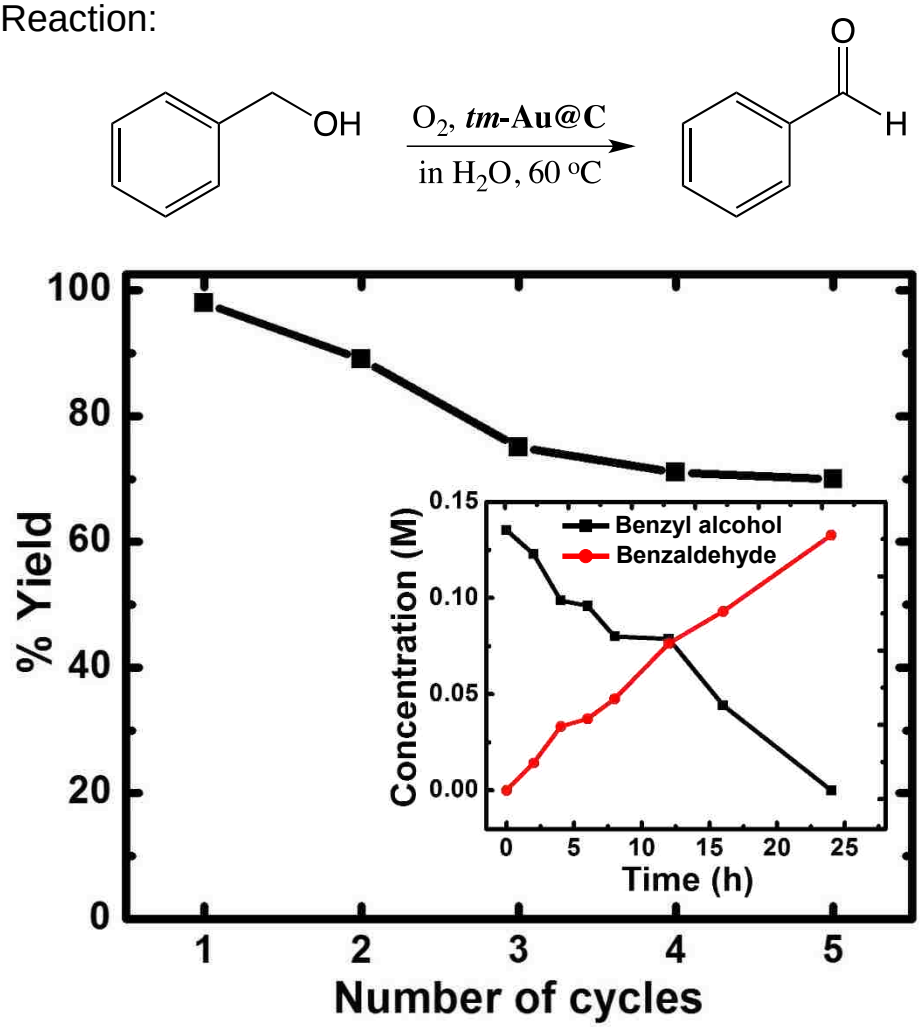

Figure S.15. Oxidation of benzyl alcohol to benzaldehyde using a *tm*-Au@C monolith as a catalyst. Inset: Evolution of reactant and product concentrations in a 24 h period (1st Cycle). Data from Figure S.14.

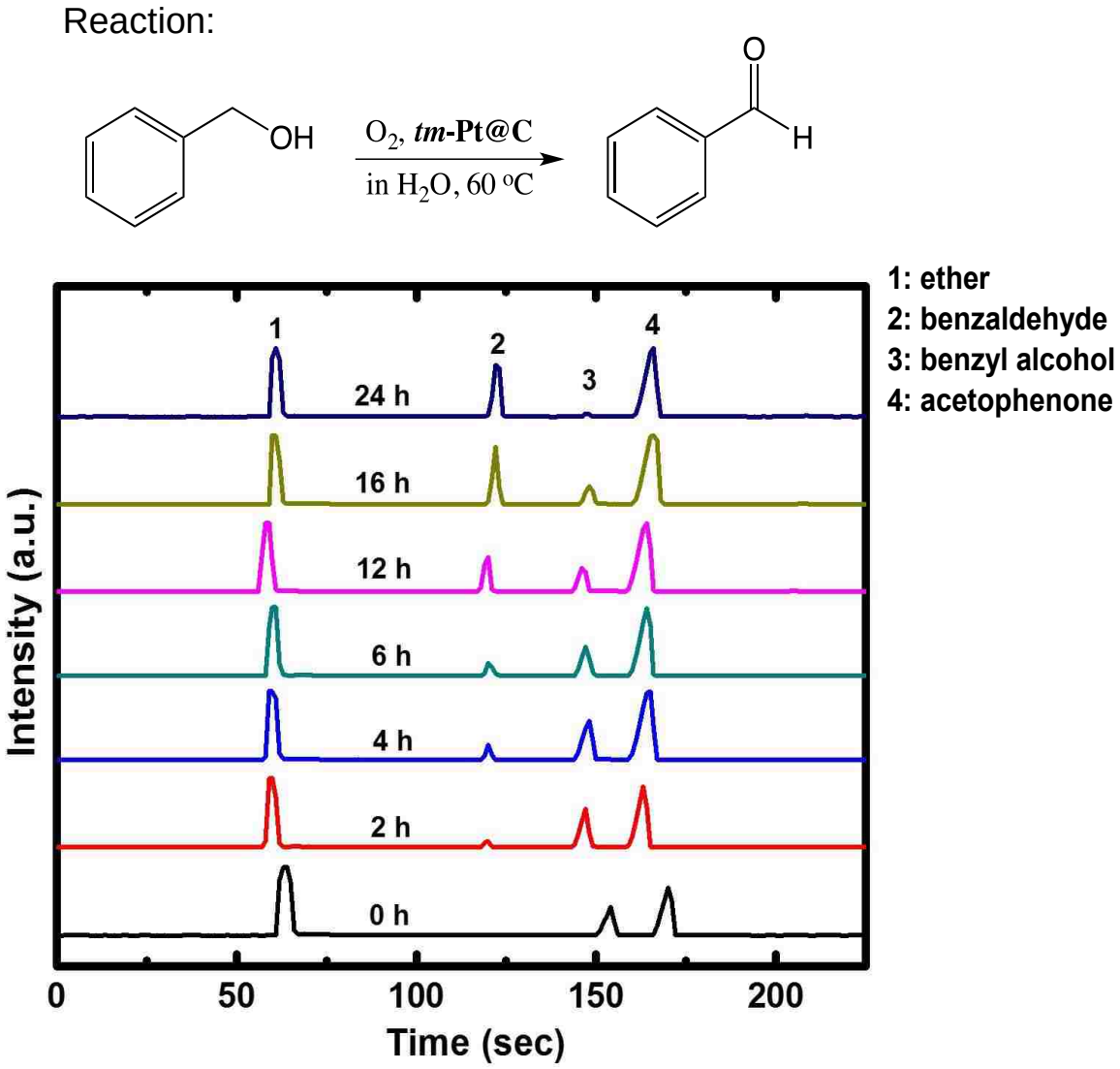

Figure S.16. GC analysis of aliquots taken out during the 1st Cycle of the oxidation of benzyl alcohol to benzaldehyde using a *tm*-Pt@C monolith as catalyst. Results are plotted in Figure S.17.

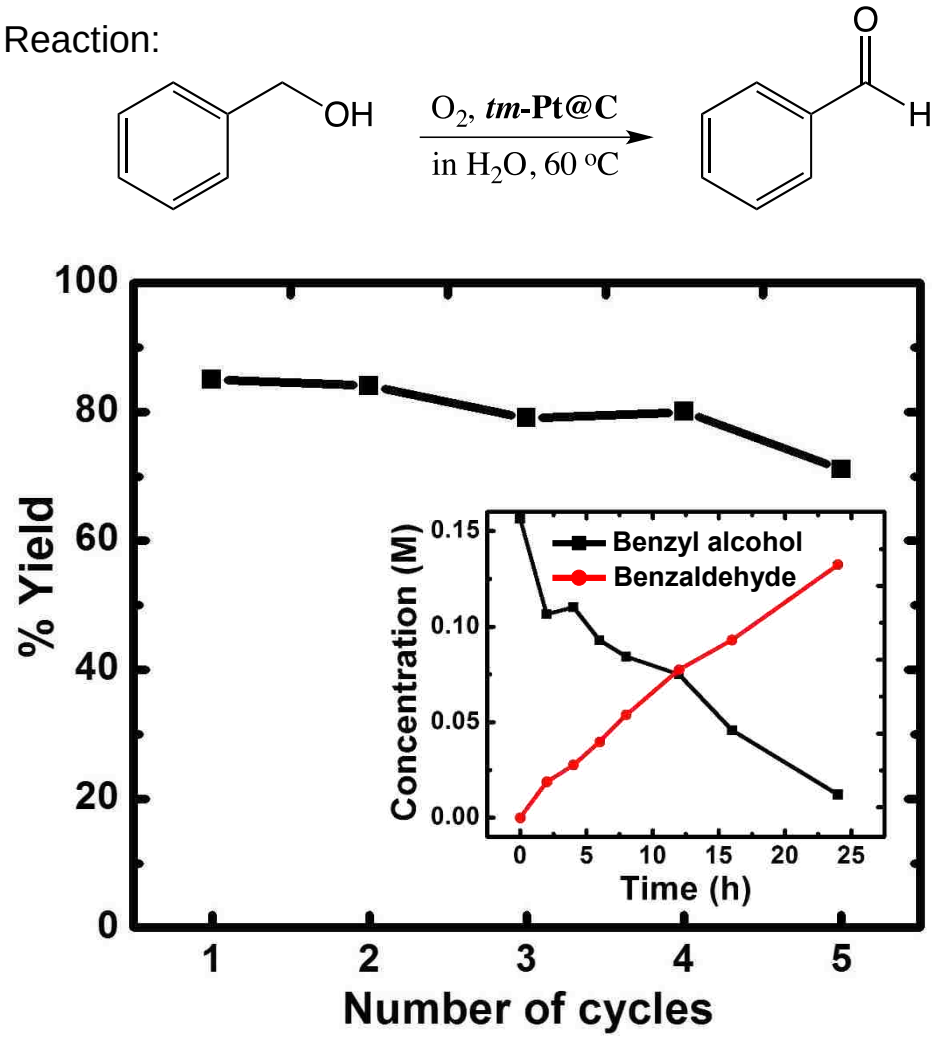

Figure S.17. Oxidation of benzyl alcohol to benzaldehyde using a *tm*-Pt@C monolith as catalyst. Inset: Evolution of reactant and product concentrations in a 24 h period (1st Cycle). Data from Figure S.16. (Note the similarity of the data with using *tm*-Au@C as a catalyst in Figure S.15.)

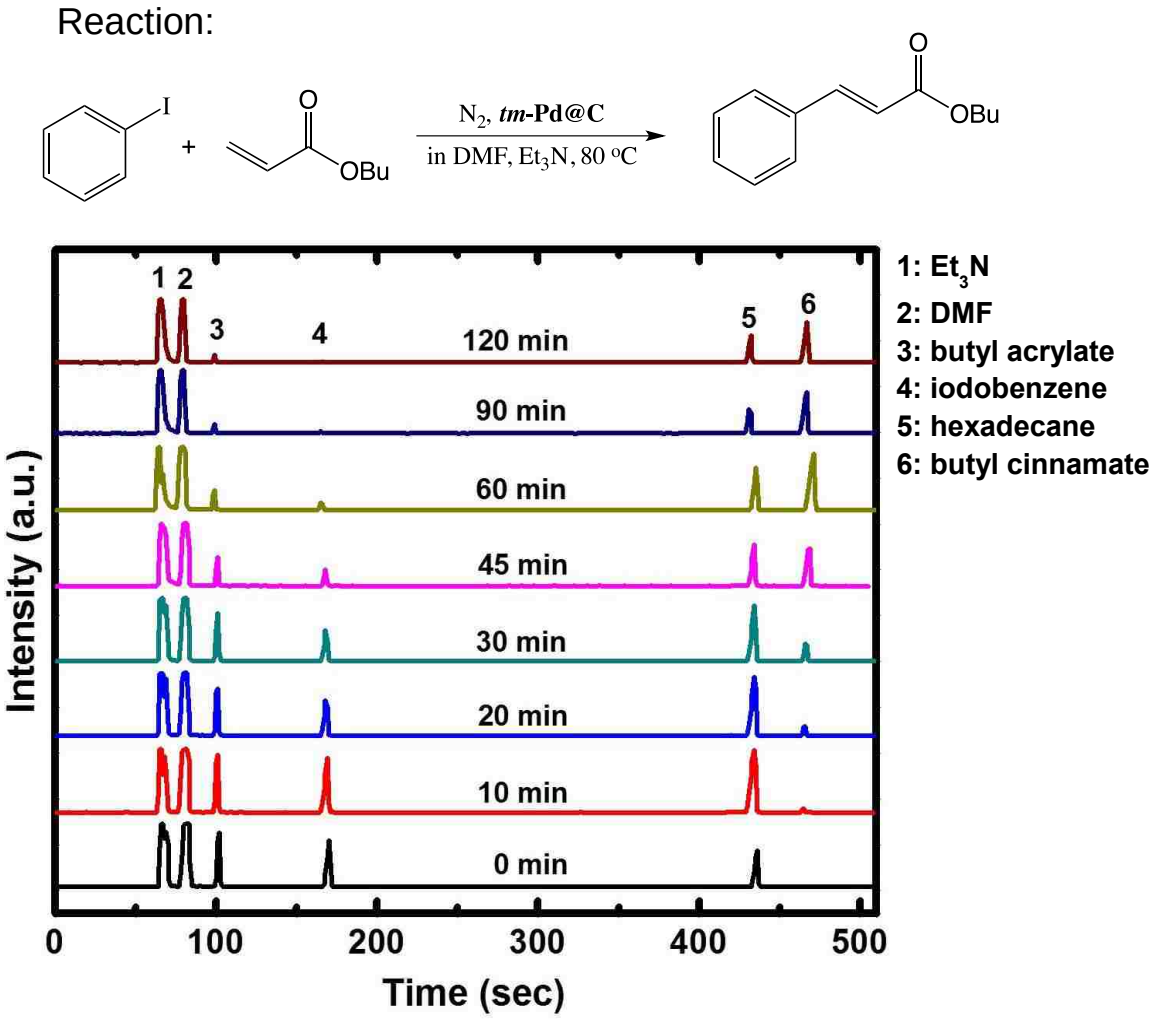

Figure S.18. GC analysis of aliquots taken out during the 1st Cycle of the Heck coupling of iodobenzene and butyl acrylate towards butyl cinnamate using a *tm*-Pd@C monolith as a catalyst. Results are plotted in Figure S.19.

Reaction:

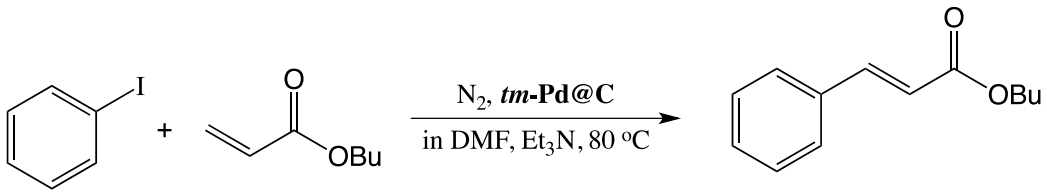

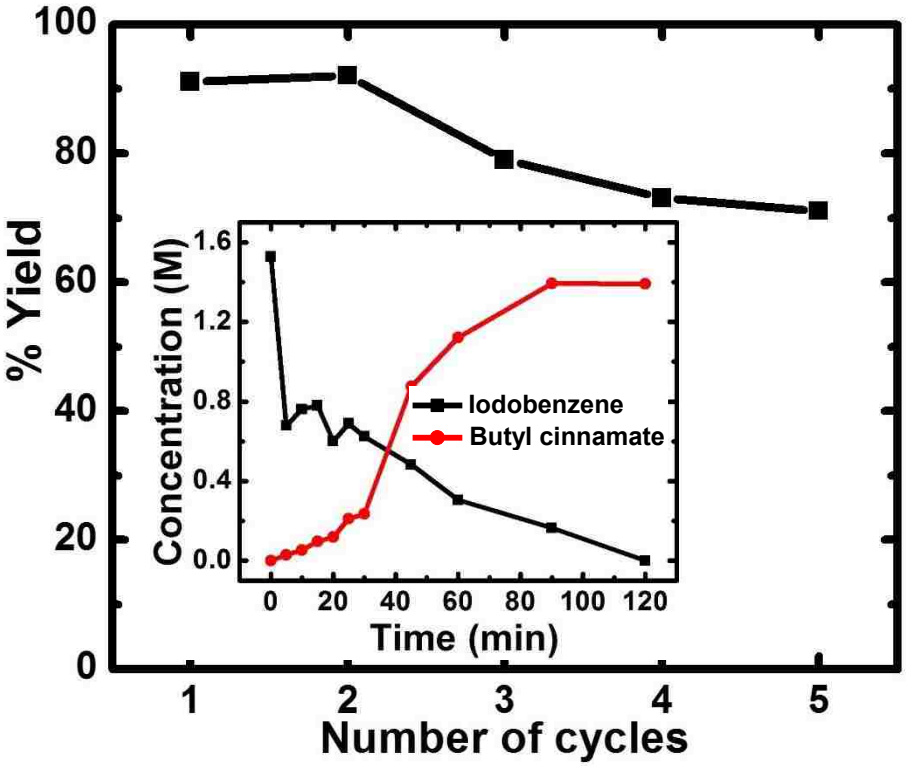

Figure S.19. Heck coupling of iodobenzene and butyl acrylate towards butyl cinnamate using a *tm*-Pd@C monolith as a catalyst. Inset: Evolution of reactant and product concentrations in a 2 h period (1st Cycle). Data from Figure S.18.

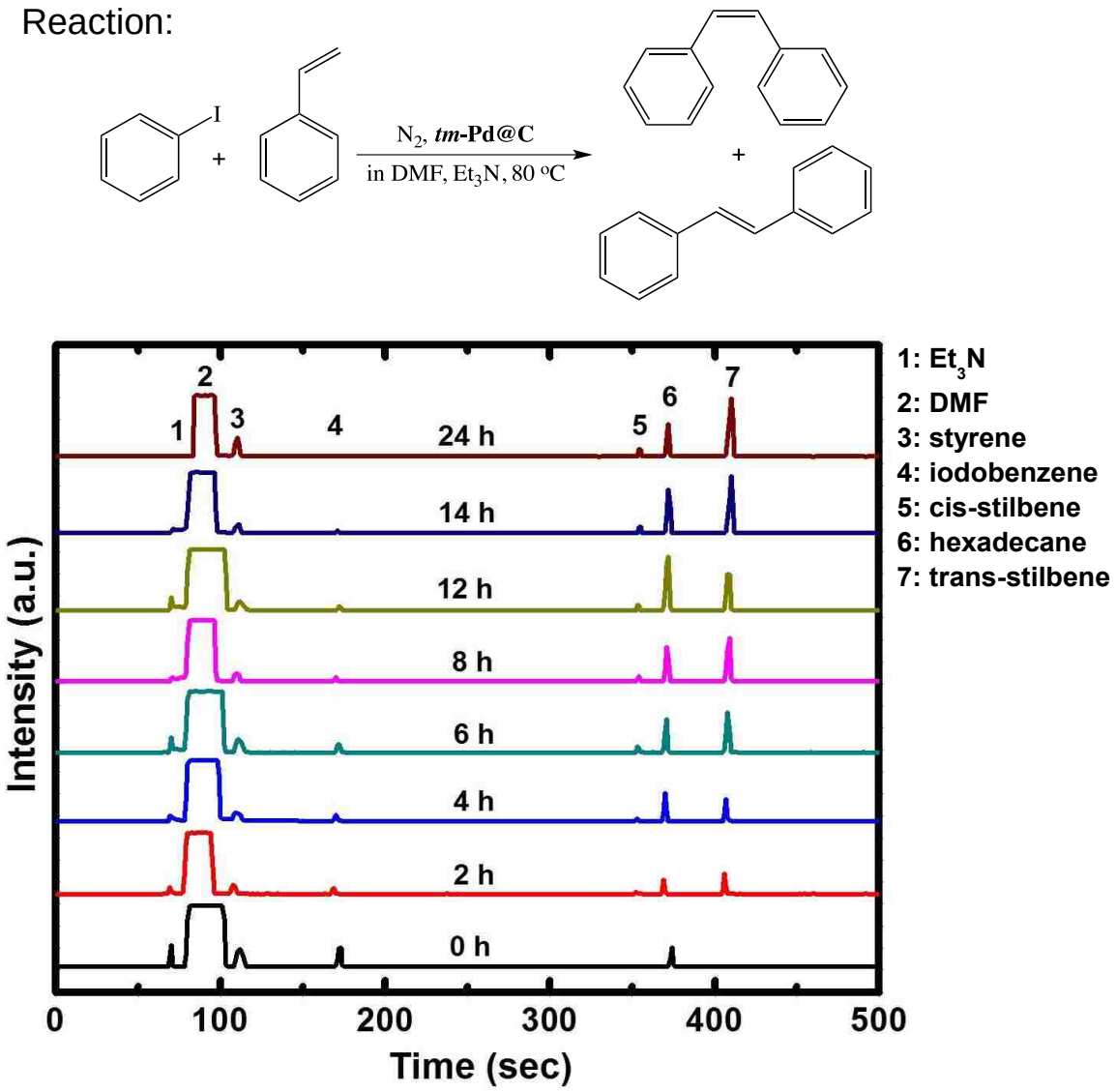

Figure S.20. GC analysis of aliquots taken out during the 1st Cycle of the Heck coupling of iodobenzene and styrene towards cis- and trans-stilbene using a *tm*-Pd@C monolith as a catalyst. Results are plotted in Figure S.21.

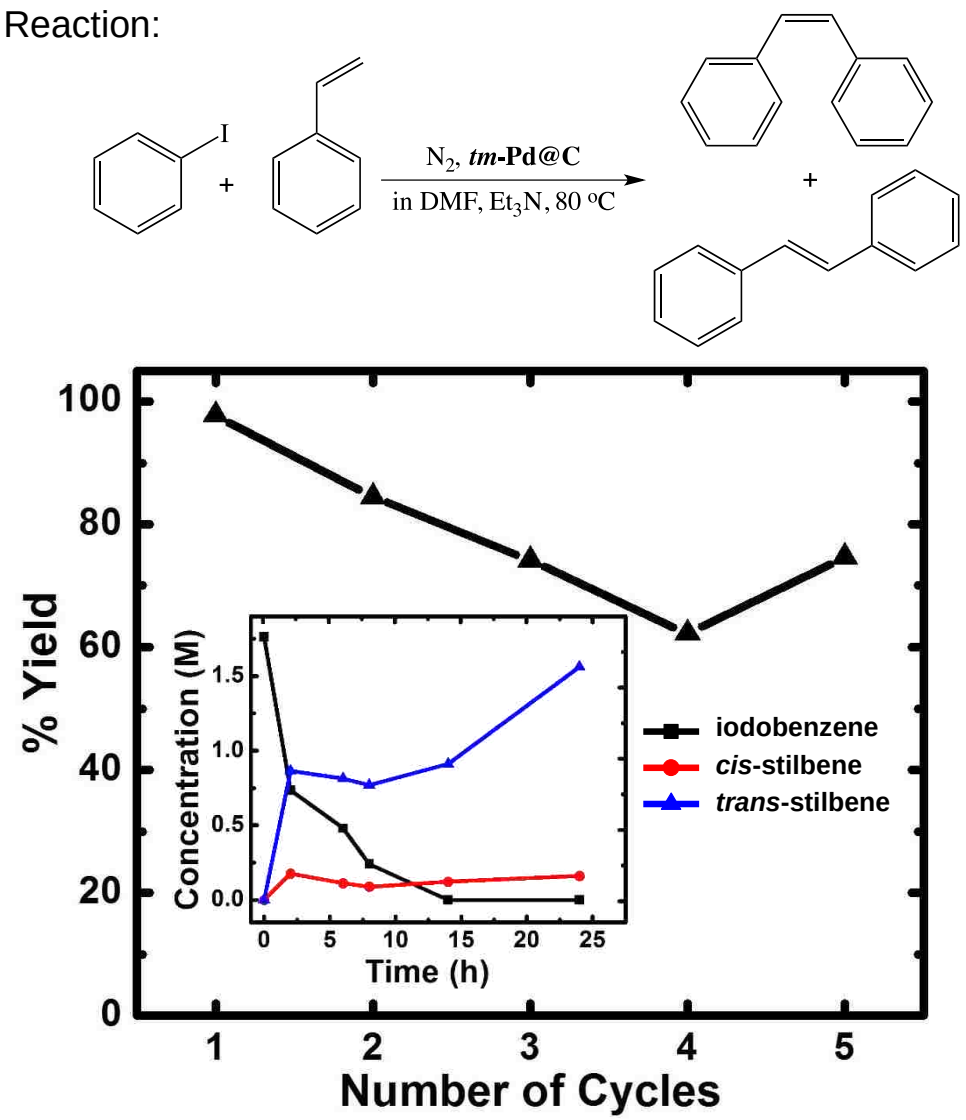

Figure S. 21. Heck coupling of iodobenzene and styrene towards cis- and trans-stilbene using a *tm*-Pd@C monolith as a catalyst. Inset: Evolution of reactant and product concentrations in a 24 h period (1st Cycle). Data from Figure S.20.

ACKNOWLEDGEMENTS

This project was funded by the Army Research Office under Award Number W911NF-14-1-0369. We also thank Covestro LLC (formerly Bayer Corporation U.S.A.) for the generous supply of Desmodur RE (TIPM), and the Materials Research Center of the Missouri University of Science and Technology for support with materials characterization.

REFERENCES

(1) Ertl, G. Reactions at Surfaces: From Atoms to Complexity (Nobel Lecture). *Angew. Chem. Int. Ed.* **2008**, *47*, 3524–3535.

(2) Mizuno, N.; Misono, M. Heterogeneous Catalysis. *Chem. Rev.* **1998**, *98*, 199-217.

(3) Wang, Y.-J.; Wilkinson, D. P.; Zhang, J. Noncarbon Support Materials for Polymer Electrolyte Membrane Fuel Cell Electrocatalysts. *Chem. Rev.* **2011**, *111*, 7625-7651.

(4) Zaera, F. Nanostructured Materials for Applications in Heterogeneous Catalysis. *Chem. Soc. Rev.* **2013**, *42*, 2746-2762.

(5) Yin, L.; Liebscher, J. Carbon−Carbon Coupling Reactions Catalyzed by Heterogeneous Palladium Catalysts. *Chem. Rev.* **2007**, *107*, 133-173.

(6) Debe, M. K. Electrocatalyst Approaches and Challenges for Automotive Fuel Cells. *Nature* **486**, 43–51.

(7) Tomasic, V.; F. Jovic, F. State-of-the-art in the Monolithic Catalysts/Reactors. *Appl. Catal., A* **2006**, *311*, 112–121.

(8) Twigg, M. V. Catalytic Control of Emissions from Cars. *Catal. Today* **2011**, *163*, 33-41.

(9) Hüsing, N.; Schubert, U. Aerogels-airy Materials: Chemistry, Structure and Properties. *Angew. Chem., Int. Ed. Engl.* **1998**, *37*, 22-45.

(10) Pierre, A. C.; Pajonk, G. M. Chemistry of Aerogels and their Applications. *Chem. Rev.* **2002**, *102*, 4243–4265.

(11) Morris, C. A.; Anderson, M. L.; Stroud, R. M.; Merzbacher, C. I.; Rolison, D. R. Silica Sol as a Nanoglue: Flexible Synthesis of Composite Aerogels. *Science* **1999**, *284*, 622–624.

(12) Pekala, R. W.; Alviso, C. T.; Kong, F. M.; Hulsey, S. S. Aerogels Derived from Multifunctional Organic Monomers. *J. Non-Cryst. Solids* **1992**, *145*, 90–98.

(13) Al-Muhtaseb, S A.; Ritter, J. A. Preparation and Properties of Resorcinol–Formaldehyde Organic and Carbon Gels. *Adv. Mater.* **2003**, *15*, 101–114.

(14) Li, W.-C.; Lu, A.-H.; Schüth, F. Preparation of Monolithic Carbon Aerogels and Investigation of Their Pore Interconnectivity by a Nanocasting Pathway. *Chem. Mater.* **2005**, *17*, 3620–3626.

(15) Leventis, N.; Mulik, S. Sotiriou-Leventis, C. Macroporous Electrically Conducting Carbon Networks by Pyrolysis of Isocyanate Cross-Linked Resorcinol-Formaldehyde Aerogels. *Chem. Mater.* **2008**, *20*, 6985-6997.

(16) Conroy, D.; Moisala, A.; Cardoso, S.; Windle, A.; Davidson, J. Carbon Nanotube Reactor: Ferrocene Decomposition, Iron Particle Growth, Nanotube Aggregation and Scale-up. *Chem. Eng. Sci.* **2010**, *65*, 2965–2977.

(17) Chidambareswarapattar, C.; Xu, L.; Sotiriou-Leventis, C.; Leventis, N. Robust Monolithic Multiscale Nanoporous Polyimides and Conversion to Isomorphic Carbons. *RSC Advances* **2013**, *3*, 26459-26469.

(18) Leventis, N.; C. Sotiriou-Leventis, C.; Chandrasekaran, N.; Mulik, S.; Larimore, Z. J.; Lu, H.; Churu, G.; Mang, J. T. Multifunctional Polyurea Aerogels from Isocyanates and Water. A Structure−Property Case Study. *Chem. Mater.* **2010**, *22*, 6692-6710.

(19) Leventis, N.; Chidambareswarapattar, C.; Mohite, D. P.; Larimore, Z. J.; Lu, H.; Sotiriou-Leventis, C. Multifunctional Porous Aramids (Aerogels) by Efficient Reaction of Carboxylic Acids and Isocyanates. *J. Mater. Chem.* **2011**, *21*, 11981–11986.

(20) Iqbal, N.; Akhter, Z.; Saeed, M. A.; Khan, M. S. Synthesis and Characterization of Some Novel Organometallic Aromatic Polyamides. *Appl. Organometal. Chem.* **2006**, *20*, 344-350.

(21) Iqbal, N.; Saeed, M. A.; Khan, M. S.; Akhter, Z. Synthesis and physicochemical studies of ferrocene-containing materials. *Appl. Organometal. Chem.* **2007**, *21*, 862-869.

(22) Rosenblum, M.; Woodward, R. B. The Structure and Chemistry of Ferrocene. *J. Am. Chem. Soc.* **1958**, *80*, 5443-5449.

(23) Leventis, N.; Sotiriou-Leventis, C.; Saeed, A. M.; Donthula, S.; Majadi Far, H.; Rewatkar, P. M.; Kaiser, H.; Robertson, J. D.; Lu, H.; Churu, G. Nanoporous Polyurea from a Triisocyanate and Boric Acid: A Paradigm of a General Reaction Pathway for Isocyanates and Mineral Acids. *Chem. Mater.* **2016**, *28*, 67-78.

(24) Blagbrough, I. S.; Mackenzie, N. E.; Ortiz, C.; Scott, A. I. The Condensation Reaction between Isocyanates and Carboxylic Acids. A Practical Synthesis of Substituted Amides and Anilides. *Tetrahedron Lett.* **1986**, *27*, 1251−1254.

(25) Sasaki, K.; Crich, D. Facile Amide Bond Formation from Carboxylic Acids and Isocyanates. *Org. Lett.* **2011**, *13*, 2256−2259.

(26) Sorenson, W. R. Reaction of an isocyanate and a carboxylic acid in dimethyl sulfoxide. *J. Org. Chem.* **1959**, *24*, 978−980.

(27) For the derivation of Eq 1 see Appendix II, Section 3 in the Supporting Information of Ref. No. 23.

(28) Leventis, N.; Chandrasekaran, N.; Sotiriou-Leventis, C.; Mumtaz, A. Smelting in the Age of Nano: Iron Aerogels. *J. Mater. Chem.* **2009**, *19*, 63-65.

(29) The Effect of Compactness on the Carbothermal Conversion of Interpenetrating Metal Oxide / Resorcinol-Formaldehyde Nanoparticle Networks to Porous Metals and Carbides. Leventis, N.; Chandrasekaran, N.; Sadekar, A. G.; Mulik, S.; Sotiriou-Leventis, C. *J. Mater. Chem.* **2010**, *20*, 7456-7471.

(30) Mahadik-Khanolkar, S.; Donthula, S.; Bang, A.; Wisner, C.; Sotiriou-Leventis, C.; Leventis, N. Polybenzoxazine Aerogels. 2. Interpenetrating Networks with Iron Oxide and the Carbothermal Synthesis of Highly Porous Monolithic Pure Iron(0) Aerogels as Energetic Materials. *Chem. Mater.* **2014**, *26*, 1318-1331.

(31) N. Leventis, N.; Donthula, S.; Mandal, C.; Ding, M. S.; Sotiriou-Leventis, C. Explosive versus Thermite Behavior in Iron(0) Aerogels Infiltrated with Perchlorates. *Chem. Mater.* **2015**, *27*, 8126-8137.

(32) Maldonado-Hódar, F. J.; Moreno-Castilla, C.; Rivera-Utrilla, J.; Hanzawa, Y.; Yamada, Y. Catalytic Graphitization of Carbon Aerogels by Transition Metals. *Langmuir* **2000**, *16*, 4367-4373.

(33) Lu, A.-H.; Li, W.-C.; Salabas, E.-L.; Spliethoff, B.; Schüth, F. Low Temperature Catalytic Pyrolysis for the Synthesis of High Surface Area, Nanostructured Graphitic Carbon. *Chem. Mater.* **2006**, *18*, 2086-2094.

(34) Sun, Z.; Yan, Z.; Yao. J.; Beitler, E.; Zhu, Y.; Tour, J. M. Growth of Graphene from Solid Carbon Sources. *Nature* **2010**, *468*, 549-552.

(35) Webb P. A.; Orr, C. Analytical Methods in Fine Particle Technology, Micromeritics Instrument Corporation, Norcross, GA, USA, **1997**, pp. 67–68.

(36) McKenzie, D. R.; Muller, D.; Pailthorpe, B. A. Compressive-stress-induced Formation of Thin-film Tetrahedral Amorphous Carbon. *Phys. Rev. Lett.* **1991**, *67*, 773-776.

(37) Pierson, H. O. Handbook of Carbon, Graphite, Diamond and Fullerenes; Noyes Publications: New Jersey, U.S.A., **1993**.

(38) Cançado, L. G.; Takai, K.; Enoki, T.; Endo, M.; Kim, Y. A.; Mizusaki, H.; Jorio, A.; Coelho, L. N.; Magalhães Paniago, R.; Pimenta, M. A. General Equation for the Determination of the Crystallite Size L_a of Nanographite by Raman Spectroscopy. *Appl. Phys. Lett.* **2006**, *88*, 163106/1−3.

(39) Fu, R.; Baumann, T. F.; Cronin, S.; Dresselhaus, G.; Dresselhaus, M. S.; Satcher, J. H., Jr. Formation of Graphitic Structures in Cobalt- and Nickel-Doped Carbon Aerogels. *Langmuir* **2005**, *21*, 2647-2651.

(40) Wang, X. X.; Tan, Z. H.; Zeng, M.; Wang, J. N. Carbon Nanocages: A New Support Material for Pt Catalyst with Remarkably High Durability. *Sci. Rep.* **2014**, *4*, 4437; DOI:10.1038/srep0443.

(41) Zhao, M.; Song, H. Catalytic Graphitization of Phenolic Resin. *J. Mater. Sci. Technol.* **2011**, *27*, 266-270.

(42) Gómez de la Fuente, J. L.; Martínez-Huerta, M. V.; Rojas, S.; Terreros, P.; Fierro, J. L. G.; Peña, M. A. Enhanced Methanol Electrooxidation Activity of PtRu Nanoparticles Supported on H_2O_2-Functionalized Carbon Black. *Carbon* **2005**, *43*, 3002-3039.

(43) Yu, C.; Sun, Y.; Fan, X.; Zhao, Z.; Qiu, J. Hierarchical Carbon-Encapsulated Iron Nanoparticles as a Magnetically Separable Adsorbent for Removing Thiophene in Liquid Fuel. *Part. Part. Syst. Charact.* **2013**, *30*, 637-644.

(44) Brankovic, S. R.; Wang, J. X.; Adzic, R. R. Metal Monolayer Deposition by Replacement of Metal Adlayers on Electrode Surfaces. *Surf. Sci.* **2001**, *474*, L173-L179.

(45) Papadimitriou, S.; Tegou, A.; Pavlidou, E.; Armyanov, S.; Valova, E.; Kokkinidis, G.; Sotiropoulos, S. Preparation and Characterisation of Platinum- and Gold-coated Copper, Iron, Cobalt and Nickel Deposits on Glassy Carbon Substrates. *Electrochim. Acta* **2008**, *53*, 6559-6567.

(46) Dass, A.; Counsil, J. A.; Gao, X.; Leventis, N. Magnetic Field Effects on the Open Circuit Potential of Ferromagnetic Electrodes in Corroding Solutions. *J. Phys. Chem. B* **2005**, *109*, 11065-11073.

(47) Selvakannan, P. R.; Sastry, M. Hollow Gold and Platinum Nanoparticles by a Transmetalation Reaction in an Organic Solution. *Chem. Commun.* **2005**, 1684-1686.

(48) Callister, W. D.; Rethwisch, D. G. Materials Science and Engineering: An Introduction, 9th Edition, Wiley, New York, N.Y., **2014**, Ch. 17. p 681.

(49) Wu, H.; Pantaleo, G.; Venezia, A.; M.; Liotta, L. F. Mesoporous Silica Based Gold Catalysts: Novel Synthesis and Application in Catalytic Oxidation of CO and Volatile Organic Compounds (VOCs). *Catalysts* **2013**, *3*, 774-793.

(50) Corma, A.; Garcia, H. Supported Gold Nanoparticles as Catalysts for Organic Reactions. *Chem. Soc. Rev.* **2008**, *37*, 2096–2126.

(51) Zhang, Y.; Cui, X.; Shi, F.; Deng, Y. Nano-Gold Catalysis in Fine Chemical Synthesis. *Chem. Rev.* **2012**, *112*, 2467–2505.

(52) Jagadeesh, R. V.; Wienhöfer, G.; Westerhaus, F. A.; Surkus, A.-E.; Pohl, M.-M.; Junge, H.; Junge, K.; Beller, M. Efficient and Highly Selective Iron-catalyzed Reduction of Nitroarenes. *Chem. Commun*. **2011**, *47*, 10972-10974.

(53) Ng, Y. H.; Ikeda, S.; Harada, T.; Morita, Y.; Matsumura, M. An Efficient and Reusable Carbon-supported Platinum Catalyst for Aerobic Oxidation of Alcohols in Water. *Chem. Commun*. **2008**, 3181-3183.

(54) Anderson, K.; Fernández, S. C.; Hardacre, C.; Marr, P. C. Preparation of Nanoparticulate Metal Catalysts in Porous Supports Using an Ionic Liquid Route; Hydrogenation and C–C Coupling. *Inorg. Chem. Commun*. **2004**, *7*, 73-76.

(55) Leventis, N.; Sadekar, A.; Chandrasekaran, N.; Sotiriou-Leventis, C. Click Synthesis of Monolithic Silicon Carbide Aerogels from Polyacrylonitrile-Crosslinked 3D Silica Networks. *Chem. Mater.* **2010**, *22*, 2790-2803.

(56) Beaucage, G. Approximations Leading to a Unified Exponential/Power-law Approach to Small-angle Scattering. *J. Appl. Crystallogr.* **1995**, *28*, 717-728.

(57) Beaucage, G. Small-angle Scattering from Polymeric Mass Fractals of Arbitrary Mass-fractal Dimension. *J. Appl. Crystallogr.* **1996**, *29*, 134-146.

III. Nanoporous Polyurea from a Triisocyanate and Boric Acid: A Paradigm of a General Reaction Pathway for Isocyanates and Mineral Acids

Nicholas Leventis,[*,1] Chariklia Sotiriou-Leventis,[*,1] Adnan M. Saeed,[1] Suraj Donthula,[1] Hojat Majedi Far,[1] Parwani M. Rewatkar,[1] Helmut Kaiser,[2] J. David Robertson,[3] Hongbing Lu,[4] Gitogo Churu[4]

1. Department of Chemistry, Missouri University of Science and Technology, Rolla, MO 65409, U.S.A.; Tel.: 573-341-4391 (NL), 573-341-4353 (CSL); E-mail: leventis@mst.edu, cslevent@mst.edu
2. University of Missouri Research Reactor, University of Missouri-Columbia, Columbia, MO 65211, U.S.A.
3. Department of Chemistry and University of Missouri Research Reactor, Columbia, MO 65211, U.S.A.
4. Department of Mechanical Engineering, The University of Texas at Dallas, Richardson, Texas 75080, U.S.A.

Published in *Chemistry of Materials* **2016**, *28*, 67–78.

TOC Graphic

ABSTRACT: Isocyanates react with carboxylic acid and yield amides. As reported herewith, however, transferring that reaction to a range of mineral acids, (anhydrous H_3BO_3, H_3PO_4, H_3PO_3, H_2SeO_3, H_6TeO_6, H_5IO_6 and H_3AuO_3) yields urea. The model system for this study was a triisocyanate, tris(4-isocyanatophenyl)methane (TIPM), reacting with boric acid in DMF at room temperature yielding nanoporous polyurea networks that were dried with supercritical fluid CO_2 to robust aerogels (referred to as BPUA-xx). BPUA-xx were structurally (CHN, solid-state ^{13}C NMR) and nanoscopically (SEM, SAXS, N_2-sorption) identical to the reaction product of the same triisocyanate (TIPM) and water (referred to as PUA-yy). Minute differences were detected in the primary particle radius (6.2-7.5 nm for BPUA-xx versus 7.0-9.0 nm for PUA-yy), the micropore size within primary particles (6.0-8.5 Å for BPUA-xx versus 8.0-10 Å for PUA-yy), and the solid-state ^{15}N NMR whereas PUA-yy showed some dangling $–NH_2$. All data together were consistent with exhaustive reaction in the BPUA-xx case, bringing polymeric strands closer together. Residual boron in BPUA-xx aerogels was quantified with prompt gamma neutron activation analysis (PGNNA). It was found very low (≤0.05 % w/w) and was shown to be primarily from B_2O_3 (by ^{11}B NMR). Thus, any mechanism for systematic incorporation of boric acid in the polymeric chain, by analogy to carboxylic acids, was ruled out. (In fact, it is shown mathematically that boron-terminated star polyurea from TIPM should contain ≥3.3% w/w B, irrespective of size.) Retrospectively, it was fortuitous that this work was conducted with aerogels, and the model system used H_3BO_3, whereas the byproduct, B_2O_3, could be removed easily from the porous network leaving behind pure polyurea. With other mineral acids results could have been misleading, because the corresponding oxides are insoluble and remain within the polymer (via skeletal density

determinations and EDS). On the positive side, the latter is a convenient method for *in situ* doping robust porous polymeric networks with oxide or pure metal nanoparticles (Au in the case of H_3AuO_3) for possible applications in catalysis.

1. INTRODUCTION

Amides, being the most stable derivatives of carbon at the +3 oxidation state, comprise the fundamental building block of life (proteins), life-sciences related products (e.g., pharmaceuticals) and high performance polymers (e.g., Nylon, Kevlar, Nomex).[1] Consequently, there is a wide range of synthetic methodology primarily involving the reaction of amines with activated carboxylic acids (anhydrides, chlorides or specialized coupling agents).[2] An older,[3] yet overlooked, synthetic route to amides that, in fact, is gaining increased attention is the reaction of isocyanates and carboxylic acids.[4,5] The process goes through a non-isolated carbamic-carboxylic anhydride adduct, is straightforward, takes place under mild conditions (room temperature) and does not require removal of side-products - the only byproduct is CO_2. We found these attributes attractive and that reaction was implemented with two trifunctional monomers, tris(4-isocyanatophenyl)methane (TIPM) and trimesic acid, demonstrating porous 3D networks of polyamide nanoparticles classified as aerogels.[6] In that vein, we became aware of a 1962 US patent claiming that reaction of toluene diisocyanate and boric acid yields a polymer with boramide (–B-NH–) linkages between repeat units.[7] At that point, noting the strength of the B-N bond, and finding further feasibility support in a 2013 patent application claiming that reaction of isocyanates with another class of mineral acids (phosphoric, phosphorous, phosphonic and their partial ester derivatives) yields products with

phosphoramide type linkages (–P-NH–),[8] we attempted the synthesis of poly(boramide) aerogels via reaction of TIPM and H_3BO_3. Instead, however, we obtained *clean* room-temperature polymerization towards the same polyurea (PUA) aerogels obtained from reaction of TIPM with water. The new reaction pattern appears to be general for isocyanates and mineral acids: besides H_3BO_3, TIPM reacted with H_3PO_4, H_3PO_3, H_2SeO_3, H_6TeO_6, H_5IO_6 and H_3AuO_3, and we always obtained the same polyurea. There was one important difference, however: side products from the reaction with H_3BO_3 could be removed easily from the porous structure, whereas side products from the reaction with the other mineral acids were insoluble rendering process characterization more difficult. Thus, focusing on the TIPM/H_3BO_3 system it was found that in analogy to the reaction of isocyanates with carboxylic acids, the reaction with H_3BO_3 proceeds via a mixed carbamic-boric anhydride adduct, which takes an intermolecular route reacting with itself. No hint could be found for any quantitative formation of –B-NH–. To our knowledge, this comprises a new route to polyurea-based materials, different from the classical routes that involve isocyanates reacting with amines or water.[9] We envision the utility of this new reaction pathway emerging from the fact that it provides the means for *in situ* doping of nanoporous polymers with nano-dispersed oxides.

2. RESULTS AND DISCUSSION

2.1. The reaction of TIPM with H_3BO_3. As summarized by Scheme 1, a 27% w/w solution of TIPM in dry ethyl acetate (courtesy of Bayer Corporation) was mixed at room temperature with an anhydrous DMF solution of the stoichiometric amount of dry boric acid. The total weight percent of TIPM+H_3BO_3 in the resulting sol is referred to as

"xx" and was varied between 4% and 16% by varying the amount of DMF. Sols gelled in reverse order to their concentration as expected from regular reaction kinetics; for example, higher concentration sols (xx=16) gelled faster (20 min) than their lower concentration counterparts (e.g., xx=4, 1 h). (Formulations and gelation times are summarized in Table S.1 of Appendix I in the Supporting Information.) Below 4%, sols did not form sturdy gels; above 16% we obtained precipitates.

Scheme 1. Parallel routes to polyurea aerogels (BPUA-xx and PUA-yy) via reaction of a triisocyanate (TIPM) with boric acid or water, respectively (Photograph, each pair: left, BPUA-xx; right, PUA-yy).

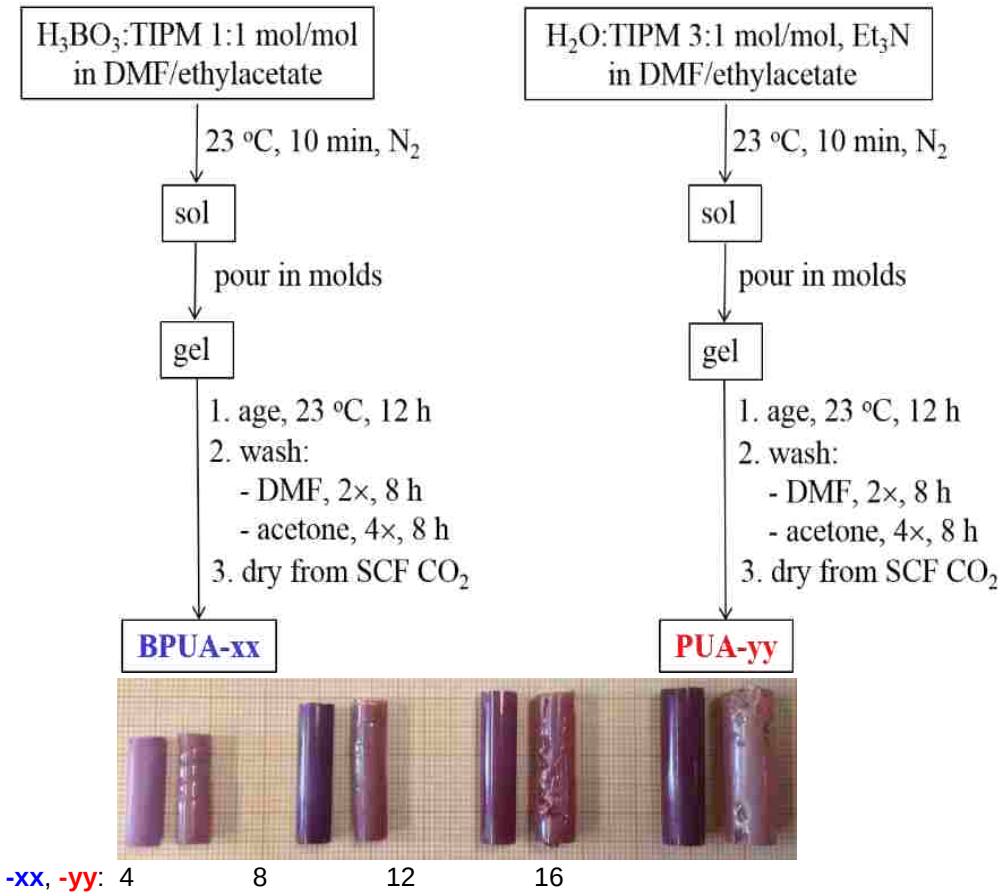

Wet-gels were aged in their molds for 12 h, washed with DMF, solvent-exchanged with acetone and finally were dried to robust, defect-free monolithic aerogels using liquid CO_2 that was removed at the end as a supercritical fluid (SCF). As it turns out, washing with DMF was essential in order to remove side products (B_2O_3 – see section 2.2 below). For further details on the drying procedure refer to the Experimental section. Sols and aerogels are abbreviated as BPUA-xx ("BPUA" for boric acid-derived polyurea), and xx was adjusted at 4, 8, 12 and 16 percent.

2.2. Evidence that shifted attention from boramides to polyurea. After heat-treatment at 200 ^oC to remove residual traces of gelation and processing solvents (DMF and acetone), BPUA-xx were found to contain: C, 71.9-73.5% w/w; H, 4.5-5.0% w/w; and N, 12.1-12.6% w/w. At first, these results were considered a reasonable match with the expected poly(boramide). For example, an idealized third-generation boramide dendrimer growing out of a boron core, and end-capped 50% with $–NH_2$ (presumably from environmental hydrolysis of unreacted terminal isocyanates) and 50% with unreacted $–B(OH)_2$ was expected to consist of (% w/w): C, 73.8; H, 5.5; N, 13.6; B, 3.1; O, 4.0. (Cumulative CHN analysis data, and detailed composition calculations concerning dendritic growth are given in Appendix II of the Supporting Information.) However, further evidence was unsettling. For instance, solid-state ^{11}B NMR showed a broad asymmetric resonance at 11.3 ppm (Appendix III, Figure S.1), superimposed with a sharp symmetric resonance at 2.2 ppm. (All ^{11}B resonances are referenced to $BF_3{\cdot}Et_2O$.) That piece of data alone was still not alerting; despite its complexity, the ^{11}B NMR spectrum of BPUA-xx was different from the ^{11}B NMR of boric acid (a single symmetric resonance at 5.1 ppm), hence, it was concluded that the latter had been involved in some sort of reaction with

TIPM as designed. However, an attempt to use solid-state ^{11}B NMR for quantitative analysis of boron by mixing known amounts of BPUA-xx and $NaBH_4$ (-41.0 ppm vs. $BF_3{\cdot}Et_2O$) produced a far lower weight percent for B (only 0.097% w/w) than what was expected for TIPM-derived poly(boramides) (around 3% w/w). At that point, owing to the uncertainties involved with quantitative solid-state ^{11}B NMR (mainly dissimilar relaxation times – see Experimental), an independent quantitative determination of boron was deemed vital. That was conducted with prompt gamma-ray neutron activation analysis (PGNAA) of ^{10}B,[10,11] using the 10 MW University of Missouri Research Reactor (MURR).[12] Results were even lower than what was found with solid-state ^{11}B NMR (B % w/w): BPUA-4, 0.031; BPUA-8, 0.028; BPUA-12, 0.028; BPUA-16, 0.050. At that point it became clear that the reaction product of TIPM and H_3BO_3 was *not* a poly(boramide), yet the invariance of the B % w/w with the sol formulation ($4 \leq xx \leq 16$) suggested that at least part of the small amount of boron present could still be part of the polymeric network.

Turning for clues to the reaction of isocyanates with carboxylic acids (Scheme 2), it is generally accepted that conversion of the carbamic-carboxylic anhydride adduct to amides involves an intramolecular rearrangement. That process may occur via either a rather strained zwitterionic intermediate (path a), or, by analogy to the reaction of isonitriles (RNC) and carboxylic acids,[13] a more favorable pathway may involve a pseudopericyclic [1,3]-acyl rearrangement to an *N*-formyl amide intermediate (path b). A third pathway, mentioned mainly in older literature,[14-16] involves disproportionation of the initial carbamic-carboxylic anhydride adduct to urea and acid anhydride, which react with one another to an amide (path c). Importantly, it is noted that for amide formation either

via unimolecular rearrangement, or via disproportionation of the carbamic-carboxylic anhydride adduct, the amount of the byproduct, CO_2, should be stoichiometrically

Scheme 2. The reaction mechanism of isocyanates with carboxylic acids.

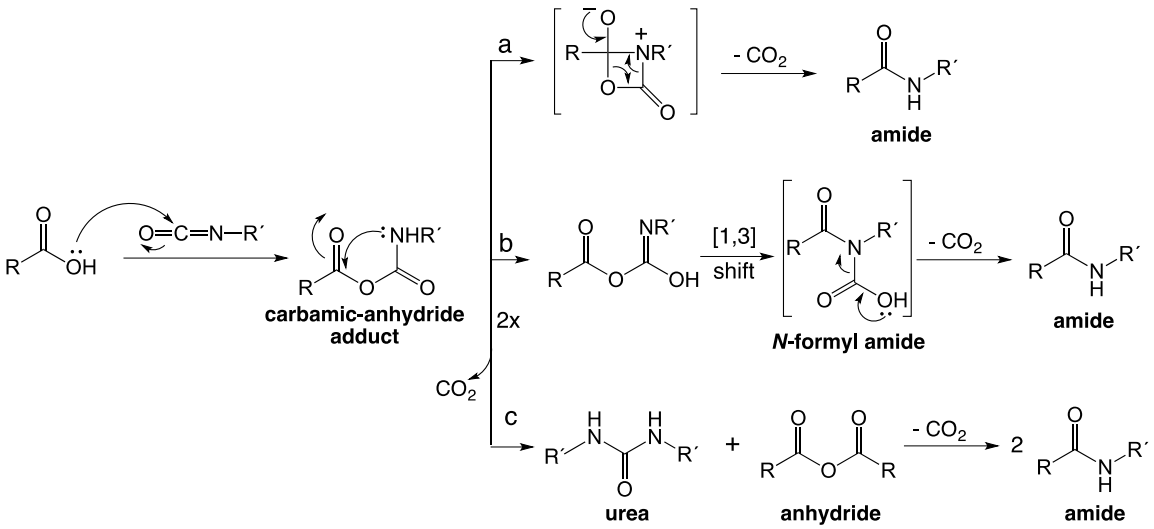

equivalent to the isocyanate groups reacting; if, however, the reaction takes the urea/anhydride route *and stops there*, the amount of CO_2 produced should be only 0.5 mol equivalents relative to the isocyanate groups reacting.[16] Based on this argument, gas evolving during gelation of the TIPM/H_3BO_3 sol was passed through an aqueous $Ca(OH)_2$ solution, and CO_2 was quantified gravimetrically at 1.5±0.15 mol equivalents relative to TIPM, i.e., at 0.5 mol equivalents relative to the isocyanate groups present. This clearly suggested formation of polyurea and anhydride, the anhydride of H_3BO_3 being B_2O_3. At that point all solvents from the solvent-exchange steps of the BPUA-xx wet-gels were

collected and evaporated to dryness (under vacuum at 120 ^{o}C for 4 days). The residue was dissolved in DMF-d_7 and was identified as B_2O_3 via ^{11}B NMR. In fact, the sharp resonance in the ^{11}B NMR spectrum of BRUA-xx at 2.2 ppm (Figure S.1) is due to a small residual amount of B_2O_3 trapped in the polymer.

2.3. Comparison of BPUA-xx with polyurea prepared independently. For positive identification, polyurea aerogels from TIPM had to be prepared independently. That was accomplished as shown in Scheme 1, namely by replacing H_3BO_3 of the BPUA-xx formulations with 3 mol equivalents of water, following a well-established triethylamine (Et_3N)-catalyzed protocol (Scheme 3).[17,18] The weight percent of reactants in the sol (TIPM+H_2O), denoted by –yy, was adjusted at the same levels as in BPUA-xx (4, 8, 12 and 16) by varying the amount of solvent (DMF). (Formulations and gelation times are summarized in Table S.2 of Appendix I in Supporting Information.) Polyurea aerogels via the water-route are referred to as PUA-yy.

Scheme 3. Et_3N-catalyzed preparation of polyurea from a triisocyanate and water.

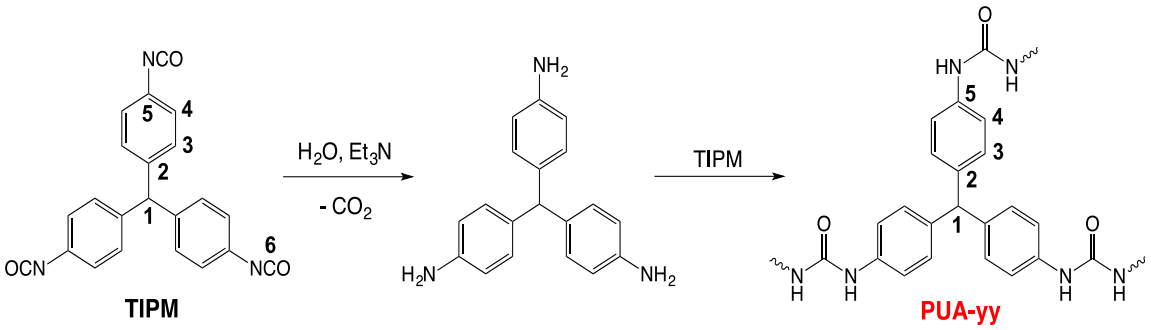

The initial goal of the following discussion is to identify similarities between BPUA-xx and PUA-yy as a means of an overall chemical identification. Gradually, the focus of our discussion shifts towards differences that illuminate subtle structural details of BPUA-xx.

PUA-yy sols gelled faster (2-5 min) than their BPUA-xx counterparts (20 min to 1 h, Tables S.1 and S.2). The only apparent difference between BPUA-xx and PUA-yy aerogels was in the integrity of the monoliths. The latter underwent severe cracking (refer to the photograph in Scheme 1) and could not be evaluated in terms of macroscopic properties that require some machining of the samples (e.g., compression testing or thermal conductivity measurements). Cracking appears at the gelation stage and is most probably caused by uneven heating during the fast exothermic reaction. The cracking problem of PUA-yy could probably be addressed by reducing the Et_3N concentration, but that was deemed beyond the purpose of this study and was not pursued.

2.3a. Comparative chemical characterization of BPUA-xx and PUA-yy. The IR spectra of BPUA-xx and PUA-yy were *identical* over the entire sol-concentration range (Figure 1). Both spectra show a broad H-bonded NH stretch at about 3380 cm^{-1}; the urea C=O stretch appears at 1660 cm^{-1}; the strongest absorption at 1506 cm^{-1} together with the absorption at 1407 cm^{-1} are assigned to the aromatic C=C stretches, while the higher-frequency shoulder at 1560 cm^{-1} is assigned to the N-H scissoring mode; the absorption at 815 cm^{-1} is assigned to the OOP C-H bending on the *p*-substituted phenyl rings of TIPM, while the sharp absorption peak at 1020 cm^{-1} is likely due to the C-N stretch.

Solid-state CPMAS ^{13}C NMR spectra of BPUA-xx and PUA-yy aerogels were again identical over the entire sol-concentration range (Figure 2A). It is also noted that both

BPUA-xx and PUA-yy have the tendency to retain some limited amounts of gelation and processing solvents (DMF and acetone). Those solvents were not confined in micropores. That was concluded from pore-volume and pore-size distributions (determined with CO_2 sorption – see section 2.3c below), which did not increase significantly (<10%) after heating aerogels at 200 ^{o}C. After removing residual solvents, CHN analyses of the two materials were, within error, identical across the entire concentration range (Figure 3 and Table S.3 in Supporting Information).

Finally, the solid-state ^{15}N NMR spectra of BPUA-xx and PUA-yy (Figure 2B) show a common resonance at 106 ppm, which is assigned to aromatic polyurea. The spectrum of PUA-yy shows an additional broad, low-intensity resonance at 53 ppm, which is assigned to dangling terminal amines (via comparison with the ^{15}N NMR spectrum of commercial 4,4´-methylenedianiline, included in Figure 2B).

2.3b. General material properties of BPUA-xx and PUA-yy. Notwithstanding cracking of PUA-yy monoliths, in all other aspects both BPUA-xx and PUA-yy systems behaved quite similarly during processing. For instance, both classes of aerogels shrunk rather significantly relative to their molds (30-60% in linear dimensions). Nevertheless, BPUA-xx consistently shrunk more than PUA-yy, particularly at higher sol concentrations (e.g., 47% and 41% for xx = 12 and 16, respectively, versus 41% and 31% for yy = 12 and 16, respectively). Shrinkage and other material properties are summarized in Table 1. At lower xx values (4 and 8), most shrinkage was allocated relatively evenly between the solvent exchange and drying steps, while at higher xx values (12 and 16), most shrinkage took place during drying. Therefore, it was concluded that shrinkage was probably related to a reorganization of the nanostructure as has been proposed recently to explain

deformation of certain polydicylopentadiene aerogels.[19] Higher shrinkages at the high xx end of BPUA-xx was reflected to a somewhat higher bulk density (ρ_b) than that of the corresponding PUA-yy aerogels. With the skeletal densities (ρ_s) of the two materials about equal (1.25 g cm^{-3}) and invariant of the sol concentration, higher ρ_b (due to shrinkage) in BPUA-16 translates into a lower porosity, Π, than in PUA-16 (Table 1).

2.3c. Nano- and micro-scopic comparison of BPUA-xx and PUA-yy. Both BPUA-xx and PUA-yy consist of random assemblies of similar-size nanoparticles (generally <20 nm in diameter, irrespective of the sol-concentration, Figure 4). A quantitative evaluation of the framework with small angle x-ray scattering (SAXS – Appendix IV in Supporting Information) agrees with SEM showing that the elementary building blocks of both nanostructures are primary particles (3.5-8.6 nm in radius, R_1) that assemble into densely-packed secondary particles (surface fractal dimensions, D_s, in the 2-3 range). Guided by SAXS for particle size, secondary particles are indicated with dashed circles in Figure 4. The porous structure in the 1.7-300 nm range, i.e., mainly around primary and within secondary particles, was evaluated with N_2-sorption porosimetry at 77 K, while free volume porosity within primary particles was probed with CO_2 adsorption at 0 ^oC.

All N_2-sorption isotherms and BJH pore-size distributions are shown in Appendix V of the Supporting Information; data are summarized in Table 1. The N_2-sorption isotherms of both materials show comparable maximum volumes of N_2 adsorbed with hysteresis loops at all formulations indicative of mesoporosity at all densities. Nevertheless, (see Table 1), the total specific pore volumes calculated via $V_{Total}=(1/\rho_b)-(1/\rho_s)$ were always larger than the cumulative volume of pores in the 1.7-300 nm range, $V_{1.7\text{-}300nm}$, calculated via the BJH desorption method. In fact, although saturation plateaus are well-pronounced and broad at

higher values of xx or yy (≥8), the $V_{Total}/V_{1.7\text{-}300nm}$ ratio remained approximately the same throughout both the xx and the yy ranges, meaning that percentage-wise, larger pores (>300 nm) persist at all densities.

Turning to average pore sizes (Table 1), we note an excellent internal consistency in both the BPUA-xx and the PUA-yy series of samples: average pore sizes calculated via the $4V/\sigma$ method, using V either as equal to V_{Total}, or taken from the total volume of N_2 absorbed along the isotherm, agree extremely well to one another. On the other hand, however, the pore sizes of BPUA-4 and BPUA-8 calculated via the $4V/\sigma$ method (30 nm and 14 nm, respectively) were lower than pore sizes obtained from the BJH pore-size distribution (42 nm and 34 nm, respectively), while in BPUA-12 and BPUA-16 as well as in all PUA-yy the two sets of data (i.e., via $4V/\sigma$ and via the BJH pore size distribution) generally agreed well with one another. Therefore, the disparity in pore sizes observed for BPUA-4 and BPUA-8 by the $4V/\sigma$ method versus the BJH pore size distribution is considered real (because of the two independent methods of calculating V), and is attributed to the higher BET surface areas, σ, of BPUA-4 and BPUA-8 than those of BPUA-12, BPUA-16 and all PUA-yy (Table 1). (In fact, for xx and yy ≥12 all σ values of both series of samples, BPUA-xx and PUA-yy, converge.) In turn, higher surface areas translate into smaller particle radii, r (via $r=3/(\rho_s\sigma)$ - see Table 1); thus, r of BPUA-xx were found in the 6.2-7.5 nm range, versus 7.0-9.0 nm for PUA-yy. Those r values (calculated from N_2-sorption data) agree well with the primary particle radii, R_1, (via SAXS - included in Table 1), and thereby are also considered reliable.

Finally, although the N_2 sorption isotherms do not show any significant uptake of N_2 at low partial pressures (P/Po<0.1), all BPUA-xx and PUA-yy adsorb CO_2 (Figure 5 -top row) that signifies the presence of free-volume microporosity,[20,21] which is related to the way

polymer molecules are stacked together. Pore size distributions within the micropore range were calculated with the density functional theory (DFT),[22] and were found to be in the 6.0-8.5 Å range for all BPUA-xx, versus in the 8.0-10 Å range for the PUA-yy (Figure 5 – bottom row). Interestingly, it is noted that somewhat smaller primary particles in BPUA-xx (6.2-7.5 nm) than in PUA-yy (7.0-9.0 nm) were accompanied by smaller micropores within said particles. Reasonably, both of those observations could be attributed to a contraction mechanism, which must be related to a common chemical factor that tends to bring polymeric strands of BPUA-xx closer together. This is discussed in the next paragraph below.

Overall, BPUA-xx and PUA-yy consist of a practically identical polymer that forms primary particles, which grow and phase-separate as soon as they reach an apparently common solubility limit. Therefore, although BPUA-xx and PUA-yy polymers *necessarily* grow through different mechanistic processes, the intermediate-stages of polymer growth must have only minute differences as far as formation (and solubility) of primary particles is concerned. Hence, boron must be expelled early from the polymer chain – as the chain grows so-to-speak. Further, as suggested by gas absorption studies, those differences should affect the compactness of the polymeric strands, ultimately reducing both the micropore and primary particle size. Reasonably, then, those differences should be localized at the perimeter of the growing polymeric branches. Indeed, at least one such difference survives to the final product and is reflected upon the ^{15}N NMR spectra of the two materials - note the small amount of dangling $–NH_2$ groups in PUA-yy (Figure 2B).

Table 1. Material characterization data of BPUA-xx and PUA-yy.

Sample I.D. **xx** or **yy**	linear shrinkage (%) [a,b]	bulk density, ρ_b (g cm^{-3}) [a]	skeletal density, ρ_s (g cm^{-3}) [c]	Π (% v/v) [d]	specific pore volume (cm^3 g^{-1})			BET surface area, σ (m^2 g^{-1})	average pore diameter (nm)		particle radius (nm)		
					V_{Total} [e]	$V_{1.7\text{-}300\_nm}$ [f]	$V_{<7.97\_Å}$ [g]		$4V/\sigma$ [h] method	BJH [i] method	r [j]	R_1 [k]	R_2 [l]
BPUA-xx													
4	52.34 ± 0.61	0.283 ± 0.008	1.254 ± 0.001	77	2.74	1.97	0.047	367	30[29]	42(21)	6.5	8.6	31
8	50.13 ± 0.20	0.467 ± 0.004	1.249 ± 0.002	62	1.34	1.27	0.033	398	14[14]	34(16)	6.2	6.5	14
12	47.19 ± 0.03	0.545 ± 0.004	1.242 ± 0.002	56	1.03	0.74	0.036	340	12[12]	14(10)	7.1	6.7	13
16	41.54 ± 0.14	0.576 ± 0.005	1.251 ± 0.002	54	0.93	0.78	0.035	317	12[12]	17(9)	7.5	7.1	15
PUA-yy													
4	54.10 ± 1.00	0.393 ± 0.033	1.231 ± 0.005	68	1.73	1.35	0.024	278	25[20]	27(17)	9.0	3.5	14.5
8	48.96 ± 0.40	0.600 ± 0.018	1.252 ± 0.001	52	0.86	0.68	0.039	291	11[10]	11(14)	8.0	6.4	13.1
12	40.45 ± 0.48	0.557 ± 0.027	1.253 ± 0.001	54	0.99	0.76	0.029	327	12[9.3]	10(13)	7.5	5.7	12.3
16	30.76 ± 0.41	0.428 ± 0.003	1.233 ± 0.003	65	1.52	1.02	0.034	353	17[12]	16(12)	7.0	6.4	12.3

[a] Average of 3 samples. [b] Linear shrinkage=100×(mold diameter – sample diameter)/(mold diameter). [c] Single sample, average of 50 measurements. [d] Porosity, Π=100×(ρ_s–ρ_b)/ρ_s. [e] Calculated via V_{Total}=(1/ρ_b)-(1/ρ_s). [f] Cumulative volume of pores between 1.7 nm and 300 nm from N_2-sorption data and the BJH desorption method. [g] Total pore volume of pores less than 7.97 Å from CO_2 sorption data at 273 K using the single-point absorption method at P/Po=0.03. [h] For the first number, V was calculated via V_{Total} =(1/ρ_b)-(1/ρ_s); for the number in [brackets], V was set equal to the maximum volume of N_2 absorbed along the isotherm as P/Po→1.0. [i] From the BJH plots: first numbers are peak maxima; numbers in (parentheses) are full widths at half maxima. [j] Particle radius, r=3/(ρ_s×σ); [k] R_1: radius of primary particles from SAXS; [l] R_2: radius of secondary particles from SAXS.

Finally, a growth mechanism should also be consistent with the fact that irrespective of sol concentration (and consequently vastly different rates of gelation), no monomers seem to persist long enough – even in the case of the slow gelling BPUA-xx – to accumulate on the primary network; that implies fast reaction among the monomers and is supported by the fact that radii by the N_2-sorption method, r, are practically equal (typically within 2 nm or less – see Table 1) to the SAXS primary particle radii, R_1, over the entire density range for both BPUA-xx and PUA-yy.

2.4. Proposed polymerization mechanism. Evidence about the polymerization mechanism was obtained with ^{13}C and ^{1}H NMR in DMF-d_7 during gelation of the slowest gelling sol, BPUA-4 (Figure 6). In both cases, at the gel point (about 60 min), only extremely weak signals were detectable, meaning that polymerization was practically complete and all material had phase-separated quantitatively. In ^{13}C NMR (Figure 6A), immediately upon adding the stoichiometric amount of H_3BO_3 into the TIPM solution (i.e., at t=0 min), both C_5 at 142.5 ppm and C_2 at 132.7 ppm decreased in intensity and obtained satellites at 143.2 ppm and at 133.0/132.4 ppm, respectively. At the same time, a new weak resonance showed up at the terminal position of C_5 in BPUA-xx (120 ppm). Also, both C_3 (131.5 ppm) and C_4 (126.0 ppm) decreased in size and a new absorption showed up at the position of C_4 in the polymer (130 ppm). Two very weak resonances showed up at 154 and 152 ppm, which are attributed to urea and urethane $\underline{C}$=O, respectively.[23] Later (20 min), all TIPM resonances had disappeared and $\underline{C}$=O resonances of any kind were no longer visible. Even later (45 min), only resonances in the terminal $C_{2\text{-}4}$ region of BPUA-xx were visible, and their intensity continued to decrease with time (60 min).

Next, turning to ^{1}H NMR for complementary information (Figure 6B), upon adding the stoichiometric amount of TIPM in a solution of H_3BO_3 in DMF-d_7, we observed: (a) an immediate (*t*=0 min) disappearance of the broad –BO<u>H</u> resonance at 8.42 ppm; (b) the simultaneous appearance of three new resonances in the 9.2-9.3 region, corresponding to carbamic (urethane) protons (–N<u>H</u>(CO)O–),[24] and, (c) a weak broad signal at around 8.9 ppm from urea (–N<u>H</u>(CO)N<u>H</u>–).[24,25] As time went by (5-20 min), the chemical shifts in the urethane region remained constant; however, the relative peak intensities varied and the overall signal intensity decreased; on the other hand, in the urea region, we noted the appearance of many more peaks whose number kept on increasing, while the whole cluster became more intense and moved progressively upfield. Beyond approximately 40 min, the urethane resonances had all but disappeared, while the urea multiplet was still relatively intense. Even later (>45 min), the urea multiplet had also decreased in size and was barely visible at the gel point (~60 min). Interestingly, at the later stages of the gelation process (>30 min), a weak broad –BO<u>H</u> resonance had reappeared.

Both ^{13}C and ^{1}H NMR data point towards a fast reaction between –N=C=O and H_3BO_3, and are consistent with upon-mixing formation of a carbamic-boric anhydride adduct, $[–NH(CO)O]_3B$, in analogy to the reaction of isocyanates with carboxylic acids (Scheme 2). Considering together that: (a) only 3-4 of such carbamic-boric anhydride adduct resonances with invariant chemical shifts and decreasing intensity were ever observed, while (b) there is a plethora of urea resonances, which moved progressively upfield and their intensity increased at the expense of the $[–N\underline{H}(CO)O]_3B$ resonances, suggests that: (a) the carbamic-boric anhydride adduct reacts towards urea, and (b) urea groups find themselves in a progressively changing environment (in this case on a growing

polymer), while urethanes are more or less confined around the initial product(s) of the TIPM/H_3BO_3 reaction. Those data and inferences are consolidated into Scheme 4.

The carbamic-boric anhydride adduct is formed via a typical nucleophilic attack on the isocyanate carbon as shown in Scheme 4. That process could be acid-catalyzed, but that is rather improbable in view of the low acidity of H_3BO_3 (pK_a=9.14). Subsequently, there are two bimolecular possibilities open for the carbamic-boric anhydride adduct, both of which lead to a common intermediate, referred to as Int-1. The first one (Route 1) involves condensation of two carbamic-boric anhydride adducts followed by expulsion of –BOH, while the second one (Route 2) involves reaction of the carbamic-boric anhydride adduct with free isocyanate. Given the fast disappearance of both the ^{13}C NMR signature of the isocyanate and the ^{1}H NMR signature of boric acid, Route 2 may be occurring only at the very early stages of the reaction. Intermediate Int-1 is prone to nucleophilic attack and reacts with –BOH either from yet unreacted boric acid, or from such –BOH groups just created together with Int-1 by the said expulsion process. The latter realization has one very important consequence: because –BOH groups are created together with Int-1, they do not need to diffuse away in order to find and react with the latter; that leads to exhaustive (quantitative) reaction of the two towards urea and B_2O_3 as shown by the final stages of Scheme 4. Presumably then, with the passage of time the segmental mobility of the growing polymer decreases, leading to a transient accumulation of –BOH groups, whose signature becomes visible in the ^{1}H NMR as the sol approaches the gel point.

There is *absolutely no indication* that boron becomes part of the network in any systematic fashion, as for example by rearrangement of Int-1 to yield boron-based end-caps, by analogy to path ‘a’ of Scheme 2 (see section 3 of Appendix II). In fact, if that were

the case, it has been shown analytically that as the polymer grows in a star-like fashion, the limit of the total mass of the caps at the tips of the branches, over the total mass of the polymer is *finite* and is given by eq 1, whereas *cap*, *TIPM*, *CO* and *H* are the

$$\lim_{n\to\infty} \frac{\sum cap}{\sum polymer\_inside + \sum cap} = \frac{cap}{(TIPM - 2CO + 3H) + cap} \quad (1)$$

molecular weights of the corresponding molecules (TIPM) or groups (cap, CO and H - for the full mathematical proof refer to section 3 of Appendix II).[26] If the cap is a boron atom connected via B-N bonds to three ureas (see Appendix II, section 3), eq 1 sets a lower limit for the percent weight of boron in BPUA-xx at 3.33 %, which was *never* the case. The amount of boron was always <0.050% w/w for all xx. Thus, we conclude safely that boron is involved neither in the polymer chain, nor in any systematic terminal group of the growing branches. Hence, the extremely low weight percent of boron found by PGNNA is attributed mainly to trapped B_2O_3 (prominent in the ^{11}B NMR spectrum of BPUA-xx – see Figure S.1), and also to boron on dangling intermediate Int-1 that remains unreacted, as well as to dangling –BOH groups that, at the last stages of the polymerization process, whereas the polymer relaxes by its internal stresses, may not be able to reach nearby Int-1 to react with. However, in order to provide perspective, data of Figure S.1 show clearly that the latter two are minor possibilities.

In summary, the carbamic-boric anhydride adduct reacts with itself exhaustively and creates urea bridges across TIPM monomer units. Within primary particles, the rigidity of TIPM is prone to generating micropores. (Refer, for example, to strategies towards intrinsically microporous polymers via rigid monomers.[27-29]) It is suggested then that

Scheme 4. Proposed mechanism for the formation of urea from an isocyanate and H_3BO_3.

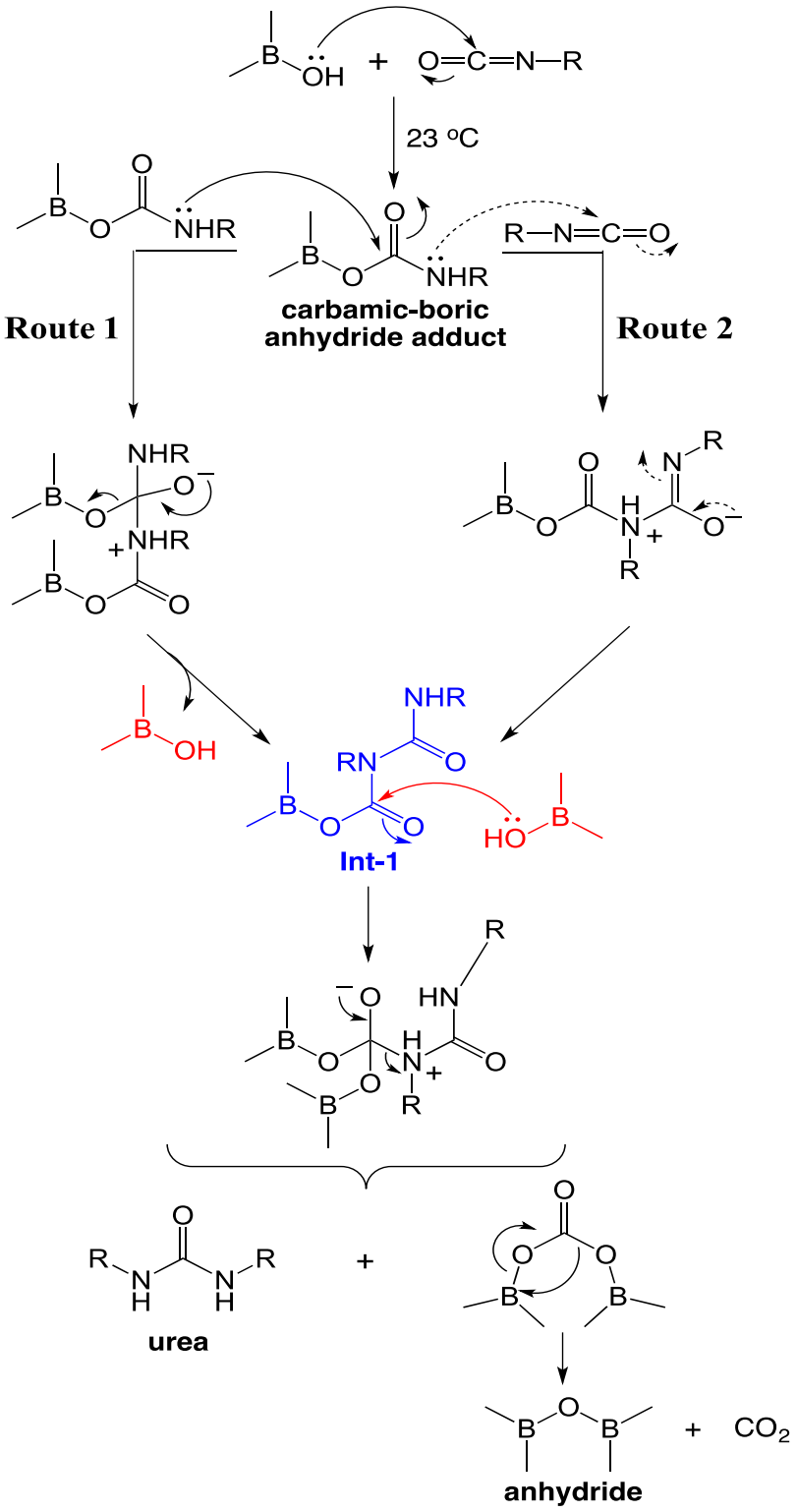

micropores are smaller in BPUA-xx than in PUA-yy, because of the exhaustive nature of the reaction of Int-1 with –BOH maximizing the urea linkages that in turn pull the polymeric strands closer together. Of course, there is nothing to restrict urea-bridging only within the mass of the developing polymer itself (i.e., within the primary particles); the same process should also take place, and perhaps owing to higher segmental mobility even more so, at the interparticle contacts. In turn, no dangling functionality and exhaustive interparticle bridging in BPUA-xx should be reflected upon macroscopic properties that depend precisely on the extent of interparticle bridging. Those include the macroscopic elastic modulus of BPUA-xx, *E*, (Appendix VI of the Supporting Information) and the thermal conductivity through the solid framework, λ_s (Appendix VII of the Supporting Information). *E* was measured using quasi-static compression. Because of cracking, PUA-yy samples could not be measured, thus the evaluation of BPUA-xx was made by comparison with other polymer aerogels. For that comparison (see Table S.6), we have matched (density-wise) the four BPUA-xx aerogels (for xx=4, 8, 12 and 16) to several other polymeric aerogels ranging from isocyanate-derived polyurethanes,[30] fibrous polyureas prepared in acetone,[17] polyamides,[6] and polyimides,[31,32] to ROMP-derived polynorbornene,[33,34] as well as several polymer-crosslinked silica[35,36] and vanadia aerogels.[37] With the exception of certain silica aerogels, whereas the modulus is dominated by the glassy silica network, BPUA-xx are much stiffer materials than all other polymeric aerogels, particularly at the density level of BPUA-16. In terms of solid thermal conductivity, that was modeled by $\lambda_s=C(\rho_b)^a$ (Figure S.5), in which the pre-exponential factor *C* depends on the extent of interparticle contacts. Table S.8 compares the *C* value of BPUA-xx (0.142 W m^{-1} K^{-1}) with that of other polymeric aerogels. The *C* value of BPUA-

xx aerogels is higher than the *C* values of most aerogels with similar particle sizes, and practically equal to those of aerogels from the most multifunctional monomers, that is of aerogels with the most chances for interparticle bonding. The latter include polyurethane aerogels derived from TIPM and phloroglucinol (0.14 W m^{-1} K^{-1})[30] and polydicyclopentadiene aerogels (0.13 W m^{-1} K^{-1}).[19] (Other high *C*-value aerogels from Table S.8 consist of much larger particles (some micron-size) and do not comprise a fair comparison; those include polyurethane aerogels from TIPM and bisphenol A,[30] polyurea aerogels made in CH_3CN,[18] and polynorbornene aerogels.[19]) Overall, both the elastic modulus and the *C*-value of BPUA-xx point to efficient coupling of its skeletal nanoparticles, as expected from exhaustive covalent bonding of trifunctional monomers.

2.5. Evaluation of the reaction of TIPM with other mineral acids. In addition to H_3BO_3, TIMP was put to react with several other mineral acids with which it shares a common inert solvent – typically DMF or DMSO. Those acids included phosphoric, phosphorous, selenous, telluric, orthoperiodic and auric. All sols were formulated at xx=16, except with H_3AuO_3 that was formulated at about xx=5, because of solubility reasons. Figure 7 shows the resulting aerogel monoliths. The reaction of TIPM with phosphoric acid (pK_{a1}=2.15) and phosphorous acid (pK_{a1}=1.3) was exceptionally fast and exothermic, but was controlled by cooling the sol in a dry-ice/acetone bath. Despite cooling, reaction with selenous acid (pK_{a1}=2.46) was so swift that the sol gelled before CO_2 had time to escape, resulting into large, visible voids in the monoliths (refer to Figure 7A). Reaction with sulfuric acid (pK_{a1}=-3) was even more violent, in fact explosive even at -78 ^oC, thus, the product of that reaction was neither isolated nor pursued. Gelations with telluric acid (pK_{a1}=7.68) and orthoperiodic acid (pK_{a1}=3.29) were room-temperature

processes, just like gelation with H_3BO_3 (pK_a=9.14). Gelation with auric acid was carried out at 90 ^oC. Synthetic details, exact formulations (Table S.9) and materials characterization data (Table S.10) are given in Appendix VIII of the Supporting Information.

Solid-state CPMAS ^{13}C NMR spectra (Figure S.6) of all aerogels shown in Figure 7 were identical to those of BPUA-xx, thereby confirming that the polymeric component of all of those materials was polyurea. Based on solid-state ^{15}N NMR (Figure S.7), several of the mineral acids considered here may not share the same mechanism for polyurea formation with boric acid. For instance, it is noted that polyurea aerogels made with several of those acids gave resonances in the 50-60 ppm region, assigned to aromatic $–NH_2$ (refer to Figure 2B). In that regard, the most prominent case was the H_3PO_4 system. No resonances in the aromatic $–NH_2$ region were observed with acids whose singly or doubly anhydrous versions do not exist or cannot be formed easily (H_3BO_3, H_2SeO_3, H_3PO_3, H_3AuO_3). That piece of information, considered together with the fact that reaction with acids having pK_{a1}<3.0 was extremely fast and exothermic points to additional mechanistic possibilities to those shown in Scheme 4, ranging from acid-catalyzed (general and/or specific) reaction with water been in equilibrium with the acid (possible candidates are reactions with H_3PO_4, $Te(OH)_6$ and H_5IO_6), to self-catalyzed reaction with the acid (possible candidates are reactions with H_3PO_3 and H_2SeO_3). It is emphasized though that those are preliminary inferences, not conclusions, and should be treated as the point of departure for further investigation.

Finally, it is noted that skeletal densities of the products with all mineral acids considered in this section were higher (in the 1.40-2.35 g cm^{-3} range – the highest with

H_3AuO_3) than those of BPUA-xx and PUA-yy (1.25 g cm^{-3}). In analogy to the reaction of TIPM with H_3BO_3, side products are expected to be the corresponding oxides, which may not be soluble in the wash solvents and thus remained trapped in the network, increasing the apparent skeletal densities of the polyurea aerogels. In most cases, that was confirmed with EDS analysis showing the presence of significant amounts of the central elements of the mineral acids (Figure S.8). In that regard, the case of aerogels made with H_3AuO_3 (Figure 7B(a)) was particularly interesting as XRD analysis showed the presence of elemental Au(0) (Figure S.9). Although by SEM (Figure 7B(b)) those aerogels were microscopically similar to BPUA-xx (Figure 4), burning off polyurea (at 600 ^oC/air) left a Au sponge whose shape (Figure 7B(c)), albeit some sintering, did prove that Au was embedded evenly throughout that microstructure over the entire monolith. In turn, TEM (Figure 7C) showed that Au(0) consisted of nanocrystals whose size approximately matched the average crystallite size calculated from the width of the (111) reflection in XRD using the Scherrer equation (18 nm). The significance of those findings is that polyurea synthesis by the route of this report allows direct *in situ* doping with inorganic oxide or Au(0) nanoparticles – in the case of H_3AuO_3. Considering that TIPM-derived polyurea aerogels can be converted pyrolytically to carbon aerogels (56% w/w carbonization yield),[17] those materials demonstrate a convenient route for the synthesis of porous carbon-supported nano-sized catalysts.

3. CONCLUSION

An aromatic triisocyanate (TIPM) reacts with mineral acids under mild conditions and yields a clean reaction to polyurea, which is chemically identical, except in minute

details at the nanoscopic level, to polyurea obtained via reaction of TIPM with water. That reaction pathway is distinctly different from the conventional path followed by isocyanates (including TIPM) with carboxylic acids to amides. Fortuitously, our work focused on open-pore polymers (aerogels) and the first system we selected to work with, TIPM+H_3BO_3, yields a soluble byproduct, B_2O_3, that could be removed easily leaving behind pure polyurea. Had we first chosen to work with other mineral acids or dense polymers (as in scarce previous reports[7,8]), results could have been misleading as the corresponding oxides are insoluble and remain within the polymer rendering correct chemical characterization difficult. In retrospect, however, in addition to the fundamental significance of the new H_3BO_3-mediated pathway for the synthesis of symmetric ureas from inexpensive isocyanates, use of other mineral acids may prove convenient for preparing porous polymers and porous pyrolytic carbons doped *in situ* with oxide or metallic nanoparticles (case of Au), which in turn may find applications in catalysis.

4. EXPERIMENTAL

4.1. Materials. All reagents and solvents were used as received, unless noted otherwise. High-purity (99.6%) boric acid was purchased from Acros Organics and was re-dried at 120 ^oC under vacuum for 24 h. For other mineral acids refer to Appendix VIII in Supporting Information. 4,4´-Methylenedianiline was also purchased from Acros Organics and was recrystallized from water before use as a structure reference in ^{15}N NMR (see Figure 2B). Anhydrous *N*,*N*-dimethylformamide (DMF) and triethylamine (Et_3N) were purchased from Sigma Aldrich Chemical Co. or Alfa Aesar. Triethylamine was distilled before use. Tris(4-isocyanatophenyl)methane (TIPM) was donated by Bayer Corp.

USA as a 27% w/w solution in dry ethyl acetate under the trade name Desmodur RE. Deuterated solvents: nitromethane-d_3 (99 atom % D) was purchased from Sigma Aldrich Chemical Co. and *N,N´*-dimethylformamide-d_7 (99.5% atom % D) containing tetramethylsilane (0.05% v/v) was purchased from Cambridge Isotope Laboratories, Inc. Siphon grade CO_2 was purchased from Ozark Gas, Rolla, MO.

4.2. Preparation of polyurea aerogels.

4.2a. Synthesis of BPUA-xx. In a typical procedure, H_3BO_3 (0.61 g, 0.01 mol) was dissolved in anhydrous DMF and the solution was added to 13.6 g of Desmodur RE (containing 3.67 g, 0.01 mol of TIPM). The resulting sol was stirred at room temperature under N_2 for 15 min, and was poured into molds (Wheaton 4 mL Polypropylene Omni-Vials 1.04 cm in inner diameter, Fisher part No. 225402), which were then sealed and left for gelation. The total weight percent concentration of monomers (TIPM+H_3BO_3) in the sol was varied by varying the amount of solvent (DMF), and is denoted by extension -xx in the sample names. Gelation of BPUA-xx for $4 \leq xx \leq 16$ took place at room temperature. BPUA-2 sols gelled at 90 ºC. All formulations and gelation times are summarized in Table S.1 of the Supporting Information. Gels were aged for 12 h at room temperature in their molds, removed from the molds, washed with DMF (2×) and acetone (4×, using 4× the volume of the gel for each wash), and were dried in an autoclave with liquid CO_2 extracted as a supercritical fluid (SCF). For details about the synthesis of polyurea aerogels using other mineral acids see Appendix VIII in Supporting Information.

4.2b. Synthesis of PUA-yy. In a typical procedure, Et_3N was added at 0.3% w/w relative to the mass of a solution of 13.6 g of Desmodur RE (containing 3.67 g, 0.01 mol of TIPM), H_2O (0.54 g, 0.03 mol) and anhydrous DMF. The resulting sol was stirred at

room temperature under N_2 for 10 min, and was poured into molds (Wheaton 4 mL Polypropylene Omni-Vials 1.04 cm in inner diameter, Fisher part No. 225402), which were sealed and left for gelation at room temperature. The total weight percent concentration of monomers (TIPM+H_2O) in the sol was varied by varying the amount of solvent (DMF), and is denoted by extension -yy in the sample names. All formulations and gelation times are summarized in Table S.2 of the Supporting Information. Gels were aged for 12 h at room temperature in their molds. Subsequently, gels were removed from the molds, washed with DMF (2×), acetone (4×, using 4× the volume of the gel for each wash), and were dried in an autoclave with liquid CO_2 extracted as a SCF.

4.3. Methods. Drying of wet-gels with supercritical fluid (SCF) CO_2 was carried out in an autoclave (SPIDRY Jumbo Supercritical Point Dryer, SPI Supplies, Inc. West Chester, PA, or in a Spe-edSFE system, Applied Separations, Allentown, PA). Samples were loaded into the autoclave and acetone was added until all samples were submerged. The pressure vessel was closed and liquid CO_2 was allowed in at room temperature. Acetone was drained out from the pressure vessel as it was being displaced by liquid CO_2. Liquid CO_2 was allowed in the vessel and subsequently drained out several more times until all acetone was extracted out of the pores of the samples. The criterion for this was that vented-out CO_2 started forming dry ice. Subsequently, the temperature of the autoclave was raised to 40 ^oC and SCF CO_2 was vented off as a gas.

Physical Characterization: Bulk densities (ρ_b) were calculated from the weight and the physical dimensions of the samples. Skeletal densities (ρ_s) were determined with helium pycnometry using a Micromeritics AccuPyc II 1340 instrument.

Chemical Characterization: Elemental analysis (CHN) was conducted with a PerkinElmer elemental analyzer (Model 2400 CHN). Prompt-gamma neutron activation analysis (PGNNA) of boron was conducted at the University of Missouri Research Reactor using the 478 keV gamma ray from the $^{10}B(n,\alpha)^{7}Li$ reaction.[10] The system was calibrated using a series of dry boric acid in graphite standards. The boron content in the standards bracketed the mass of boron observed in the samples and ranged from 28 to 283 micrograms of boron. The response function (counts per second per microbram of boron) was linear over this mass range. The slope of the calibration curve (r^2=0.997) was 0.133±0.005.

Infrared (IR) spectra were obtained in KBr pellets, using a Nicolet-FTIR Model 750 spectrometer.

Liquid ^{1}H and ^{13}C-NMR spectra were recorded in deuterated solvents as indicated in the individual spectra using a 400 MHz Varian Unity Inova NMR instrument (100 MHz carbon frequency). Solid-state ^{13}C-NMR spectra were obtained with samples ground into fine powders on a Bruker Avance III 400 MHz spectrometer with a carbon frequency of 100 MHz, using magic-angle spinning (at 5 kHz) with broadband proton suppression and the CPMAS TOSS pulse sequence for spin sideband suppression. Solid-state ^{13}C NMR spectra were referenced externally to glycine (carbonyl carbon at 176.03 ppm). Solid-state ^{15}N-NMR spectra were also obtained on the same Bruker Avance III 400 MHz Spectrometer with a 40.557 MHz nitrogen frequency using either a 4mm or a 7mm Bruker MAS probe with broadband proton suppression and magic angle spinning at 14 kHz and 5 kHz, respectively. The relaxation delay was set at 5 s in all experiments. The number of scans varied from around 8,000 with the 7 mm probe, and from about 15,000 up to 65,000

with the 4 mm probe. Solid-state ^{11}B-NMR MAS NMR with high power ^{1}H decoupling was obtained at room temperature on a Bruker Avance DRX300WB spectrometer equipped with a 7mm CPMAS probe and ZrO_2 rotor. The spin rate was 7 kHz. Bruker supplied "hpdec" pulse sequence was used with a 14-s pre-acquisition delay, 1.4-μs (15 degree) excitation pulse, and 35-ms acquisition delay. The total experiment time was 15 h. $NaBH_4$ was used as both chemical shift (-41 ppm) and quantitation standard. A long ^{11}B T_1 relaxation time is expected for $NaBH_4$ due to the boron's tetrahedral environment. With Bruker-supplied "t1ir1d" sequence the T_1 of $NaBH_4$ was determined to be 14 s. Subsequently, a 14 s repetition delay was used for the experiment, because the T_1 for BPUA-xx was expected to be much shorter due to a lack of tetrahedral or octahedral symmetry. Data were processed using 20 Hz line-broadening before Fourier transformation and baseline correction. At the maximum spin rate of this NMR spectrometer (7 kHz), the BPUA-xx signal shows a sharper centreband (2.2 ppm) and a broader second-order quadrupole distortion (11.3 ppm).[38] A pair of spinning sideband was observed for $NaBH_4$ but no spinning sideband was observed for BPUA-xx. The integration values of all the observed signals were used to obtain the estimated boron content of the sample.

Structural Characterization: BET surface areas and pore size distributions for pore sizes in the 1.7-300 nm range were determined with N_2-sorption porosimetry at 77 K using a Micromeritics ASAP 2020 surface area and porosity analyzer. Micropore analysis was conducted with CO_2-sorption up to 760 torr (relative pressure of 0.03) at 0^{o} C using a Micromeritics Tristar II 3020 version 3.02.

Scanning electron microscopy (SEM) was conducted with Au-coated samples on a Hitachi Model S-4700 field-emission microscope. In the case of the product from the

reaction of TIPM and H_3AuO_3, transmission Electron Microscopy (TEM) was conducted with an FEI Tecnai F20 instrument employing a Schottky field emission filament operating at a 200 kV accelerating voltage. The aerogel sample was finely ground by hand in a mortar with a pestle and was mixed with isopropanol in 5 mL glass vials. The vials were ultrasonicated for 20 min to disperse the small particles in the solvent. After removing from the ultrasonic bath and just before particle settling was complete, a single drop was taken and placed on a 200 mesh copper grid bearing a lacey Formvar/carbon film. Grid was allowed to air-dry over night before microscopy. At least 6 different areas/particles were examined to ensure that the results were uniform over the entire sample. Images were processed with Image J, freely available software that allows measurements of the spacing between the lattice fringes.

Powder X-ray diffraction (XRD) was conducted with a PANalytical X'Pert Pro multipurpose diffractometer (MPD) with Cu Kα radiation (λ = 1.54 Å) and a proportional counter detector equipped with a flat graphite monochromator. Phase composition was estimated via Rietveld refinement of the x-ray diffraction patterns utilizing RIQAS software (Materials Data, Inc., version 4.0.0.26). Structural information for crystalline phases was obtained from the ICSD database version 2.01. Crystallite size measurements were obtained utilizing the Scherrer equation and the FWHM of lowest angle peak. A Gaussian correction for instrumental broadening was applied utilizing NIST SRM 660a LaB_6 to determine the instrumental broadening.

The fundamental building blocks of all aerogels were probed with small angle X-ray scattering (SAXS), using ~2 mm thick disks cut with a diamond saw. SAXS was conducted with the same PANalytical X'Pert Pro multipurpose diffractometer (MPD)

configured for SAXS, using a 1/32° SAXS slit, a 1/16° antiscatter slit on the incident beam side, and a 0.1 mm antiscatter slit together with a Ni 0.125 mm automatic beam attenuator on the diffracted beam side. Samples were placed in circular holders between thin Mylar sheets, and scattering intensities were measured by running 2θ scans from −0.1° to 5° with a point detector in the transmission geometry. All scattering data were reported in arbitrary units as a function of *Q*, the momentum transferred during a scattering event. Data analysis was conducted using the Beaucage Unified Model[39,40] applied with the Irena SAS tool for modeling and analysis of small angle scattering within the Igor Pro application (a commercial scientific graphing, image processing, and data analysis software from Wave Metrics, Portland, OR).[41]

Mechanical Characterization: Mechanical testing under quasi-static compression was conducted with an Instron 4469 universal testing machine using a 50 kN load cell, following the testing procedures and specimen length (2.0 cm) to diameter (1.0 cm) ratio specified in ASTM D1621-04a (Standard Test Method for Compressive Properties of Rigid Cellular Plastics).

Thermal Characterization: Thermogravimetric analysis (TGA) was conducted under N_2 or air with a TA Instruments Model TGA Q50 thermogravimetric analyzer, using a heating rate of 5 °C min^{-1}. Thermal conductivity, λ, was calculated at 23 °C via $\lambda = R \times c_p \times \rho_b$. Thermal diffusivity, *R*, was determined at room temperature and atmospheric pressure with a Netzsch NanoFlash Model LFA 447 flash diffusivity instrument using disk samples ~1 cm in diameter, 2-3 mm thick. Solid thermal conductivity, λ_s, was calculated via $\lambda_s = \lambda - \lambda_g$, whereas the gaseous thermal conductivity, λ_g, was calculated using the Knudsen equation (see Appendix VII in Supporting Information). Specific heat capacities,

c_p, at 23 °C were measured with powders (5 − 10 mg) using a TA Instruments Differential Scanning Calorimeter Model Q2000 calibrated against a sapphire standard and run from 0 to 30 °C at 0.5 °C min^{-1} in the modulated T4P mode. Raw c_p data were multiplied by a factor of 1.10 based on measuring the heat capacities of rutile, graphite, and corundum and comparing with the literature values.

FIGURES

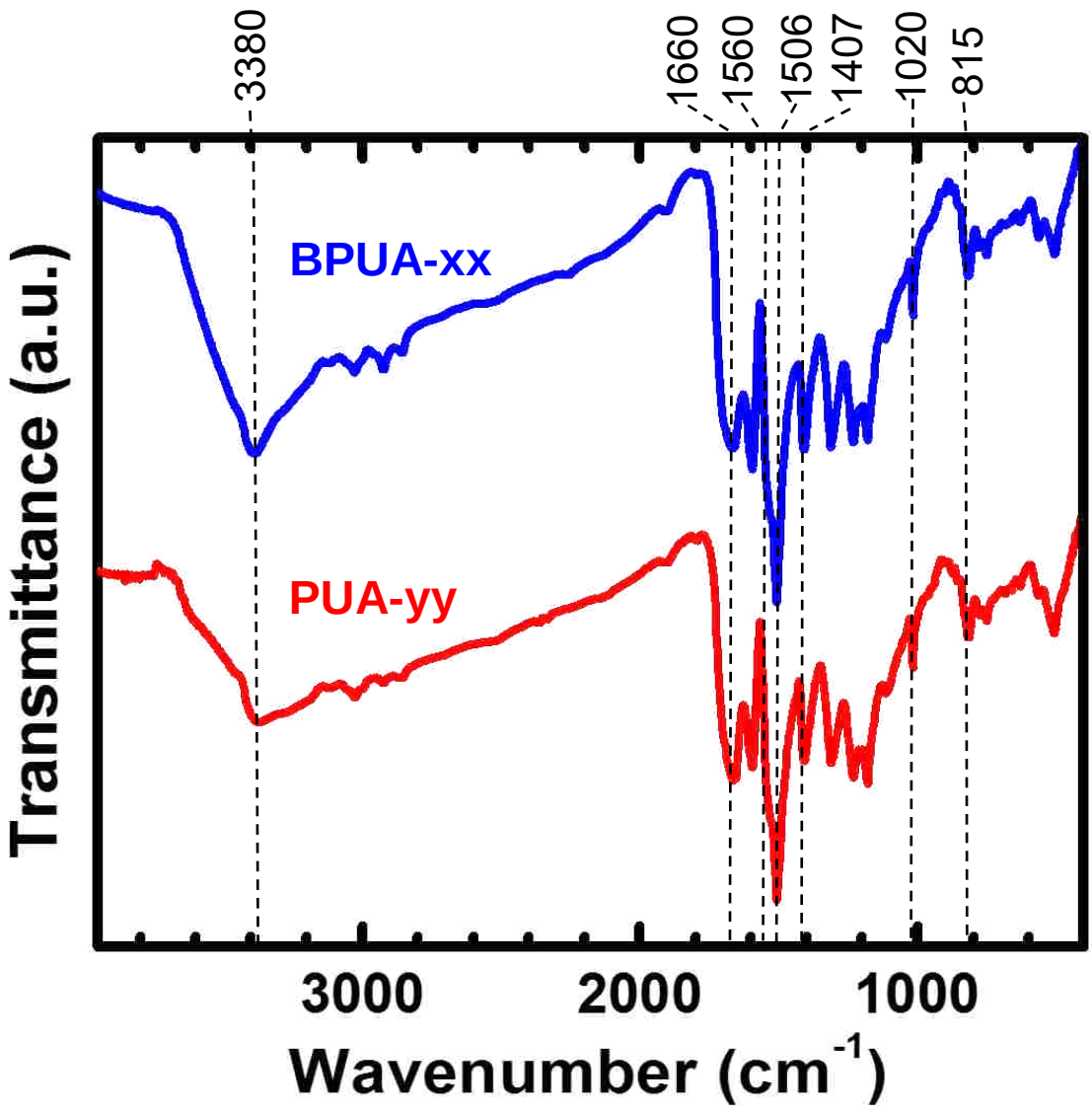

Figure 1. Infrared spectra of representative BPUA-xx and PUA-yy aerogels. Absorptions marked with dashed lines are discussed in the text.

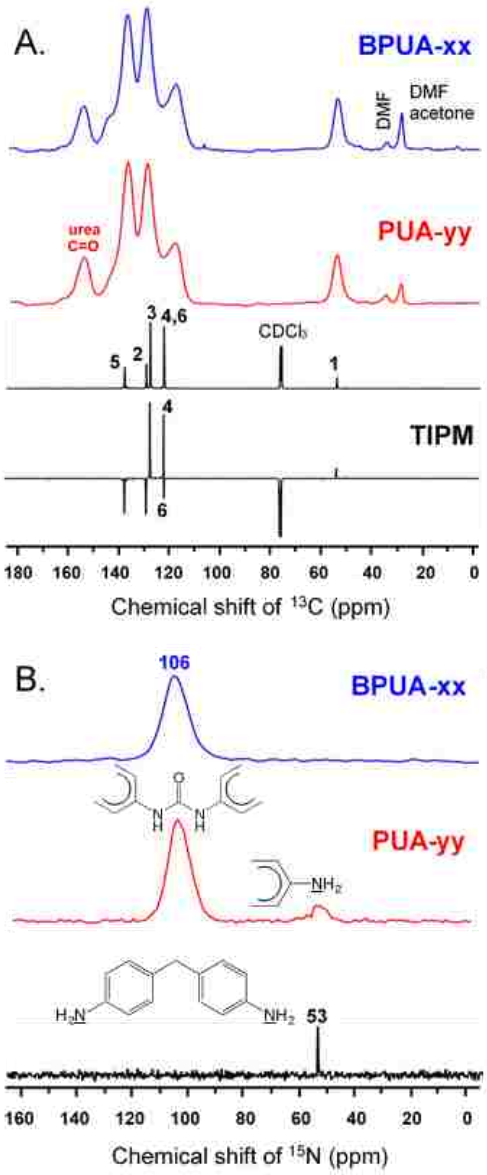

Figure 2. A Solid-state ^{13}C CPMAS NMR spectra of BPUA-xx and PUA-yy as indicated. The broad-band ^{1}H decoupled liquid-phase ^{13}C NMR spectrum of the monomer (TIPM) in the APT and the normal mode (bottom, and second from bottom, respectively) is included for comparison. Those spectra were obtained using 10 mg of chromium(III) trisacetylacetonate and 30 s relaxation delay. Peak assignment (refer to Scheme 3) was based on integrated intensities and the APT spectrum. (Residual gelation (DMF) and processing (acetone) solvents are marked explicitly.) B. Top two spectra: Solid-state CPMAS ^{15}N NMR spectra of BPUA-xx and PUA-yy as indicated. Structural features shown within the frame are discussed in the text. Bottom spectrum: Liquid-phase ^{15}N NMR spectrum of methylene dianiline in CD_3NO_2**.**

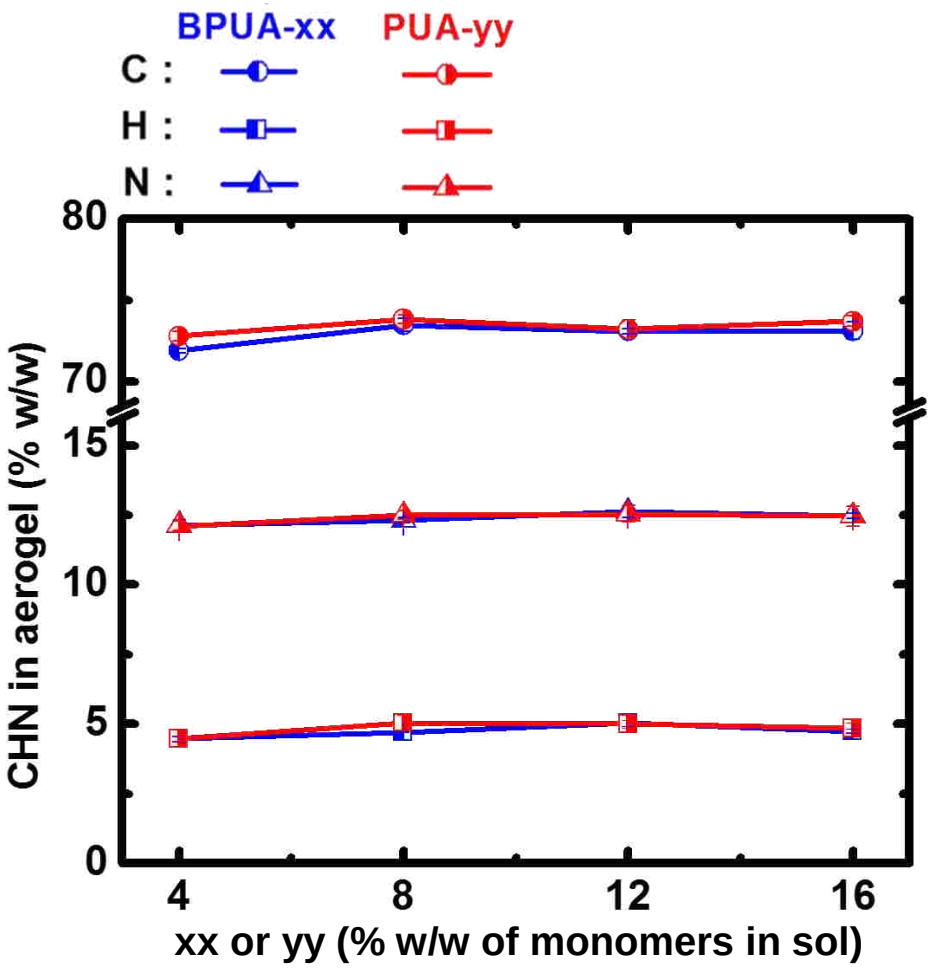

Figure 3. CHN elemental analysis data of BPUA-xx and PUA-yy treated at 200 ^{o}C to drive off residual gelation and processing solvents (refer to Figure 2).

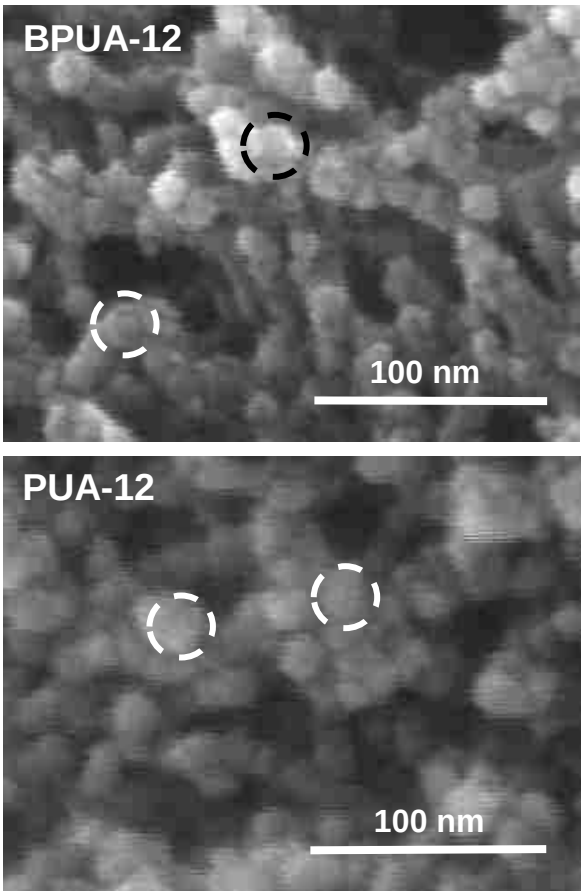

Figure 4. High magnification (x250K) SEM of representative BPUA-xx and PUA-yy as shown.

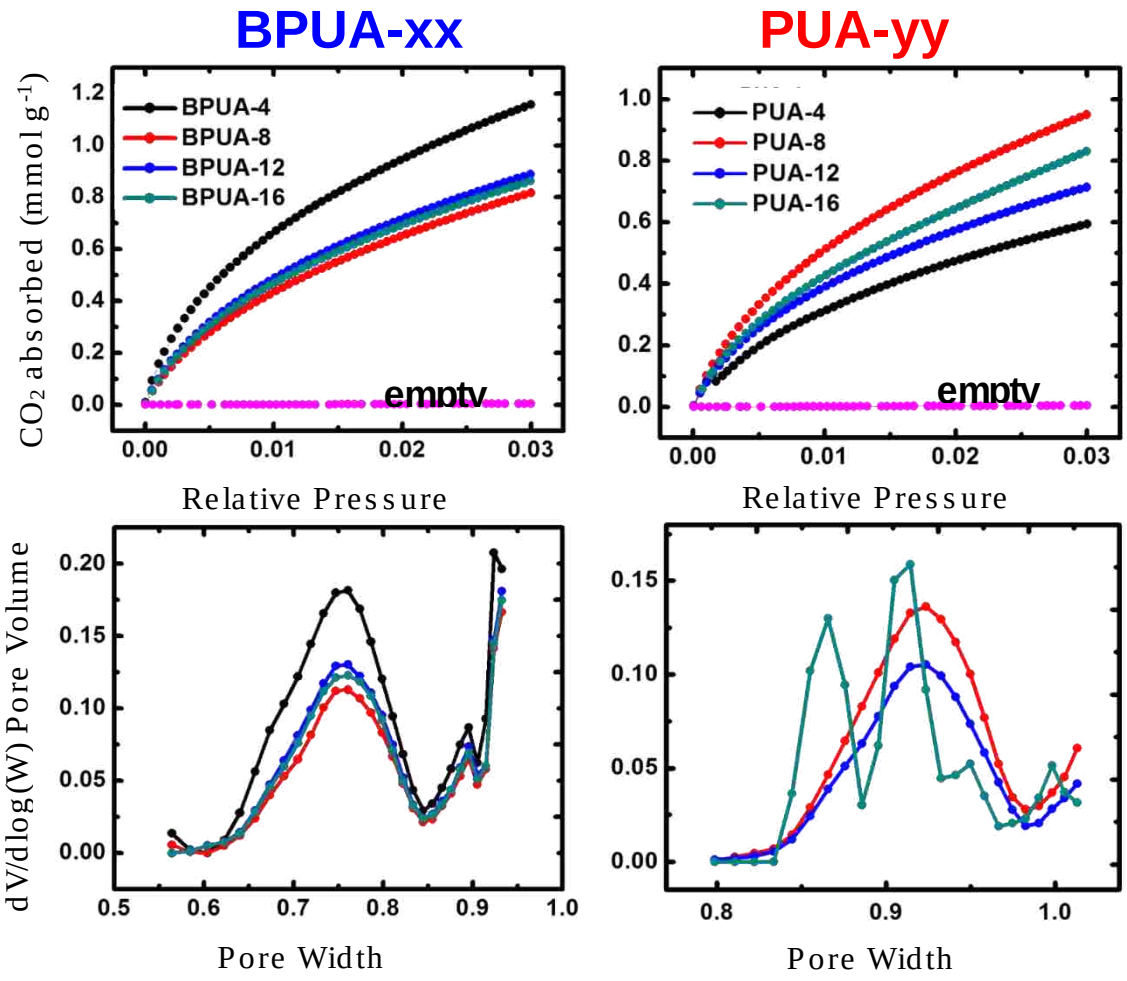

Figure 5. Top: CO_2 sorption isotherms at 273 K of BPUA-xx and PUA-yy as indicated. Bottom: Micropore size distributions using the DFT method.

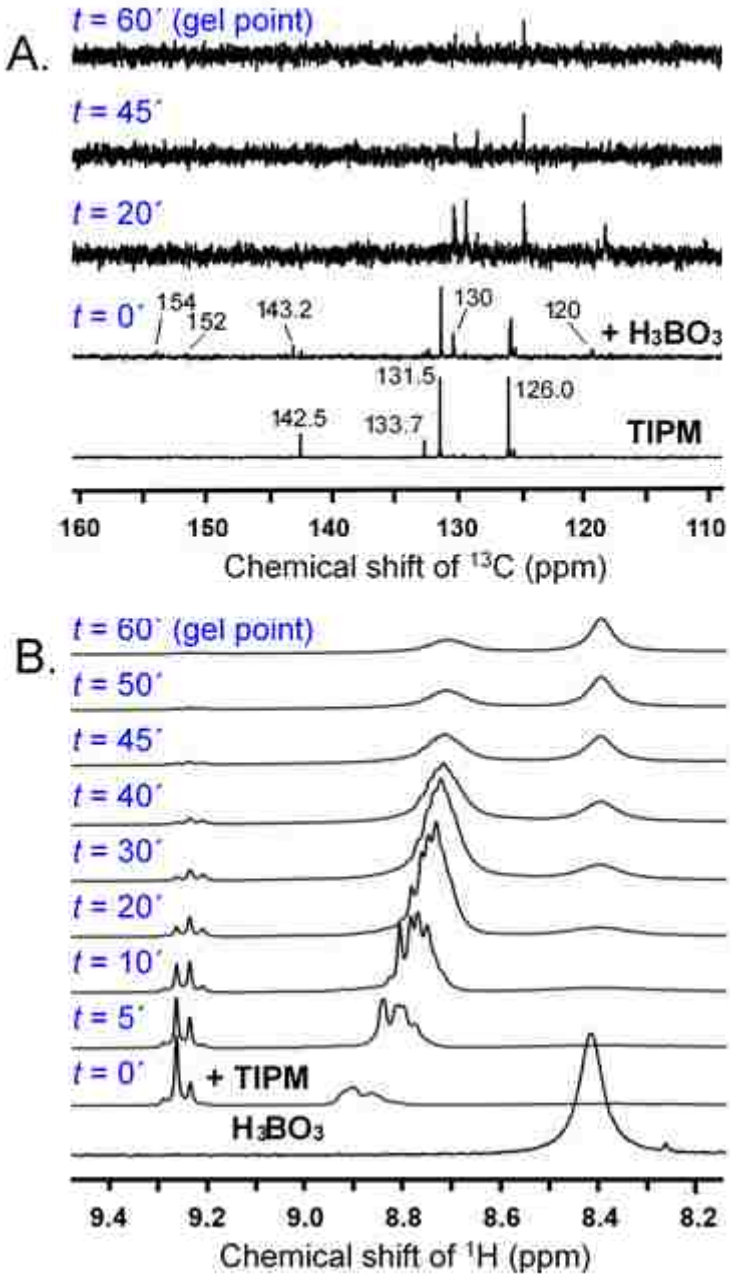

Figure 6. A. Liquid-phase ^{13}C NMR of a BPUA-4 sol in DMF-d_7 during gelation. B. ^{1}H NMR of a similar sol during gelation.

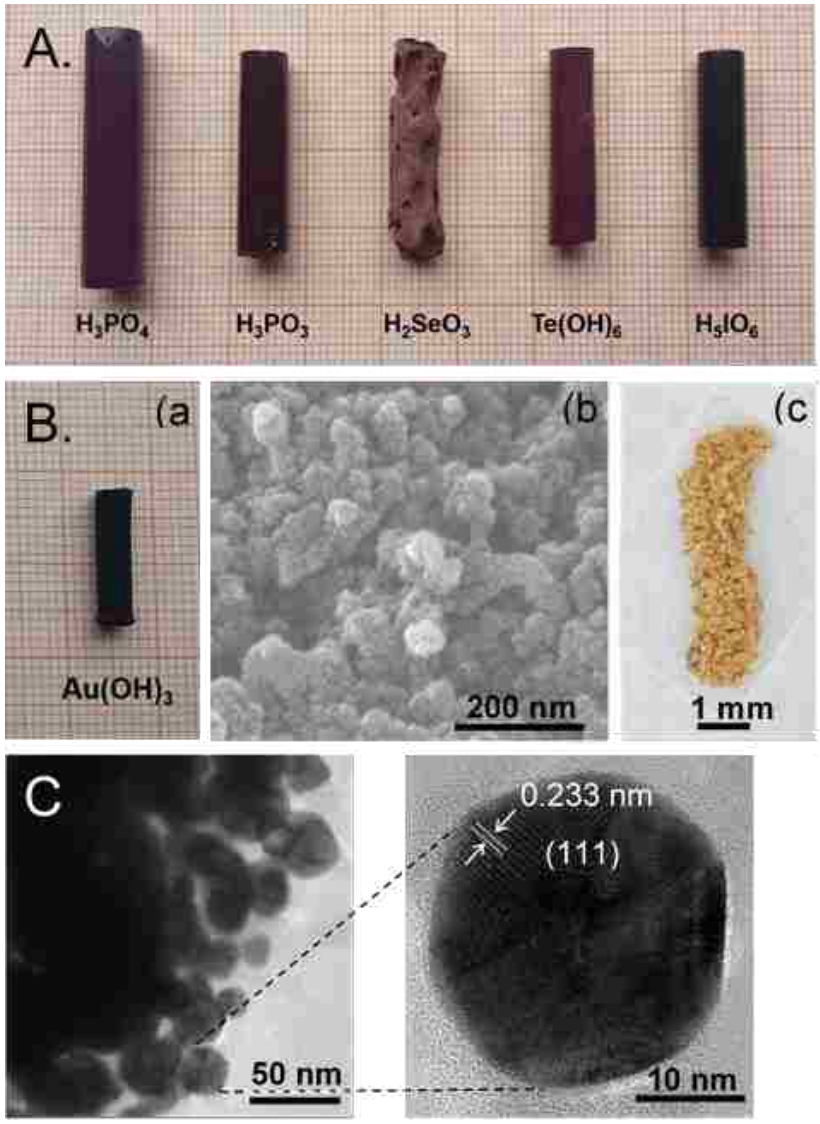

Figure 7. A. Polyurea aerogel monoliths prepared from tris(4-isocyanatophenyl)methane (TIPM) and the acids indicated. B. (a) A polyurea aerogel monolith prepared in DMF from tris(4-isocyanatophenyl)methane (TIPM) and H_3AuO_3. (b) Its microstructure. (c) Residue after pyrolysis at 600 ^oC/air underwent partial sintering and significant shrinkage, proves though that Au was evenly distributed throughout the monolith. C. TEM of B (a). d-spacing close to the literature value (0.2355 nm) for (111) of fcc Au(0).[42]

SUPPORTING INFORMATION

Appendix I: formulations for all aerogels. Appendix II: CHN elemental analysis data and molecular formulas derived via star-like growth from triisocyanate cores. Appendix III: solid-state ^{11}B MAS NMR of BPUA-xx. Appendix IV: small-angle X-ray scattering (SAXS) data. Appendix V: N_2-sorption data. Appendix VI: mechanical characterization data. Appendix VII: thermal conductivity data. Appendix VIII: reaction of TIPM with various mineral acids. This material is available free of charge via the Internet at http://pubs.acs.org.

Figure S.6. Solid-state CPMAS ^{13}C NMR of the aerogels obtained from the gelation of TIPM with various mineral acids, as indicated. For peak assignment refer to Scheme 3 of the main article. Peaks marked with ** are residual gelation and processing solvents.

Figure S.7. Solid-state CPMAS ^{15}N NMR of the aerogels obtained from the gelation of TIPM with various mineral acids as indicated. Note the prominence of NH_2 groups bonded to aromatic rings (peaks in the 50 ppm region) in several of those products and the complete absence from others. For relevant discussion see Section 2.4 of the main article.

Figure S.8. EDS of powdered polyurea aerogel monoliths synthesized from TIPM and the mineral acids indicated. (Note: For accuracy, the percent compositions indicated must be corrected for the amount of H contained in the samples.)

Figure S.9. XRD of as-prepared polyurea aerogels from TIPM and auric acid. (Line spectrum for fcc Au(0). Scherrer equation analysis of the (111) reflection gives the average crystallite size at 18 nm.)

Appendix I. Formulations of all BPUA-xx and PUA-yy aerogels

Table S.1. Formulations and gelation times of BPUA-xx aerogels.

Sample	Boric acid				Desmodur RE [b]		TIPM			DMF		gelation time
	mass (g)	volume [a] (mL)	mmol	C (M)	volume (mL)	mass (g)	mass [c] (g)	mmol	C (M)	mass (g)	volume (mL)	23 °C
BPUA-4	0.062	0.043	1.00	0.089	1.33	1.359	0.367	1.00	0.089	9.30	9.79	~ 1 h
BPUA-8	0.062	0.043	1.00	0.181	1.33	1.359	0.367	1.00	0.181	3.94	4.14	45 min
BPUA-12	0.062	0.043	1.00	0.275	1.33	1.359	0.367	1.00	0.275	2.15	2.26	35 min
BPUA-16	0.062	0.043	1.00	0.371	1.33	1.359	0.367	1.00	0.371	1.26	1.32	20 min

[a] The volume of boric acid was calculated based on its density: 1.43 g cm^{-3}. [b] The mass of commercial Desmodur RE was calculated based on its density as measured in our lab (1.022 g cm^{-3}). [c] The mass of TIPM in Desmodur RE was calculated based on the 27% w/w concentration given by the supplier.

Table S.2. Formulations and gelation times of PUA-yy aerogels.

Sample	Desmodur RE [a]		TIPM			H_2O [c]			DMF		Et_3N [d]			gelation time
	volume (mL)	mass (g)	mass [b] (g)	mmol	C (M)	volume (mL)	mass (g)	mmol	mass (g)	volume (mL)	volume (mL)	mass (g)	w/w (%)	23°C
PUA-4	1.33	1.359	0.367	1.00	0.103	0.05	0.05	3.0	7.81	8.22	0.041	0.030	0.3	~ 5 min
PUA-8	1.33	1.359	0.367	1.00	0.208	0.05	0.05	3.0	3.22	3.39	0.022	0.016	0.3	~ 4 min
PUA-12	1.33	1.359	0.367	1.00	0.314	0.05	0.05	3.0	1.69	1.78	0.016	0.012	0.3	~ 3 min
PUA-16	1.33	1.359	0.367	1.00	0.422	0.05	0.05	3.0	0.93	0.98	0.009	0.007	0.3	~ 2 min

[a] The mass of commercial Desmodur RE was calculated based its density as measured in our lab (1.022 g cm^{-3}). [b] The mass of TIPM in Desmodur RE was calculated based on the 27% w/w concentration given by the supplier. [d] The amount of the catalyst (Et_3N) was varied so that its concentration remained constant at 0.3% w/w relative to the sol (Desmodur RE+H_2O+DMF). [c] The amount of H_2O was set at a stoichiometric amount to the NCO groups of TIPM, namely at 3 mol equivalents relative to TIPM**.**

Appendix II. CHN elemental analysis data and molecular formulas derived via star-like growth from trifunctional cores

1. CHN Elemental Analysis Data

Table S.3. Elemental analysis data for all BPUA-xx and PUA-yy, including the standards run before and after the samples.[a]

Sample ID	Theoretical (% w/w)			Experimental (% w/w)		
	C	H	N	C	H	N
Standards before running BPUA-xx and PUA-yy						
Acetanilide	71.09	6.71	10.36	71.28 ± 0.09	6.75 ± 0.05	10.06 ± 0.05
Benzophenone	85.69	5.53	0	85.78 ± 0.08	5.64 ± 0.04	0.00 ± 0.00
Stilbene	93.29	6.71	0	93.42 ± 0.12	6.32 ± 0.09	0.00 ± 0.00
Urea	20.00	6.71	46.65	20.17 ± 0.13	6.92 ± 0.09	46.79 ± 0.12
Glycine	32.00	6.71	18.66	32.32 ± 0.11	6.97 ± 0.05	18.37 ± 0.08
BPUA-xx [b]						
4 [c]	-	-	-	70.70 ± 0.23	4.99 ± 0.09	11.97 ± 0.03
4 - 200 ºC heated	-	-	-	71.90 ± 0.12	4.46 ± 0.11	12.13 ± 0.19
8 [c]	-	-	-	68.55 ± 0.45	4.62 ± 0.15	11.55 ± 0.11
8 – 200 ºC heated	-	-	-	73.47 ± 0.39	4.70 ± 0.02	12.30 ± 0.09
12 [c]	-	-	-	68.55 ± 0.28	4.62 ± 0.13	11.55 ± 0.14
12 – 200 ºC heated	-	-	-	73.08 ± 0.18	5.03 ± 0.10	12.61 ± 0.21
16 [c]	-	-	-	71.79 ± 0.31	5.19 ± 0.14	12.15 ± 0.22
16 – 200 ºC heated	-	-	-	73.13 ± 0.52	4.73 ± 0.07	12.46 ± 0.10
PUA-yy [b]						
4 [c]	-	-	-	70.93 ± 0.16	4.95 ± 0.12	12.06 ± 0.13
4 - 200 ºC heated	-	-	-	72.80 ± 0.28	4.46 ± 0.07	12.10 ± 0.17
8 [c]	-	-	-	72.03 ± 0.31	4.42 ± 0.21	12.53 ± 0.21
8 - 200 ºC heated	-	-	-	73.82 ± 0.27	5.03 ± 0.28	12.49 ± 0.16
12 [c]	-	-	-	72.81 ± 0.29	5.19 ± 0.13	12.83 ± 0.32
12 - 200 ºC heated	-	-	-	73.31 ± 0.54	4.99 ± 0.14	12.53 ± 0.29
16 [c]	-	-	-	71.72 ± 0.61	4.85 ± 0.22	12.50 ± 0.37
16 - 200 ºC heated	-	-	-	73.70 ± 0.32	4.85 ± 0.17	12.46 ± 0.35
Standards after running BPUA-xx and PUA-yy						
Acetanilide	71.09	6.71	10.36	71.37	6.40	10.27
Benzophenone	85.69	5.53	0	86.01	4.82	0.06
Stilbene	93.29	6.71	0	93.36	6.57	0.12
Urea	20.00	6.71	46.65	20.48	6.67	46.84
Glycine	32.00	6.71	18.66	32.27	6.35	18.63

[a] All samples were run in triplicates, except the standards after analysis of BPUA-xx and PUA-yy. Those standards were run once. [b] CHN data analysis of samples after heating heated at 200 deg are provided immediately below the samples as prepared. [c] Samples as prepared.

2. Molecular Formulas of Star Polymers from Two Trifunctional Units

Trifunctional Units (e.g., monomers): B and T

G_n: generation along isotropic symmetric star growth

Scheme S.1. Core and 1st Generation (G_1) Dendritic Growth From Two Trifunctional Monomers.

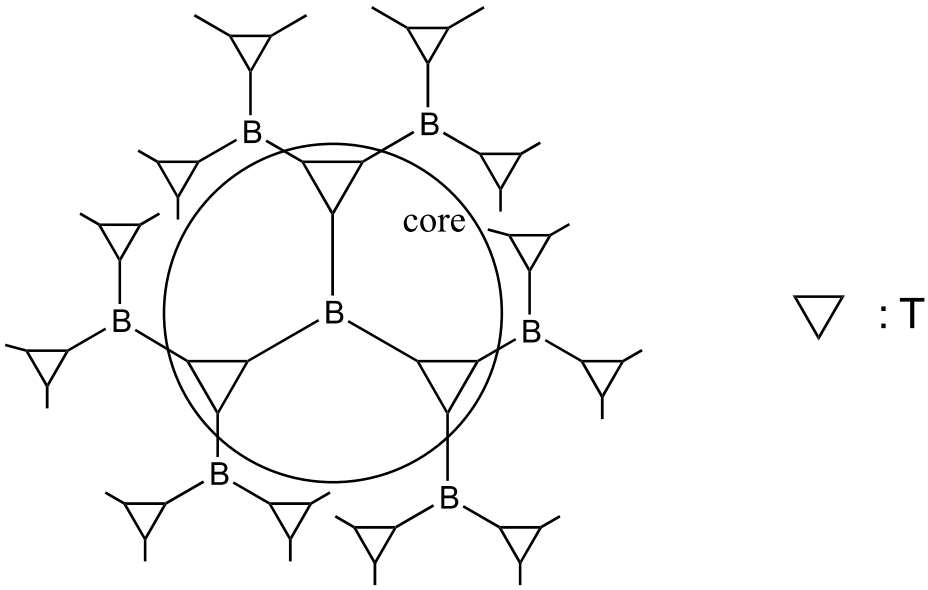

Molecular Formulas **without end-caps**: Sum of (B+2T) terms:

G_0 (the core) = B+3T

G_1 = G_0 + [6B + 12T] = G_0 + 6 (B+2T) 6

G_2 = G_1 + [24B + 48T] = G_1 + 24 (B+2T) 30

G_3 = G_2 + [96B + 192T] = G_2 + 96 (B+2T) 126

G_4 = G_3 + [384B + 768T] = G_3 + 384 (B+2T) 510

Coefficients of (B+2T) from G_1 to G_n

for G_1: $6 = 6 \times 1 = 6 \times 4^0$

for G_2: $24 = 6 \times 4 = 6 \times 4^1$

for G_3: $96 = 6 \times 4 \times 4 = 6 \times 4^2$

for G_4: $384 = 6 \times 4 \times 4 \times 4 = 6 \times 4^3$

Therefore:

for G_n: $6 \times 4^{n-1}$

Hence, Molecular Formula for G_n:

$G_n = G_{n-1} + 6 \times 4^{n-1} \times (B+2T)$ [for $n \geq 1$]

Recasting:

$G_0 = B+3T$

$G_1 = G_0 + 6\,(B+2T) = G_0 + 6 \times 4^0 \times (B+2T)$

$G_2 = G_1 + 24\,(B+2T) = G_1 + 6 \times 4^1 \times (B+2T)$

$G_3 = G_2 + 96\,(B+2T) = G_2 + 6 \times 4^2 \times (B+2T)$

$G_4 = G_3 + 384\,(B+2T) = G_3 + 6 \times 4^3 \times (B+2T)$

… ……..

$G_n = G_{n-1} + 6 \times 4^{n-1} \times (B+2T)$

By adding by parts, the terms shown in same color cancel out and:

$G_n = (B+3T) + 6 \times (B+2T) \times [4^0 + 4^1 + 4^2 + 4^3 + \ldots. + 4^{n-1}]$

In brackets is the sum of the n-terms of a geometric sequence with: first term = 1, ratio = 4, which is given by: first term × [1-(ratio)^n] / [1-ratio]

Hence:

$[4^0 + 4^1 + 4^2 + 4^3 + \ldots. + 4^{n-1}] = 1 \times (1-4^n) / (1-4) = -\,(1-4^n)/3$

Hence the molecular formula of the n-generation dendrimer from two trifunctional monomers **without the end caps** is given by:

$$\mathbf{G_n = (B+3T) - 2\,(B+2T)\,(1-4^n)} \quad [\text{for } n \geq 0]$$

which is confirmed easily by reproducing the sums of the (B+2T) terms in the G_0-G_4 generation dendrimers as shown above.

Now, to complete the molecular formula, we consider the number of end caps needed (in **bold face**):

			end caps as powers of n
G_0 (the core) =	B+3T +	**6 caps**	6×2^0
G_1 =	G_0 + 6 (B+2T) +	**24 caps**	6×2^2
G_2 =	G_1 + 24 (B+2T) +	**96 caps**	6×2^4
G_3 =	G_2 + 96 (B+2T) +	**384 caps**	6×2^6
G_4 =	G_3 + 384 (B+2T) +	**1,536 caps**	6×2^8
……	……	……..	……..
for G_n:			6×2^{2n}

Therefore, the general molecular formula of a star polymer growing from two trifunctional monomers is:

$$\mathbf{G_n = (B+3T) - 2\,(B+2T)\,(1-4^n) + 6 \times 2^{2n}\ caps} \quad [\text{for } n \geq 0]$$

3. Molecular Formulas of Star Polymers from one Tri- and one Difunctional Unit

Units (e.g., monomers or groups): T (trifunctional) and C (bifunctional)

G_n: generation along isotropic symmetric star growth

Scheme S.2. Dendritic Growth From a Trifunctional core (T) and a Difunctional Monomer (C, yellow block).

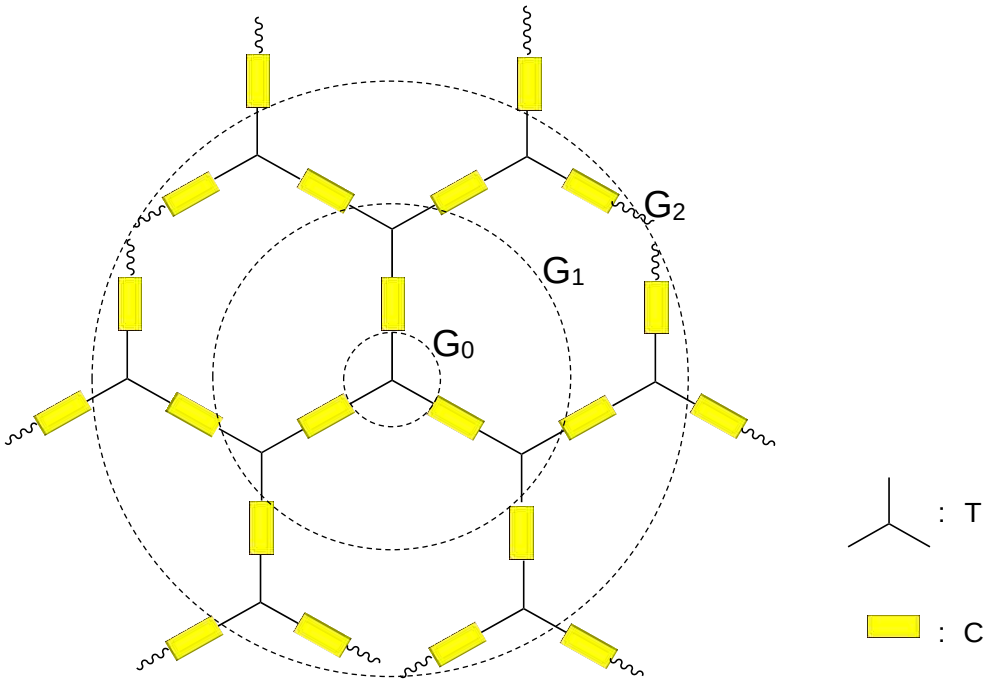

Molecular Formulas **without end-caps**:

		coefficients of the (C+T) terms	Sum of (C+T) terms
G_0 (the core) =	T		
G_1 =	G_0 + [3C + 3T] = G_0 + 3 (C+T)	$3 = 3 \times 2^0$	3
G_2 =	G_1 + [6C + 6T] = G_1 + 6 (C+T)	$6 = 3 \times 2^1$	9

$G_3 =$ $G_2 + [12C + 12T] = G_2 + 12\,(C+T)$ $12 = 3 \times 2^2$ 21

$G_4 =$ $G_3 + [24C + 24T] = G_3 + 24\,(C+T)$ $24 = 3 \times 2^3$ 45

…… …….. $3 \times 2^{n-1}$

$G_n =$ $G_{n-1} + 3 \times 2^{n-1} \times (C+T)$ [for $n \geq 1$]

Recasting:

$G_0 = T$

$G_1 = G_0 + 3\,(C+T)$ $= G_0 + 3 \times 2^0 \times (C+T)$

$G_2 = G_1 + 6\,(C+T)$ $= G_1 + 3 \times 2^1 \times (C+T)$

$G_3 = G_2 + 12\,(C+T)$ $= G_2 + 3 \times 2^2 \times (C+T)$

$G_4 = G_3 + 24\,(C+T)$ $= G_3 + 3 \times 2^3 \times (C+T)$

… ……..

$G_n =$ $G_{n-1} + 3 \times 2^{n-1} \times (C+T)$

By adding by parts, the terms shown in same color cancel out and:

$$G_n = T + 3 \times (C+T) \times [2^0 + 2^1 + 2^2 + 2^3 + \ldots. + 2^{n-1}]$$

In brackets is the sum of the n-terms of a geometric sequence with: first term = 1, ratio = 2, which is given by: first term × [1-(ratio)^n] / [1-ratio]

Hence:

$$[2^0 + 2^1 + 2^2 + 2^3 + \ldots. + 2^{n-1}] = 1 \times (1-2^n) / (1-2) = -\,(1-2^n)$$

Hence the molecular formula of the n-generation dendrimer from a trifunctional and difunctional monomer **without the end caps** is given by:

$$\mathbf{G_n = T - 3\,(C+T)\,(1-2^n)} \quad [\text{for } n \geq 0]$$

which is confirmed easily by reproducing the sums of the (C+T) terms in the G_0-G_4 generation dendrimers as shown above.

Now, to complete the Molecular Formula, we consider the number of end caps needed (in **bold face**):

			end caps as powers of n
G_0 (the core) =	T +	**3 caps**	3×2^0 caps
G_1 =	G_0 + 3 (C+T) +	**6 caps**	3×2^1 caps
G_2 =	G_1 + 6 (C+T) +	**12 caps**	3×2^2 caps
G_3 =	G_2 + 12 (C+T) +	**24 caps**	3×2^3 caps
G_4 =	G_3 + 24 (C+T) +	**48 caps**	3×2^4 caps
……	……	……..	……..
for G_n:			3×2^n caps

Therefore, the general molecular formula of a star polymer growing from one trifunctional and one bifunctional monomer is:

$$\mathbf{G_n = T - 3\,(C+T)\,(1-2^n) + 3 \times 2^n\ cap}\ [\text{for } n \geq 0]$$

Next, we consider the limit as n ----> ∞ of the ratio of all end-caps, Σ(cap) [= 3×2^n cap] to the polymer inside, Σ(polymer_inside) [= $T-3(C+T)\,(1-2^n)$], plus the end caps, that is:

$$\frac{\sum cap}{\sum polymer\_inside + \sum cap} = \frac{3 \times 2^n cap}{T - 3(C+T)(1 - 2^n) + 3 \times 2^n cap}$$

As 'n' increases, $-3(C+T)\,(1-2^n) >> T$, therefore the ratio becomes:

$$\frac{\sum cap}{\sum polymer\_inside + \sum cap} \approx \frac{2^n cap}{-(C+T)(1 - 2^n) + 2^n cap} = \frac{cap}{(C+T)(1 - \frac{1}{2^n}) + cap}$$

And said limit is:

$$\lim_{n\to\infty}\frac{\sum cap}{\sum polymer\_inside+\sum cap}=\frac{cap}{(C+T)+cap}$$

Now, let's assume, for the sake of argument, that the condensation product of two carbamic-boric anhydride adducts (referred to as Int-1, see Scheme 4 of the main article) finds itself at the end of growing polymeric chains. Conceivably, if Int-1 cannot find, or more accurately if it cannot be found by a –BOH, it may rearrange into urea-boramid caps (either via a 4-membered or a six-membered intermediate):

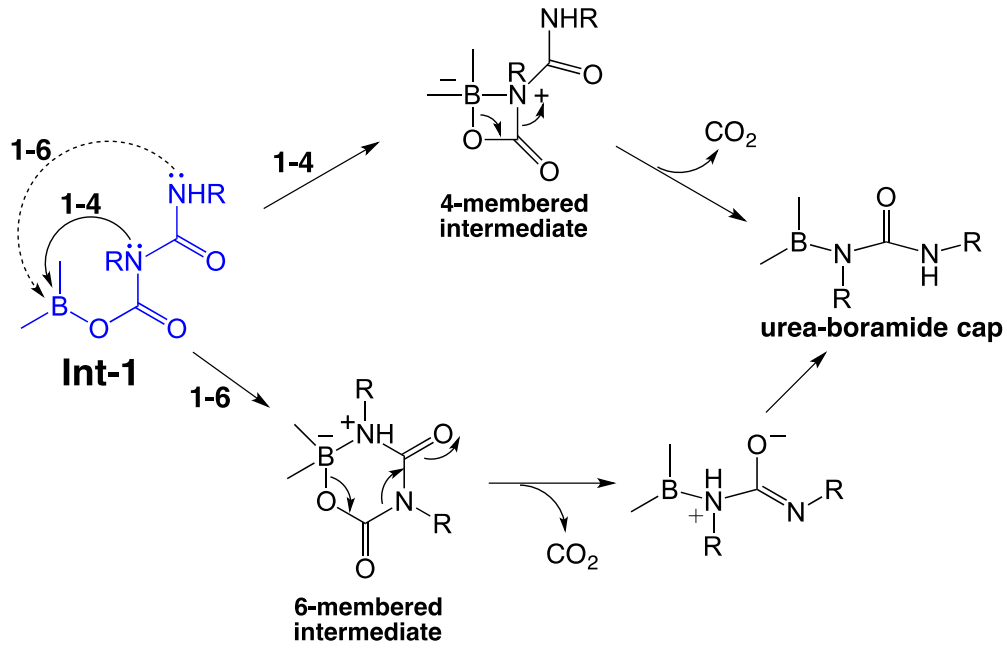

Hence, all polymer chains will be terminated with boron, i.e., cap = B. (It is assumed that the terminal boron atom will be the end-point of another two branches of other star polymers.) Then, because in this case:

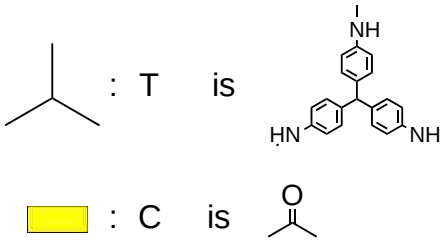

The numerical value of the limit above is calaculated as

$$\lim_{n\to\infty}\frac{\sum cap}{\sum polymer\_inside+\sum cap}=\frac{10.81}{314+10.81}=0.0333$$

That is, the lowest limit for the percent content of boron is 3.33%.

Since the experimental weight percent of boron is always less than 0.05%, we are forced to conclude that the termination process above does not take place in any significant extend. Therefore, **Int-1** intermediate is consumed quantitatively as discussed in conjunction with Scheme 4 in the main article.

Appendix III. Solid-State ^{11}B NMR of a BPUA-xx

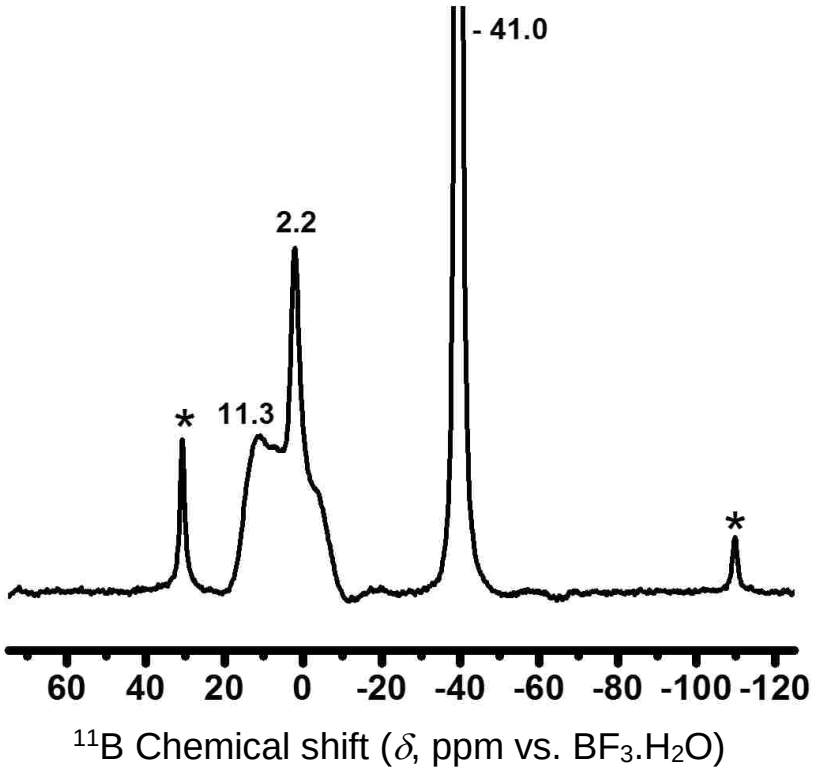

Figure S.1. Solid-state ^{11}B MAS NMR of a typical BPUA-xx (301.03 mg) mixed with $NaBH_4$ (2.13 mg) using high power ^{1}H decoupling and a ZrO rotor spun at 7 kHz. Peaks marked with *'s are side spinning bands of $NaBH_4$ (at -41.0 ppm). No spinning sideband was observed for BPUA-xx. Integrated areas: BPUA-xx: 1.000; $NaBH_4$ (including side spinning bands: 2.081. Quantification: %B w/w in BPUA-xx = (1.000/2.081)×(2.13/301.03)×28.58 (B% w/w in $NaBH_4$) = 0.097% w/w.

Appendix IV. SAXS data for BPUA-xx and PUA-yy aerogels

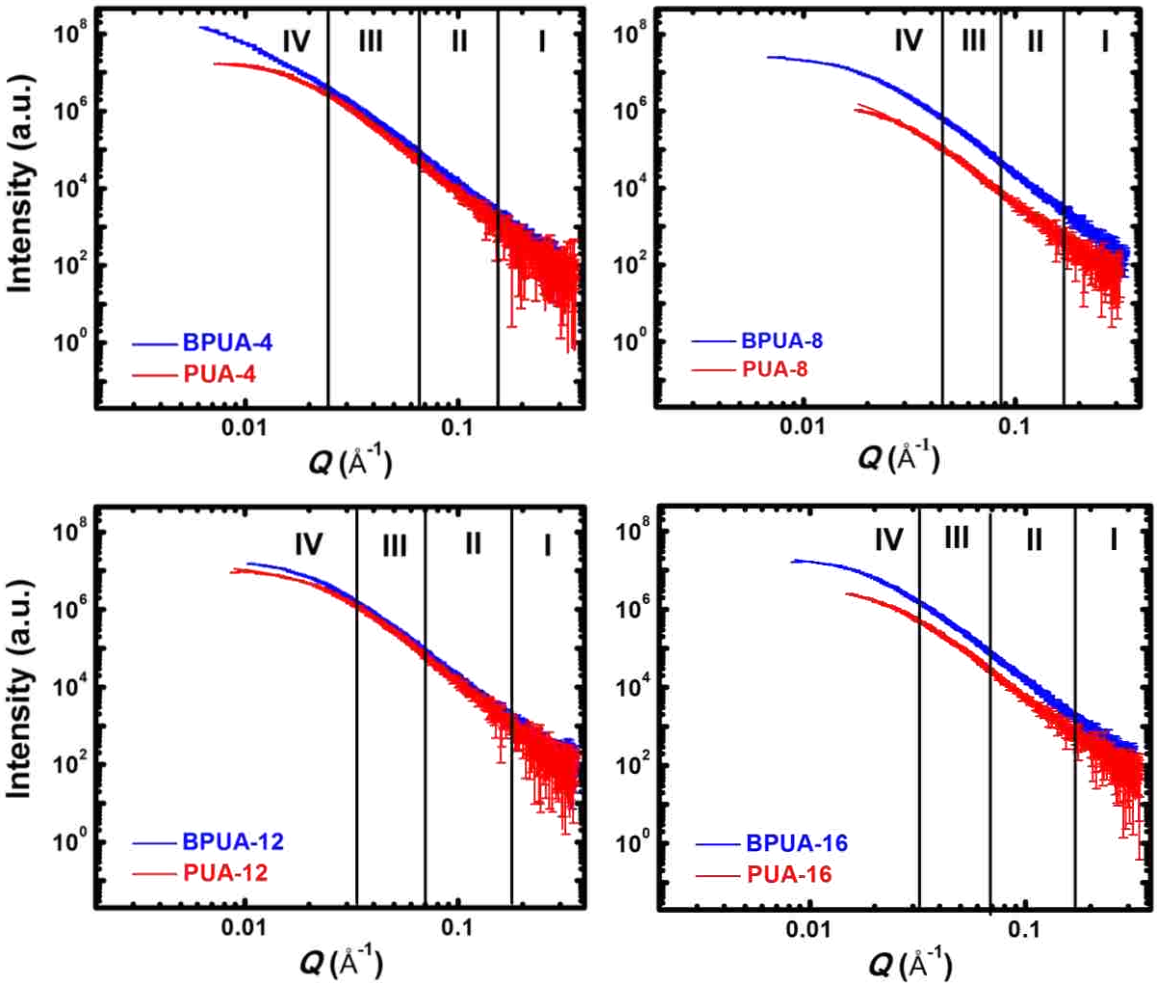

Figure S.2. Small angle X-ray scattering for samples as shown. Curve-fitting according to the Beaucage Unified Model.

Table S.4. Data from analysis of the SAXS scattering profiles of Figure S.2.

Sample I.D. **xx** or **yy**	Primary Particles			Secondary Particles		
	high-*Q* slope [a]	R_G(I) [b] (nm)	diameter [c] (nm)	low-*Q* slope [d]	R_G(II) [e] (nm)	diameter [f] (nm)
BPUA-xx						
4	-4.32±0.00$_8$	6.61±0.15	17.18±0.38	-3.81±0.10	23.84±0.80	61.94±2.08
8	-4.27± .01	4.96±0.19	12.91±0.49	-3.68±0.61	10.84±0.04	28.15±0.10
12	-4.21±0.01	4.54±0.31	11.80±0.81	-3.20±0.55	9.91±0.02	25.74±0.05
16	-4.25±0.01	5.51±0.45	14.33±1.17	-3.00±0.64	11.81±0.09	30.67±0.23
PUA-yy						
4	-4.20±0.12	2.70±0.10	7.01±0.26	-3.45±0.06	11.13±0.03	28.91±0.08
8	-3.96±0.06	4.93±0.90	12.81±2.34	-2.68±1.00	10.11±1.46	26.26±3.79
12	-4.27±0.03	4.36±0.31	11.32±0.81	-3.13±0.76	10.07±0.40	26.16±1.04
16	-4.01±0.03	4.90±0.41	12.73±1.06	-2.79±3.68	9.44±0.16	24.52±0.42

Using the Beaucage Unified Model[S.R-1] and referring to Figure S.2: [a] From power-law Region I. Slopes <-4.0, signify primary particles with density-gradient boundaries. [b] Radius of gyration of primary particles, R_G(I), from Region II (first Guinier knee). [c] Primary particle diameter = 2(R_G(I)/0.77). [d] From power-law Region III. If slope>-3, mass fractal dimension of secondary particles, D_M=|slope|; if slope<-3 (as in this case), surface fractal dimension of secondary particles, D_s=6-|slope|. [e] Radius of gyration of secondary particles, R_G(II), from Region IV (second Guinier knee). [f] Secondary particle diameter = 2(R_G(II)/0.77).

S.R-1 (a) Beaucage, G. *J. Appl. Crystallogr.* **1995**, *28*, 717-728.

(b) Beaucage, G. *J. Appl. Crystallogr.* **1996**, *29*, 134-146.

Appendix V. N_2-Sorprion data for BPUA-xx and PUA-yy aerogels

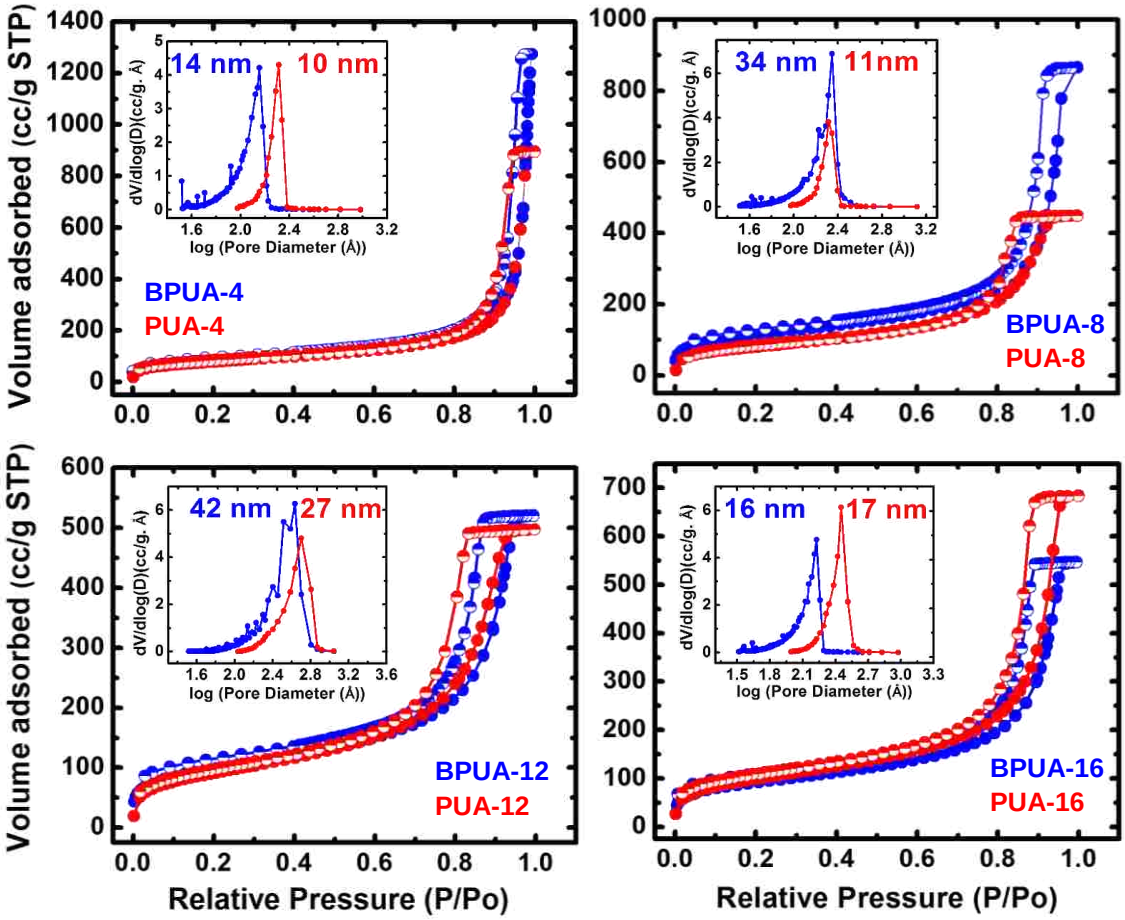

Figure S.3. Isotherms and BJH pore size distributions (Insets) of samples as shown.

Appendix VI. Mechanical Characterization of BPUA-xx aerogels and comparison with the literature

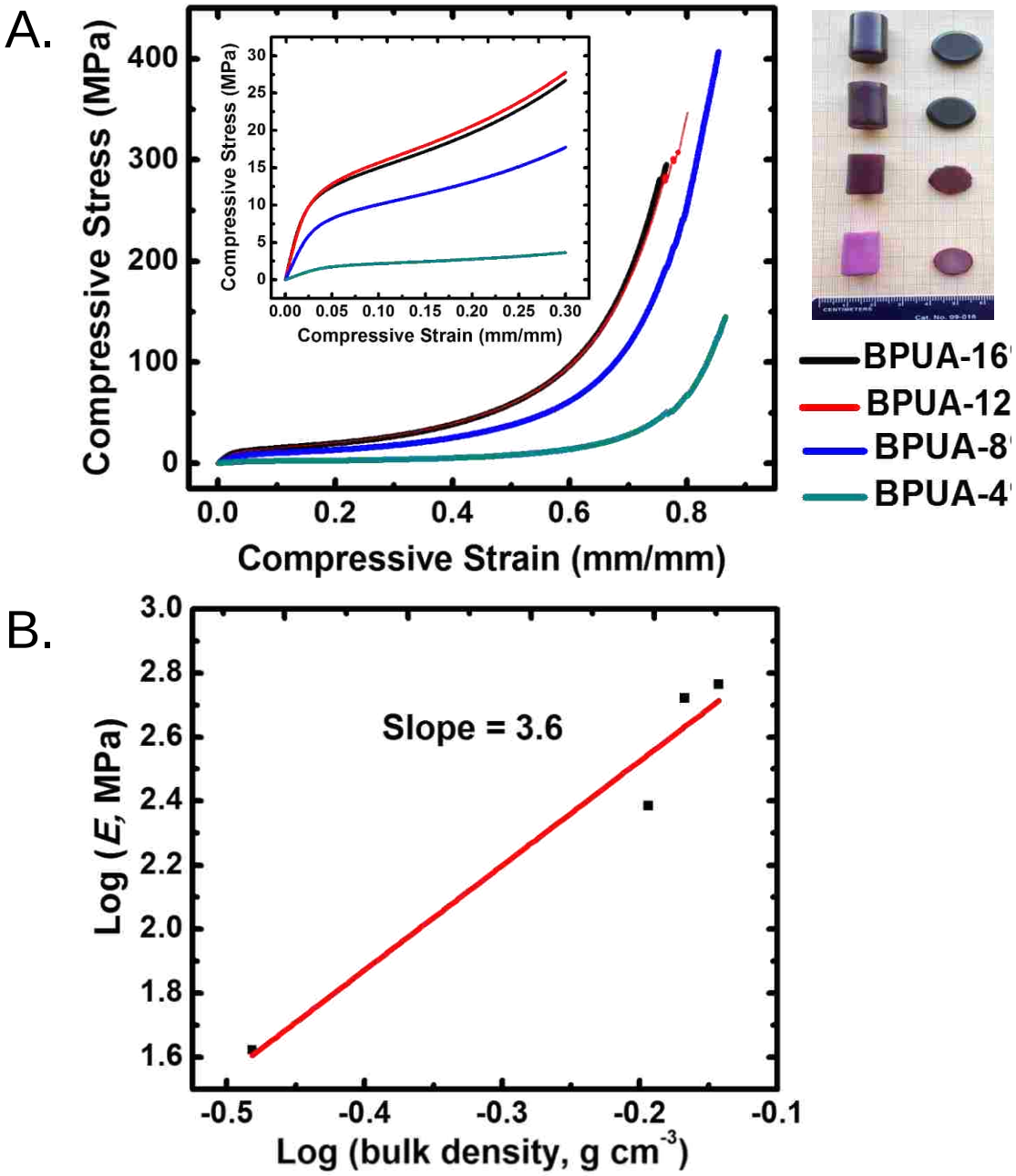

Figure S.4. A. Stress-strain curves. Inset: Magnified early elastic region. To the right: photographs of aerogels before and after compression, starting with BPUA-16 on top. B. Log-Log plot of the elastic modulus, E, vs. ρ_b.

Table S.5. Results from quasi-static compression of BPUA-xx.

BPUA-xx	bulk density, ρ_b (g cm^{-3})	Young's Modulus, *E* (MPa)	Strain (ε_y) at Yield (mm/mm)	Stress (σ_y) at Yield (MPa)	Ultimate Strength, UCS, (MPa)	Energy Density (J/g)
4	0.283±0.008	42.3±4.5	0.043±0.005	1.79±0.01	143.8±0.52	43.26±6.47
8	0.467±0.004	243.3±36.0	0.037±0.010	8.85±1.19	406.56±1.25	90.35±0.00
12	0.545±0.004	528.8±30.4	0.022±0.003	11.55±0.74	345.19±0.64	84.31±3.63
16	0.576±0.005	582.5±62.5	0.018±0.004	10.56±1.35	294.86±2.32	67.31±1.17

Table S.6. Comparison of Young's modulus (E) of BPUA-xx with the Young's modulus of all other organic aerogels published by our group. Only aerogels whose density matches with one of BPUA-4, BPUA-8, BPUA-12 and BPUA-16 have been included.

		BPUA-xx			
		xx=4	**xx**=8	**xx**=12	**xx**=16
	ρ_b (g cm^{-3})	0.283	0.407	0.545	0.576
	E (MPa)	42.3	243	529	583
	ρ_b (g cm^{-3})	*E* (MPa)			
TIPM-based polyurethanes with aromatic alcohols [S.R-2]					
aR-BPA-15	0.293	3			
aR-BPA-20	0.46		220		
aR-BPA-25	0.567				400
aR-POL-10	0.298	22.7			
aR-POL-15	0.477			203	
aR-DHB-15	0.243	1.2			
aR-DHB-20	0.309	7			
aR-DHB-25	0.432		15		
aR-SDP-15	0.307	8.7			
aR-SDP-20	0.422		133		
aR-SDP-25	0.541			340	
aR-HPE-15	0.315	49			
aR-HPE-20	0.426		1.4		
aR-HPE-25	0.567				343
aL-HPE-25	0.563				363
aR-RES-15	0.404		108		
aR-RES-20	0.565				390
TIPM-based poly(urethane-acrylates) [S.R-3]					
30-aR-Pac	0.499			155	
Same poly(urethane-acrylates) with chain extenders (EG, HD) [S.R-3]					
20-aR-Pac-EG	0.307	16			
30-aR-Pac-EG	0.479			142	

20-aR-Pac-HD	0.29	13			
30-aR-Pac-HD	0.466		180		
20-aL-Pac-EG	0.306	11			
30-aL-Pac-EG	0.478			71	
40-aL-Pac-EG	0.594				284
Aliphatic triisocyanate (N3300A)-based poly(urethane acrylates) [S.R-3]					
30-aL-Pac	0.511			83	
Same poly(urethane-acrylates) with a chain extender (HD) [S.R-3]					
20-aL-Pac-HD	0.337	23			
30-aL-Pac-HD	0.504			112	
TIPM-based poly(urethane-norbornenes) [S.R-3]					
20-aRNor	0.259	9			
30-aRNor	0.458		90		
Aliphatic triisocyanate (N3300A)-based poly(urethane norbornenes) [S.R-3]					
15-aLNor	0.209	4.4			
20-aLNor	0.298	21			
30-aLNor	0.545			144	
Aliphatic triisocyanate (N3300A)-based polyurea made in acetone [S.R-4]					
aL-PUA	0.550			300	
TIPM-based polyamides with trimesic acid [S.R-5]					
PA-10	0.288	33			
PA-15	0.324	46			
PA-25	0.399		0.9		
TIPM-based polyimidess with BTDA and PMDA anhydrides [S.R-6]					
aR-BTDA-6	0.259	44			
aR-BTDA-20	0.426		140		
aR-PMDA-6	0.437		143		
Polyimides made via the amine route from MDA and PMDA [S.R-7]					
PI-AMN-190-20	0.291	27.25			
Polyimides made via ROMP of a bisnadimide [S.R-8]					
bis-NAD-10	0.39		48		
bis-NAD-15	0.528			173	
Polynorbornene aerogels [S.R-9]					
pNB-30 (10:90)	0.457		97		
pNB-30 (30:70)	0.507			152	
pNB-30 (0:100)	0.502			92	
Polymer (polyurea)-crosslinked vanadia aerogels [S.R-10]					
X-VO_x in N3200	0.466		287		

Polymer (polynorbornene)-crosslinked silica aerogels [S.R-11]					
X-SiNAD-10	0.273	108			
X-SiNAD-20	0.382		187		
Polymer (polystyrene)-crosslinked silica aerogels [S.R-12]					
X-Si-1-PS-25	0.232	7.81			

S.R-2 Chidambareswarapattar, C.; McCarver, P. M.; Luo, H.; Lu, H.; Sotiriou-Leventis, C.; Leventis, N. *Chem. Mater*. **2013**, *25*, 3205.

S.R-3 Bang, A.; Buback, C.; Sotiriou-Leventis, C.; Leventis, N. *Chem. Mater*. **2014**, *26*, 6979.

S.R-4 Leventis, N.; Sotiriou-Leventis, C.; Chandrasekaran, N.; Mulik, S.; Larimore, Z; Luo, H.; Churu, G.; Mang, J. T. *Chem. Mater*. **2010**, *22*, 6692.

S.R-5 Leventis, N.; Chidambareswarapattar, C.; Mohite, D. P.; Larimore, Z; Lu, H.; Sotiriou-Leventis, C. *J. Mater. Chem*. **2011**, *21*, 11981.

S.R-6 Chidambareswarapattar, C.; Xu, L; Sotiriou-Leventis, C.; Leventis, N. *RSC Adv.* **2013**, *3*, 26459.

S.R-7 Chidambareswarapattar, C.; Larimore, Z; Mang, J, T.; Sotiriou-Leventis, C.; Leventis, N. *J. Mater. Chem*. **2010**, *20*, 9666.

S.R-8 Leventis, N.; Sotiriou-Leventis, C.; Mohite, D. P.; Larimore, Z; Mang, J. T.; Churu, G.; Lu, H. *Chem. Mater*. **2011**, *23*, 2250.

S.R-9 Mohite, D. P.; Mahadik-Khanolkar, S.; Luo, H.; Lu, H.; Sotiriou-Leventis, C.; Leventis, N. *Soft Matter*. **2013**, *9*, 1516.

S.R-10 Luo, H.; Churu, G.; Fabrizio, F. E.; Schnobrich, J.; Hobbs, A.; Dass, A.; Mulik, S.; Zhang, Y.; Grady, P. B.; Capecelatro, A.; Sotiriou-Leventis, C.; Leventis, N. *J Sol-Gel Sci Technol.* **2008**, *48*, 113.

S.R-11 Mohite, D. P.; Larimore, Z; Lu, H.; Mang, J. T.; Sotiriou-Leventis, C.; Leventis, N. *Chem. Mater*. **2012**, *24*, 3434.

S.R-12 Mulik, S.; Sotiriou-Leventis, C.; Churu, G.; Lu, H.; Leventis, N. *Chem. Mater*. **2008**, *20*, 5035.

Appendix VII. Thermal conductivity data of BPUA-xx aerogels and comparison with the literature

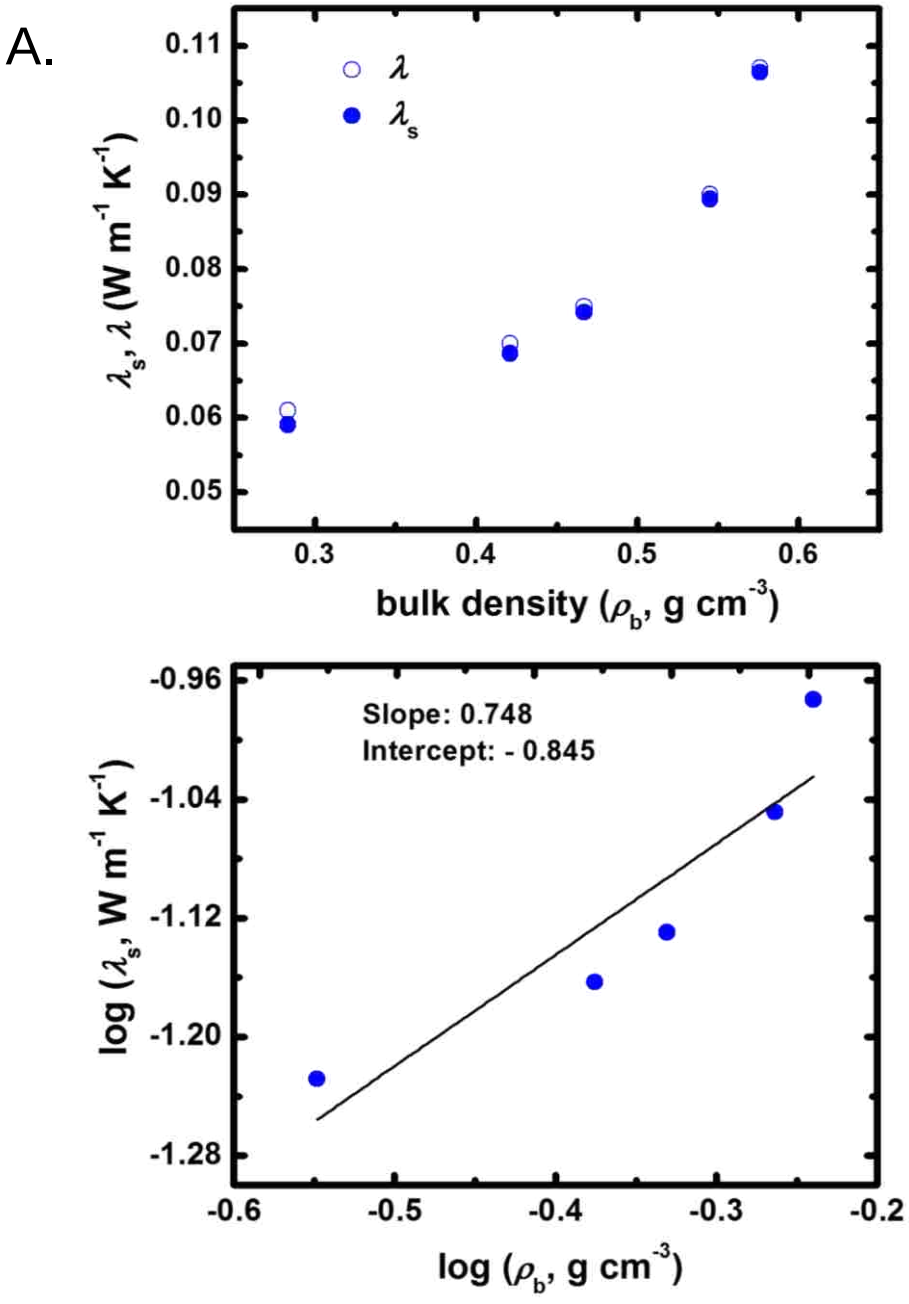

Figure S.5. A. Total thermal conductivity, λ, and solid thermal conduction, λ_s vs. bulk density (ρ_b). B Log-Log plot of the solid thermal conduction (λ_s) vs. bulk density (ρ_b).

Table S.7. Thermal Conductivity data of BPUA-xx by the laser flash method.

-xx	Bulk density ρ_b (g cm^{-1})	Heat capacity c_p @ 23 °C (J g^{-1} K^{-1})	Thermal diffusivity R (mm^2 s^{-1})	Total thermal conductivity, λ (W m^{-1} K^{-1}) [a]	Π [b]	Avg. pore diameter Φ (nm) [c]	Gaseous thermal conductivity, λ_g (W m^{-1} K^{-1}) [d]	Solid thermal conductivity, λ_s (W m^{-1} K^{-1}) [e]
4	0.283±0.008	1.352±0.034	0.162±0.016	$0.061\pm0.000_3$	0.77	29	0.002	0.059
6	0.421±0.002	1.352±0.034	0.123±0.007	$0.070\pm0.000_1$	0.66	23	0.001	0.068
8	0.467±0.004	1.352±0.034	0.119±0.007	$0.075\pm0.000_1$	0.62	14	0.000_7	0.074
12	0.545±0.004	1.352±0.034	0.123±0.002	$0.090\pm0.000_0$	0.56	12	0.000_6	0.095
16	0.576±0.005	1.352±0.034	0.138±0.012	$0.107\pm0.000_0$	0.54	12	0.000_5	0.106

[a] Via $\lambda=\rho_b\times c_P\times R$

[b] Porosity in decimal notation (from data in Table 1 of the main article).

[c] Via the $4V_{Total}/\sigma$ method using $V_{Total} = (1/\rho_b) - (1/\rho_s)$ (from data in Table 1 of the main article).

[d] From Knudsen's equation: $\lambda_g = \dfrac{\lambda_{g,o} P}{1+2\beta(l_g/\Phi)}$

whereas: $\lambda_{g,o}$ is the intrinsic conductivity of the pore-filling gas (for air at 300 K at 1 bar, $\lambda_{g,o} = 0.02619$ W m^{-1} K^{-1}), β is a parameter that accounts for the energy transfer between the pore-filling gas and the aerogel walls (for air $\beta = 2$), l_g is the mean free path of the gas molecules (for air at 1 bar pressure, $l_g \approx 70$ nm)

[e] From $\lambda_s = \lambda - \lambda_g$.

Table S.8. Comparison of C coefficient (a measure of interparticle connectivity) of BPUA-xx with the C coefficient of other polymeric aerogels as has been determined by our group.

Aerogel type	a (slope)	*C* (W m^{-1} K^{-1})
BPUA-xx (this study)	0.748	0.142
TIPM-based polyurethane aerogels with aromatic alcohols		
aR-POL-5	1.41	0.14
aR-HPE-5	0.43	0.074
aR-RES-15	1.18	0.11
aR-SPD-10	-0.22	0.047
aR-BPA-15	3.06	0.625
Polyurea (PUA) aerogels based on an aliphatic triisocyanate (N3300A)		
PUA-made in CH_3CN	0.99	0.13
PUA-made in acetone	1.00	0.10
Polydicyclopentadiene based aerogels		
pDCPD	1.2	0.133
Polynorbornene based aerogels		
pNB	1.5	0.910

Appendix VIII. Reaction of TIPM with various mineral acids

1. Synthesis and properties of polyurea aerogels from TIPM and mineral acids

Phosphoric acid (pure), was purchased from Acros Organics, phosphorous acid (98%) was purchased from Alfa Aesar, telluric acid (≥ 99%), selenous acid (98%), periodic acid (≥ 99%) and auric acid were purchased from Sigma-Aldrich. All sols were formulated so that the weight percent of monomers (TIPM+mineral acid) was kept constant at 16%. All formulations and gelation times are summarized in Table S.9. Materials characterization data are provided in Table S.10. Specifically:

***Gelation of TIPM and H_3PO_4*:** H_3PO_4 (0.98 g, 0.010 mol) was dissolved in anhydrous DMSO (13.1 mL, 14.5 g) and the solution was cooled in a dry ice/acetone bath (-78 ºC). As that solution thawed, it was added to cold (-78 ºC) 13.6 g of Desmodur RE (containing 3.67 g, 0.01 mol of TIPM) and the mixture was stirred vigorously.

***Gelation of TIPM and H_3PO_3*:** H_3PO_3 (1.23 g, 0.015 mol) was dissolved in anhydrous DMSO (14.3 mL, 15.8 g) and the solution was cooled in a dry ice/acetone bath (-78 ºC). As that solution thawed, it was added to cold (-78 ºC) 13.6 g of Desmodur RE (containing 3.67 g, 0.01 mol of TIPM) and the mixture was stirred vigorously.

***Gelation of TIPM and H_2SeO_3*:** H_2SeO_3 (1.93 g, 0.015 mol) was dissolved in anhydrous DMF (20.5 mL, 19.4 g), and the solution was cooled in a dry ice/acetone bath (-78 ºC). The cold solution was added to cold (-78 ºC) 13.6 g of Desmodur RE (containing 3.67 g, 0.01 mol of TIPM) and the mixture was stirred vigorously.

Gelation of TIPM and* $Te(OH)_6$*: $Te(OH)_6$ (1.14 g, 0.005 mol) was dissolved in anhydrous DMF (16.1 mL, 15.3 g), the solution was added at room temperature to 13.6 g of Desmodur RE (containing 3.67 g, 0.01 mol of TIPM) and the mixture was stirred vigorously.

***Gelation of TIPM and H_5IO_6*:** H_5IO_6 (1.36 g, 0.006 mol) was dissolved in anhydrous DMF (17.3 mL, 16.4 g), and the solution was added at room temperature to 13.6 g of Desmodur RE (containing 3.67 g, 0.01 mol of TIPM) and the mixture was stirred vigorously.

***Gelation of TIPM and H_3AuO_3*:** H_3AuO_3 (2.48 g, 0.01 mol) was dissolved in anhydrous DMF (112.5 mL, 106.9 g), and the solution was added at room temperature to 13.6 g of Desmodur RE (containing 3.67 g, 0.01 mol of TIPM) and the mixture was stirred vigorously.

The resulting sols were poured in molds and were left at room temperature to gel, except the H_3AuO_3 sols, which were placed in an oven at 90 ºC. After aging (12 h at room temperature, except the H_3AuO_3 gels, which were aged at 90 ºC) gels were removed from the molds, were washed with DMF (2×), acetone (4×, using 4× the volume of the gel for each wash) and were dried in an autoclave with liquid CO_2 taken out at the end as a supercritical fluid (SCF).

Table S.9. Formulations and gelation times of polyurea aerogels made from TIPM reacting with selected mineral acids as shown.

Mineral acid used	Mineral acid				Desmodur RE [b]		TIPM			Solvent [d]		gelation time
	mass (g)	volume [a] (mL)	mmol	C (M)	volume (mL)	mass (g)	mass [c] (g)	mmol	C (M)	mass (g)	volume (mL)	
H_3PO_4	0.098	0.051	1.00	0.371	1.33	1.359	0.367	1.00	0.371	1.45	1.31	~ 10 min [e]
H_3PO_3	0.123	0.074	1.50	0.529	1.33	1.359	0.367	1.00	0.352	1.58	1.43	~ 8 min [e]
H_2SeO_3	0.193	0.064	1.50	0.436	1.33	1.359	0.367	1.00	0.290	1.94	2.05	~ 1 min [e]
$Te(OH)_6$	0.114	0.037	0.50	0.168	1.33	1.359	0.367	1.00	0.336	1.53	1.61	~ 5 min [f]
H_5IO_6	0.136	0.097	0.60	0.190	1.33	1.359	0.367	1.00	0.316	1.64	1.73	~ 5 min [f]
H_3AuO_3	0.248	0.023	1.00	0.079	1.33	1.359	0.367	1.00	0.079	10.69	11.25	90 min [g]

[a] The volume of mineral acids were calculated based on their densities cited in the literature, except for auric acid, whereas its density was measured in our lab using He pycnometry and was found equal to 10.783 g cm^{-3}. [b] The mass of commercial Desmodur RE was calculated based on its density as measured in our lab (1.022 g cm^{-3}). [c] The mass of TIPM in Desmodur RE was calculated based on the concentration (27% w/w) given by the manufacturer. [d] DMF or DMSO – see above. [e] Requires cooling. [f] Room temperature. [g] Heated at 90 ^oC.

Table S.10. **Material properties characterization of polyurea aerogels made from TIPM reacting with selected mineral acids as shown.**

Mineral acid used	linear shrinkage (%) [a,b]	bulk density, ρ_b (g cm^{-3}) [a]	skeletal density, ρ_s (g cm^{-3}) [c]	Π (% v/v) [d]	specific pore volume (cm^3 g^{-1})			BET surf. area, σ (m^2 g^{-1})	av. pore diameter, (nm)		particle radius, r (nm) [i]
					V_{Total} [e]	$V_{1.7\text{-}300\ nm}$ [f]	$V_{Total}/V_{1.7\text{-}300\ nm}$		$4V/\sigma$ [g]	BJH [h]	
H_3PO_4	30.3 ± 0.2	0.41 ± 0.03	1.40 ± 0.01	70.57	1.71	1.29	1.32	218	31.6 [23.9]	27.5	9.83
H_3PO_3	39.1 ± 0.5	0.55 ± 0.01	1.40 ± 0.01	60.92	1.11	0.92	1.21	298	15.0 [12.4]	13.3	7.19
H_2SeO_3	39.7 ± 0.5	0.21 ± 0.03	1.85 ± 0.06	88.91	4.33	0.04	108	17	1021 [9.7]	11.1	95
$Te(OH)_6$	44.7 ± 0.4	0.63 ± 0.03	1.83 ± 0.06	65.46	1.03	0.78	1.32	335	12.5 [9.7]	12.3	4.89
H_5IO_6	45.2 ± 0.8	0.78 ± 0.03	1.60 ± 0.01	51.18	0.65	0.60	1.08	330	7.94 [7.32]	7.44	5.68
H_3AuO_3	55.4 ± 0.6	0.32 ± 0.04	2.38 ± 0.05	86.23	2.695	0.571	4.71	177	60.92[11.5]	7.4[-]	7.12

[a] Average of 3 samples. [b] Shrinkage=100×(mold diameter–sample diameter)/(mold diameter). [c] Single sample, average of 50 measurements. [d] Porosity=$100\times(\rho_s-\rho_b)/\rho_s$. [e] $V_{Total}=(1/\rho_b)-(1/\rho_s)$. [f] $V_{1.7\text{-}300\_nm}$ from N_2- BJH adsorption volume. [g] For the first number, $V=V_{Total}$; for the number in [brackets] V via the single-point adsorption method. [h] BJH plot maxima. [i] $r = 3/(\rho_s\times\sigma)$.

2. Spectroscopic characterization of polyurea aerogels from TIPM and the mineral acids considered in this study

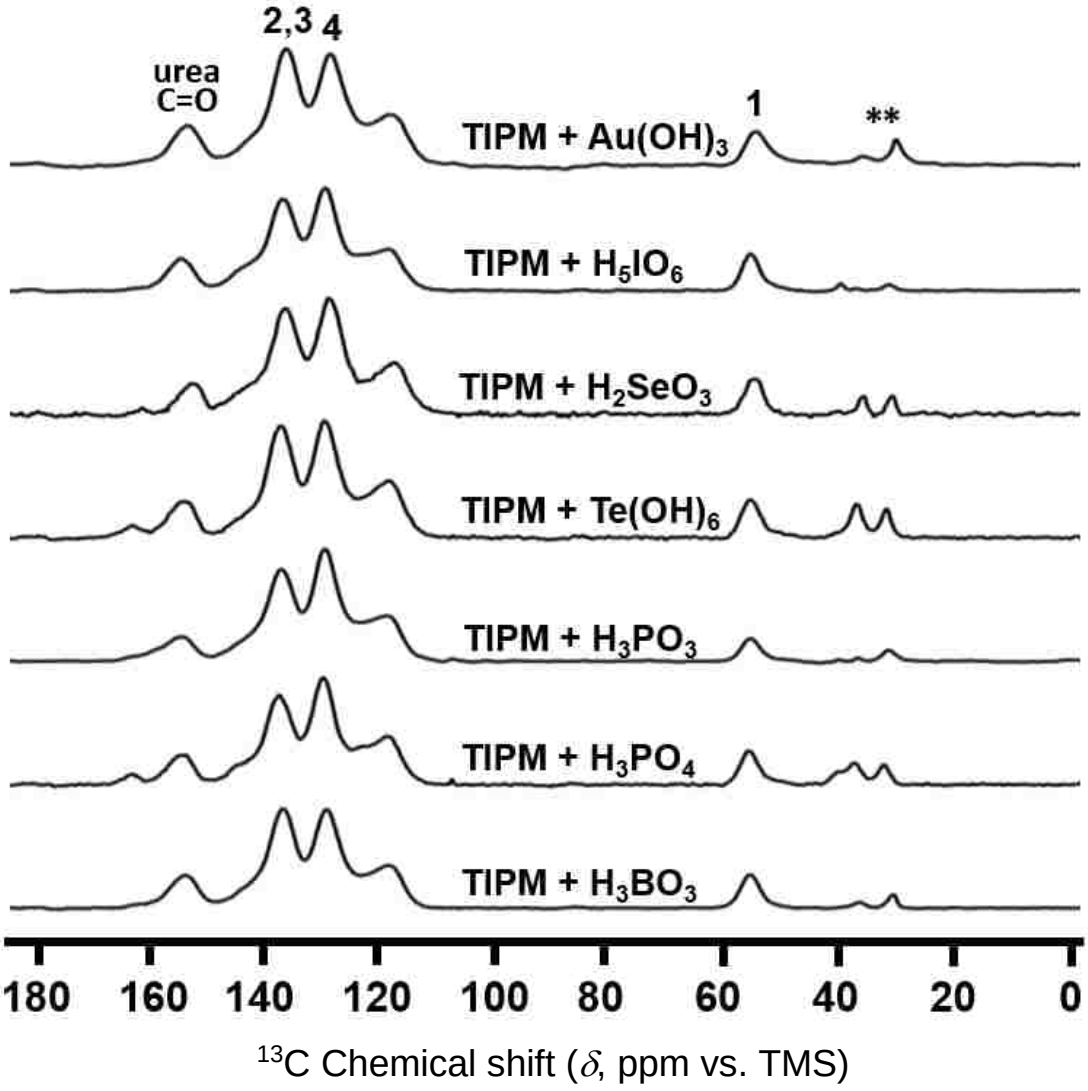

Figure S.6. Solid-state CPMAS ^{13}C NMR of the aerogels obtained from the gelation of TIPM with various mineral acids, as indicated. For peak assignment refer to Scheme 3 of the main article. Peaks marked with ** are residual gelation and processing solvents

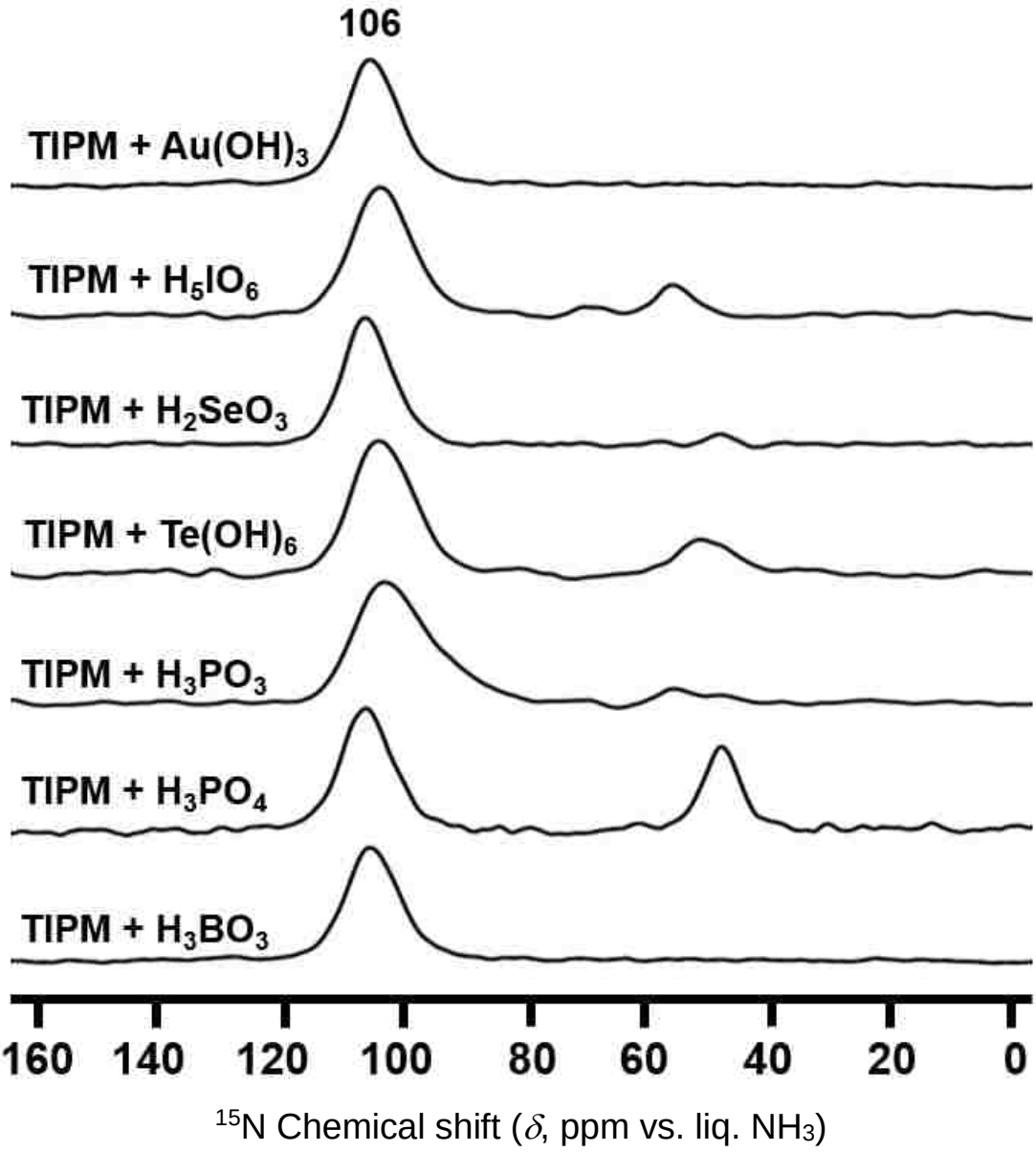

Figure S.7. Solid-state CPMAS ^{15}N NMR of the aerogels obtained from the gelation of TIPM with various mineral acids as indicated. Note the prominence of NH_2 groups bonded to aromatic rings (peaks in the 50 ppm region) in several of those products and the complete absence from others. For relevant discussion see Section 2.4 of the main article.

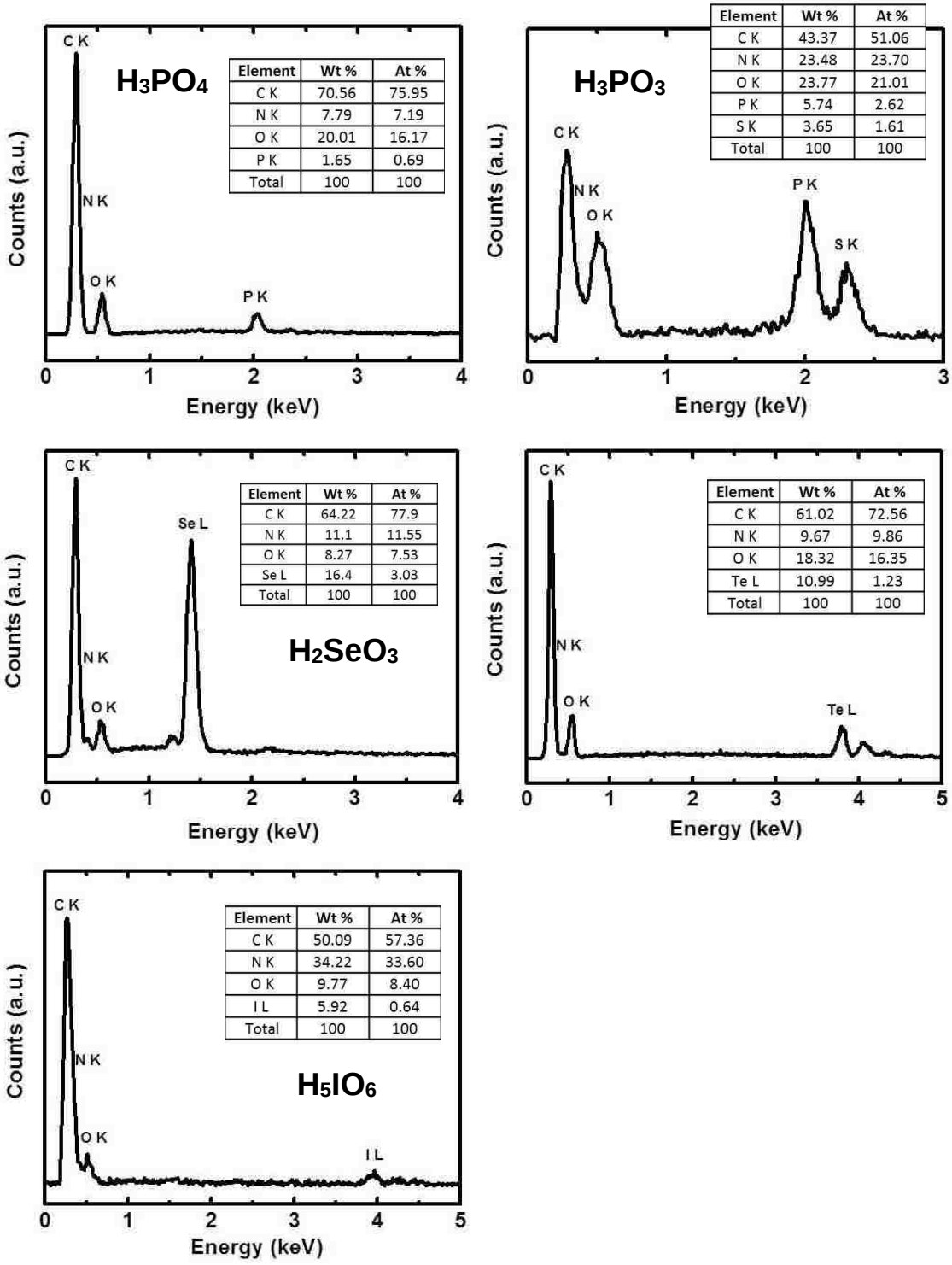

Figure S. 8. EDS of powdered polyurea aerogel monoliths synthesized from TIPM and the mineral acids indicated. (Note: For accuracy, the percent compositions indicated must be corrected for the amount of H contained in the samples.)

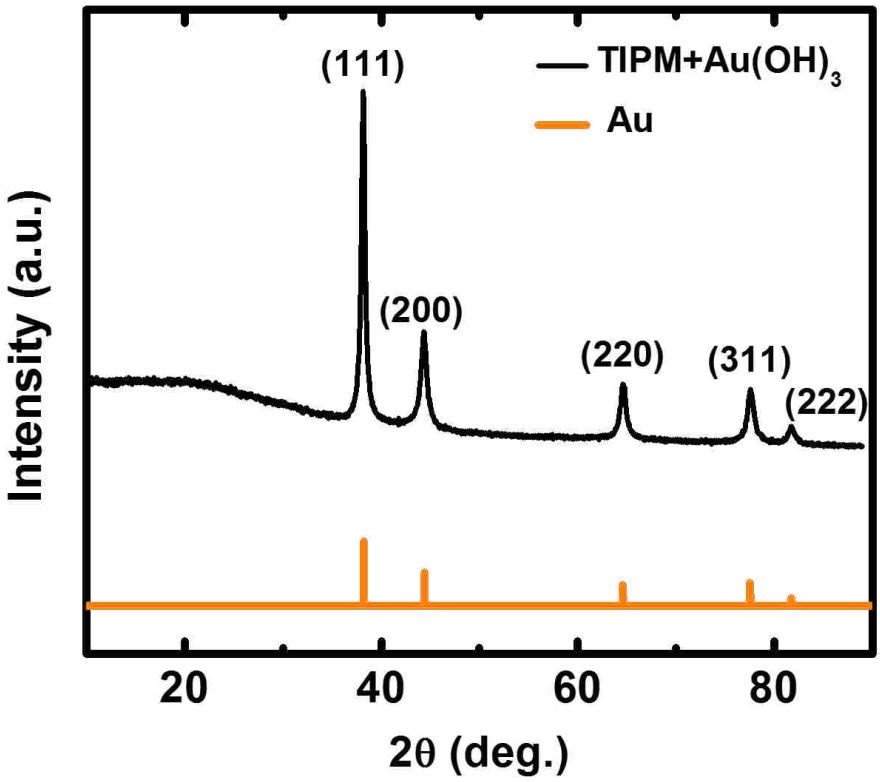

Figure S. 9. XRD of as-prepared polyurea aerogels from TIPM and auric acid. (Line spectrum for fcc Au(0). Scherrer equation analysis of the (111) reflection gives the average crystallite size at 18 nm.)

ACKNOWLEDGEMENTS

This project was funded by the Army Research Office under Award Number W911NF-14-1-0369. Partial support was also received from BASF Polyurethanes GmbH. We thank Bayer Corporation, U.S.A. for the generous supply of Desmodur RE (TIPM) triisocyanates, as well as the Materials Research Center of the Missouri University of Science and Technology for support with materials characterization. Special thanks to Dr. Wei Wycoff for her assistance with solid-state ^{11}B NMR.

REFERENCES

(1) Odian, G. *Principles of Polymerization*, Wiley Interscience, New York, NY, USA, 4th ed., **2004**, pp. 99–101.

(2) Joullie, M. M.; Lassen, K. M. "Evolution of amide bond formation." *ARKIVOC **2010***, VIII, 189-250.

(3) Haller, A. "Action of phenylic isocyanate on campholic, camphocarboxylic, and phthalic acids." *C. R. Acad. Sci.* **1895**, *120*, 1326-1329.

(4) Blagbrough, I. S.; Mackenzie, N. E.; Ortiz, C.; Scott, A. I. "The condensation reaction between isocyanates amd carboxylic acids. A Practical synthesis of substituted amides and anilides." *Tetrahedron Lett.* **1986**, *27*, 1251-1254.

(5) Sasaki, K.; Crich, D. "Facile amide bond formation from carboxylic acids and isocyanates." *Org. Lett.* **2011**, *13*, 2256-2259.

(6) Leventis, N.; Chidambareswarapattar, C.; Mohite, D. P.; Larimore, Z. J.; Lu, H.; Sotiriou-Leventis, C. "Multifunctional porous aramides (aerogels) by efficient reaction of carboxylic acids and isocyanates." *J. Mater. Chem.* **2011**, *21*, 11981-11986.

(7) Aries, R. S. "Polymers from boric acid and organic diisocyanates." U.S. Patent No. 2,945,841 (7-19-1960).

(8) Kumar, R.; Lebedinski, N. "Modified isocyanate compositions and methods of preparing the same." U.S. Patent Application Publication US 2013/0245222 (9-19-2013).

(9) Dodge, J. “Polyurethanes and Polyureas” in “Synthetic Methods in Step-Growth Polymers;” Rogers, M. E.; Long, T. E. Eds.; Wiley: New York, **2003**, p 197.

(10) Robertson, J. D.; Dyar, D. M.; “Nuclear Methods for Analysis of Boron in Minerals.” *Reviews of Mineralogy* **1996**, *33*, 805-820.

(11) Acharya, R. “Prompt gamma-ray neutron activation analysis methodology for determination of boron from trace to major contents.” *J. Radional. Nucl. Chem.* **2009**, *282*, 291-294.

(12) http://www.murr.missouri.edu (07-01-2015).

(13) Jones, G. O.; Li, X.; Hayden, A. E.; Houk, K. N.; Danishefsky, S. J. “The Coupling of isonitriles and carboxylic acids occurring by sequential concerted rearrangement mechanisms.” *Org. Lett.* **2008**, *10*, 4093-4096.

(14) Naegeli, C.; Tyabji, A.“Über den Umsatz aromatischer Isocyansäure-ester mit organischen Säuren. I. Theorie und Anwendung der Reaktion für die präparative Darstellung von Säure-anhydriden.” *Helv. Chim. Acta* **1934**, *17*, 931-957.

(15) Naegeli, C.; Tyabji, A.“Über den Umsatz aromatischer Isocyansäure-ester mit organischen Säuren II. Isolierung einiger Carbaminsäure-carbonsäure-anhydride.” *Helv. Chim. Acta* **1935**, *18*, 142-160.

(16) Sorenson, W. R. “Reaction of an isocyanate and a carboxylic acid in dimethyl sulfoxide.” *J. Org. Chem.* **1959**, *24*, 978-980.

(17) Leventis, N.; Sotiriou-Leventis, C.; Chandrasekaran, N.; Mulik, S.; Larimore, Z. J.; Lu, H.; Churu, G.; Mang, J. T. “Multifunctional Polyurea Aerogels from Isocyanates and Water. A Structure-Property Case Study.” *Chem. Mater.* **2010**, *22*, 6692-6710.

(18) Leventis, N.; Chidambareswarapattar, C.; Bang, A.; Sotiriou-Leventis, C. “Cocoon-in-Web-like Superhydrophobic Aerogels from Hydrophilic Polyurea and Use in Environmental Remediation.” *ACS Appl. Mater. Interfaces* **2014**, *6*, 6872-6882.

(19) Mohite, D. P.; Mahadik-Khanolkar, S.; Luo, H.; Lu, H.; Sotiriou-Leventis, C.; Leventis, N. “Polydicyclopentadiene Aerogels Grafted with PMMA: II. Nanoscopic Characterization and Origin of Macroscopic Deformation.” *Soft Matter* **2013**, *9*, 1531-1539.

(20) Farha, O. K.; Spokoyny A. M.; Hausen, B. G.; Bae, Y.-S.; Brown, S. E.; Snurr, R. Q.; Mirkin, C. A.; Hupp, J. T. “Synthesis, Properties, and Gas Separation Studies of a Robust Diimide-Based Microporous Organic Polymer.” *Chem. Mater.* **2009**, *21*, 3033–3035.

(21) Farha, O. K.; Bae, Y.-S.; Hauser, B. G.; Spokoyny, A. M.; Snurr, R. Q.; Mirkin, C. A.; Hupp, J. T. “Chemical reduction of a diimide based porous polymer for selective uptake of carbon dioxide versus methane.” *Chem. Commun.* **2010**, *46*, 1056–1058.

(22) Webb, P. A.; Orr, C. *Analytical Methods in Fine Particle Technology*. Micromeritcs Instrument Corp. 1997 pp. 81-88.

(23) Wang, H.-L.; Kao, H.-M.; Digar, M.; Wen, T.-C. "FTIR and solid state ^{13}C NMR studies of the interaction of lithium cations with polyether poly(urethane urea)." *Macromolecules* **2001**, *34*, 529-537.

(24) Du, P.; Liu, X.; Zheng, Z.; Wang, X.; Joncheray, T.; Zhang, Y. "Synthesis and characterization of linear self-healing polyurethane based on thermal reversible Diels-Alder reaction." *RSC Advances* **2013**, *3*, 15475-15482.

(25) Li, X.-L.; Chen, D.-J. "Synthesis and characterization of aromatic/aliphatic co-polyureas." *J. Appl. Polym. Sci.* **2008**, *109*, 897-902.

(26) It is noted that Eq 1 is counterintuitive and is attributed to the fractal growth of the star polymer. For non-fractal growth that lim is zero.

(27) McKeown N. B.; Budd, P. M. "Polymers of intrinsic microporosity (PIMs): organic materials for membrane separations, heterogeneous catalysis and hydrogen storage." *Chem. Soc. Rev.* **2006**, *35*, 675–683.

(28) McKeown, N. B.; Budd, P. M.; Msayib, K. J.; Ghanem, B. S.; Kingston, H. J.; Tattershall, C. E.; Makhseed, S.; Reynolds, K. J.; Fritsch, D. "Polymers of intrinsic microporosity (PIMs): Bridging the void between microporous and polymeric materials." *Chem.–Eur. J.* **2005**, *11*, 2610–2620.

(29) McKeown, N. B.; Budd, P. M. "Exploitation of Intrinsic Microporosity in Polymer-Based Materials." *Macromolecules* **2010**, *43*, 5163–5176.

(30) Chidambareswarapattar, C.; McCarver, P. M.; Luo, H.; Lu, H.; Sotiriou-Leventis, C.; Leventis, N. "Fractal multiscale nanoporous polyurethanes: flexible to extremely rigid aerogels from multifunctional small molecules." *Chem. Mater.* **2013**, *25*, 3205-3224.

(31) Chidambareswarapattar, C.; Xu, L; Sotiriou-Leventis, C.; Leventis, N. "Robust monolithic multiscale nanoporous polyimides and conversion to isomorphic carbons." *RSC Adv.* **2013**, *3*, 26459-26469.

(32) Leventis, N.; Sotiriou-Leventis, C.; Mohite, D. P.; Larimore, Z; Mang, J. T.; Churu, G.; Lu, H. "Polyimide aerogels by ring-opening metathesis polymerization (ROMP)." *Chem. Mater.* **2011**, *23*, 2250-2261.

(33) Bang, A.; Buback, C.; Sotiriou-Leventis, C.; Leventis, N. "Flexible aerogels from hyperbranched polyurethanes: probing the role of molecular rigidity with poly(urethane acrylates) versus poly(urethane norbornenes)." *Chem. Mater.* **2014**, *26*, 6979-6993.

(34) Mohite, D. P.; Mahadik-Khanolkar, S.; Luo, H.; Sotiriou-Leventis, C.; Leventis, N. "Polydicyclopentadiene aerogels grafted with PMMA: II. Nanoscopic characterization and origin of macroscopic deformation." *Soft Matter* **2013**, *9*, 1531-1539.

(35) Mohite, D. P.; Larimore, Z; Lu, H.; Mang, J. T.; Sotiriou-Leventis, C.; Leventis, N. "Monolithic hierarchical fractal assemblies of silica nanoparticles cross-linked with polynorbornene via ROMP: A structure−property correlation from molecular to bulk through nano." *Chem. Mater*. **2012**, *24*, 3434-3448.

(36) Mulik, S.; Sotiriou-Leventis, C.; Churu, G.; Lu, H.; Leventis, N. "Cross-linking 3D assemblies of nanoparticles into mechanically strong aerogels by surface-initiated free radical polymerization." *Chem. Mater.* **2008**, *20*, 5035-5046.

(37) Luo, H.; Churu, G.; Fabrizio, F. E.; Schnobrich, J.; Hobbs, A.; Dass, A.; Mulik, S.; Zhang, Y.; Grady, P. B.; Capecelatro, A.; Sotiriou-Leventis, C.; Leventis, N. "Synthesis and characterization of the physical, chemical and mechanical properties of isocyanate-crosslinked vanadia aerogels." *J Sol-Gel Sci Technol.* **2008**, *48*, 113-134.

(38) Mackenzie, K. J. D.; Smith, M. E. *Multinuclear Solid-State NMR of Inorganic Materials*. Pergamon, Materials Series Vol 6 (2002), ISBN 0080437877.

(39) Beaucage, G. "Approximations leading to a unified exponential/power-law approach to small-angle scattering." *J. Appl. Crystallogr.* **1995**, *28*, 717-728.

(40) Beaucage, G. "Small-angle scattering from polymeric mass fractals of arbitrary mass-fractal dimension." *J. Appl. Crystallogr.* **1996**, *29*, 134-146.

(41) Ilavsky, J.; Jemian, P. R. "*Irena*: tool suite for modeling and analysis of small-angle scattering." *J. Appl. Crystallogr.* **2009**, *42*, 347-353.

(42) Mejías, N.; Serra-Muns, A.; Pleixats, R.; Shafir, A.; Tristany, M. "Water-soluble metal nanoparticles with PEG-tagged 15-membered azamacrocycles as stabilizers." *Dalton Trans.* **2009**, 7748-7755.

SECTION

2. CONCLUSIONS

Polymeric aerogels similar in nanostructure and interparticle connectivity as those of polymer cross-linked silica aerogels were synthesized using isocyanate chemistry. Materials were synthesized using polyamide chemistry and they were studied and explored from an aerogels perspective.

In Paper I, polyamide aerogels (PA-xx) based on two multifunctional rigid aromatic monomeric have been prepared and their structure-property relationships have been examined. Chemical characterizations reveal that (PA-xx) is a statistical co-polymer of polyamide, polyurea, polyimide that also contained carbamic-anhydride intermediate. Multiscale monolithic polymeric aerogels may provide a sensible approach to the problem of packaging microporous materials in practical forms. Despite use of multifuncional monomers, only a small fraction of the surface area of PA-xx could be associated with micropores. However, successive thermal decomposition of the component polymers created both open and closed microporosity. Reactive etching opened access to closed pores, and the accessible micropore volume increased by four-fold. Such carbon aerogels demonstrated a good balance of adsorption capacity for CO_2 and selectivity towards other gasses; those attributes in combination with low monomer cost, and physicochemical stability, render those materials reasonable candidates for consideration in CO_2 capture and sequestration (CCS).

In Paper II, ferrocene polyamide (FcPA-xx) aerogels with ferrocene as a monomer repeat unit were prepared in one-step from ferrocene dicarboxylic acid and tris(4-isocyanatophenyl)methane. Pyrolysis at ≥800 ^{o}C yielded nanoporous carbons doped

throughout with crystallites of α-Fe shrouded in graphitic ribbons, which in turn were transmetalated with aqueous solutions of Au, Pt, Pd, Rh and Ni salts, via a path akin to galvanic corrosion, leaving behind empty cage-like formations previously occupied by the Fe(0) nanoparticles. All metal-doped carbons were monolithic, and their catalytic activity was demonstrated with a variety of different reactions. The distinguishing feature of those catalysts was that they could be just picked up, for example with a pair of tweezers, and re-deployed in a new reaction mixture without going through the time-consuming and expensive protocol of powder catalysts.

In Paper III, an attempt was made to synthesize polyboramide aerogels by reacting tris(4-isocyanatophenyl)methane with boric acid. Advanced chemical characterization techniques like prompt gamma neutron activation analysis (PGNNA) and solid-state ^{11}B NMR unveil that the boron content in those aerogels was very low ($\leq$0.05 % w/w), and was assigned to B_2O_3. Thus, any mechanism for systematic incorporation of boric acid in the polymeric chain, by analogy to carboxylic acids, was ruled out. The polymer identified was polyurea. We report a new route to polyurea via a range of mineral acids, (anhydrous H_3BO_3, H_3PO_4, H_3PO_3, H_2SeO_3, H_6TeO_6, H_5IO_6 and H_3AuO_3). On the positive side, the new polyurea route is a convenient method for *in situ* doping robust porous polymeric networks with oxide or pure metal nanoparticles (Au in the case of H_3AuO_3) that in combination with high elastic modulus, high ultimate strength, high specific energy absorption (toughness) relatively-low thermal conductivities and low cost render those materials reasonable candidates for commercial applications like for example in catalysis.

BIBLIOGRAPHY

1. http://www.aerogeltechnologies.com/about-aerogels (06-18-2016).

2. Aegerter, M. A.; Leventis, N.; Koebel, M. M. Aerogels Handbook; Springer: New York, NY, USA, **2011**.

3. Pierre, A. C.; Pajonk, G. M. Chemistry of Aerogels and their Applications. *Chem. Rev*. **2002**, *102*, 4243–4265.

4. (a) Baumann, T. F.; Gash, A. E.; Chinn, S. C.; Sawvel, A. M.; Maxwell, R. S.; Satcher, J. H. Synthesis of High-surface-area Alumina Aerogels without the Use of Alkoxide Precursors. *Chem. Mater*. **2005**, *17*, 395–401. (b) Baumann, T. F.; Kucheyev, S. O.; Gash, A. E.; Satcher, J. H. Facile Synthesis of a Crystalline, High-surface-area SnO_2 Aerogel. *Adv. Mater*. **2005**, *17*, 1546–1548. (c) Gash, A. E.; Satcher, J. H.; Simpson, R. L. Strong Akaganeite Aerogel Monoliths Using Epoxides: Synthesis and Characterization. *Chem. Mater*. **2003**, *15*, 3268–3275. (d) Gash, A. E.; Satcher, J. H.; Simpson, R. L. Monolithic Nickel (II)-Based Aerogels Using an Organic Epoxide: The Importance of the Counterion. *J. Non-Cryst. Solids* **2004**, *350*, 145–151. (e) Kucheyev, S. O.; Sadigh, B.; Baumann, T. F.; Wang, Y. M.; Felter, T. E.; van Buuren, T.; Gash, A. E.; Satcher, J. H.; Hamza, A. V. Electronic Structure of Chromia Aerogels from Soft X-ray absorption spectroscopy. *J. Appl. Phys.* **2007**, *101*, 124315:1–124315:8. (f) Gan, L. H.; Yue, T. Y.; Chen, L. W.; Li, G. M.; Zhou, B. Preparation and Characterization of beta-FeOOH Aerogels. *Acta Phys. Chim. Sin.* **1997**, *13*, 48–51.

5. (a) Pala, I. R.; Brock, S. L. ZnS Nanoparticle Gels for Remediation of Pb^{2+} and Hg^{2+} Polluted Water. *ACS Appl. Mater. Interfaces* **2012**, *4*, 2160–2167. (b) Ganguly, S.; Zhou, C.; Morelli, D.; Sakamoto, J.; Brock, S. L. Synthesis and Characterization of Telluride Aerogels: Effect of Gelation on Thermoelectric Performance of Bi_2Te_3 and $Bi_{2-x}Sb_xTe_3$ Nanostructures. *J. Phys. Chem. C.* **2012**, *116*, 17431–17439. (c) Yu, H.; Bellair, R.; Kannan, R. M.; Brock, S. L. Engineering Strength, Porosity, and Emission Intensity of Nanostructured CdSe Networks by Altering the Building-Block Shape. *J. Am. Chem. Soc.* **2008**, *130*, 5054–5055. (d) Kalebaila, K. K.; Georgiev, D. G.; Brock, S. L. Synthesis and Characterization of Germanium Sulfide Aerogels. *J. Non-Cryst. Solids* **2006**, *352*, 232–240. (e) Arachchige, I. U.; Brock, S. L. Sol-gel Assembly of CdSe Nanoparticles to Form Porous Aerogel networks. *J. Am. Chem. Soc*. **2006**, *128*, 7964–7971.

6. (a) Jones, S. M.; Flynn, G. Hypervelocity Capture of Meteoritic Particles in Nonsilica Aerogels. *Meteorit. Planet. Sci.* **2011**, *46*, 1253–1264. (b) Horz, F.; Bastien, R.; Borg, J.; Bradley, J. P.; Bridges, J. C.; Brownlee, D. E.; Burchell, M. J.; Chi, M. F.; Cintala, M. J.; Dai, Z. R.; *et al.* Impact Features on Stardust: Implications for Comet 81P/Wild 2 Dust. *Science* **2006**, *314*, 1716–1719.

7. (a) Zou, J. H.; Liu, J. H.; Karakoti, A. S.; Kumar, A.; Joung, D.; Li, Q. A.; Khondaker, S. I.; Seal, S.; Zhai, L. Ultralight Multiwalled Carbon Nanotube Aerogel. *ACS Nano* **2010**, *4*, 7293–7302. (b) Aliev, A. E.; Oh, J. Y.; Kozlov, M. E.; Kuznetsov, A. A.; Fang, S. L.; Fonseca, A. F.; Ovalle, R.; Lima, M.D.; Haque, M. H.; Gartstein, Y. N.; et al. Giant-Stroke, Superelastic Carbon Nanotube Aerogel Muscles. *Science* **2009**, *323*, 1575–1578.

8. (a) Xu, Z.; Zhang, Y.; Li, P. G.; Gao, C. Strong, Conductive, Lightweight, Neat Graphene Aerogel Fibers with Aligned Pores. *ACS Nano* **2012**, *6*, 7103–7113. (b) Worsley, M. A.; Pauzauskie, P. J.; Olson, T. Y.; Biener, J.; Satcher, J. H.; Baumann, T. F. Synthesis of Graphene Aerogel with High Electrical Conductivity. *J. Am. Chem. Soc.* **2010**, *132*, 14067–14069.

9. (a) Chen, K.; Bao, Z. H.; Liu, D.; Zhu, X. R.; Zhang, Z. H.; Zhou, B. Confined Synthesis and Properties of Porous Silicon from Silica Aerogel Templates by Magnesiothermic Reduction. *Acta Phys. Chim. Sin.* **2011**, *27*, 2719–2725 (b) Leventis, N.; Sadekar, A.; Chandrasekaran, N.; Sotiriou-Leventis, C. Click Synthesis of Monolithic Silicon Carbide Aerogels from Polyacrylonitrile-coated 3D Silica Networks. *Chem. Mater.* **2010**, *22*, 2790–2803. (c) Worsley, M. A.; Kuntz, J. D.; Pauzauskie, P. J.; Cervantes, O.; Zaug, J. M.; Gash, A. E.; Satcher, J. H.; Baumann, T. F. High surface Area Carbon Nanotube-supported Titanium Carbonitride Aerogels. *J. Mater. Chem.* **2009**, *19*, 5503–5506.

10. http://www.aerogel.org/?p=3 (06-18-2016)

11. Wagh, P.; Begag, R.; Pajonk, G.; Rao, A.V.; Haranath, D. Comparison of Some Physical Properties of Silica Aerogel Monoliths Synthesized by Different Precursors. *Mater. Chem. Phys.* **1999**, *57*, 214–218.

12. Du, A.; Zhou, B.; Zhang.; Z.; Shen, J. A Special Material or a New State of Matter: A Review and Reconsideration of the Aerogel. *Materials*. **2013**, *6*, 941–968.

13. http://science.howstuffworks.com/aerogel1.htm, (09-15-2015).

14. Hench, L. L.; West, J. K. The Sol-Gel Process. *Chem. Rev*. **1990**, *90*, 33–72.

15. Brinker, C.; Scherer, G. Sol-Gel Science: The Physics and Chemistry of Sol-Gel Processing. Academic Press, Inc. New York, NY, USA, **1990**.

16. Livage, J.; Sanchez, C. Sol-Gel Chemistry. *J. Non-Cryst. Solids.* **1992**, *145*, 11–19.

17. (a) Zarzycki, J.; Prassas, M.; Phalippou, J. Synthesis of Glasses from Gels: The Problem of Monolithic Gels. *J. Mat. Sci.* **1982**, *17*, 3371–3379. (b) Tewari, P. H.; Hunt, A. J.; Lofftus, K. D. Ambient-Temperature Supercritical Drying of Transparent Silica Aerogels. *Mater. Lett.* **1985**, *3*, 363–367.

18. Wittwer, V. Development of Aerogel Windows. *J. Non-Cryst. Solids* **1992**, *145*, 233–236. (b) Gerlach, R.; Kraus, O.; Fricke, J.; Eccardt, P. C.; Kroemer, N.; Magori, V. Modified SiO_2 Aerogels as Acoustic Impedance Matching Layers in Ultrasonic Devices. *J. Non-Cryst. Solids* **1992**, *145*, 227–232.

19. Jo, M. H.; Park, H. H. Leakage Current and Dielectric Breakdown Behavior in Annealed SiO_2 Aerogel Films. *Appl. Phys. Lett.* **1998**, *72*, 1391–1393.

20. Pajonk, G. M. Aerogel Catalysts. *Appl. Catal*. **1991**, *72*, 217–266.

21. Morris, C. A.; Anderson, M. L.; Stroud, R. M.; Merzbacher, C. I.; Rolison, D. R. Silica Sol as a Nanoglue: Flexible Synthesis of Composite Aerogels. *Science* **1999**, *284*, 622–624.

22. (a) daCunha, J. P.; Neves, P.; Lopes, M. On the Reconstruction of Cherenkov Rings from Aerogel Radiators. *Nucl. Instrum. Methods Phys. Res., Sect. A* **2000**, *452*, 401–421. (b) http://ammtiac.alionscience.com/ammt/iacdocs.do?AM034027.

23. Woignier, T.; Phalippou, J. *J. Rev. Phys. Appl.* **1989**, *24*, 179–184.

24. (a) Katti, A.; Shimpi, N.; Roy, S.; Lu, H.; Fabrizio, E. F.; Dass, A.; Capadona, L. A.; Leventis, N. Chemical, Physical, and Mechanical Characterization of Isocyanate Cross-linked Amine-Modified Silica Aerogels. *Chem. Mater*. **2006**, *18*, 285–296. (b) Meador, M. A.; Capadona, L. A.; McCorkle, L.; Papadopoulos, D. S.; Leventis, N. Structure−Property Relationships in Porous 3D Nanostructures as a Function of Preparation Conditions: Isocyanate Cross-Linked Silica Aerogels. *Chem. Mater*. **2007**, *19*, 2247–2260. (c) Ilhan, U. F.; Fabrizio, E. F.; McCorkle, L.; Scheiman, D. A.; Dass, A.; Palczer, A.; Meador, M. A. B.; Johnston, J. C.; Leventis, N. Hydrophobic Monolithic Aerogels by Nanocasting Polystyrene on Amine-Modified Silica. *J. Mater. Chem.* **2006**, *16*, 3046–3054. (d) Mulik, S.; Sotiriou-Leventis, C.; Churu, G.; Lu, H.; Leventis, N. Cross-Linking 3D Assemblies of Nanoparticles into Mechanically Strong Aerogels by Surface-Initiated Free-Radical Polymerization. *Chem. Mater*. **2008**, *20*, 5035–5046.

25. Husing, N.; Schubert, U.; Mezer, R.; Fratzl, P.; Riegel, B.; Kiefer, W.; Kohler, D.; Mader, W. Formation and Structure of Gel Networks from $Si(OEt)_4/(MeO)_3Si(CH_2)_3NR'_2$ Mixtures ($NR'_2 = NH_2$ or $NHCH_2CH_2NH_2$) *Chem. Mater*. **1999**, *11*, 451–457.

26. Meador, M. A. B.; Fabrizzio, E. F.; Ilhan, F.; Dass, A.; Zhang, G.; Vassilaras, P.; Johnston, J. C.; Leventis, N. "Cross-linking Amine-Modified Silica Aerogels with Epoxies: Mechanically Strong Lightweight Porous Materials," Chem. Mater. **2005**, 17, 1085–1098.

27. (a) Leventis, N. Three-Dimensional Core-Shell Superstructures: Mechanically Strong Aerogels. *Acc. Chem. Res*. **2007**, *40*, 874–884. (b) Leventis, N.; Mulik, S.; Wang, X.; Dass, A.; Sotiriou-Leventis, C.; Lu, H. Stresses at the Interface of Micro with Nano. *J. Am. Chem. Soc*. **2007**, *129*, 10660-10661. (c) Leventis, N.; Sotiriou-Leventis, C.; Zhang, G.; Rawashdeh, A.-M. M. Nano Engineering Strong Silica Aerogels. *NanoLetters* **2002**, *2*, 957–960.

28. Lee, S. T.; Ramesh, N. S. In *Polymeric Foams: Mechanism and Materials*. CRC Press: Florida, **2004**, pp 150–267.

29. Saunders, J. H.; Frisch, K. C. In *Polyurethane Chemistry and Technology I. Chemistry*, Interscience publishers, New York, NY, USA, **1963**, pp 63–118.

30. (a) Furukawa, I.; Hashiyama, M.; Hashimoto, S. Synthesis of Polymaides with [(1,2,3-benzotriazine-4-one(-3-yl]diphenyl phosphate as a New Activating Agent. *J. Macromo. Sci.–Chem.* **1985**, *A26*, 761–771. (b) Onder, K.; Chen, A. T. A New Semicrystalline Reinforced Polyamide Engineering Thermoplastic. *Polym. Eng. Sci.* **1985**, *25*, 942–946. (c) Simionescu, C.; Comaniţă, E.; Vâcţă, M. Amides and Polyamides of m-phenylenedioxydiacetic acid. *Angew. Makromol. Chem.* **1975**, *46*, 135–142.

31. (a) Onder, K.; Smith, C. P. Catalytic Condensation of Isocyanates and Carboxylic acids or Anhydrides. U. S. Patent No. 4,156,065, **1979**. (b) Toyoda, T.; Kawamata, M.; Osawa, M.; Itoh, M.; Mizutani, K. Process for the Preparation of Polyamide Compounds by the Reaction of Polycarboxylic Acids with Diisocyanates in the Presence of at Least One Mono-Alkali Metal Salt of Dicarboxylic Acid. U. S. Patent No. 4,395,531. **1983**.

32. Wei, Y.; Jia, X.; Jin, D.; Davis, F. A. A Facile Synthesis of Polyamides from Aromatic Diisocyanates and Dicarboxylic Acid Catalyzed by Lewis Acids. *Macromol. Rapid Commun*. **1996**, *17*, 897–903.

33. Ahmad, Z.; Sarwar, M. I.; Mark, J. E. Chemically Bonded Silica–Polymer Composites from Linear and Branched Polyamides in a Sol–Gel Process. *J. Mater Chem*. **1997**, *7*, 259–263.

34. (a) Wicks, Z. W. Jr.; Jones, F. N.; Pappas, S. P. In *Organic Coatings, Science & Technology*. Wiley-Interscience: New York, **1999**, p 180. (b) Odian, G. In *Principle of Polymerization*. Wiley-Interscience: New York, **2004**.

35. Omae, I. *Applications of Organometallic Compounds.* John Wiley & Sons Inc. **1998**.

36. Zeng, Y.; Feng, H.; Xie, Y.; King, R. B.; Schaefer III, H. F. Eu. Sandwich Compounds of the First-Row Transition Metals (M, M′ = Fe, Co, Ni) Containing a Metallacyclopentadiene Ring. *J. Inorg. Chem*. **2013**, *12*, 2070–2077. (b) Pauson, P. L. Ferrocene —How it All Began. *J. Organomet. Chem*. **2001**, *3*, 637–639.

37. (a) Iqbal, N.; Akhter, Z.; Saeed, M. A.; Khan, M. S. Synthesis and Characterization of Some Novel Organometallic Aromatic Polyamides. *Appl. Organometal. Chem*. **2006**, *20*, 344–350. (b) Iqbal, N.; Saeed, M. A.; Khan, M. S.; Akhter, Z. Synthesis and Physicochemical Studies of Ferrocene-Containing Materials. *Appl. Organometal. Chem.* **2007**, *21*, 862–869.

38. (a) Miriuchi, T.; Nomoto, A.; Yoshida, K.; Ogawa, A.; Hirao T. Chirality Organization of Ferrocenes Bearing Podand Dipeptide Chains: Synthesis and Structural Characterization. *J. Am. Chem. Soc*., **2001**, *123*, 68–75. (b) Semencic, M. C.; Siebler, D.; Heinze K.; Rapic, V. Bis- and Trisamides Derived From 1′-Aminoferrocene-1-Carboxylic Acid and α-Amino Acids: Synthesis and Conformational Analysis. *Organometallics*, **2009**, *28*, 2028–2037.

39. Knobloch, F. W.; Rauscher, W. H. Condensation Polymers of Ferrocene Derivatives. *J. Polym. Sci. Part A.* **1961**, *54*, 651–656.

40. Consalves, K.; Zhanru, L.; Rausch, M. D. Ferrocene-Containing Polyamides and Polyureas. *J. Am. Chem. Soc.* **1984**, *106*, 3862–3863.

41. Javed, F.; Altaf, A. A.; Badshah, A.; Tahir, M. N.; Siddique, M.; Rehman, Z.; Shah, A.; Ullah, S.; Lal, B. New Supramolecular Ferrocenyl Amides: Synthesis, Characterization, and Preliminary DNA-Binding Studies. *J. Coord. Chem*. **2012**, *65*, 969–979.

42. Zhang, J.; Zhao, L.; Song, M.; Mak, T. C. W.; Wu, Y. Highly Efficient Cyclopalladated Ferrocenylimine Catalyst for Suzuki Cross-Coupling Reaction of 3-Pyridylboronic Pinacol Ester with Aryl Halides. *Journal of Organometallic Chemistry*. **2006**, *691*, 1301–1306.

43. Zhang, J.; Yan, B.; Wu, H.; Kong, Q. Self-assembled Synthesis of Carbon-Coated Fe_3O_4 Composites with Firecracker-Like Structures from Catalytic Pyrolysis of Polyamide. *RSC Adv.* **2014**, *4*, 6991–6997.

44. Bernard, S.; Miele, P. Polymer-Derived Boron Nitride: A Review on the Chemistry, Shaping and Ceramic Conversion of Borazine Derivatives. *Materials* **2014**, *7*, 7436–7459.

45. Robert, W. U. Polymeric Boronamides. US Patent 2,517,944, **1946**.

46. Robert, S. A. Polymers from Boric Acid and Organic Diisocyanates. US Patent 2,945,841, **1960.**

47. Kumar, R.; Lebedinski, N. Modified Isocyanate Compositions and Methods of Preparing the Same, US Patent 0245222 A1, **2013**.

48. Leventis, N.; Chidambareswarapattar, C.; Mohite, D. P.; Larimore, Z. J.; Lu, H.; Sotiriou-Leventis, C. Multifunctional Porous Aramids (Aerogels) by Efficient Reaction of Carboxylic Acids and Isocyanates. *J. Mater. Chem.* **2011**, *21*, 11981–11986.

49. Williams, J. C.; Meador, M. A.; McCorkle, L.; Mueller, C.; Wilmoth, N. Synthesis and Properties of Step-Growth Polyamide Aerogels Crosslinked with Triacid Chlorides. *Chem. Mater.* **2014**, *26*, 4163−4171.

50. Lee, J.; Kim, J.; Hyeon, T. Recent Progress in the Synthesis of Porous Carbon Materials. *Adv. Mater*. **2006**, *18*, 2073–2094.

51. Liang, C.; Li, Z.; Dai, S. Mesoporous Carbon Materials: Synthesis and Modification. *Angew. Chem., Int. Ed.* **2008**, *47*, 3696−3717. (b) White, R. J.; Budarin, V.; Luque, R.; Clark, J. H.; Macquarriea, D. J. Tuneable Porous Carbonaceous Materials from Renewable Resources. *Chem. Soc. Rev.* **2009**, *38*, 3401−3418. (c) Hanai, T. Separation of Polar Compounds Using Carbon Columns. *J. Chromatogr. A* **2003**, *989*, 183−196.

52. Kabbour, H.; Baumann, T. F.; Satcher, J. H.; Saulnier, A.; Ahn, C. C. Toward New Candidates for Hydrogen Storage: High-Surface-Area Carbon Aerogels. *Chem. Mater*. **2006**, *18*, 6085−6087.

53. Marques, L. M.; Carrott, P. J. M.; Ribeiro Carrott, M. M. L. Amine-Modified Carbon Aerogels for CO_2 Capture. *Adsorpt. Sci. Technol*. **2013**, *31*, 223–232.

54. (a) Antolini, E. Carbon Supports for Low-Temperature Fuel Cell Catalysts. *Appl. Catal. B* **2009**, *88*, 1–24. (b) Stüber, F.; Font, J.; Fortuny, A.; Bengoa, C.; Eftaxias, A.; Fabregat, A. Carbon Materials and Catalytic Wet Air Oxidation of Organic Pollutants in Wastewater. *Top. Catal*. **2005**, *33*, 3–50.

55. Gaweł, B.; Gaweł, K.; Øye, G. Sol-Gel Synthesis of Non-Silica Monolithic Materials. Materials. **2010**, *3*, 2815–2833.

56. (a) Davis.; M. E. Ordered Porous Materials for Emerging Applications. *Nature* **2002**, *417*, 813–821. (b) Yuan.; Z. Y, Su.; B. L. Insights into Hierarchically Meso–Macroporous Structured Materials. *J. Mater. Chem*. **2006**, *16*, 663–667.

57. Pekala.; R. W. Organic Aerogels from the Polycondensation of Resorcinol with Formaldehyde. *J. Mater. Sci.* **1989**, *24*, 3221–3227.

58. Mulik, S.; Sotiriou-Leventis, C.; Leventis, N. Time-Efficient Acid-Catalyzed Synthesis of Resorcinol−Formaldehyde Aerogels. *Chem. Mater*. **2007**, *19*, 6138−6144.

59. Leventis, N.; Sotiriou-Leventis, C.; Chandrasekaran, N.; Mulik, S.; Larimore, Z. J.; Lu, H.; Churu, G.; Mang, J. T. Multifunctional Polyurea Aerogels from Isocyanates and Water. A Structure-Property Case Study. *Chem. Mater*. **2010**, *22*, 6692–6710.

60. Chidambareswarapattar, C.; McCarver, P. M.; Luo, H.; Lu, H.; Sotiriou-Leventis, C.; Leventis, N. Fractal Multiscale Nanoporous Polyurethanes: Flexible to Extremely Rigid Aerogels from Multifunctional Small Molecules. *Chem. Mater*. **2013**, *25*, 3205–3224.

61. Chidambareswarapattar, C.; Xu, L.; Sotiriou-Leventis, C.; Leventis, N. Robust Monolithic Multiscale Nanoporous Polyimides and Conversion to Isomorphic Carbons. *RSC Adv.* **2013**, *3*, 26459−26469.

62. Maldonado-Hódar, F. J.; Moreno-Castilla, C.; Rivera-Utrilla, J.; Hanzawa, Y.; Yamada Y. Catalytic Graphitization of Carbon Aerogels by Transition Metals. *Langmuir* **2000**, *16*, 4367–4373.

63. Moreno-Castilla, C.; Maldonado-Ho'dar, F. J. Carbon Aerogels for Catalysis Applications: An Overview. *Carbon* **2005**, *43*, 455–465.

64. Kolla, P.; Kerce, K.; Zhao,Y.; Houk, J.; Normah, Y.; Rhine, W.; Smirnova, A. Iron Modified Graphitized Carbon Aerogels for Sustainable Energy Applications. *Mater. Res. Symp. Proc.* **2013**, 1491.

65. Fort, C. I.; Cotet, L. C.; Danciu, V.; Turdean, G. L.; Popescu, I. C. Iron Doped Carbon Aerogel – New Electrode Material for Electrocatalytic Reduction of H_2O_2. *Mater. Chem. Phys.* **2013**, *138*, 893–898.

66. Steiner, S. A.; Baumann, T. F.; Kong, J.; Satcher Jr., J. H.; Dresselhaus, M. S. Iron-Doped Carbon Aerogels: Novel Porous Substrates for Direct Growth of Carbon Nanotubes. *Langmuir* **2007**, *23*, 5161–5166.

67. Kealy, T. J.; Pauson, P. L. A New Type of Organo-Iron Compound. *Nature* **1951**, *168*, 1039-1040.

68. Lu, Y.; Zhu, Z.; Liu, Z. Carbon-Encapsulated Fe Nanoparticles from Detonation-Induced Pyrolysis of Ferrocene. *Carbon* **2005**, *43*, 369–374.

69. Furukawa, H.; Hibino, M.; Zhou, H. S.; Honma, I. Synthesis of Mesoporous Carbon-Containing Ferrocene Derivative and Its Electrochemical Property. *Chem. Lett*. **2003**, *32*, 132–133.

70. Schnitzler, M. C.; Oliveira, M. M.; Ugarte, D.; Zabrin, A. J. G. One-Step Route to Iron Oxide-Filled Carbon Nanotubes and Bucky-Onions Based on the Pyrolysis of Organometallic Precursors. *Chem. Phys. Lett*. **2003**, *381*, 541–548.

71. Ndamanisha, J. C.; Hou, Y.; Bai, J.; Guo, L. Effects of Ferrocene Derivative on the Physico-Chemical and Electrocatalytic Properties of Ordered Mesoporous Carbon. *Electrochim. Acta*. **2009**, *54*, 3935–3942.

72. Wang, M.; Wang, J.; Qiao, W.; Ling, L.; Long, D. Scalable Preparation of Nitrogen-enriched Carbon Microspheres for Efficient CO_2 Capture. *RSC Adv.* **2014**, *4*, 61456−61464.

73. Mikroyannidis. J. A. Comparison of the properties of the polyimides, polyamides and polyureas derived from 1-[(dialkoxyphosphinyl)-methyl]-2,4- and -2,6-diaminobenzenes and *m*-phenylenediamine. *Eur. Polym. J.* **1986**, *22*, 277–284.

74. Jenkins, G. M.; Kawamura, K. In Polymeric Carbons, Carbon Fibre, Glass and Char; Cambridge University Press: New York, **1976**.

75. Banerjee, R.; Phan, A.; Wang, B.; Knobler, C.; Furukawa, H.; O'Keeffe, M.; Yaghi, O. M. High-Throughput Synthesis of Zeolitic Imidazolate Frameworks and Application to CO_2 Capture. *Science* **2008**, *319*, 939–943.

76. Sun, Z.; Yan, Z.; Yao. J.; Beitler, E.; Zhu, Y.; Tour, J. M. Growth of Graphene from Solid Carbon Sources. *Nature* **2010**, *468*, 549–552.

77. Papadimitriou, S.; Tegou, A.; Pavlidou, E.; Armyanov, S.; Valova, E.; Kokkinidis, G.; Sotiropoulos, S. Preparation and Characterisation of Platinum- and Gold-Coated Copper, Iron, Cobalt and Nickel Deposits on Glassy Carbon Substrates. *Electrochim. Acta* **2008**, *53*, 6559–6567.

78. (a) Jagadeesh, R. V.; Wienhöfer, G.; Westerhaus, F. A.; Surkus, A.-E.; Pohl, M.-M.; Junge, H.; Junge, K.; Beller, M. Efficient and Highly Selective Iron-Catalyzed Reduction of Nitroarenes. *Chem. Commun*. **2011**, *47*, 10972–10974. (b) Ng, Y. H.; Ikeda, S.; Harada, T.; Morita, Y.; Matsumura, M. An Efficient and Reusable Carbon-Supported Platinum Catalyst for Aerobic Oxidation of Alcohols in Water. *Chem. Commun*. **2008**, 3181–3183. (c) Anderson, K.; Fernández, S. C.; Hardacre, C.; Marr, P. C. Preparation of Nanoparticulate Metal Catalysts in Porous Supports Using an Ionic Liquid Route; Hydrogenation and C–C Coupling. *Inorg. Chem. Commun.* **2004**, *7*, 73–76.

VITA

Malik Adnan Saeed, a native of Islamabad, Pakistan, received his Master of Philosophy in materials chemistry from Quaid-i-Azam University Islamabad, in 2005. He worked for two years as a quality control chemist with Chevron Global Lubricants, and in 2007 he joined the National Engineering and Scientific Commission, Pakistan (NESCOM), where he was employed until 2011 as a Manager. In the fall of 2011, he came to the United States to pursue his Ph.D. degree in chemistry under Prof. Nicholas Leventis at the Missouri University of Science and Technology. His research work focused on functional organic aerogels. During the course of his Ph.D. work, he published three journal articles, he has submitted one more article for publication, and has presented his research in numerous National ACS Meetings. He won the Chemistry Department's Best Teaching Assistant Award in 2014, and the Best Graduate Researcher Award in 2016. He was co-inventor in one issued U.S. patent, and in five U.S. and E.U. patent applications, all based on his dissertation work. He defended his Ph.D. dissertation on October 10, 2016 and was awarded with the PhD degree in December 2016.